

# **ACTIVE CONTROL OF RADIATED SOUND WITH INTEGRATED PIEZOELECTRIC COMPOSITE STRUCTURES**

## **FINAL REPORT**

**VOLUME III  
APPENDICES (CONCL.)**

**OFFICE OF NAVAL RESEARCH  
PROJECT NO. N00014-94-1-1140**

**19981204  
020**

**APPROVED FOR PUBLIC RELEASE  
DISTRIBUTION UNLIMITED**

CHRISTOPHER R. FULLER  
VIBRATION AND ACOUSTICS LABORATORIES  
VIRGINIA POLYTECHNIC INSTITUTE AND STATE UNIVERSITY

L. ERIC CROSS  
MATERIALS RESEARCH LABORATORY  
THE PENNSYLVANIA STATE UNIVERSITY



VIRGINIA POLYTECHNIC INSTITUTE AND STATE UNIVERSITY

**Reproduced From  
Best Available Copy**

## REPORT DOCUMENTATION PAGE

Form Approved  
OMB No. 0704-0188

Public reporting burden for this collection of information is estimated to average 1 hour per response, including the time for reviewing instructions, searching existing data sources, gathering and maintaining the data needed, and completing and reviewing the collection of information. Send comments regarding this burden estimate or any other aspect of this collection of information, including suggestions for reducing this burden, to Washington Headquarters Services, Directorate for Information Operations and Reports, 1215 Jefferson Davis Highway, Suite 1204, Arlington, VA 22202-4302, and to the Office of Management and Budget, Paperwork Reduction Project (0704-0188), Washington, DC 20503.

1. AGENCY USE ONLY (Leave blank)	2. REPORT DATE	3. REPORT TYPE AND DATES COVERED	
	6 -November 1998	Final Report, 9/15/94 - 3/31/98	
4. TITLE AND SUBTITLE  Active Control of Radiated Sound with Integrated Piezoelectric Composite Structures		5. FUNDING NUMBERS	
6. AUTHOR(S)  C. R. Fuller and L. E. Cross			
7. PERFORMING ORGANIZATION NAME(S) AND ADDRESS(ES)  Vibration and Acoustics Laboratories, Department of Mechanical Engineering VPI & SU, Blacksburg, VA 24061		8. PERFORMING ORGANIZATION REPORT NUMBER	
9. SPONSORING/MONITORING AGENCY NAME(S) AND ADDRESS(ES)  Dr. Kam Ng Office of Naval Research Code 334 800 North Quincy Street Arlington, VA 22217		10. SPONSORING/MONITORING AGENCY REPORT NUMBER	
11. SUPPLEMENTARY NOTES			
12a. DISTRIBUTION / AVAILABILITY STATEMENT		12b. DISTRIBUTION CODE	
13. ABSTRACT (Maximum 200 words)  See Following Pages			
14. SUBJECT TERMS		15. NUMBER OF PAGES	
		16. PRICE CODE	
17. SECURITY CLASSIFICATION OF REPORT	18. SECURITY CLASSIFICATION OF THIS PAGE	19. SECURITY CLASSIFICATION OF ABSTRACT	20. LIMITATION OF ABSTRACT

**GENERAL INSTRUCTIONS FOR COMPLETING SF 298**

The Report Documentation Page (RDP) is used in announcing and cataloging reports. It is important that this information be consistent with the rest of the report, particularly the cover and title page. Instructions for filling in each block of the form follow. It is important to stay *within the lines* to meet optical scanning requirements.

**Block 1. Agency Use Only (Leave blank).**

**Block 2. Report Date.** Full publication date including day, month, and year, if available (e.g. 1 Jan 88). Must cite at least the year.

**Block 3. Type of Report and Dates Covered.**

State whether report is interim, final, etc. If applicable, enter inclusive report dates (e.g. 10 Jun 87 - 30 Jun 88).

**Block 4. Title and Subtitle.** A title is taken from the part of the report that provides the most meaningful and complete information. When a report is prepared in more than one volume, repeat the primary title, add volume number, and include subtitle for the specific volume. On classified documents enter the title classification in parentheses.

**Block 5. Funding Numbers.** To include contract and grant numbers; may include program element number(s), project number(s), task number(s), and work unit number(s). Use the following labels:

C - Contract	PR - Project
G - Grant	TA - Task
PE - Program Element	WU - Work Unit
	Accession No.

**Block 6. Author(s).** Name(s) of person(s) responsible for writing the report, performing the research, or credited with the content of the report. If editor or compiler, this should follow the name(s).

**Block 7. Performing Organization Name(s) and Address(es).** Self-explanatory.

**Block 8. Performing Organization Report Number.** Enter the unique alphanumeric report number(s) assigned by the organization performing the report.

**Block 9. Sponsoring/Monitoring Agency Name(s) and Address(es).** Self-explanatory.

**Block 10. Sponsoring/Monitoring Agency Report Number. (If known)**

**Block 11. Supplementary Notes.** Enter information not included elsewhere such as: Prepared in cooperation with...; Trans. of...; To be published in.... When a report is revised, include a statement whether the new report supersedes or supplements the older report.

**Block 12a. Distribution/Availability Statement.**

Denotes public availability or limitations. Cite any availability to the public. Enter additional limitations or special markings in all capitals (e.g. NOFORN, REL, ITAR).

DOD - See DoDD 5230.24, "Distribution Statements on Technical Documents."

DOE - See authorities.

NASA - See Handbook NHB 2200.2.

NTIS - Leave blank.

**Block 12b. Distribution Code.**

DOD - Leave blank.

DOE - Enter DOE distribution categories from the Standard Distribution for Unclassified Scientific and Technical Reports.

NASA - Leave blank.

NTIS - Leave blank.

**Block 13. Abstract.** Include a brief (*Maximum 200 words*) factual summary of the most significant information contained in the report.

**Block 14. Subject Terms.** Keywords or phrases identifying major subjects in the report.

**Block 15. Number of Pages.** Enter the total number of pages.

**Block 16. Price Code.** Enter appropriate price code (*NTIS only*).

**Blocks 17. - 19. Security Classifications.** Self-explanatory. Enter U.S. Security Classification in accordance with U.S. Security Regulations (i.e., UNCLASSIFIED): If form contains classified information, stamp classification on the top and bottom of the page.

**Block 20. Limitation of Abstract.** This block must be completed to assign a limitation to the abstract. Enter either UL (unlimited) or SAR (same as report). An entry in this block is necessary if the abstract is to be limited. If blank, the abstract is assumed to be unlimited.

## ABSTRACT

The work investigated in this URI project is concerned with the active control of radiated sound using advanced structural systems with fully integrated actuators and sensors driven by realistic forms of disturbances. The overall goal was to demonstrate active control of sound radiated from vibrating structures with a *fully integrated, practical* active material including multiple actuators and sensors. This ultimately implies addressing the requirements for realistic active structures with integrated actuators and sensors as well as developing new sensing, control theory and design approaches so that the active material systems can be correctly and efficiently implemented.

This report summarizes three years of research work to achieve these goals. The work was evenly split between two main groups. The Materials Research Laboratory (MRL) at Penn State University addressed the development and construction of a suitable actuator system. The Vibration and Acoustics Laboratories (VAL) at Virginia Tech focussed upon developing new approaches for radiation control, system component development and integration and integrated system testing and demonstration. The work essentially followed a general theme of continual component development, system integration and testing through various phases tightly coordinated between MRL and VAL.

The two core technologies of the project were a new air piezoceramic actuator system conceived and developed by MRL and a new radiation control approach based upon a continuous active skin conceived and developed by VAL.

The report describes work by MRL-PSU on developing and constructing a new actuator called PANEL based upon using double amplification obtained from a system of orthogonal bimorph piezoelectric elements covered with an acoustic diaphragm configured in a flexensional type manner. The resultant PANEL source after many iterations of analysis, development, construction and testing was found to provide amplification ratios of around 250:1 and generate diaphragm vibration levels of the order of 500 microns (on resonance) and 200 microns (off resonance) over a frequency range of 0 to 1500Hz. The corresponding sound pressure levels generated by the PANEL source at 1m ranged from 80dB at 200Hz to 90dB above 400Hz. These performance levels were considered high enough to enable the PANEL source to be applied to a number of practical noise problems such as interior noise in aircraft and cars as well as electrical transformer noise and jet engine inlet noise. For applications below 200Hz, where the performance of the PANEL falls off, a new pseudo-shear multi-layer actuator utilizing folded multi-layer piezoelectric elements was developed and tested. The new pseudo-shear actuator was found to have significantly enhanced very low frequency performance below 200Hz.

The report also describes the new active noise control approach based upon implementing an active-skin which completely covers the structure conceived by VAL-

VPI. In the VAL part of the project, multiple PANEL actuators were integrated into a continuous skin system with independently controllable sections. A new structural acoustic sensing approach which enable the integration of sensors directly into the skin and yet allowed estimation of far-field sound radiation was developed and implemented in the active skin system. New control approaches and system optimization and design approaches were developed and used to efficiently configure and control the skin system. New active-passive approaches, which take advantage of the system natural dynamics to lower control authority requirements and increase robustness, were investigated. Finally the component technologies were integrated into an active skin approach designed to control broadband sound radiation from a test panel. The active skin system with integrated sensors was tested and found to provide total attenuation of the plate radiated sound power of 7.3dB over a bandwidth from 200 to 600Hz. This bandwidth encompasses multiple plate mode resonances. In order to handle the very low frequency region below 200Hz a new distributed active vibration absorber was implemented and tested. The work has demonstrated the high potential of an active skin with integrated piezoelectric amplifier elements and structural sensors for controlling structurally radiated sound with realistic loads.

The report is divided into two main parts. The first part summarizes work at MRL-PSU on developing the new actuator systems. The second part describes the system integration and testing performed at VAL-VPI. Throughout the report, reference is made to a set of published papers which describe the project work in detail. These papers are provided for convenience of the reader in Appendices at the end of the report.

## APPENDICES

1. "Piezoelectric Air Transducer for Active Noise Control," B. Xu, Q. Zhang, V.D. Kugel, and L.E. Cross. *Smart Structures and Materials: SPIE 2717*, 388-398(1996).
2. "Bimorph Based Piezoelectric Air Acoustic Transducer Model," V.D. Kugel, B. Xu, Q.M. Zhang, and L.E. Cross. *Sensors and Actuators A69*, 234-242(1998).
3. "Optimization of Bimorph Based Double Amplifier Actuators under Quasistatic Conditions," B. Xu, Q.M. Zhang, V.D. Kugel, Q.-M. Wang, and L.E. Cross. *Proc. of Tenth IEEE International Symposium on Application of Ferroelectrics 1*, 217 (1996).
4. "Crescent: A Novel Piezoelectric Bending Actuator," S. Chandran, V.D. Kugel, and L.E. Cross. *Smart Structures and Materials: SPIE 2717*, 522-530 (1996).
5. "Dynamic Characteristics of Rainbow Ceramics," C. Elissalde and L.E. Cross. *J. Am. Ceram. Soc. 78* (8), 2233-2235 (1995).
6. "Characterization of the Linear and Non-Linear Dynamic Performance of RAINBOW Actuator," S. Chandran, V.D. Kugel, and L.E. Cross. *Proc. of Tenth IEEE International Symposium on Application of Ferroelectrics 2*, 743-746 (1996).
7. "Structural-Property Relations in a Reduced and Internally Biased Oxide Wafer (RAINBOW) Actuator Material," C. Elissalde, L.E. Cross, and C.A. Randall. *J. Am. Ceram. Soc. 8*, 2041-2048 (1996).
8. "Determination of the Young's Modulus of the Reduced Layer of a Piezoelectric RAINBOW Actuator," Q.-M. Wang and L.E. Cross. *J. Appl. Phys. 83* (10), 5358-5363 (1998).
9. "Caterpillar-Type Piezoelectric  $d_{33}$  Bimorph Transducer," V.D. Kugel, S. Chandran, and L.E. Cross. *Appl. Phys. Lett. 69* (14), 2021-2023 (1996).
10. "Characteristics of Shear Mode Piezoelectric Actuators," Q.-M. Wang, B. Xu, V.D. Kugel, and L.E. Cross. *Proc. of Tenth IEEE International Symposium on Application of Ferroelectrics 2*, 767-770 (1996).
11. "A Comparative Analysis of Piezoelectric Bending Mode Actuators," V.D. Kugel, S. Chandran, and L.E. Cross. *Smart Structures and Materials: SPIE 3040*, 9-19 (1997).

12. "Behavior of Piezoelectric Actuators Under High Electric Field," V.D. Kugel, Q.M. Zhang, B. Xu, Q.-M. Wang, S. Chandran, and L.E. Cross. *Proc. of Tenth IEEE International Symposium on Application of Ferroelectrics* 2, 655-659 (1996).
13. "Behavior of Soft Piezoelectric Ceramics Under High Sinusoidal Electric Fields," V.D. Kugel and L.E. Cross. *J. Appl. Phys.* 84 (5), 2815-2830 (1998).
14. "A Piezoelectric Pseudo-Shear Multilayer Actuator," Q.-M. Wang and L.E. Cross. *App. Phys. Lett.* 72 (18), 2238-2240 (1998).
15. "Pseudo-Shear Universal Actuator Driving Flexextensional Panel Diaphragm Low Frequency Acoustic Source," R. Liu, Q. -M. Wang, Q. Zhang, V.D. Kugel, and L.E. Cross. *MRL Internal Report*, (1998).
16. "Advanced Time Domain Wave-Number Sensing for Structural Acoustic Systems. Part III. Experiments on Active Broadband Radiation Control of a Simply Supported Plate," J. P. Maillard and C. R. Fuller. *J. Acoust. Soc. Am.* 98(5),2613-2621 (1995).
17. "Active Control of Sound Radiation from Cylinders with Piezo-electric Actuators and Structural Acoustic Sensing," J. P. Maillard and C. R. Fuller. *Proc. Active* 97,1021-1034, Budapest, Hungary (August 21-23, 1997).
18. "Active Control of Sound Radiation from Cylinders with Piezoelectric Actuators and Structural Acoustic Sensing," J. P. Maillard and C. R. Fuller. Accepted for publication in *J.Sound Vib.* (November 1997).
19. "Comparison of Two Structural Sensing Approaches for Active Structural Acoustic Control," J. P. Maillard and C. R. Fuller submitted to *J.Acoust. Soc. Amer.* (1997).
20. "Implementation of Fast Recursive Estimation Techniques for Active Control of Structural Sound Radiation," M. J. Bronzel and C. R. Fuller. *Proc. Active* 95, 359-368, Newport Beach, CA(1995)
21. "Multiple Reference Feedforward Active Noise Control. Part I. Analysis and Simulation of Behavior," Y. Tu and C. R. Fuller, accepted for publication in *J. Sound Vib.*(1998)
22. "Multiple Reference Feedforward Active Noise Control. Part II. Reference Reprocessing and Experimental Results," Y. Tu and C. R. Fuller, accepted for publication in *J. Sound Vib.*(1998)

23. "Design of Active Structural Acoustic Control Systems Using a Nonvolumetric Eigenproperty Assignment Approach," Z. Li, C. Guigou, C. R. Fuller, and R. A. Burdisso. *J. Acoust. Soc. Am.* **101**(4), 2088-2096 (1997).
24. "Optimum Design for Feedforward Active Structural Acoustic Control of Complex Structures," H. M. Rodriguez, R. A. Burdisso, and C. R. Fuller. *Proc. Active 95*, Newport Beach, CA, 335-346 (July 6-8, 1995).
25. "Structural-Acoustic Control of System Design by Multi-Level Optimization," H. M. Rodriguez and R. A. Burdisso. *J. Acoust. Soc. Am.* **104**(2), 926-936 (1998).
26. "Broadband Control of Plate Radiation Using a Piezoelectric, Double-Amplifier Active-Skin, Part I. Analytical," B. D. Johnson and C. R. Fuller, submitted to *J. Acoust. Soc. of Amer.* (1998)
27. "Broadband Control of Plate Radiation Using a Piezoelectric, Double-Amplifier Active-Skin, Part II. Experimental," B. D. Johnson and C. R. Fuller, submitted to *J. Acoust. Soc. of Amer.* (1998)
28. "Simultaneous Active/Passive Control of Extensional and Flexural Power Flows in Thin Beams," F. L. Deneufve, C. Guigou, and C. R. Fuller. *Proc. Noise-Con 97*, University Park, PA, 281-290 (June 15-17, 1997).
29. "Simultaneous Active/Passive Control of Extensional and Flexural Power Flows in Thin Beams," F. L. Deneufve, C. Guigou, and C. R. Fuller. Submitted to *J. Acoust. Soc. Am.* (1997).
30. "Study of Globally Detuned Absorbers for Controlling Aircraft Interior Noise," C. Guigou, J. P. Maillard, and C. R. Fuller. *Proc. 4<sup>th</sup> International Congress on Sound and Vibration*, St. Petersburg, Russia, 1769-1777 (June 24-27, 1996).
31. "Adaptive Vibration Absorbers for Control of Sound Radiation from Panels," F. Charette, C.R. Fuller, and J. P. Carneal. *Proc. of 3<sup>rd</sup> AIAA/CEAS Aeroacoustics Conference*, Atlanta, GA (May 1997).
32. "Biomorph and Pseudo Shear Mode Actuation," L. E. Cross, *Proc. US Japan Meeting on Dielectric and Piezoelectric Ceramics*, Plymouth, MA (1997).

33. "Piezoelectric Double Amplifier Systems for Air Acoustic Noise Control," L. E. Cross, *Proc. 4<sup>th</sup> European Conference on Smart Structures and Materials*, Harrogate, England (July 6-8, 1998).
34. "Piezoelectric Pseudo-Shear Mode Actuator Made by L-Shape Joint Bonding", R.Lui, Q. Wang, Q.Zhang and L.E.Cross, *MRL Internal Report* (1998).
35. "Recent Advances in the Active Control of Structurally Radiated Sound," C. R. Fuller. *Proc. 5<sup>th</sup> International Congress on Sound and Vibration*, University of Adelaide, Australia (December 1997).
36. "Advanced Actuators and Sensors for the Active Control of Sound and Vibration," C. R. Fuller. *Proc. of Active Control of Noise and Vibrations*, CETIM, Senlis, France (April 1996).
37. "Control of Sound Radiation from Structures Using Active Skins," C. R. Fuller, C. Guigou, and B. D. Johnson. *Proc. I<sup>st</sup> Congress of Iberoamericano de Acustica*, Florianopolis, SC, Brazil, 186-197 (April 1998).
38. "Active Vibration Control," C. R. Fuller. *Encyclopedia of Acoustics*, Chapter 72, Wiley, New York, 893-907 (1997).

## **APPENDIX 23**

# Design of active structural acoustic control systems using a nonvolumetric eigenproperty assignment approach

Z. Li, C. Guigou, C. R. Fuller, and R. A. Burdisso

Vibration and Acoustic Laboratories, Mechanical Engineering Department, Virginia Polytechnic Institute and State University, Blacksburg, Virginia 24061-0238

(Received 5 March 1996; accepted for publication 11 October 1996)

Sound radiation of planar radiators such as beams and plates is known to be directly related to the velocity distribution over the structural surface at low frequencies. For example, nonvolumetric modes correspond to poor sound radiators for small  $k_0a$ . In this work, to achieve significant sound attenuation in the low-frequency range, the SISO eigenassignment technique is used to modify the eigenproperties of a planar structure using structural actuators and sensors so that all the modes of the controlled structure are nonvolumetric. The main advantage of such an approach is that the design is independent of the disturbance characteristics (i.e., type, position, and frequency content) and does not require sensors in the radiation field. The design procedure for the control system in the modal domain is presented. The formulation is applied to a simply supported beam with SISO feedforward control. Radiation efficiency, far-field sound radiated power and mean-square surface velocity are extensively studied. The results show that the control scheme proposed here is very efficient in reducing sound radiation at low frequencies. © 1997 Acoustical Society of America. [S0001-4966(97)03604-7]

PACS numbers: 43.40.Vn, 43.50.Ki [PJR]

## INTRODUCTION

The attenuation of sound radiation from vibrating structures is an important issue in practical engineering. Passive noise control approaches are inefficient at low frequencies and difficult to implement. In recent years, active control of sound radiation has emerged as a very promising method to reduce noise, especially at low frequencies. Extensive research has been conducted in developing efficient control strategies. One such strategy is active structural acoustic control (ASAC) proposed by Fuller.<sup>1</sup> In this approach, control inputs are applied directly to the vibrating structures (which is responsible for the sound radiation) while minimizing sound pressure or other related quantities. It is shown that, in general, this strategy requires a small number of control inputs for a global sound reduction in acoustic field. The efficiency of this approach in conjunction with adaptive feedforward control is now widely recognized.

The traditional design approach in adaptive feedforward control is to select the error sensors and actuators based on some physical understanding of the dynamical characteristics of the uncontrolled system or use standard optimization techniques.<sup>1,2</sup> In their recent work,<sup>3–5</sup> Burdisso and Fuller extensively studied the dynamics of the adaptive feedforward controlled system and revealed that the adaptive feedforward control, similar to feedback control, will alter the eigenproperties of the controlled system. They further developed a design methodology, the eigenassignment design technique, based on their findings for single-input, single-output systems. In this work, the eigenassignment method is adopted to design a system whose vibration modes under control are nonvolumetric and thus radiate sound weakly at low frequencies.

Efficient control methods are usually based on a full understanding of the physics involved in sound radiation.

Low-frequency sound radiation of planar radiators such as beams and plates is known to be directly related to velocity distribution over the structural surface. In recent publications,<sup>6,7</sup> the radiated acoustic power has been expressed in terms of the contributions from a number of independently radiating surface velocity distributions. It is shown that velocity distributions corresponding to vibration modes of the system will in general be coupled in the acoustic field. The “radiation modes” are surface velocity distributions that radiate sound power independently in the acoustic far field. It can be shown that, in the low-frequency range, i.e., for dimensionless frequency  $k_0a \ll 1$  (where  $k_0$  is the wave number in the air and  $a$  is the characteristic dimension of the structure), the shape of radiation modes is reasonably independent of frequency and only the first radiation mode is significant in terms of sound radiation.<sup>8</sup> The first radiation mode is the piston-type mode, which represents the monopole behavior of the structure and whose amplitude corresponds to the net volume velocity of the structure. It can then be further deduced that the first radiation mode is a combination of structural modes associated with a volumetric component (i.e., structural modes corresponding to a nonzero net volume velocity). These “volumetric modes” radiate sound efficiently at low frequencies (small  $k_0a$ ), since they behave as monopole radiators.<sup>9–12</sup> On the other hand, “nonvolumetric modes” (i.e., structural modes corresponding to a zero net volume velocity), radiate poorly in the low-frequency region where their directivity patterns resemble dipoles, quadrupoles, or higher-order patterns. This observation provides the physical background for the current work.

In this work, the overall goal is to design a control system with structural actuators and sensors so as to markedly reduce the low-frequency sound radiation efficiency. To achieve this, a SISO feedforward control is used to modify

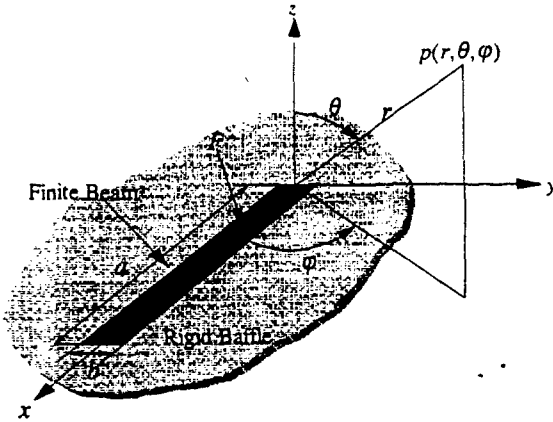


FIG. 1. Schematic of beam system and coordinate system.

the eigenproperties of a planar beam structure so that the vibration modes of the controlled system are nonvolumetric and radiate sound weakly. The complete design procedure consists of two parts: first, the design of global control system parameters in the modal domain by eigenassignment is carried out; second, the design of physical system (realistic structural error sensors and actuators) to implement the control strategy is performed.<sup>5</sup> In this paper, only the first stage is presented; a companion paper will discuss the experimental implementation of the proposed design. The main advantage of the method presented here is that the design is independent of the characteristics of the disturbance applied to the system (i.e., independent of form, location, and frequency content). A simply supported beam is studied to demonstrate the efficiency of the described design. However, the approach can be easily extended to more complicated boundary conditions and structures as the proposed design only requires knowledge of the system eigenproperties (which could be experimentally obtained by modal analysis for example). The radiation efficiency, far-field radiated power and mean-square velocity are extensively studied to understand the controlled system acoustic and structural behavior. The results of the proposed control approach are also compared with that obtained using a similar control approach except that a volume velocity sensor, as described in Ref. 10, and an accelerometer at the beam center are implemented as error sensors. These comparisons are used to evaluate the relative efficiency of the approach proposed here.

## I. THEORETICAL ANALYSIS

### A. System response

The studied system is presented in Fig. 1 and consists of a baffled finite beam of length  $a$  and width  $b$ . Simply supported boundary conditions are applied at  $x=0$  and  $x=a$ . The beam is assumed to be excited by a harmonic point force disturbance input  $\hat{F}e^{j\omega t}$  located at  $x=x_d$ . The analysis is carried out in frequency domain. The cross-sectional dimensions of the beam are considered small compared with its length and the frequency of vibration to be low so that both the shear and rotatory inertia effects can be neglected. The equation of motion of the beam can then be written as

$$\frac{\partial^2}{\partial x^2} \left[ EI(x) \frac{\partial^2 w(x,t)}{\partial x^2} \right] + m(x) \frac{\partial^2 w(x,t)}{\partial t^2} = \hat{F} e^{j\omega t}. \quad (1)$$

In the frequency domain, the response of the beam can be generally described as

$$w(x, \omega) = \sum_{n=1}^N q_n(\omega) \phi_n(x), \quad (2)$$

where  $w(x, \omega)$  is the displacement distribution, and  $\phi_n(x)$  is the  $n$ th eigenfunction depending on the beam boundary conditions. The eigenfunctions are assumed to be normalized with respect to mass distribution. The generalized coordinates in the frequency domain,  $q_n(\omega)$ , can be expressed as

$$q_n(\omega) = [f_n \hat{F}(\omega) + u_n U(\omega)] H_n(\omega), \quad (3)$$

where  $U(\omega)$  is the magnitude of control input, and  $f_n$  and  $u_n$  are the unit modal disturbance and unit modal control input, respectively.<sup>3</sup> The  $n$ th modal frequency response function is represented by  $H_n(\omega) = (\omega_n^2 - \omega^2 + 2j\zeta_n \omega_n)^{-1}$ , where  $\zeta_n$  and  $\omega_n$  are the  $n$ th modal damping ratio and natural frequency, respectively. The optimal control input can be obtained by minimizing the square of an error sensor output  $e(\omega)$ , represented as the sum of a linear contribution of each mode, i.e.,

$$e(\omega) = \sum_{n=1}^N q_n(\omega) \xi_n, \quad (4)$$

where  $\xi_n$  is the  $n$ th modal error sensor component and is a function of the characteristics of the error sensor.<sup>3</sup> Minimizing Eq. (4) leads to the control input magnitude expressed as<sup>3</sup>

$$U(\omega) = -G(\omega) \hat{F}(\omega) = -\frac{\sum_{n=1}^N \xi_n f_n H_n(\omega)}{\sum_{n=1}^N \xi_n u_n H_n(\omega)} \hat{F}(\omega). \quad (5)$$

### B. Radiation in acoustic far field

The sound pressure in the far field for a planar radiator can be written as<sup>13</sup>

$$p(r, \theta, \varphi) = -\omega^2 \frac{\rho_0 e^{-jk_0 r}}{2\pi r} \times W(k_0 \sin \theta \cos \varphi, k_0 \sin \theta \sin \varphi), \quad (6)$$

where  $k_0 = \omega/c_0$  is the acoustic wave number in the acoustic medium,  $\rho_0$  and  $c_0$  are the density of the acoustic medium (air in this case) and sound velocity, respectively;  $W(k_x, k_y)$  is the displacement wave number spectrum defined as the double spatial Fourier transform of the displacement distribution over the surface of the structure, i.e.,

$$W(k_x, k_y) = \int_{-\infty}^{+\infty} \int_{-\infty}^{+\infty} w(x, y) e^{jk_x x} e^{jk_y y} dx dy. \quad (7)$$

For the baffled beam, the system out-of-plane displacement depends only on the  $x$  coordinate and is constant along the beam width. The spatial displacement distribution can then be rewritten as

$$w(x, y) = \begin{cases} w(x), & \text{for } 0 \leq x \leq a, -b/2 \leq y \leq b/2 \\ 0, & \text{otherwise.} \end{cases} \quad (8)$$

The total acoustic power radiated by the structure is the integral over a hemisphere of the far-field acoustic intensity, i.e.,

$$\Pi(\omega) = \int_0^{2\pi} \int_0^{\pi/2} \frac{|p(r, \theta, \varphi)|^2}{2\rho_0 c} r^2 \sin \theta d\theta d\varphi. \quad (9)$$

The radiation efficiency of a vibrating structure is defined as<sup>12</sup>

$$\sigma = \frac{\Pi(\omega)}{\rho_0 c_0 ab \langle \dot{w}^2(x) \rangle}, \quad (10)$$

where  $\langle \dot{w}^2(x) \rangle$  is the spatial average mean square velocity defined as<sup>10,12</sup>

$$\langle \dot{w}^2(x) \rangle = \frac{\omega^2}{2a} \int_0^a |w(x)|^2 dx. \quad (11)$$

### C. Controlled system eigenproperties

Feedforward control has been successfully applied in the active control of sound and vibration. In their recent study, Burdisso and Fuller<sup>3</sup> revealed that the feedforward control, similar to feedback control, will generally alter the eigenproperties of the controlled structure. It is shown that the feedforward-controlled system effectively responds with a new set of eigenfunctions and eigenvalues to the disturbance input. Based on this observation, they further developed an eigenassignment design technique.<sup>4,5</sup> This technique is outlined in this section.

The eigenproperties of the feedforward-controlled structure are governed by the characteristics of the controller defined by  $G(\omega)$  [see Eq. (5)]. The controlled eigenvalues  $\lambda_l$  are the roots of the following characteristic equation of the controlled system<sup>5</sup>

$$\prod_{n=1}^N \xi_n u_n \prod_{\substack{m=1 \\ m \neq n}}^N (\mu_m - \lambda_l) = 0, \text{ for } l = 1, 2, \dots, N-1, \quad (12)$$

where  $\mu_m = \omega_m^2$  is the  $m$ th eigenvalue of the uncontrolled system. The controlled eigenvalues  $\lambda_l$  are therefore only a function of the unit modal control input, modal error sensor components, and eigenproperties of the uncontrolled structure and are independent of the disturbance loading, i.e., type, location, and frequency content. It is also important to note that the applied control input reduces the dynamic degrees of freedom of the structure by one due to the constraint imposed by driving the response of error sensor to zero.<sup>3</sup> The corresponding eigenfunctions of the controlled system  $\phi_l^c(x)$  are linear combinations of those of the uncontrolled system expressed as<sup>3</sup>

$$\phi_l^c(x) = \sum_{n=1}^N G_{ln} \phi_n(x), \text{ for } l = 1, 2, \dots, N-1, \quad (13)$$

where the expansion coefficients  $G_{ln}$  for  $n = 1, 2, \dots, N$  and  $l = 1, 2, \dots, N-1$  are defined as<sup>3</sup>

$$G_{ln} = \begin{cases} \frac{u_n}{\lambda_l - \mu_n} \left\{ \sum_{n=1}^N [\mu_n / (\lambda_l - \mu_n)]^2 \right\}^{-1/2}, & \text{for } \lambda_l \neq \mu_n \\ \delta_{ln}, & \text{for } \lambda_l = \mu_n. \end{cases} \quad (14)$$

For  $\lambda_l = \mu_n$ , the  $l$ th controlled eigenfunction is identical to the corresponding  $n$ th uncontrolled one (i.e.,  $G_{ln} = \delta_{ln}$ ), regardless of the unit modal control input  $u_n$ . Therefore, once the control actuator and error sensor are selected, the eigenstructure of the controlled system is then completely determined by Eqs. (12)–(14), independent of the nature of disturbance loading including frequency content, location, and distribution. On the other hand, if the controlled system eigenstructure is specified, then the unit modal control input and modal error sensor components can be determined such that the controlled system dynamics have these characteristics. This aspect is discussed further in the following section.

### D. Proposed control scheme

As discussed previously, some vibration modes are more efficient sound radiators at low frequencies ( $k_0 a \ll 1$ ) than others. "Nonvolumetric modes" are defined as modes with a zero integral of the normal velocity distribution over the surface of the planar structure. These modes radiate poorly at low frequencies where their directivity patterns resemble dipoles, quadrupoles, or higher-order patterns. On the other hand, volumetric modes, corresponding to monopole radiators, are responsible for most sound radiation at low frequencies ( $k_0 a \ll 1$ ). Therefore, the basic concept of this approach is to achieve a controlled structure that responds only with nonvolumetric modes so as to attenuate the radiated sound power. Thus, the structural eigenproperties have to be altered in such a way that the controlled eigenfunctions are all nonvolumetric and preferably orthogonal. To allow flexibility in the design process, it was chosen to construct the  $p$ th controlled eigenfunction as a linear combination of the first  $(p+1)$  uncontrolled eigenfunctions, i.e.,

$$\phi_p^c(x) = \sum_{k=1}^{p+1} \bar{G}_{pk} \phi_k(x), \text{ for } p = 1, 2, \dots, N-1, \quad (15)$$

where the coefficients  $\bar{G}_{pk}$  are derived by imposing the nonvolumetric and the orthogonality conditions, as well as normalizing the new eigenfunction to unity, i.e.,

$$\int_0^a \phi_p^c(x) dx = 0 \quad (\text{nonvolumetric condition}) \quad (16a)$$

$$\int_0^a \phi_p^c(x) \phi_{p'}^c(x) dx = \delta_{pp'}, \quad (16b)$$

for  $p' \leq p$  (orthonormal condition), (16b)

where  $\delta_{pp'}$  represents the Kronecker delta function (i.e.,  $\delta_{pp'} = 1$  for  $p = p'$  and  $\delta_{pp'} = 0$  for  $p \neq p'$ ). Thus, it can be noticed from Eqs. (15) and (16) that the first controlled eigenfunction is constructed from a linear combination of the first and second uncontrolled eigenfunctions. In general, the  $p$ th controlled eigenfunction is a linear combination of the

first ( $p+1$ ) uncontrolled eigenfunctions. If the number of uncontrolled modes (to be taken into account in the frequency range of concern) has to be increased, new controlled eigenfunctions are added without changing the lower order ones. By placing Eq. (15) into Eqs. (16a) and (16b), it is easily shown that the coefficients  $\bar{G}_{pk}$  can be expressed as

$$G_{pk} = \begin{cases} \gamma_k \gamma_{p+1} \left[ \sum_{j=1}^p \gamma_j^2 \sum_{i=1}^{p+1} \gamma_i^2 \right]^{-1/2}, & \text{for } 1 < k \leq p \\ \left( \sum_{j=1}^p \gamma_j^2 \right) \left[ \sum_{j=1}^p \gamma_j^2 \sum_{i=1}^{p+1} \gamma_i^2 \right]^{-1/2}, & \text{for } k = p+1 \\ 0, & \text{for } p+1 < k \leq N, \end{cases} \quad (17)$$

where  $\gamma_n$  is defined as

$$\gamma_n = \int_0^a \phi_n(x) dx. \quad (18)$$

If  $\gamma_n$  is zero, the  $n$ th mode then obeys the nonvolumetric condition [Eq. (16a)]. Equation (17) shows that the  $p+1$  uncontrolled mode is the most significant contributor to the  $p$ th controlled mode and that the contribution of the  $k$ th uncontrolled mode ( $1 \leq k \leq p$ ) to the controlled mode decreases as the controlled mode order is increased. This is also related to the fact that controlled eigenfunctions become more complex (i.e., with increasing number of nodes) as the mode order  $p$  increases. The expansion coefficients  $G_{ln}$  are also defined by Eq. (14) as functions of the unit modal control inputs  $u_n$ , and the uncontrolled and controlled system eigenvalues  $\mu_n$  and  $\lambda_l$ , respectively. Thus, the objective is to find the  $N$  unit modal control inputs  $u_n$  and the  $N-1$  controlled system eigenvalues  $\lambda_l$ , that yield the desired expansion coefficients as defined in Eq. (17). Since there are  $(N-1) \times N$  expansion coefficients to match and only  $N+(N-1)$  unknown, a solution can only be accomplished in some least-square sense. The controlled eigenvalues  $\lambda_l$  and unit modal control inputs  $u_n$  can then be obtained by solving a constrained least-square minimization problem,<sup>5</sup> where the objective function to be minimized is

$$F(u_n, \lambda_l) = \sum_{l=1}^{N-1} \sum_{n=1}^N [\bar{G}_{ln} - G_{ln}]^2 \quad (19)$$

subject to

$$\begin{cases} \sum_{n=1}^N u_n^2 = 1 \\ (\lambda_l)_{\text{lower}} \leq \lambda_l \leq (\lambda_l)_{\text{upper}} \\ 0 \leq \lambda_1 \leq \lambda_2 \leq \dots \leq \lambda_{N-1} \end{cases} \quad (20)$$

where the equality constraint represents the normalization of modal control input (since the relative controllability of the modes is the only relevant information), and  $(\lambda_l)_{\text{lower}}$  and  $(\lambda_l)_{\text{upper}}$  are the lower and upper bounds for the  $l$ th controlled eigenvalue. These lower and upper bounds for the  $l$ th controlled eigenvalues, i.e.,  $(\lambda_l)_{\text{lower}}$  and  $(\lambda_l)_{\text{upper}}$  are selected to ensure that the optimal expansion coefficients  $G_{ln}$  be as close as possible to the desired expansion coefficients  $\bar{G}_{ln}$ , and such that the following equation is satisfied:

$$\mu_1 \leq \lambda_1 \leq \mu_2 \leq \lambda_2 \leq \mu_3 \leq \dots \leq \mu_{N-1} \leq \lambda_{N-1} \leq \mu_N. \quad (21)$$

If, for example, the excitation consists of multiple harmonics, the controlled eigenvalues can also be selected (by properly choosing the upper and lower bounds) such that they do not coincide with any of these harmonics. The above nonlinear optimization problem can be carried out by using any of several standard routines. In this work, it was solved by using the program CONSTR in MATLAB optimization toolbox.<sup>14</sup>

Once the optimal unit modal control input  $u_n$  and the controlled system eigenvalues  $\lambda_l$  are determined, the modal error sensor components  $\xi_n$  can be obtained by solving a linear system of equations given by Eq. (12). Assuming that the  $N$ th mode is fully observable, and setting  $\xi_n = 1$ , the error sensor modal components are obtained by solving the following linear system<sup>4</sup>

$$\begin{bmatrix} \eta_{11} & \eta_{12} & \cdots & \eta_{1N-1} \\ \eta_{21} & \eta_{22} & \cdots & \eta_{2N-1} \\ \vdots & \vdots & \vdots & \vdots \\ \eta_{N-1,1} & \eta_{N-1,2} & \cdots & \eta_{N-1,N-1} \end{bmatrix} \begin{Bmatrix} \xi_1 \\ \xi_2 \\ \vdots \\ \xi_{N-1} \end{Bmatrix} = \begin{Bmatrix} \eta_{1,N} \\ \eta_{2,N} \\ \vdots \\ \eta_{N-1,N} \end{Bmatrix}, \quad (22)$$

where

$$\eta_{ln} = u_n \prod_{m=1}^N (\mu_m - \lambda_l). \quad (23)$$

The determination of optimal modal error sensor components  $\xi_n$  and the unit modal control input  $u_n$  completely defines the control system configuration in the modal domain. The performance of the controlled system can then be investigated. The physical implementation of the control system, i.e., the design of structural error sensors and actuators, is not be presented in this paper. However, it can be obtained following the steps as described in Ref. 5.

## II. NUMERICAL SIMULATIONS, RESULTS AND DISCUSSION

In this section numerical simulations for a vibrating simply supported finite beam are presented to demonstrate the design methodology and the effectiveness of the method. The beam is constructed from steel (i.e., density  $\rho = 7860 \text{ kg/m}^3$  and Young modulus  $E = 200 \text{ Gpa}$ ) with a length  $a = 0.38 \text{ m}$ , a width  $b = 0.038 \text{ m}$ , and a thickness  $h = 0.0048 \text{ m}$ . The beam is assumed to have a damping factor of  $\zeta_n = 1\%$  for all modes, and  $N = 7$  modes are included in the analysis to describe the response of the system. The first seven natural frequencies for the simply supported beam are listed in Table I. The beam is assumed to be driven by harmonic disturbance point force of  $1N$  amplitude located at  $x_d = 0.1 \text{ m}$ . The excitation frequency is varied in the frequency band 10–3000 Hz.

### A. Implementation for simply supported beam

This section presents some simplifications of the previously developed general formulation for the case of a lightly

TABLE I. Simply supported beam natural frequencies.

Mode	Uncontrolled (Hz)	Controlled (Hz)
1	76.03	304.13
2	304.13	653.12
3	684.30	1216.52
4	1216.53	1876.79
5	1900.82	2737.19
6	2737.18	3677.88
7	3725.61	

damped, simply supported beam. For simply-supported boundary conditions, the  $n$ th eigenfunction is

$$\phi_n(x) = \sqrt{\frac{2}{\rho Sa}} \sin(k_n x), \quad (24)$$

where  $k_n = n\pi/a$  is the  $n$ th structural wave number and the  $n$ th associated eigenvalue is  $\mu_n = \omega_n^2 = k_n^4 EI/\rho S$  ( $EI$  is the beam bending stiffness,  $\rho$  the density, and  $S$  the cross-section area). From Eq. (24), it can easily be noticed that the even-order modes of the beam are nonvolumetric, i.e., the parameter  $\gamma_n$  in Eq. (18) becomes

$$\gamma_n = \sqrt{\frac{2}{\rho Sa}} \left( \frac{1 - (-1)^n}{k_n} \right), \quad n = 1, 2, \dots, N. \quad (25)$$

Thus, the even-order uncontrolled modes do not need to be changed by the control as they already satisfy the nonvolumetric condition. From Eq. (25) and Eq. (17), it can be found that the controlled eigenfunctions can be expressed as

$$\phi_{2n-1}^c(x) = \phi_{2n}(x), \quad (26a)$$

$$\phi_{2n}^c(x) = \sum_{j=1}^{n+1} G_{2n,2j-1} \phi_{2j-1}(x), \quad (26b)$$

where the coefficients  $G_{2n,2j-1}$  are defined by Eq. (17), and  $n = 1, 2, \dots$ . Equations (26) state that the controlled eigenfunctions with odd order are identical to the uncontrolled ones with even order: for example the first controlled mode is  $\phi_1^c(x) = \phi_2(x)$ . On the other hand, the controlled eigenfunctions with even order are only a linear combination of the uncontrolled eigenfunctions with odd order: for example the second controlled mode is  $\phi_2^c(x) = G_{1,1}\phi_1(x) + G_{1,3}\phi_3(x)$ .

Having obtained the expansion coefficients and the controlled eigenfunctions for the finite beam considered in this example; the constrained least-square minimization problem [as expressed in Eqs. (19) and (20)] is solved for the controlled eigenvalues  $\lambda_l$  and the unit modal control input  $u_n$ . The modal error sensor components  $\xi_n$  are then found using Eqs. (22) and (23). Once these components are found correctly, the controlled system will respond with the desired nonvolumetric eigenfunctions or modes.

## B. Optimal controller in the modal domain

The controlled nonvolumetric modes [see Eq. (17)] are given by

$$\phi_1^c(x) = \phi_2(x),$$

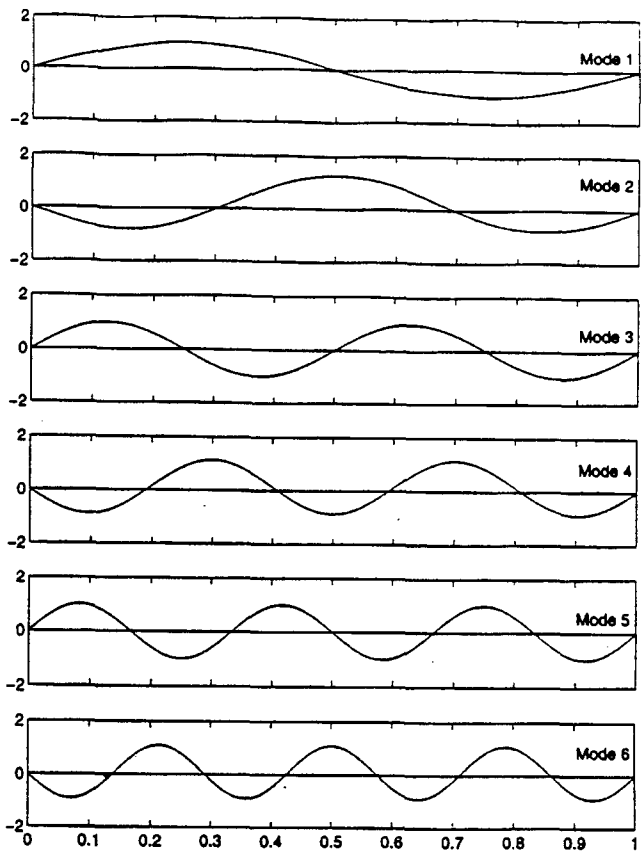


FIG. 2. Optimal controlled mode shapes of simply supported beam.

$$\begin{aligned} \phi_2^c(x) &= 0.3162\phi_1(x) - 0.9487\phi_3(x), \\ \phi_3^c(x) &= \phi_4(x), \\ \phi_4^c(x) &= 0.1768\phi_1(x) + 0.0589\phi_3(x) - 0.9487\phi_5(x), \\ \phi_5^c(x) &= \phi_6(x), \\ \phi_6^c(x) &= 0.123\phi_1(x) + 0.041\phi_3(x) + 0.0246\phi_5(x) \\ &\quad - 0.9913\phi_7(x), \end{aligned} \quad (27)$$

and the associated mode shapes are shown in Fig. 2. As mentioned previously, the odd-order controlled modes correspond to the even-order uncontrolled ones (i.e., the first controlled mode is the second mode of the uncontrolled system). On the other hand, the controlled modes with even order only depend on the uncontrolled ones with odd order (i.e., the second controlled mode is a combination of mode 1 and 3 of the uncontrolled system). It can also be noticed in Eqs. (27) that the largest expansion coefficient for controlled modes corresponds to the highest order uncontrolled mode in the decomposition. This can be associated with the fact that the mode shape becomes more complex (increasing number of nodes) with increasing mode order as seen in Fig. 2. Then, the  $N-1$  controlled system eigenvalues  $\lambda_l$  and the  $N$  unit modal control inputs  $u_n$  are obtained by solving the optimization problem [Eqs. (19) and (20)] and are used to solve for the modal error sensor components defined by Eq. (22).

The eigenfrequencies of the controlled system are given in Table I. As expected, the resonant frequency of the odd-

TABLE II. Optimal modal control input and error sensor modal components.

Mode	Modal control components $u_n$	Modal error sensor components $\xi_n$
1	0.931	0.925
2	0.000	0.013
3	0.277	0.306
4	0.000	0.010
5	0.135	0.182
6	0.000	-0.006
7	0.195	0.132

order controlled modes are identical to those of the even-order uncontrolled modes (as their associated eigenfunctions are the same). The modal parameters for the control input and the error sensor, presented in Table II, completely define the controlled system in the modal domain. As discussed previously, the optimization process is independent of the type, location and frequency content of the disturbance acting on the beam. The design process is different from that presented in Ref. 5 where the eigenfunctions are found to minimize the radiation efficiency at one particular frequency. The eigenstructure of the system has been changed in such a way that all the controlled modes are nonvolumetric, which radiate poorly in the low-frequency region.

After carrying out the above steps the eigenassignment has been completed and the controlled eigenstructure is fixed. The performance of the design is then examined by studying the acoustic and vibrational responses of the uncontrolled and controlled systems when the excitation frequency is varied from 10 to 3000 Hz ( $0.069 < k_0 a < 20.76$ ).

### C. Control design performance

As expected, the controlled modes radiate less efficiently than the uncontrolled modes. Figure 3 shows the radiation efficiencies of modes 1–4 for both the uncontrolled and controlled systems. At low frequencies, the radiation efficiencies of controlled modes decrease compared to those of the uncontrolled modes corresponding to monopole radia-

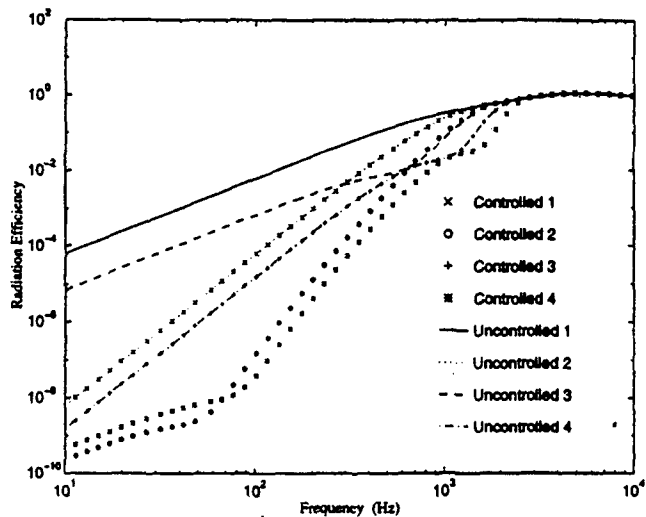


FIG. 3. Modal radiation efficiencies of modes 1–4 of a simply supported beam.

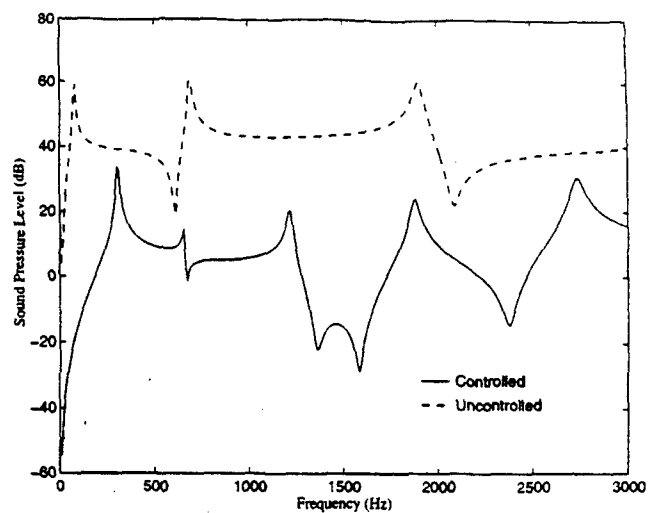


FIG. 4. Far-field radiated pressure in a direction perpendicular to the beam ( $\theta=0^\circ$ ).

tors. This decrease implies that the controlled modes are weaker radiators than the uncontrolled ones. It is also interesting to note that the radiation efficiency is even lower for the second controlled mode, which is a linear combination of the first and third uncontrolled modes (monopole radiators), than for the second uncontrolled mode (dipole radiator). This is probably because the second controlled mode has one more degree of freedom than the second uncontrolled mode. Similar observations hold true for other even-order controlled modes.

To illustrate the effectiveness of the control strategy, the far-field sound-pressure levels (in dB, re:  $20 \mu\text{Pa}$ ) before and after control at  $(5 \times a, \theta=0, \varphi=0)$ , i.e., in the direction perpendicular to the center of the finite beam, are shown in Fig. 4. The sound-pressure level is significantly reduced over a wide frequency range (10–3000 Hz). This reduction is mainly due to the fact that the nonvolumetric controlled modes are associated with a dipole radiation pattern in the far field, and therefore have a minimum radiation in the direction perpendicular to the vibrating structure. The far-field pressure directivity in the  $x-z$  plane is shown in Figs. 5 and 6 for frequencies of 76 and 200 Hz, respectively, where negative value of  $\theta$  corresponds to  $\phi=0$  in the positive  $x$

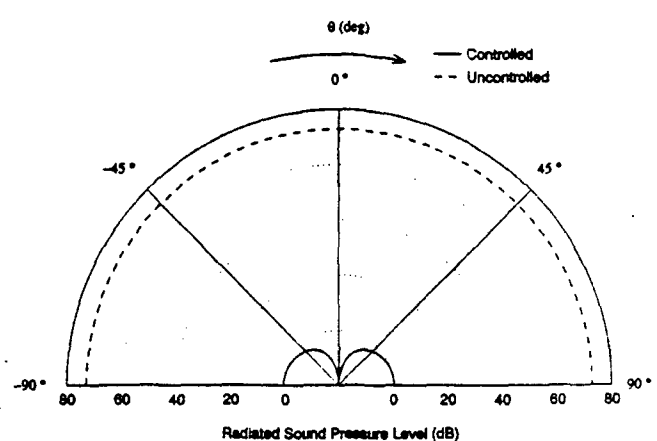


FIG. 5. Radiation directivity at 76 Hz (first uncontrolled resonance).

plane. The sound-pressure levels are calculated at a radius  $r = 5 \times a$ . For an excitation frequency of 76 Hz, corresponding to the first resonant frequency of the uncontrolled system, significant global sound attenuation has been achieved. Similar results can be observed when the system is driven at other uncontrolled resonant frequencies. At 200 Hz, i.e., an off-resonant frequency of the uncontrolled and controlled system, excellent global sound attenuation is also obtained as seen in Fig. 6. However, the global sound attenuation decreases as the frequency increases. The results show that the controlled system behaves very much like a dipole type radiator.

Sound radiation at the controlled resonant frequencies is also studied. Figure 7 shows the far-field pressure directivity at 653.1 Hz, corresponding to the second controlled resonant frequency. The sound radiation decreases near  $\theta=0$  but increases elsewhere. However, the global radiation level does not increase significantly. Similar conclusion holds for other controlled resonant frequencies.

To evaluate the overall performance of the controlled systems obtained, the total radiated sound power (in dB re:  $10^{-12}$  W) and radiation efficiency for both the uncontrolled and controlled systems are shown in Figs. 8 and 9, respectively. Figure 8 shows excellent sound power attenuation below the first controlled (or second uncontrolled) natural frequency. The radiation efficiency plot (see Fig. 9) shows that the controlled system efficiency is decreased when the frequency is below the second controlled (or third uncontrolled) natural frequency. In general, the controlled system corresponds to an inefficient radiator for frequencies below the first controlled resonant frequency. Figure 8 also shows good sound power attenuation for off-resonance frequencies, in contrast to the work described in Ref. 10. To further understand the underlying mechanism for the controlled system, the spatial average mean-square velocity before and after control [see Eq. (11)] is presented in Fig. 10. It can be seen that the controlled vibrational levels are in general reduced in the studied frequency range. This fact suggests that the "modal reduction"<sup>15</sup> is an important mechanism in the proposed control process. On the other hand, the controlled modes are a linear combination of the uncontrolled modes and the controller is designed to make all the controlled modes nonvolumetric. This fact implies that "modal-restructuring"<sup>15</sup> is also

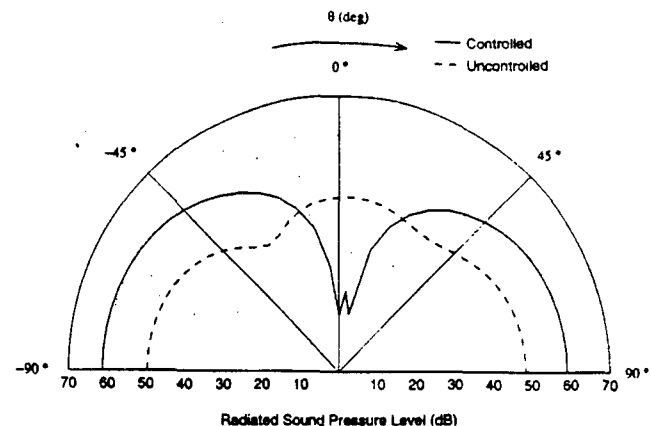


FIG. 7. Radiation directivity at 653.1 Hz (second controlled resonance).

an important mechanism in the control behavior. In general, the overall performance of the controlled system is limited by the first natural frequency of the controlled system. To overcome this limit, one may want to increase this first controlled resonant frequency. However, as expressed in Eq. (21), the upper bound for the first controlled natural frequency is given by the second uncontrolled resonant frequency. Thus, for the present design, the control efficiency is restricted in frequency by the constraint on the controlled resonant frequencies. This limitation could be overcome by adopting a similar control design using a MIMO feedforward controller and a recursive formulation as proposed in Ref. 16.

#### D. Control performance comparison

In this section, different control methods are compared for the previous system of the simply supported beam. The "nonvolumetric design" corresponds to the approach proposed in this paper (results from the previous section). The "volume velocity sensing design" considers the use of a volume velocity sensor on the simply supported beam as described in Ref. 10. The "accelerometer sensing design" uses an accelerometer located at the center of the beam as error

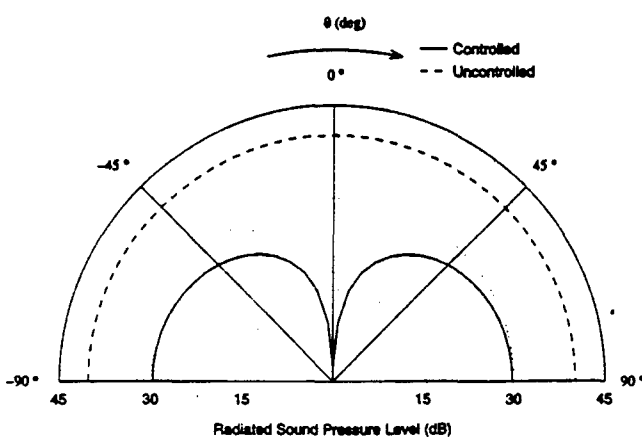


FIG. 6. Radiation directivity at 200 Hz (off resonance).

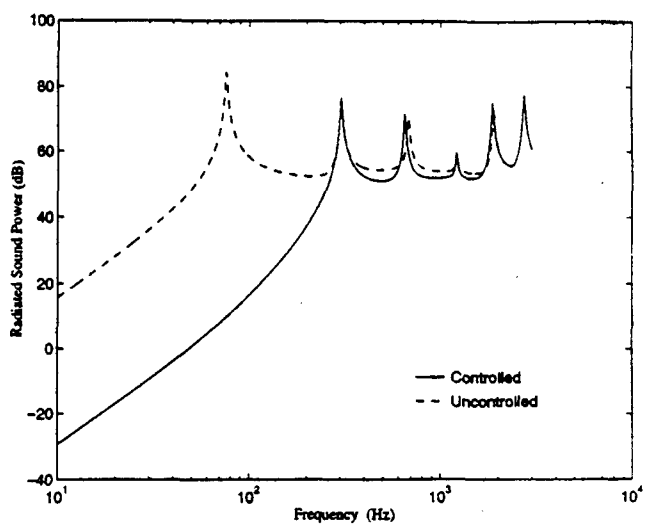


FIG. 8. Total radiated sound power.

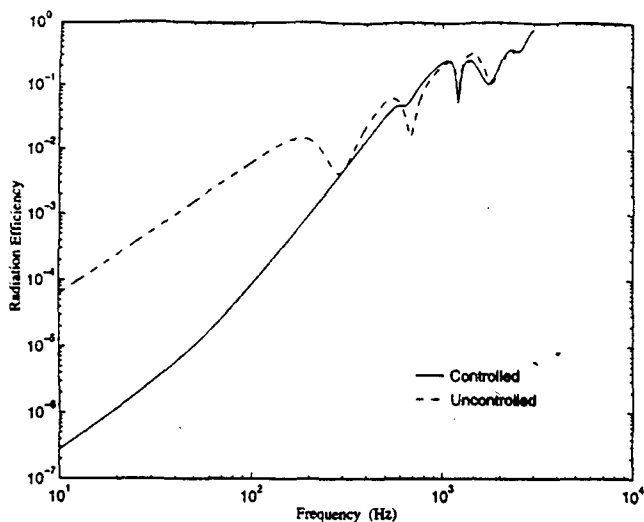


FIG. 9. Radiation efficiency.

sensor. All other system parameters are identical. For the latter two approaches, the error sensor detects only odd-order modes as they are the only ones that are nonvolumetric. The control input in these two cases is assumed to be a control force located at the middle of the beam. This location was selected to avoid the control force coupling into the even-order modes that are already nonvolumetric sources and thus radiate weakly. The last two methods do not include design of the actuator load; indeed, they are purely based upon a sensing strategy and the control load is only chosen based upon physical insight.

The radiation efficiency of the three different controlled systems is shown in Fig. 11. All methods provide a large decrease of the radiation efficiency in the low-frequency domain. However, the use of the accelerometer as an error sensor leads the poorest results (an increase of the radiation efficiency can be noticed at high frequencies) as its signal is not directly related to sound radiation. The method proposed in this paper gives better results at low frequencies than volume velocity sensing design as it provides the modal char-

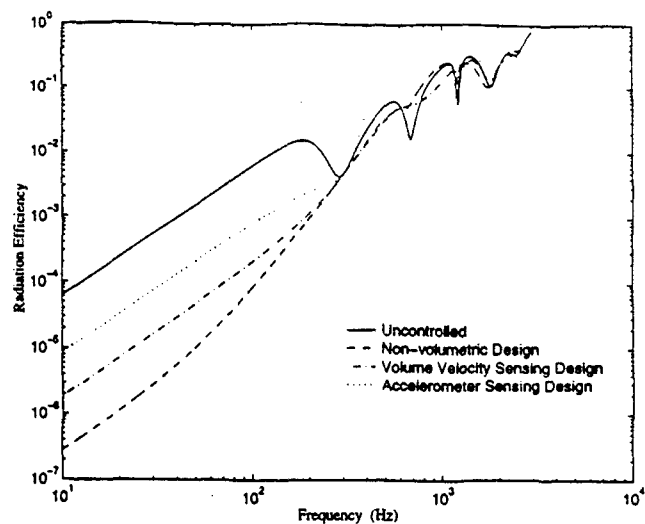


FIG. 11. Comparison of radiation efficiency for different control methods.

acteristics of both the sensor and the actuator simultaneously. At higher frequencies, both nonvolumetric design and the volume velocity sensing design give similar results. The associated controlled radiated sound power and mean-square velocity are shown in Figs. 12 and 13, respectively. The nonvolumetric design is the most efficient in the low-frequency region (up to 10 dB improvement) in terms of controlling sound radiation. It is also apparent from Fig. 12 that the nonvolumetric design (the procedure of this paper) does not lead to a large increase of radiated sound and vibrational levels at off-resonance excitation of the uncontrolled system while the other two methods do. For the volume velocity sensing design, the sound radiation is increased significantly around 1 kHz because of a large increase of the displacement in the same frequency range (see Fig. 13). It can be noticed in Fig. 13 that the volume velocity sensing design and the accelerometer sensing design are associated with very large increase of vibrational levels in the higher-frequency region. Thus, it appears that the method developed

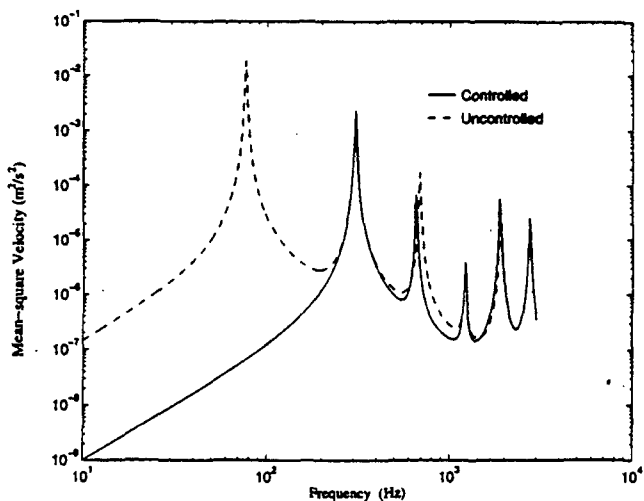


FIG. 10. Mean-square velocity.

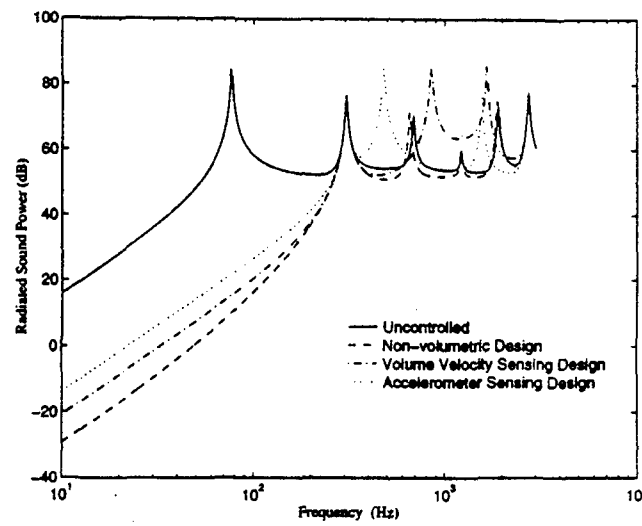


FIG. 12. Comparison of total radiated power for different control methods.

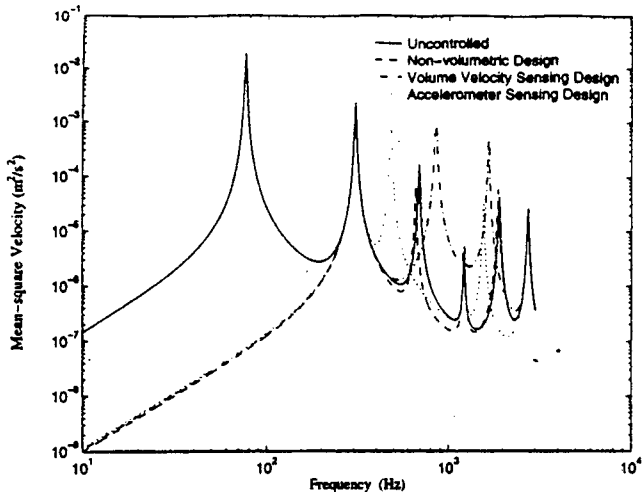


FIG. 13. Comparison of mean-square velocity for different control methods.

in this paper provides a better controlled system as the vibrational and acoustic levels are generally not increased for off-resonance of the uncontrolled and controlled system while the low-frequency performance is significantly improved. This improvement is due to the fact that the sensor and the control input are optimized at the same time regardless of frequency and excitation characteristics, thus limiting control spillover effects.

### III. CONCLUSIONS

In this paper a new formulation for the design of ASAC systems is proposed. The design methodology proposed here is based on the fact that elemental radiators with zero integrals of normal velocity over their surface (i.e., nonvolumetric) are inefficient radiators of sound at low frequencies. A SISO eigenassignment method is thus developed in order to modify the system eigenstructure so that all controlled modes are nonvolumetric, therefore leading to an overall sound attenuation in the far field. Although the design procedure is carried out in the modal domain for a simple one-dimensional structure located in rigid baffle, it is readily extensible to more general planar structures since it is based upon a normal mode analysis. One main advantage of this method is that the design does not depend on the characteristics of the external disturbance, such as the form, location, and frequency contents. The design is only based on the modal behavior of the structure. The effectiveness of this formulation is demonstrated through numerical simulation

for control of radiation from a simply supported beam. Significant sound power attenuation is achieved in the low frequencies, up to the first controlled resonant frequency. The present approach is also compared to other approaches employing a volume velocity sensor or an accelerometer as a sensor at the center of the beam. The control method discussed in this paper provides larger attenuation of both sound radiation and vibrational levels than the two latter cases. This increased control performance is associated with the fact that the proposed method optimizes both the error sensor and control input simultaneously.

### ACKNOWLEDGMENT

The authors gratefully acknowledge the support of this work by the Office of Naval Research under Grant No. ONR N00014-92-J-470, Dr. Kam Ng, Technical Monitor.

- <sup>1</sup>C. R. Fuller, "Active control of sound transmission/radiation from elastic plates by vibrational inputs: I. Analysis," *J. Sound Vib.* **136**, 1–15 (1990).
- <sup>2</sup>B. T. Wang, R. A. Burdisso, and C. R. Fuller, "Optimal placement of piezoelectric actuators for active control of sound radiation from elastic plates," *Proc. Noise-Conf.* **91**, 267–275 (1991).
- <sup>3</sup>R. A. Burdisso and C. R. Fuller, "Theory of feedforward controlled system eigenproperties," *J. Sound Vib.* **153**, 437–452 (1992).
- <sup>4</sup>R. A. Burdisso and C. R. Fuller, "Feedforward controller design by eigenvalue assignment," *AIAA J. Guidance Control* **17**, 466–472 1994.
- <sup>5</sup>R. A. Burdisso and C. R. Fuller, "Design of active structural acoustic control systems by eigenproperty assignment," *J. Acoust. Soc. Am.* **96**, 1582–1591 (1994).
- <sup>6</sup>K. A. Cunefare, "The minimum multimodal radiation efficiency of baffled finite beams," *J. Acoust. Soc. Am.* **90**, 2521–2529 (1991).
- <sup>7</sup>R. F. Keltie and H. Peng, "The effects of modal coupling on the acoustic power radiation from panels," *Trans. ASME J. Vib. Acoust. Stress Reliability Design* **109**, 48–54 (1987).
- <sup>8</sup>S. J. Elliott and M. E. Johnson, "Radiation modes and the active control of sound power," *J. Acoust. Soc. Am.* **94**, 2194–2204 (1993).
- <sup>9</sup>R. L. Clark and C. R. Fuller, "Modal sensing of efficient acoustic radiators with PVDF distributed sensors in active structural acoustic control approaches," *J. Acoust. Soc. Am.* **91**, 3321–3329 (1992).
- <sup>10</sup>C. Guigou, F. Charette, and A. Berry, "Active control of sound by minimization of volume velocity on finite beam," *Proceedings of 3rd International congress on Air- and Structure-Borne Sound and Vibration, Montreal, Canada, May 1994*, 169–174.
- <sup>11</sup>M. E. Johnson and S. J. Elliott, "Volume velocity sensors for active control," *Proc. Inst. Acoust.* **15**, 411–420 (1993).
- <sup>12</sup>F. Fahy, *Sound and Structural Vibration/Radiation, Transmission and Response* (Academic, London, 1985), pp. 64–77.
- <sup>13</sup>M. C. Junger and D. Feit, *Sound, Structures, and Their Interaction* (MIT, Cambridge, 1986), 2nd. ed.
- <sup>14</sup>*Matlab Optimization Toolbox* (The MathWorks, Inc., South Natick, MA, 1992).
- <sup>15</sup>J. Pan, S. D. Snyder, C. H. Hansen, and C. R. Fuller, "Active control of far-field sound radiated by a rectangular panel—A general analysis," *J. Acoust. Soc. Am.* **91**, 2056–2066 (1992).
- <sup>16</sup>R. A. Burdisso, C. R. Fuller, and Z. Li, "Eigenproperties of MIMO feedforward controlled flexible systems" (unpublished).

# **APPENDIX 24**

Newport Beach, CA, USA  
**ACTIVE 95**  
1995 July 06-08

## OPTIMUM DESIGN FOR FEEDFORWARD ACTIVE STRUCTURAL ACOUSTIC CONTROL OF COMPLEX STRUCTURES

Héctor M. Rodríguez  
Ricardo A. Burdisso  
Chris R. Fuller

Vibration and Acoustics Laboratories  
Department of Mechanical Engineering  
Virginia Polytechnic Institute and State University  
Blacksburg, Virginia 24061-0238

### INTRODUCTION

Active structural acoustic control (ASAC), where the acoustic response produced by a vibrating structure is minimized by applying the control inputs directly to the structure [1], has been demonstrated to be more effective than traditional active noise control (ANC) approaches for the abatement of structurally radiated noise [2]. The typical ASAC design approach, in particular for simple structures, consists in selecting the actuators and sensors based on some physical understanding of the uncontrolled system such as placing the control inputs at the antinodes of the most efficient modes [3-6]. More recent investigations have shown that using this simplistic design approach for the case of more complex structures could result in an inefficient control system with a large number of control inputs [7-8]. Wang et. al. investigated the optimum location of rectangular PZT actuators with fixed microphones as error sensors to minimize the radiation from a simply supported plate excited at a single tone [7]. It is demonstrated in this work that optimally located actuators provide a far better sound reduction, at both on and off resonance excitations, than actuators whose position are chosen based in some physical consideration. In the same way, Clark and Fuller studied the optimization of location of PZT actuators and both the size and location of Polyvinylidene Fluoride (PVDF) structural sensors [8]. Analytical and experimental results confirm the previous results from Wang et. al. [7]. A single optimally located actuator/sensor pair rivals the sound reduction obtained with three arbitrarily located actuators and sensors and three error microphones. However it is clear from Clark's results using PVDF sensors that in order to implement structural sensors for ASAC applications an efficient design procedure is critical due to the inability of structural sensors to measure directly the acoustic response, which is the variable to minimize in structural acoustic applications.

There are several drawbacks in these optimization procedures that prevent the same approaches to be implemented in complex realistic structures. First, only simple systems, where analytical predictions for structural and acoustic response exist, have been used. Real industrial structures will require numerical approaches to obtain the necessary responses. Both Wang and Clark have used the mean square value of the sound pressure as a function of the physical characteristics of the transducers as a cost function and finite differences techniques in the sensitivity computation. Therefore, the acoustic response needed to be computed many times during the optimization process. The estimation of the acoustic response by numerical techniques represents a lengthy procedure, hence their approach resulted in an inefficient and impractical design formulation for complex structures and excitations.

In this paper, an efficient design formulation for feedforward ASAC of complex structures and disturbances is presented. The approach consists in a two-stage multi-level optimization scheme. The formulation takes advantage of the fact that both the structural response and the acoustic radiation from a controlled structure can be completely defined in terms of modal quantities. All the physical parameters that define the control inputs and the error sensors have their counterpart in the modal domain through the unit modal control forces and the modal error sensor components, respectively. Therefore, the upper level of the optimization is defined in the modal domain and solves for the optimum unit modal control forces and modal error sensor components that minimize the total radiated power, expressed in terms of modal quantities. Then, these optimum unit modal control forces and modal error components are used in a set of lower level optimization problems to determine the physical characteristics of the actuators and sensors to be implemented. A finite element model is used to obtain the natural frequencies, mode shapes and modal disturbance forces of the system. The computed mode shapes are used in turn in a boundary element model to provide the acoustic radiation due to each mode. This modal domain information, i.e. natural frequencies, mode shapes, modal disturbances and modal acoustic pressures, is the only input that is needed to formulate the problem in the upper level optimization and has to be computed only once during the design process. Therefore, the formulation permits that any complex structure could be analyzed in an efficient manner. The proposed approach is demonstrated for the case of a simply supported cylinder excited by a point force. Several different control system configurations are investigated. It is shown that the proposed approach represent an efficient way of designing ASAC systems.

### FEEDFORWARD STRUCTURAL ACOUSTIC CONTROL

In feedforward structural-acoustic control, the response of a system due to an input disturbance  $F(\omega)$  is reduced by applying secondary control inputs  $U_k(\omega)$  as shown in figure 1. The control inputs are obtained by feeding forward a reference signal fully coherent to the input disturbance into the compensators  $G(\omega)$ . This reference signal is assumed to be obtained by tapping the disturbance input. The compensators are designed such that the output from the error sensors  $E_s(\omega)$  is minimized. Assuming that the disturbance input is stationary, the analysis is performed in the frequency domain by taking the Fourier Transform (FT) of any time dependent variable.

**Structural Response.** The structural response can be obtained by modal superposition after solving the eigenvalue problem, i.e. natural frequencies and mode shapes. For the case of a complex system, these natural frequencies and mode shapes can be obtained by using numerical techniques such as the finite element method (FEM). For the case of sound radiation from structural systems submerged in light fluids (e.g. air), it is necessary to consider only the vibration in which the response normal to the radiating surface

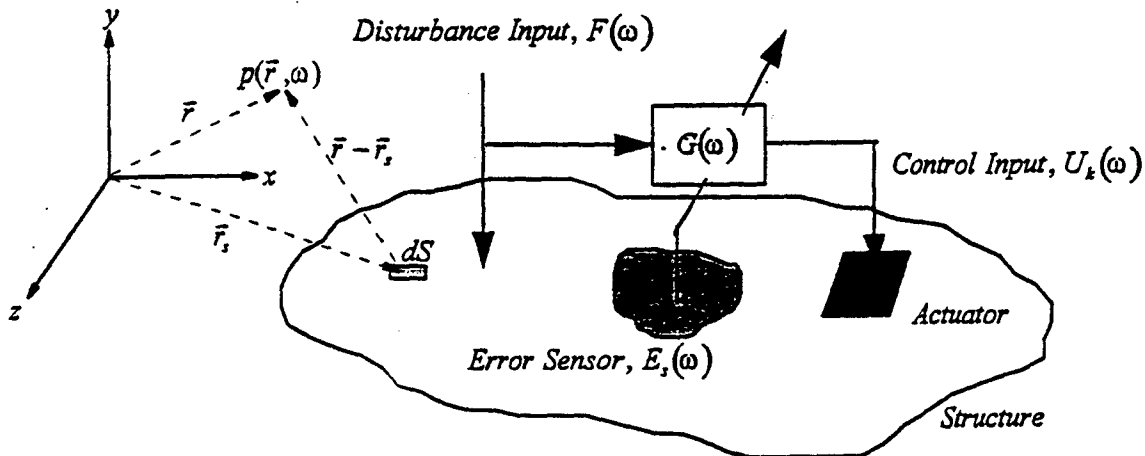


Figure 1. Feedforward structural-acoustic control arrangement.

is dominant [9]. After solving for the natural frequencies and mode shapes, the FT of the response in the normal direction at any location  $\vec{r}_s$  over the structural domain can be obtained as a linear combination of the modes as

$$w(\vec{r}_s, \omega) = \sum_{n=1}^N q_n(\omega) \phi_n(\vec{r}_s) \quad (1)$$

where  $\phi_n(\vec{r}_s)$  is the component normal to the surface of the  $n^{th}$  mass normalized mode shape,  $q_n(\omega)$  is the FT of the  $n^{th}$  modal displacement,  $N$  is the total number of modes included in the analysis, and  $\omega$  is the excitation frequency. The modal displacement  $q_n(\omega)$  is expressed as

$$q_n(\omega) = \left( F(\omega) \cdot f_n + \sum_{k=1}^{N_c} U_k(\omega) \cdot u_{nk} \right) \cdot H_n(\omega) \quad (2)$$

where  $F(\omega) \cdot f_n$  and  $U_k(\omega) \cdot u_{nk}$  are the modal domain forces applied to the  $n^{th}$  mode due to the disturbance force and the  $k^{th}$  control input, respectively, and  $N_c$  is the total number of control inputs. The unit modal forces ( $f_n$  and  $u_{nk}$ ) serve as weighting coefficients that dictate how much force is applied to each mode and are related to the physical implementation of the forces. For example, point forces will result in the unit modal forces to take the value of the mode shape at the force location. Similarly, distributed strain induced actuators will yield modal parameters related to the first derivative of the mode shapes [10]. Finally,  $H_n(\omega)$  is the  $n^{th}$  modal frequency response function which is defined as

$$H_n(\omega) = (\omega_n^2 - \omega^2 + 2j\beta_n\omega_n\omega)^{-1} \quad (3)$$

where  $\omega_n$  is the  $n^{th}$  natural frequency,  $\beta_n$  is the  $n^{th}$  modal damping ratio, and  $j$  is the imaginary number. Equation (1) represents the controlled response of a vibrating structure. The uncontrolled response is obtained by simply setting the control inputs  $U_k(\omega)$  to zero in eq. (2).

**Optimum Control Inputs.** The complex amplitude of the control inputs  $U_k(\omega)$  are obtained by minimizing a quadratic cost function of a measurable response quantity. This cost function, which is referred here as the *control cost function*, is defined as the sum of the mean-square-value (msv) of the error sensor outputs. That is

$$C = \sum_{s=1}^{N_s} \int_{-\infty}^{+\infty} E_s(\omega) E_s^*(\omega) d\omega \quad (4)$$

where  $E_s(\omega)$  is the Fourier transform of the  $s^{th}$  error sensor output,  $N_s$  is the total number of error sensors, and (\*) denotes the complex conjugate.

It is assumed that only structural error transducers are considered. Thus the error variable can always be expressed as a linear combination of modal terms as [11,12]

$$E_s(\omega) = \sum_{n=1}^N q_n(\omega) \xi_{ns} \quad (5)$$

where  $\xi_{ns}$  is the  $n^{th}$  modal error component of the  $s^{th}$  error sensor. Again, the modal error components are related to the physical implementation of the transducers. A discrete sensor such an accelerometer will yield a modal error component that is the value of the mode shape at the sensor's location.

As it is shown in the literature, the *control cost function* in eq. (4) is a positive definite function with respect to  $U_k(\omega)$ , and therefore there exists only one minimum [13]. By differentiating eq. (4) with respect to the real and imaginary part of the control forces  $U_k(\omega)$  and setting them to zero, it can be shown that the set of the optimum control inputs at a single frequency is the solution of the following linear system of equations

$$[T(\omega)]\{U(\omega)\} = -F(\omega)\{B(\omega)\} \quad (6)$$

where matrix  $[T(\omega)]$  contains the transfer functions between the control inputs and error outputs and has dimension  $N_s \times N_c$ , and the elements of vector  $\{B(\omega)\}$  are the transfer functions between the disturbance and the error outputs. The  $(s,k)$  element of matrix  $[T(\omega)]$  and the  $s$  element of vector  $\{B(\omega)\}$  are computed as

$$T(s, k) = \sum_{n=1}^N u_{nk} \xi_{ns} H_n(\omega) \quad (7a,b)$$

$$B(s) = \sum_{n=1}^N f_n \xi_{ns} H_n(\omega)$$

From eqs. (1) and (6), it is clear that the response of both the controlled and uncontrolled system can be expressed in terms of modal parameters where the control inputs and error sensors are defined in terms of the unit modal control forces  $u_{nk}$  and the modal error sensor components  $\xi_{ns}$ , respectively.

**Acoustic Response.** The acoustic radiation from a vibrating structure can be estimated after solving the boundary integral formulation of the Helmholtz wave equation. For the case of complex structures this equation is solved using numerical techniques. The Indirect Boundary Element Method (IBEM) estimates the acoustic radiation at any external field point of the vibrating structure after solving the modified integral equation [14]

$$p(\vec{r}, \omega) = \int_S \mu(\vec{r}_s, \omega) \cdot \frac{\partial G(\vec{r}_s, \vec{r})}{\partial \vec{n}} - G(\vec{r}_s, \vec{r}) \cdot \sigma(\vec{r}_s, \omega) dS \quad (8)$$

where  $\mu(\vec{r}_s, \omega)$  and  $\sigma(\vec{r}_s, \omega)$  represent the differences or "jumps" of the acoustic pressure and the normal velocities between the external part and the internal part of the structural surface  $S$ , respectively;  $\vec{n}$  is an outward normal directional vector and  $G(\vec{r}_s, \vec{r})$  is the 3-D Green's function that has the form

$$G(\vec{r}_s, \vec{r}) = \frac{e^{-jk|\vec{r} - \vec{r}_s|}}{4\pi \cdot |\vec{r} - \vec{r}_s|} \quad (9)$$

in which  $k = \omega/c$  is the acoustic wave number,  $c$  is the phase speed in the fluid, and  $|\vec{r} - \vec{r}_s|$  is the distance between the external field points and the points over surface. Equation (8) is usually solved in conjunction with the *Neumann* and *Sommerfeld* boundary conditions [14]. The *Neumann* condition relates the gradient of the acoustic pressure over the surface of the structure to the normal structural velocity as

$$\frac{\partial p(\vec{r}_s, \omega)}{\partial \vec{n}} = \rho \omega^2 w(\vec{r}_s, \omega) \quad (10)$$

where  $\rho$  is the fluid's density. The *Sommerfeld* boundary condition implies that energy can only flow from the vibrating structure towards infinity. In order to estimate the acoustic radiation at any field point  $p(\vec{r}, \omega)$ , the formulation first compute the quantities  $\mu(\vec{r}_s, \omega)$  and  $\sigma(\vec{r}_s, \omega)$  on the basis of the known *Neumann* boundary condition.

By substituting the modal expansion solution of eq. (1) into the *Neumann* boundary condition in eq. (10), the acoustic pressure field can also be obtained as a linear contribution of the structural modes as

$$p(\vec{r}, \omega) = \sum_{n=1}^N q_n(\omega) p_n(\vec{r}, \omega) \quad (11)$$

where for a particular frequency  $\omega$  the modal pressure  $p_n(\vec{r}, \omega)$  can be easily estimated from the BEM code considering the modal distribution  $\phi_n(\vec{r}_s)$  as the surface normal response in eq. (10).

The total acoustic radiated power can be estimated by integrating the acoustic time average intensity over a sphere of area  $A$  that surrounds the structure as

$$\Pi(\omega) = \int_A \frac{|\dot{P}(\vec{r}, \omega)|^2}{2\rho c} dA \quad (12)$$

Replacing eq. (11) into (12) gives

$$\Pi(\omega) = \{q(\omega)\}^H [K(\omega)] \{q(\omega)\} \quad (13)$$

where  $H$  implies conjugate transpose and the elements of matrix  $[K(\omega)]$  are

$$K_{mn}(\omega) = \int_A \frac{p_m(\vec{r}_f, \omega) p_n(\vec{r}_f, \omega)}{2\rho c} dA \quad (14)$$

The diagonal elements of the matrix  $[K(\omega)]$  represent the power radiated by each one of the modes while the off-diagonal terms is the radiated power due to the coupling of the modes.

Equation (13) defines the total radiated power at a single frequency. The general case of multiple frequency excitations is expressed as a linear combination of the contributions due to each frequency as

$$\Pi_T = \sum_{i=1}^{NF} \left( \{q(\omega_i)\}^H [K(\omega_i)] \{q(\omega_i)\} \right) = \sum_{i=1}^{NF} \Pi(\omega_i) \quad (15)$$

where  $NF$  is the total number of frequencies.

As can be seen from eqs. (11) and (13) the acoustic response is directly affected, through the modal displacements  $q_n(\omega)$ , by the vibration of the structure. This relationship between the structural and acoustical responses contains the essence of the ASAC technique, that is the acoustic radiation is controlled by modifying the vibration behavior of the structure. Therefore, the main task in the ASAC design is the proper selection of the type, size, number and location of the actuators and sensors that will modify the structural response in such way that the desired acoustic response is minimized. In the next section a multi-level optimization procedure is proposed for the optimum selection of these control system components.

### DESIGN APPROACH: MULTI-LEVEL OPTIMIZATION

In multi-level optimization a complex problem is broken into a set of simpler problems that offers computational advantages. The process of decomposition consists of separating the optimization process in an upper level problem, in which a global cost function is minimized with respect to global design variables, and a set of lower level problems, in which a set of local design variables are related to each global design variable. From eqs. (1), (6), (11) and (15), it is clear that the structural and acoustic responses, both before and after control, can be computed without any knowledge of the physical characteristics of the transducers, i.e. only modal domain information is required. Based on this, a two-level optimization formulation is ideal for the design of feedforward control systems. Since the physical design variables of the control system can be completely defined as modal quantities it brings out the possibility of separating the design process into an upper level or modal domain optimization and a set of lower level or physical domain optimizations.

The total radiated acoustic power expressed in terms of the modal quantities  $u_{nk}$  and  $\xi_{ns}$  as in eq. (15), is selected as the *global cost function* to be minimized in the upper level or modal domain. The global design variables in the upper level are the unit modal control forces  $u_{nk}$  and the modal error sensor components  $\xi_{ns}$ . The physical parameters that define the actuators and sensors to be implemented, i.e. size, location, etc., are the local design variables in the lower level or physical domain problems. Each lower level problem will consist in finding the optimum physical parameters or local variables for each actuator and sensor that best match the optimum unit modal control forces  $u_{nk}$  and modal error sensor components  $\xi_{ns}$ , respectively.

Some of the advantages of this approach over the previous optimization attempts could be summarized as follows: (1) the design process is broken into two simpler problems; (2) since the upper level optimization is performed in the modal domain, the formulation is applicable to any structure modeled using FE/BE codes; (3) the highest computational cost in this upper level is related to the estimation of the matrices  $[K(\omega_i)]$  in eq. (15) and is carried out only once; (4) the optimum modal control parameters are determined after solving a simple continuous optimization problem, therefore different arrangements in the number of control and error signals (control system configurations) can be investigated with a low computational cost; and finally (5) once these optimum modal quantities are obtained in the upper level, different types of actuators and error sensors can be investigated in the lower level optimization without the need of any further expensive computation. The focus of this paper is to present the upper level or modal domain design formulation. The lower level optimization will be addressed in future publications.

**Modal Domain or Upper Level Optimization.** As mentioned before, the modal domain or upper level optimization consists in solving for the optimum modal control forces  $u_{nk}$  and the modal error sensor components  $\xi_{ns}$  that will minimize the total radiated power. A straightforward approach to solve this problem could be to minimize the expression in eq. (15) as a function of the design variables  $u_{nk}$  and  $\xi_{ns}$ . This results in a continuous unconstrained optimization problem that could be solved by any gradient search technique such as a Newton or Quasi-Newton Method [15]. The major drawback of this approach is that it does not provide any bound in the amount of the required control input. It is most likely that the optimum solution of this unconstrained problem will be at the expense of a great amount of input energy through the control forces, which is an aspect of major concern if an optimum control system is desired.

The modal domain optimization problem is better expressed as

$$\begin{aligned}
 \text{Min } \Pi_R &= \frac{\Pi_{TC}}{\Pi_{TU}} \\
 \text{such that: } &\sum_{n=1}^N \frac{|U_k(\omega_i) \cdot u_{nk}|^2}{|F(\omega_i) \cdot f_n|^2} \leq \lambda_m \quad k = 1, \dots, N_c; i = 1, \dots, NF \\
 &\sum_{n=1}^N u_{nk}^2 = 1 \quad k = 1, \dots, N_c \\
 &\sum_{n=1}^N \xi_{ns}^2 = 1 \quad s = 1, \dots, N_s
 \end{aligned} \tag{16}$$

This formulation seeks to minimize the ratio  $\Pi_R$  of the total radiated power of the controlled system  $\Pi_{TC}$  to the total radiated power of the uncontrolled system  $\Pi_{TU}$ . The inequality constraints impose restrictions in the control effort in the modal domain. By having the penalty parameter  $\lambda$  with a value less than one it is implied that the modulus square of each one of the modal control forces ( $U_k(\omega_i) \cdot u_{nk}$ ) will be, in average, less than the modulus square of the modal disturbances ( $F(\omega_i) \cdot f_n$ ). There is an inequality constraint of this type for each one of the  $N_c$  control inputs at each one of the  $NF$  frequencies ( $m = N_c \times NF$ ). The equality constraints imply a normalization of the design variables since the only relevant information is their relative values, which defines the relative controllability and observability of the modes, respectively.

By minimizing the ratio  $\Pi_R$  in eq. (16), instead of minimizing directly the radiated power of the controlled system  $\Pi_{TC}$ , the cost function will always acquire a value between zero and one. In the same way, the equality constraints will keep the values of the design variables between -1 and 1. The reason for these normalizations is related to the implementation of numerical algorithms to solve optimization problems. Within optimization routines, convergence tolerances and other criteria are necessarily based

upon an implicit definition of "small" and "large", and thus variables with widely varying orders of magnitude may cause difficulties for some algorithms [15].

This upper level or modal domain optimization is solved using the Goal Attainment Method of Gembicky [16]. This method is a multi-objective optimization procedure in which the cost function and the constraints are both expressed as design objectives with individual goals to reach. The advantage of this method over other conventional nonlinear constrained optimization routines is that instead of having to satisfy hard constraints it allows the design goals to be under or over achieved. Therefore, it is always possible to obtain a solution even if the constraints are violated.

### NUMERICAL EXAMPLE

The applicability of the formulation presented here is demonstrated for the ASAC of a simply supported cylinder driven by a multiple-frequency point disturbance as shown in figure 2. In order to keep the solution of the numerical acoustics problem simple, and avoid any irregular frequency [14], the cylinder is assumed to be open. The analysis of a cylindrical structure is interesting from the point of view that it represents a structure of involved complexity on its vibration and acoustic response that is not tractable under previous design approaches. The disturbance force is located at  $x=0.00m$ ,  $y=0.30m$  and  $z=0.00m$  with frequency components at 180Hz, 240Hz and 300Hz. The amplitude of the disturbance force at the three frequencies is 10N, 15N and 2N respectively. This combination of disturbance frequencies and amplitudes has been chosen in order to have more than one mode producing significant contributions to the total radiated power in eq. (15). The analysis includes the first eight modes that will be excited by that force, i.e. symmetric with respect to the axial direction. The respective natural frequencies, mode shapes and modal disturbances are computed using the FE code IBM-CAEDS using 720 thin-shell quadrilateral linear elements. The results are presented in Table I where "a" and "b" are the modal indices in the circumferential and axial direction, respectively. A constant modal damping ratio of 0.05% ( $\beta_n=0.005$ ) is assumed in all the modes.

The modal acoustic radiation at each one of the disturbance frequencies is obtained using the boundary element code SYSNOISE in conjunction with the same mesh used in the finite element analysis [14]. From the estimated modal acoustic pressures, the modal power matrices  $[K(\omega_i)]$  in eq. (15) are generated. The contribution of each one of the modes and the cross coupling between the modes, including the dynamics of the structure, to the total radiated power given by eq. (15) can be

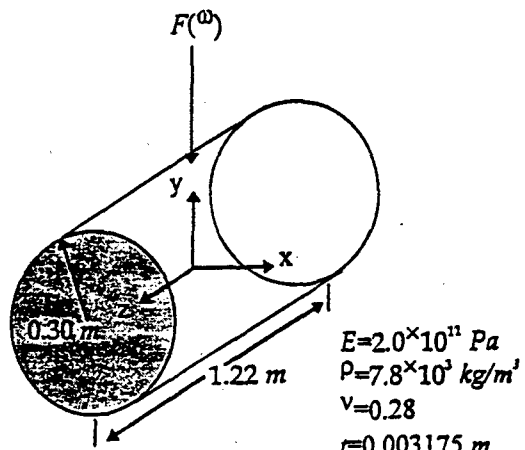


*Table I. FE modal data.*

Mode	Index		Nat. Freq. (Hz)	$f_n$
	a	b		
1	4	1	159	-0.256
2	3	1	174	0.249
3	5	1	213	-0.259
4	6	1	303	-0.263
5	2	1	314	0.230
6	7	1	416	0.261
7	6	3	484	-0.260
8	7	3	522	0.261

*Figure 2. Simply-supported cylinder with disturbance.*

observed in figure 3. The dark and white bars represent positive and negative contributions (dB of the absolute values) to the total radiated power. It can be noticed that even though modes 2 and 4 are near on-resonance conditions, it is mode 5 who dominates the contributions to the total radiated power (75.7 dB). This result is of no surprise, since the radiation efficiency of this mode is the highest compared to the other modes included in the analysis. From figure 3, it is observed that most of the radiated power is due to the direct contributions of modes 2 and 5 and the coupling between modes 4 and 5.

The next step is to perform the upper level or modal domain optimization to investigate different control system configurations. In particular, we are interested in six different combinations: 1I1O, 1I2O, 1I3O, 2I2O, 2I3O and 3I3O where "I" and "O" denote control inputs and error sensor outputs, respectively. Therefore, we need to compute the optimum unit modal control forces  $u_{nk}$  and modal error sensor components  $\xi_{ns}$  related to each one of the control and error channels for each one of the mentioned configurations. These modal domain optimization problems are solved using Matlab's Goal Attainment subroutine [17], in conjunction to previously developed analytic sensitivity formulations [18], in a personal computer.

The reductions in the total radiated power,  $\Delta\Pi = \Pi_{TC} - \Pi_{TU}$ , due to each one of the optimum control configurations as a function of the control effort penalty parameter  $\lambda$  (the same value for all constraints) are presented in figure 4. Notice that, since at this stage all the formulations are expressed in terms of modal quantities, these results will be the same regardless of the type of transducer that is implemented. This represents one of the greatest advantages of this approach over previous optimum ASAC design formulations which require a different formulation for each different type of transducer [7,8]. From this information, the designer is allowed to decide which particular configuration is more suitable early in the design process with a relative low computational cost.

Inspection of figure 4 shows that the single control input cases seem to approach slowly an upper bound in the reduction of the total radiated power of around 8 dB. On the other hand, when the number of control inputs is equal or greater than two, there is a significant reduction in the total radiated power with less control effort, i.e. small  $\lambda$ . This result is due to the fact that there are two modes (2 and 5) responsible for

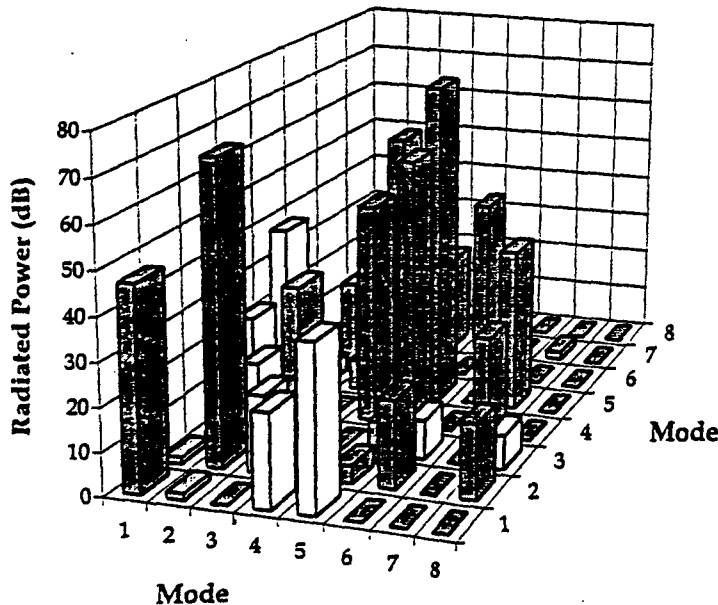


*Figure 3. Modal contributions to total radiated power. Radiated power: 77.3 dB.*

most of the total acoustic power and at least two control inputs are needed to effectively control their responses.

Another relevant aspect in the results in figure 4 is related to the number of error signals. According to the results, there is no apparent advantage in using more error channels than control inputs. As can be observed from the chart, for a particular number of control inputs, the reduction in the total radiated power will be the same regardless the number of error signals.

As can be noticed, there are thirty different control system configurations that were investigated in figure 4. For the sake of brevity the results for the case of 2I2O and  $\lambda=0.4$  are presented. Table II contains the optimum unit modal control forces and modal error sensor components. As could be expected, the optimum unit modal control forces show that in order to reduce the total acoustic power, modes 2 and 5 must be controlled. On the other hand, the results show that the optimum modal error sensor components do not necessarily need to "observe" those modes that contribute more to the total radiated power. The outcome of this results is explained as follows. The contribution to the total radiated power in eq. (15) by a particular mode or its combination with any other mode (cross-coupling) is related to both the radiation efficiency of the involved mode(s), through the elements of matrices  $[K(\omega_i)]$ , and its (their) related modal displacements  $q_n(\omega_i)$ . In particular, the contribution due to modal cross-coupling could be either positive or negative. Thus, reduction in the total radiated power is achieved by either minimizing the modal displacements related to the highest contributors or increasing the values of the modal displacements related to negative cross terms. By inspecting eq. (2) it could be seen that if the values of the control inputs are fixed, as is the case when the inequality constraints in eq. (16) are active, the only parameters that change from mode to mode, besides the modal disturbances are the unit modal control forces. Therefore, the total radiated power is minimized by assigning values to the unit modal control forces that will allow to control the most effective modes. However, the relevance of the modal error sensor components stands in providing the allowed amplitudes for the control inputs in eq. (6) and not in observing a particular mode due to its radiation characteristics. This also explains why is that there is no improvement in the reduction in the

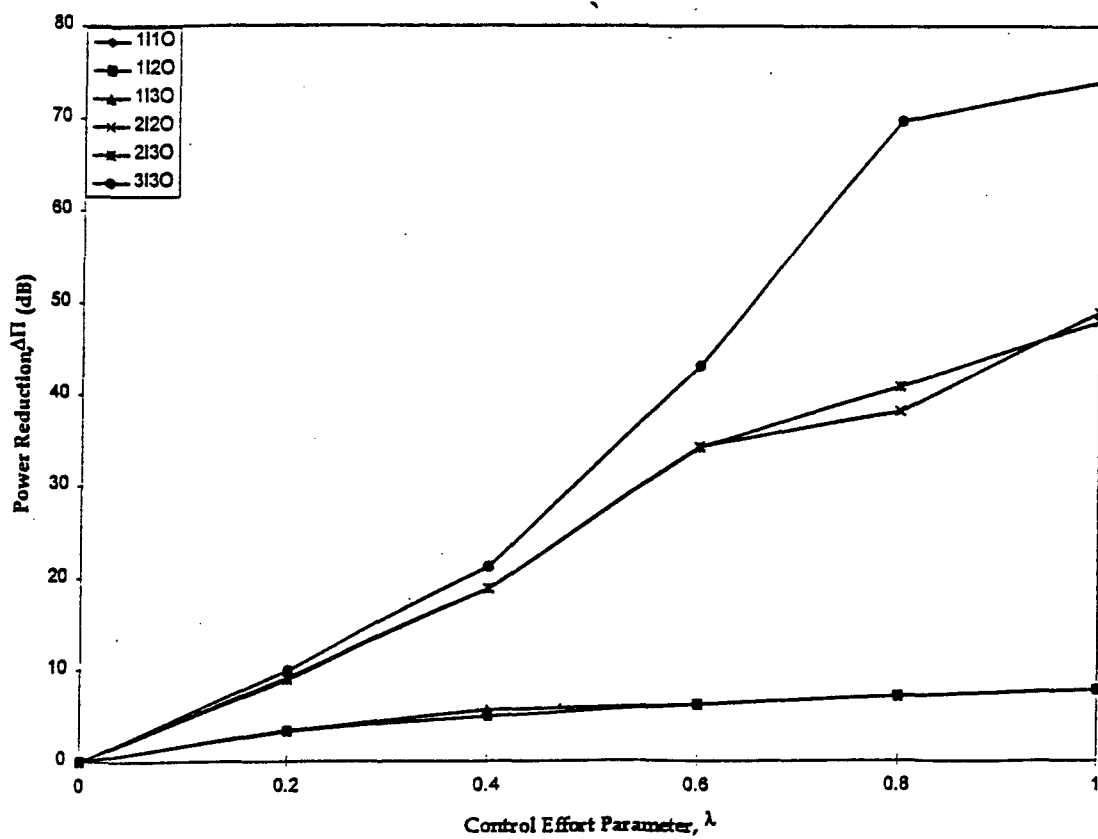


Figure 4. Reductions in total radiated power.

radiated power by increasing the number of error signals. This will only provide different mean the required control inputs.

After applying the  $2I2O-\lambda=0.40$  control configuration the total radiated power is reduced by Figure 5 presents the modal contributions to the total radiated power of the controlled structure. these results are compared to the ones in figure 3, it can be noticed that the direct contributions modes 2 and 5 were significantly reduced. In particular the radiated power due to modes 2 and 5 have reduced by 14 dB and 31 dB, respectively.

Finally, it is also possible to investigate the reduction in the far-field pressure after applying the  $2I$   $\lambda=0.40$  control configuration. Figures 6 and 7 present the before and after control sound pressure lev. (ref  $20\mu Pa$ ) at  $5.00m$  from the center of the structure. Figure 6 presents the radiation directivity in a plan parallel to the axial direction of the cylinder while figure 7 includes a plane perpendicular to the axia

*Table II. Optimum modal parameters for  $2I2O-\lambda=0.40$ .*

Mode	Unit Modal Control Forces		Modal Error Sensor Components	
	$u_{n1}$	$u_{n2}$	$\xi_{n1}$	$\xi_{n2}$
1	-0.011	0.184	0.056	0.258
2	0.671	-0.658	0.023	0.378
3	-0.002	0.001	0.027	-0.037
4	-0.048	0.049	-0.005	-0.000
5	0.740	-0.751	0.753	0.101
6	-0.000	-0.000	-0.198	0.272
7	-0.003	-0.004	0.594	0.838
8	-0.000	-0.000	0.193	0.052

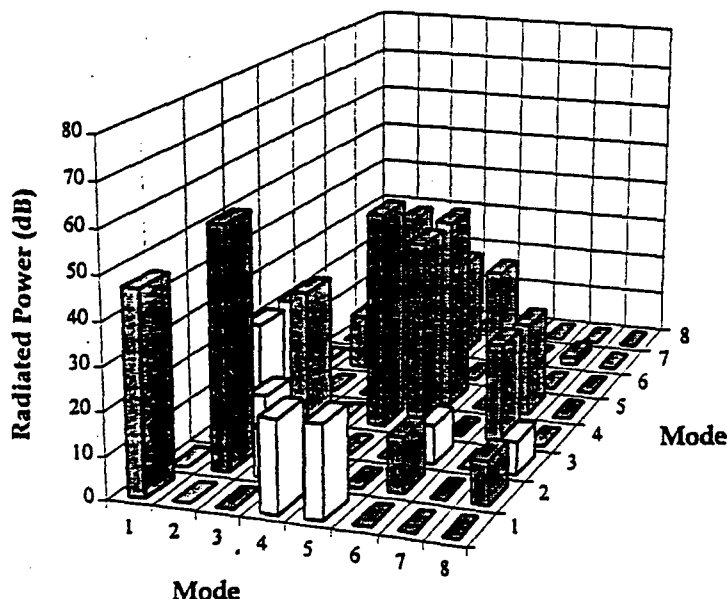


*Figure 5. Modal contribution to radiated power after  $2I2O-\lambda=0.40$ . Total radiated power: 58.5 dB.*

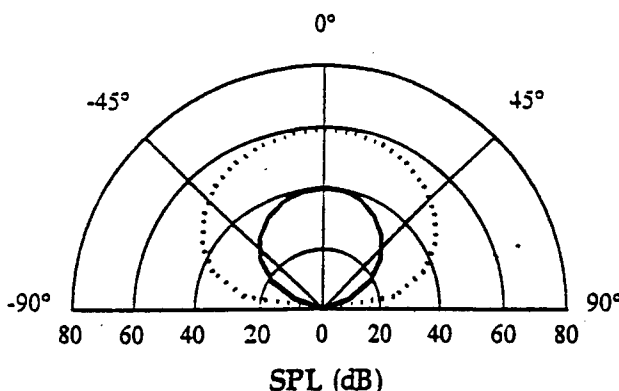


Figure 6. Radiation directivity on the z-y half plane; - - - uncontrolled — controlled.

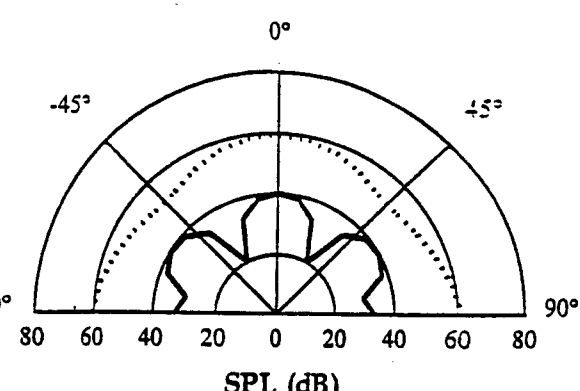


Figure 7. Radiation directivity on the x-y half plane; - - - uncontrolled — controlled.

direction at  $z=0.00m$ . The figures show that the controlled structure produce global sound reduction. Again these plots can be obtained using only the modal information of the system. The next step is to use the lower level design optimization to implement the transducers that will yield the modal parameters in Table II. This will be the topic of a future paper, however an example of this procedure for a planar radiator has been given by Burdisso and Fuller [19].

## CONCLUSIONS

An efficient formulation for the optimum design of ASAC of complex structures has been presented. The approach is based in a multi-level optimization scheme that allows the implementation of numerical techniques, such as FE and BE, during the analysis. The utilization of such numerical techniques permits the applicability of the proposed approach to complex systems that are not tractable under previous optimum ASAC design formulations. The upper level optimization of the design approach has been demonstrated for the ASAC design of a simply supported cylinder under a multiple frequency excitation. Several different control system configurations were investigated in this upper level analysis. The results showed that an optimum control configuration consists of equal number of error signals and control inputs. In addition, the optimum values of the unit modal control forces show a preference for those modes that are related to the highest contributions to the total radiated power. On the other hand, the optimum modal error sensor components will tend to observe those modes that lead to the required amplitudes of the control inputs. A sample of one of the optimum configurations was presented in detail showing very good reductions in the total radiated power.

## ACKNOWLEDGMENT

The authors gratefully acknowledge the support of this work by the Office of Naval Research Grant No. ONR-N00014-92-J-1170.

## REFERENCES

1. "Apparatus and methods for global noise reduction", C.R. Fuller, U.S. Patent No.4,715,599 (1987)
2. "Active Control of Sound Radiation from a Rectangular Panel by Sound Sources and Vibration Inputs: an Experimental Comparison", C.R. Fuller, C.H. Hansen and S.D. Snyder, J. Sound Vib. 145(2), 195-215 (1991)
3. "Active Control of Sound Transmission/Radiation from Elastic Plates by Vibrating Inputs-I Analysis", C.R. Fuller, J. Sound Vib. 136(1), 1-15 (1990)

4. "Active Control of Sound Transmission/Radiation from Elastic Plates by Vibration Inputs-II Experiments", V.L. Metcalf,C. R. Fuller, R. J.Silcox and D. E. Brown, *J. Sound Vib.* **153**(3), 387-401 (1992)
5. "Experiments on Active Control of Sound Radiation from a Panel using a Piezoceramic Actuator", C.R.Fuller, C.H. Hansen and S.D. Snyder, *J. Sound Vib.* **150**(2), 179-190 (1991)
6. "Experiments on Active Control of Structurally Radiated Sound Using Multiple Piezoceramic Actuators", R.L. Clark and C. R. Fuller., *J. Acoust. Soc. Am.* **91**(6), 3313-3320 (1992)
7. "Optimal Placement of Piezoelectric Actuators for Active Control of Sound Radiation from Elastic Plates", B. T. Wang, R.A. Burdisso and C.R. Fuller, *Proceedings of Noise-Con 91*, 267- 275 (1991)
8. "Optimal Placement of Piezoelectric Actuators and Polyvinylidene Fluoride (PVDF) Error Sensors in Active Structural Acoustic Control Approaches", R.L. Clark and C.R. Fuller, *J. Acoust. Soc. Am.* **92**(3), 1521-1533 (1992)
9. F. Fahy, *Sound and Structural Vibration* (Academic Press, Orlando Fl.,1985)
10. "Piezoelectric Actuators for Distributed Vibration Excitation of Thin Plates", E.K. Dimitriadis, C.R. Fuller and C.R. Rogers, *J. Vib. Acoust.* **113**, 100-107 (1989)
11. "Theory of Feedforward Controlled System Eigenproperties," R.A. Burdisso and C.R. Fuller, *J. Sound Vib.* **153**(3), 437-452 (1992)
12. "Dynamic Behavior of Structural-Acoustic Systems in Feedforward Control of Sound Radiation", R.A. Burdisso and C.R. Fuller, *J. Acoust. Soc. Am.* **92**(1), 277-286(1992)
13. P.A. Nelson and S.J. Elliot, *Active Control of Sound* (Academic Press, San Diego ,CA., 1993)
14. Numerical Integration Technologies NV, *Sysnoise Rev. 5.1 User's Manual* (Leuven, August 1994)
15. P.E. Gill, W. Murray and M.H. Wright, *Practical Optimization* (Academic Press, San Diego, CA.,1981)
16. "Vector Optimization for Control with Performance and Parameter Sensitivity Indices," F.W. Gembicki, Ph.D. Dissertation, Case Western Univ., (1974)
17. The MathWorks, Inc., *Optimization Toolbox User's Guide* (Natick, Mass., 1992)
18. "Sensitivity Analysis for Feedforward Control System Design", H.M. Rodriguez and R.A. Burdisso, submitted for publication to *J. Acoust. Soc. Am.* (1994)
19. "Design of Active Structural Acoustic Control Systems by Eigenproperty Assignment", R.A. Burdisso and C.R. Fuller, to appear in *J. Acoust. Soc. Am.* **96**(3), 1582-1591 (1994)

## **APPENDIX 25**

# STRUCTURAL-AcouSTIC CONTROL SYSTEM DESIGN BY MULTI-LEVEL OPTIMIZATION

Héctor M. Rodríguez

Department of General Engineering, University of Puerto Rico, Mayagüez Campus, Mayagüez,  
Puerto Rico 00681-9044

Ricardo A. Burdisso

Vibration and Acoustics Laboratories, Department of Mechanical Engineering, Virginia Polytechnic  
Institute and State University, Blacksburg, Virginia 24061-0238

(Received 29 August 1997; accepted for publication 2 April 1998)

A multi-level optimization approach for the design of feedforward active structural acoustic control (ASAC) systems is presented. The formulation takes advantage that both the structural response and the acoustic radiation from a controlled structure can be completely defined in the modal domain. All the physical parameters that define the control inputs and the error sensors are defined in the modal domain in terms of the unit modal control forces and the modal error sensor components, respectively. The upper level of the optimization solves for the optimum modal parameters that minimize the total radiated acoustic power. Then, these optimum modal parameters are used in a set of lower level or physical domain optimization problems to determine the physical characteristics of the actuators and sensors to be implemented. Since the response of the system is evaluated in the upper level using a modal approach, the formulation permits the implementation of numerical techniques and/or experimental data during the design process. Therefore, the proposed methodology can be used for the design of control systems for realistic structures with complex disturbances in an efficient manner. The design formulation is illustrated for the case of a simply supported plate excited by an off-resonance disturbance. © 1998 Acoustical Society of America.  
[S0001-4966(98)03707-2]

PACS numbers: 43.40.Vn [PJR]

## INTRODUCTION

An approach for the attenuation of structurally radiated noise consists in modifying the vibration behavior of the structure by applying control force inputs directly to the structure. This technique is known as Active Structural Acoustic Control (ASAC) and was first introduced by Fuller.<sup>1</sup> The combination of this technique in conjunction with new developments in specialized actuators and sensor materials have permitted the implementation of the concept of "smart" or adaptive systems where the transducers being an integral part of the structure. At present, such advanced control systems have been successfully implemented to control sound radiation from plates and cylinders; sound transmission/radiation from single and double panels; and interior noise from cylindrical structures among others.<sup>2</sup>

Although the concept of ASAC systems along with "smart" structures has been successfully tested, the design aspects of such systems is still under much investigation. A formal optimization approach in ASAC implementations was first introduced by Wang and co-workers.<sup>3</sup> This investigation consisted in the direct optimization of the location of rectangular piezoelectric (PZT) actuators to minimize the sound radiation from a simply supported plate. The results demonstrated that optimally located actuators provided a far better sound reduction, at both on- and off-resonance excitations, than actuators whose position were chosen based in some physical consideration. More recently, other optimum design approaches for structural-acoustic control systems have been

proposed such as using subset selection techniques,<sup>4</sup> cluster analyses,<sup>5</sup> eigenproperty assignments,<sup>6</sup> and genetic algorithms.<sup>7</sup> These previous works have demonstrated that optimally designed actuators and sensors can have a significant impact on the performance of active control systems to reduce both sound radiation and acoustic fields inside enclosures. They have shown that significant levels of attenuation can be obtained with far fewer optimally located transducers, thus reducing the dimensionality and complexity of the control system. However, there are still limitations that prevent the same approaches from being implemented in the design of complex realistic structures.

For the case of minimizing sound radiation from complex structures, the design approach of ASAC systems is virtually nonexistent. In most of the previous optimization approaches, the design formulation consisted of using a non-linear optimization algorithm to minimize an expression related to the total radiated acoustic power as a function of the physical characteristics (i.e., location, size, etc.) of the actuators and sensors. The main problem with this straightforward approach is that the computation of the acoustic response for complex structural systems as a function of the physical characteristics of the actuators and sensors results in a computationally expensive procedure.

In this work an efficient formulation for the design of feedforward ASAC systems to suppress acoustic radiation from complex structural systems under light fluid loading (i.e., no acoustic feedback) is presented. The approach consists in a two-stage multi-level optimization scheme. The for-

response and the acoustic radiation from a controlled structure can be completely defined in terms of modal quantities. All the physical parameters that define the control inputs and the error sensors have their counterpart in the modal domain through the unit modal control forces and the modal error sensor components, respectively. Therefore, the upper level of the optimization is defined in the modal domain and solves for the optimum unit modal control forces and modal error sensor components that minimize the total radiated power. Then, these optimum modal parameters are used in a set of lower level optimization problems to determine the physical characteristics of the actuators and sensors to be implemented. Since in the formulation the response is evaluated in the upper level or modal domain, it permits the implementation of numerical techniques and/or experimental data during the design process. In addition, since the upper level optimization problem is universal for any type of structure/transducer combination, a previously developed general analytical sensitivity formulation<sup>8</sup> is implemented to improve the performance of the optimization algorithm during the solution process. Therefore, the formulation is capable to handle complex structures with complex disturbances (e.g., multiple frequencies) in an efficient manner. Once the optimum modal parameters are obtained, different types of transducers can be investigated with a minimum computational effort. The proposed approach is illustrated for the case of a simply supported plate excited by an off-resonance disturbance. The study of a plate will serve as a benchmark to implement the design methodology for more complex systems.

## I. STRUCTURAL-ACOUSTIC RESPONSE

### A. Structural response

The response of a structure can be obtained by modal superposition once the eigenproperties of the system (i.e., natural frequencies and mode shapes) are known. These eigenproperties can be estimated using numerical techniques such as the finite element method (FEM) or experimentally using modal analysis techniques. For the case of sound radiation from structures submerged in light fluids such as air, it is necessary to consider only the vibration in which the response normal to the radiating surface is dominant.<sup>9</sup> The Fourier transform (FT) of the response in the direction normal to the structural surface can be obtained as a linear combination of the modes as

$$\begin{aligned} w(\mathbf{r}_s, \omega) &= \sum_{n=1}^N q_n(\omega) \phi_n(\mathbf{r}_s) \\ &= \sum_{n=1}^N F(\omega) f_n H_n(\omega) \phi_n(\mathbf{r}_s), \end{aligned} \quad (1)$$

where  $\omega$  is the excitation frequency,  $\phi_n(\mathbf{r}_s)$  is the  $n$ th mode shape,  $N$  is the total number of modes included in the analysis,  $\mathbf{r}_s$  is a point on the structure, and  $q_n(\omega) = F(\omega) f_n H_n(\omega)$  is the FT of the  $n$ th modal displacement where  $F(\omega)$  is the amplitude of the external excitation and  $f_n$  is the  $n$ th unit modal force defined as

$$f_n = \int_S \phi_n(\mathbf{r}_s) f(\mathbf{r}_s) dS. \quad (2)$$

where the integral is extended over the structural domain  $S$  and  $f(\mathbf{r}_s)$  is a function that defines the spatial distribution of the excitation. Finally,  $H_n(\omega)$  is the  $n$ th modal frequency response function defined as  $H_n(\omega) = (\omega_n^2 - \omega^2 + 2j\beta_n\omega_n\omega)^{-1}$ , where  $j$  is the imaginary number and  $\beta_n$  is the  $n$ th modal damping ratio.

### B. Acoustic response

The acoustic radiation  $p(\mathbf{r}, \omega)$  from a harmonically vibrating structure can be obtained after solving the Helmholtz wave equation<sup>10</sup>

$$\nabla^2 p(\mathbf{r}, \omega) + k^2 p(\mathbf{r}, \omega) = 0 \quad (3)$$

in conjunction with the boundary conditions

$$\nabla p(\mathbf{r}_s, \omega) = \omega^2 \rho w(\mathbf{r}_s, \omega) \quad (4a)$$

and

$$\lim_{|\mathbf{r}| \rightarrow \infty} p(\mathbf{r}, \omega) \rightarrow 0, \quad (4b)$$

where  $\mathbf{r}$  is a field point location;  $\nabla(\cdot)$  is the Laplacian operator;  $k = \omega/c$  is the acoustic wave number; and  $c$  and  $\rho$  are the phase speed and density in the fluid that surrounds the structure, respectively. Equation (4a) relates the structural response with the acoustic pressure at the structural surface while Eq. (4b) represents the Sommerfeld far-field condition that requires that the acoustic pressure decreases as the field point is moved away from the structure. Equations (3) and (4) do not possess closed-form solution for any but very simple cases. For the case of structures with complex geometries, they are solved using numerical techniques such as the boundary element method (BEM).<sup>11</sup>

The strategy in this work is to obtain the acoustic response by considering the contributions of each of the structural modes separately. By substituting the modal expansion in Eq. (1) into Eq. (4), the acoustic pressure field can be obtained as a linear contribution of the structural modes as

$$p(\mathbf{r}, \omega) = \sum_{n=1}^N q_n(\omega) p_n(\mathbf{r}, \omega), \quad (5)$$

where  $p_n(\mathbf{r}, \omega)$  is the acoustic pressure at  $\mathbf{r}$  due to the  $n$ th mode shape, i.e., modal pressure.

The total acoustic radiated power can be estimated by integrating the far-field acoustic intensity over a sphere of surface area  $A$  that surrounds the structure as

$$\Pi(\omega) = \int_A \frac{|p(\mathbf{r}, \omega)|^2}{2\rho c} dA. \quad (6)$$

Replacing Eq. (5) into Eq. (6), the acoustic power can be written in a general quadratic form as

$$w = \int_{A/2pc}^{q_n(\omega)} q_n(\omega) d\omega$$

$$= \{q(\omega)\}^H [K(\omega)] \{q(\omega)\}, \quad (7)$$

where the superscripts (\*) and  $H$  imply complex conjugate and conjugate transpose, respectively; and the elements of matrix  $[K(\omega)]$  are given by the integral in Eq. (7).

The diagonal elements of the matrix  $[K(\omega)]$  represent the power radiated due to the direct contributions of the modes, while the off-diagonal terms contain the power radiated due to the coupling of the modes. In particular, the off-diagonal terms could be either positive or negative depending if the interaction between the modes is constructive or destructive. For the case of complex structures, this matrix has to be evaluated by numerical techniques and therefore represents the highest computational effort during the evaluation of the acoustic response. Finally,  $\{q(\omega)\}$  is the vector of modal displacements.

Equation (7) defines the total radiated power at a single frequency. The general case of multiple frequency excitations is expressed as a linear combination of the contributions due to each frequency as

$$\Pi_T(\omega) = \sum_{i=1}^{N_F} (\{q(\omega_i)\}^H [K(\omega_i)] \{q(\omega_i)\}) = \sum_{i=1}^{N_F} \Pi(\omega_i), \quad (8)$$

where  $N_F$  is the total number of frequencies.

Inspection of Eqs. (7) and (8) show that the relative contributions to the acoustic power due to the modes depend on two factors: the complex amplitudes of the modal displacements  $\{q(\omega_i)\}$  and the relative values of the modal power matrices  $[K(\omega_i)]$ . The modal displacements  $\{q(\omega_i)\}$  depend on the dynamics of the structure under a particular disturbance  $F(\omega)$ . In the same way, the matrices  $[K(\omega_i)]$  depend on the capacity of the structural modes to generate sound and their coupling characteristics. For a mode excited on-resonance, its modal displacement will be significantly larger than the other ones and therefore this mode will most likely dominate the acoustic field. On the other hand, at off-resonance conditions the acoustic field will probably be mainly due to the radiation of the modes with the higher radiation efficiency.

### C. Optimum feedforward control inputs

Equation (1) represents the steady-state or frequency domain structural response due to an external disturbance  $F(\omega)$ . The response due to this disturbance can be controlled by applying  $N_c$  secondary control forces  $U_k(\omega)$  where  $k = 1, \dots, N_c$ . The response of the controlled system can be expressed as<sup>6</sup>

$$w^c(\mathbf{r}_s, \omega) = \sum_{n=1}^N q_n^c(\omega) \phi_n(\mathbf{r}_s), \quad (9)$$

where, using the principle of superposition, the  $n$ th modal displacement of the controlled system is

$$q_n(\omega) = q_n(\omega) - U_n(\omega) \sum_{k=1}^{N_c} U_k(\omega) u_{nk}. \quad (10)$$

where  $U_k(\omega)$  and  $u_{nk}$  are the amplitude and the  $n$ th unit modal control force of the  $k$ th control input, respectively. As can be seen in Eq. (10), the unit modal control forces  $u_{nk}$  dictate the relative *controllability* of the different modes by the control inputs  $U_k(\omega)$ . Similarly to the unit modal disturbances, the unit modal control forces are given as

$$u_{nk} = \int_S \phi_n(\mathbf{r}_s) u_k(\mathbf{r}_s) dS, \quad (11)$$

where  $u_k(\mathbf{r}_s)$  defines the spatial distribution of the control forces. Similar to the unit modal disturbances, the unit modal control forces depend completely on the physical implementation of the actuators, e.g., shakers, PZT ceramics, etc.

In feedforward control, the complex amplitude of the control inputs  $U_k(\omega)$  are obtained by "feeding forward" a reference signal  $x(\omega)$ , fully coherent to the original disturbance  $F(\omega)$ , through an array of compensators. The compensators are designed such that a measurable control cost function is minimized. This cost function is usually obtained as the sum of the mean-square-value (msv) of the response at the error sensors as

$$J = \sum_{s=1}^{N_s} |E_s(\omega)|^2, \quad (12)$$

where  $E_s(\omega)$  is the FT of the response due to the  $s$ th error sensor output and  $N_s$  is the total number of error outputs.

In ASAC applications, the error signals could be obtained by measuring directly the acoustic field using microphones or the structural vibration using structural sensors. In many applications the use of far-field microphones as error sensors is not practical. Since one of the objectives in this work is to eliminate the need for the use of microphones and design a completely adaptive system with the actuators and sensors integrated to the structure, only structural sensors are considered here. For the case of such sensors, the response can always be expressed as a linear combination of modal terms as<sup>6</sup>

$$E_s(\omega) = \sum_{n=1}^N q_n^c(\omega) \xi_{ns}, \quad (13)$$

where  $\xi_{ns}$  is the  $n$ th modal component of the  $s$ th error sensor. Again, the modal error components are related to the physical implementation of the sensors and they dictate the relative *observability* of the different modes

By differentiating Eq. (13) with respect to the real and imaginary part of the control inputs  $U_k(\omega)$  and setting them to zero, it can be shown that the set of the optimum control inputs is the solution of the following linear system of equations

$$[T_{ce}(\omega)] \{U(\omega)\} = -F(\omega) \{T_{de}(\omega)\}, \quad (14)$$

where vector  $\{U_k(\omega)\}$  contains the  $N_c$  control inputs. the elements of matrix  $[T_{ce}(\omega)]$  are the transfer functions be-

(10)

the error outputs and the elements of vector  $\{T_{de}(\omega)\}$  contain the transfer functions between the disturbances and the error outputs.

Once the optimum feedforward control inputs  $U_k(\omega)$  are obtained from the solution of Eq. (14) they are substituted into Eq. (10) to compute the modal displacements of the controlled system  $q_n^c(\omega)$ . Finally, the controlled modal displacements can be substituted for the uncontrolled modal displacements in Eq. (7) to yield the total radiated power of the controlled system as

(11)

$$\Pi^c(\omega) = \{q^c(\omega)\}^H [K(\omega)] \{q^c(\omega)\}, \quad (15)$$

where  $\{q^c(\omega)\}$  is the vector of controlled modal displacements. In the same way, the total controlled radiated power due to the contribution of  $N_F$  frequencies is given as

$$\begin{aligned} \Pi_T^c(\omega) &= \sum_{i=1}^{N_F} (\{q^c(\omega_i)\}^H [K(\omega_i)] \{q^c(\omega_i)\}) \\ &= \sum_{i=1}^{N_F} \Pi^c(\omega_i). \end{aligned} \quad (16)$$

control nodal dimensions of the "d" a disturbance-com cost ined se at

(12)

rror ob ro In tor his nd nd re se ul

3)

re e

i i

Equation (16) describes the acoustic response of a feed-forward controlled structure. This equation clearly shows the advantage of evaluating the response as a combination of modal contributions, especially in terms of the computational effort. This advantage is specially critical during the design of the control system. This design procedure involves a systematic update of the physical characteristics of the transducers (i.e., type, size, number, location, etc.) and the evaluation of the acoustic response for each configuration. This process is continued until the desired attenuation is obtained. Using Eq. (16), the evaluation of the acoustic response is just a matter of simple algebraic manipulations once the elements of matrices  $[K(\omega_i)]$  are known.

## II. CONTROL SYSTEM DESIGN BY MULTI-LEVEL OPTIMIZATION

As shown in Eq. (16), the total radiated power from the controlled system is a function of the forces  $U_k(\omega)$  which in turn are defined from the modal characteristics of the uncontrolled system, i.e.,  $F(\omega)f_n$  and  $H_n(\omega)$ , and of the actuators and sensors, i.e.,  $u_{nk}$  and  $\xi_{ns}$ . The unit modal control forces  $u_{nk}$  and modal error sensor components  $\xi_{ns}$  are directly related to the physical implementation of the actuators and sensors, respectively. Therefore, the design of the control system consists in finding the transducers that, when implemented, yield the proper unit modal control forces  $u_{nk}$  and modal error sensor components  $\xi_{ns}$ . The significance of the unit modal control forces and the modal error sensor components in the response of the controlled system is that they represent the relative *controllability* and *observability* of the modes by the control actuators and the error sensors, respectively. Regardless of the type of actuators and sensors, the unit modal control forces and the modal error sensor components play the role of weighting coefficients that can be normalized between  $\pm 1$ .

The fact that the response of the controlled system can be obtained without the knowledge of the physical characteristics of the transducers but from their effect on the different modes brings out the opportunity of designing the control system using a multi-level optimization approach. In multi-level optimization a complex problem is broken into a set of simpler problems that offers computational advantages. The process of decomposition consists of separating the optimization process in an upper level problem, in which a global cost function is minimized with respect to global design variables, and a set of lower level problems, in which a set of local design variables are related to all the global design variables or a subset of them. The upper level or modal domain optimization consists in finding the optimum unit modal control forces and modal error sensor components that minimize the total radiated acoustic power. Therefore, at the upper level optimization, the global cost function is the total radiated acoustic power as presented in Eq. (16) and the global design variables are the modal quantities  $u_{nk}$  and  $\xi_{ns}$ . Once the optimum modal parameters are obtained, a set of lower level or physical domain optimization problems can be solved in which the actuators and sensors that yield the optimum unit modal control forces  $u_{nk}$  and modal error sensor components  $\xi_{ns}$  are obtained. Therefore, the local design variables at the lower level are the physical parameters that define the actuators and sensors, i.e., number, size, location, etc., while the local cost functions are the sum of the squares of the differences between the optimum modal quantities and the "actual" modal parameters due to the implementation of a particular transducer. The outcome of this procedure is an optimally designed control system.

The main advantages of the proposed design approach can be listed as:

- (1) The design process is broken into the solution of two simple problems. The modal domain or upper optimization problem consists in the minimization of a continuous function of the modal control parameters. On the other hand, the physical domain or lower level formulations consist in a set of much simpler problems that involves matching the "actual" modal parameters of the transducers as closely as possible to the "ideal" modal parameters. The simplicity in the solution in this two-level approach should be contrasted to the difficulty in solving a straightforward optimization problem in which the acoustic response is directly expressed in terms of the physical characteristics of the transducers.
- (2) Since the upper level is solved in the modal domain, the formulation is applicable to the design of any complex structure modeled using FEM/BEM codes or using experimental modal analysis data. The highest computational effort at this level is in computing the matrices  $[K(\omega_i)]$  using Eq. (7). The computation of these matrices has to be carried out only once for each disturbance frequency during the design process.
- (3) Since the modal domain is universal for any type of structure, a sensitivity analysis of the cost function and the constraints can be developed in this stage. The use of

greatly improves the performance of optimization algorithms.<sup>8</sup>

- (4) Since the response of the controlled system is completely defined in the modal domain, the upper level formulation can be used to investigate and evaluate the performance of different control system configurations. At this level, the designer can decide with relative ease the required number of control inputs  $N_c$  and error outputs  $N_s$  that are necessary to obtain a desired attenuation.
- (5) Since the design of the transducers to be implemented in the control system is carried out after solving simple sets of optimization problems, different models of actuators and sensors can be easily investigated at the lower level without the need to recompute the response of the structure.

### A. Upper level or modal domain optimization

The modal domain or upper level optimization problem is posed as follows:

$$\text{Min } R(u_{nk}, \xi_{ns}) = \frac{\Pi_T^c(\omega)}{\Pi_T(\omega)} \quad (17a)$$

such that

$$g_m^c(u_{nk}, \xi_{ns}) = \sum_{n=1}^N \frac{|U_k(u_{nk}, \xi_{ns}, \omega_i) \cdot u_{nk}|^2}{|F(\omega_i) \cdot f_n|^2} \leq \lambda_m, \\ i = 1, \dots, N_F \quad m = N_c \times N_F \quad (17b)$$

$$g_k^n(u_{nk}) = \sum_{n=1}^N u_{nk}^2 = 1, \quad k = 1, \dots, N_c \quad (17c)$$

$$g_s^\xi(\xi_{ns}) = \sum_{n=1}^N \xi_{ns}^2 = 1, \quad s = 1, \dots, N_s. \quad (17d)$$

The optimization problem stated in Eq. (17) seeks to minimize the ratio  $R(u_{nk}, \xi_{ns})$  of the total radiated power of the controlled system  $\Pi_T^c(\omega)$  to the total radiated power of the uncontrolled system  $\Pi_T(\omega)$ . The inequality constraints in Eq. (17b) impose restrictions on the effort, through the penalty parameter  $\lambda_m$ . By setting the penalty parameter  $\lambda_m$  to less than one, Eq. (17b) implies that the modulus square of each one of the modal control forces,  $|U_k(\omega_i)u_{nk}|^2$ , will be in a weighted average sense less than the modulus square of the modal disturbances,  $|F(\omega_i)f_n|^2$ . Therefore, by satisfying these constraints the control force applied to each mode will be less than the modal force due to the disturbance. There is an inequality constraint of this type for each one of the  $N_c$  control inputs at each one of the  $N_F$  frequencies. It is important to mention that the constraints in the control effort Eq. (17b) could also be implemented as a penalty in the cost function. Finally, the equality constraints in Eqs. (17c), (17d) imply a normalization of the design variables since the only relevant information is their relative values, which defines the relative *controllability* and *observability* of the modes, respectively. This continuous optimization problem in the upper level or modal domain can be solved by any con-

tinuous algorithm in conjunction with previously developed analytical sensitivity formulations.<sup>8</sup>

### B. Lower level or physical domain optimization

Once the optimum modal parameters are obtained they are used as goals to reach in a set of physical domain optimization problems. The purpose of the optimization problems at this level is to find the physical characteristics of the desired actuators and sensors that when implemented in the real structure induce unit modal control forces and modal error sensor components as close as possible to the optimum values obtained from the upper level optimization. For the sake of clarity, from now on the optimum modal parameters obtained in the upper level are denoted as "ideal" while the modal parameters of the physical transducers are denoted as "actual." The "actual" modal parameters are functions of the physical design parameters of the transducers such as type, location, dimensions, etc. Hence, the first requirement at this level is to have mechanical models for the transducers that relate the modal parameters to the physical design variables. In addition, a single control input (error output) can be implemented using multiple actuators (sensors) wired in- or out-of-phase. Therefore, the cost functions at this level are a measure of the difference between the "ideal" and "actual" modal parameters while the design variables are the physical characteristics of the implementation of the transducers (i.e., size, location, relative phases, etc.).

#### 1. Optimum actuator design

The set of lower level or physical domain optimization problems to obtain the optimum physical design parameters  $\{a\}$  for the control actuators can be expressed in formal optimization notation as

$$\min C_k(\{a\}) = \sum_{n=1}^N |u_{nk} - \hat{\Psi}_{nk}(\{a\})|^2, \quad (18)$$

where the cost function  $C_k(\{a\})$  represents a measure of the error between the "ideal" optimum unit modal control forces  $u_{nk}$  and the "actual" unit modal control forces given by the function  $\hat{\Psi}_{nk}(\{a\})$  for the  $k$ th control input. Then, the  $n$ th component of the "actual" unit modal control force  $\hat{\Psi}_{nk}(\{a\})$  driven by the  $k$ th control signal is obtained by including the contributions of all the  $n$ th unit modal forces produced by each one of the  $N_A$  actuators as

$$\hat{\Psi}_{nk}(\{a\}) = \sum_{i=1}^{N_A} \Psi_{ni}(\{a\}_i), \quad (19)$$

where  $\Psi_{ni}(\{a\}_i)$  is the mechanical model that defines the  $n$ th unit modal force produced by the  $i$ th actuator and vector  $\{a\}_i$  contains the design variables for the  $i$ th actuator.

#### 2. Optimum sensor design

Similarly, the set of lower level or physical domain optimization problems to obtain the optimum physical design parameters for the error sensors can be expressed as

wh  
the  
"ac  
con  
uni  
tua  
sig  
tior  
eac

wh  
the  
abl

con  
low  
can  
tain  
sens  
tatic

III.

pos  
sig  
por  
of  
stud  
ple:  
elas  
Ns  
pla  
m.  
p=  
is :  
anc

Mode ( $n_x, n_y$ )	Nat. freq. Hz	$f_n$	"Ideal" $u_{nl}$	"Ideal" $\xi_{nl}$	"Actual" $u_{nl}$	"Actual" $\xi_{nl}$
(1,1)	85.9	1.370	-0.070	0.161	0.144	0.380
(2,1)	184.9	-1.100	-0.166	-0.235	-0.290	-0.069
(1,2)	244.8	0.570	0.005	0.359	-0.022	-0.146
(2,2)	343.8	-0.460	-0.002	-0.102	0.050	-0.274
(3,1)	349.9	-0.480	-0.002	0.186	-0.048	0.096
(3,2)	508.5	-0.200	0.001	0.094	-0.053	-0.295
(1,3)	509.5	-1.130	-0.154	-0.143	-0.122	-0.124
(4,1)	581.0	1.490	0.963	-0.460	0.927	0.451
(2,3)	608.5	0.910	0.127	0.455	0.130	0.500
(4,2)	739.8	0.620	0.002	0.534	-0.036	-0.218
(3,3)	773.5	0.400	0.001	-0.110	0.030	0.380

$$\min C_s(\{b\}) = \sum_{n=1}^N |\xi_{ns} - \hat{\Omega}_{ns}(\{b\})|^2, \quad (20)$$

where  $C_s$  is the cost function relating the difference between the optimum modal error sensor components  $\xi_{ns}$  and the "actual" modal error sensor components given by  $\hat{\Omega}_{ns}(\{b\})$  connected to the  $s$ th error channel. Similar to the case of the unit modal control forces, the  $n$ th component of the "actual" modal error sensor component due to the  $s$ th error signal  $\hat{\Omega}_{ns}(\{b\})$  can be obtained by including the contributions of all the  $n$ th modal error sensor components due to each one of the  $N_E$  error sensors as

$$\hat{\Omega}_{ns}(\{b\}) = \sum_{j=1}^{N_E} \Omega_{nj}(\{b\}_j), \quad (21)$$

where  $\Omega_{nj}(\{b\}_j)$  is the  $n$ th modal error sensor component of the  $j$ th error sensor and vector  $\{b\}_j$  contains the design variables for the  $j$ th sensor.

Equations (18) and (21), solved for each one of the  $N_c$  control and  $N_s$  error channels, define completely the set of lower level or physical domain optimization problems. As can be seen, once the optimum modal parameters are obtained in the upper level optimization different actuators and sensor models can be investigated with a minimum computational effort.

### III. NUMERICAL RESULTS

This section illustrates the implementation of the proposed multi-level optimization design approach for the design of an optimum control system for a baffled simply supported plate. Since both the structural and acoustic responses of a simply supported plate can be obtained analytically, the study of this structure is ideal as a benchmark for more complex systems. The plate is made of steel with a modulus of elasticity  $E = 2 \times 10^{11}$  N/m<sup>2</sup>, mass density  $\rho_s = 7800$  Ns<sup>2</sup>/m<sup>4</sup>, and Poisson's ratio  $\nu = 0.28$ . The dimensions of the plate are  $L_x = 0.38$  m,  $L_y = 0.30$  m, and thickness  $h = 0.002$  m. The plate is assumed to be vibrating in air with a density  $\rho = 1.21$  kg/m<sup>3</sup> and phase speed  $c = 343$  m/s. The disturbance is assumed to be a point force with amplitude  $F(\omega) = 1$  N and frequency  $\omega = 3454$  rad/s (i.e., 550 Hz) and located at  $x_f$ .

=0.24 m,  $y_f = 0.13$  m. The case of multiple frequency excitations has already been studied<sup>12</sup> and will be reported in a future publication.

#### A. Uncontrolled system response

For the case of a simply supported plate, the natural frequency and mass normalized mode shape, identified by their modal indices ( $n_x, n_y$ ), are easily computed.<sup>10</sup> In the present case, it is assumed a modal damping ratio of 1% (i.e.,  $\beta_n = 0.01$ ) for all the modes. A total of 11 modes (i.e.,  $N = 11$ ) are considered in the analysis. The natural frequencies and unit modal disturbance force,  $f_n$ , are summarized in the second and third column in Table I. From the values of the natural frequencies, it can be seen that the disturbance excitation is off-resonance between the (1,3) and the (4,1) modes. In addition, the values of the unit modal disturbances indicate that the disturbance couples well with modes (4,1), (1,1), (1,3), and (1,2) while is less effective in driving, for example, modes (3,2) and (3,3).

Similarly, the far-field acoustic response due to the  $n$ th mode of a baffled simply supported plate can also be obtained analytically from the solution of the Raleigh integral as<sup>9</sup>

$$p_n(r, \theta, \gamma, \omega) = -\omega^2 \rho \frac{L_x L_y}{2\pi n_x n_y} \sqrt{\frac{4}{\rho_s h L_x L_y}} \left( \frac{(-1)^{n_x} e^{-j\tau_1} - 1}{(\tau_1/n_x \pi)^2 - 1} \right) \times \left( \frac{(-1)^{n_y} e^{-j\tau_2} - 1}{(\tau_2/n_y \pi)^2 - 1} \right) e^{-jkr}, \quad (22)$$

where  $k = \omega/c$ ;  $\tau_1 = kL_x \sin \theta \cos \gamma$  and  $\tau_2 = kL_y \times \sin \theta \sin \gamma$ ; and  $\theta$  and  $\gamma$  are the angles defining the far-field direction.

Using Eq. (22), the contribution due to the modes, both direct and cross terms, to the total radiated power at 550 Hz including the dynamics of the system can be presented graphically. To this end, each one of the elements in the double summation in Eq. (7) is shown in Fig. 1. The results are presented in decibels (dB ref  $1 \times 10^{-12}$  W) where the negative contributions (i.e., light shaded columns) are included in the figure as the dB of the absolute value. This figure shows that mode (4,1) is the highest contributor to the

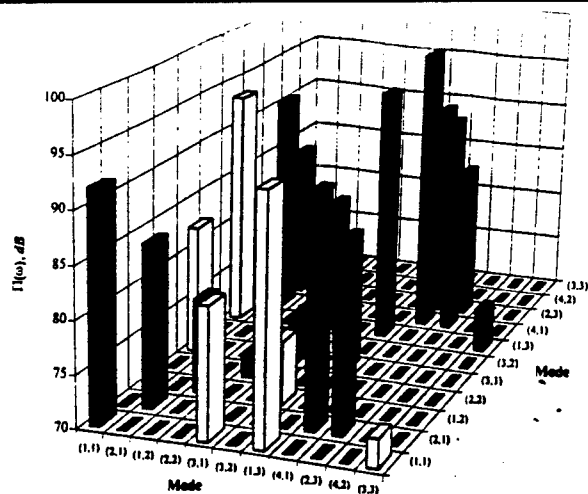


FIG. 1. Modal contributions to total radiated power. Total radiated power: 101.8 dB.

total radiated power in spite of having low radiation efficiency. This is due to the fact that the force strongly drives this mode. These results demonstrate the significant effect that the disturbance plays in the modal contributions to the total radiated power, in particular for spectrally white inputs. On the other hand, the effect of the radiation efficiency can be observed in the fact that even though the excitation frequency is far away from the resonance of the (1,1) mode the power due to this mode is only about 6 dB below the power produced by mode (4,1). Thus this shows that both the dynamics and the radiation properties of the modes are important in the modal breakdown of the total acoustic power.

## B. Control system design: Results and discussion

### 1. Modal domain design

The goal in the upper level or modal domain optimization is to find the optimum values of the unit modal control forces and modal error sensor components that minimize the total radiated power of the controlled system  $\Pi_T^c(\omega)$  in the presence of designer selected constraints in the modal control effort. In the present example, this optimization problem has been solved using the Goal Attainment Method.<sup>13</sup> Six different control configurations were studied: 1I1O, 1I2O, 1I3O, 2I2O, 2I3O, and 3I3O where "I" and "O" denote control and error channels, respectively. The acoustic power reduction for each of the six control configurations as a function of the penalty in the control effort are shown in Fig. 2. Each one of the configurations in the figure represents a set of optimum unit modal control forces  $u_{nk}$  and optimum modal error sensor components  $\xi_{ns}$ . It can be observed that for a particular number of control channels, there is no increase in the reduction in the total radiated power by increasing the number of error outputs. For that reason, the curves for configurations with identical number of control inputs are overlapped in the figure (e.g., curves 1I1O, 1I2O, and 1I3O). As can be seen in the figure, the reduction in the total radiated power can be accomplished by relaxing the constraint in the control effort and/or increasing the number of control channels. The results in Fig. 2 are very useful during the

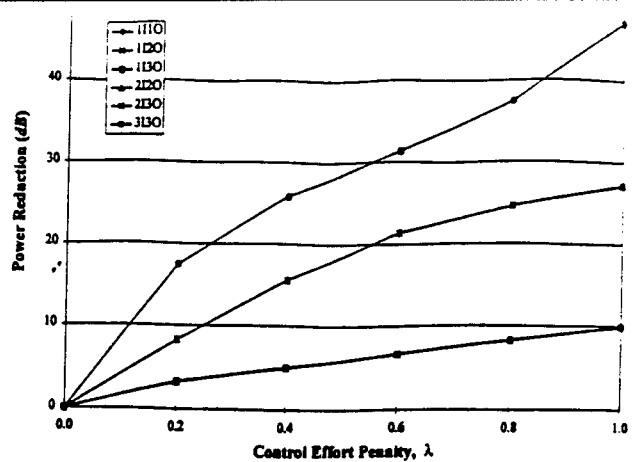


FIG. 2. Reductions in total radiated power.

design process since the designer can decide at a very early stage how many control channels are needed and what relative expense (modal control effort) is required to accomplish a desired attenuation. Since the acoustic response (before and after control) is expressed in terms of modal parameters, the same reductions will be expected for any type of actuator/sensor configuration that yields the same unit modal control forces and modal error sensor components as the optimum ones. This is one of the main advantages of the present approach versus optimizing directly the physical characteristics of the transducers.

In order to investigate in detail the optimum results, the values for the optimum modal parameters for the 1I1O configuration with a  $\lambda = 1.0$  are also presented in the fourth and fifth columns of Table I. As shown in the table, the optimum unit modal control forces,  $u_{nk}$ , suggest that most of the control effort should be dedicated to mode (4,1) with significantly less effort into modes (2,1), (1,3), (2,3), and (1,1). This behavior is explained by plotting the modal contributions to the controlled total radiated power. This is shown in Fig. 3. Comparison of this figure and Fig. 1 shows that the mechanism of control is by mainly reducing the contribution due to mode (4,1). As shown in Fig. 1, mode (4,1) is the

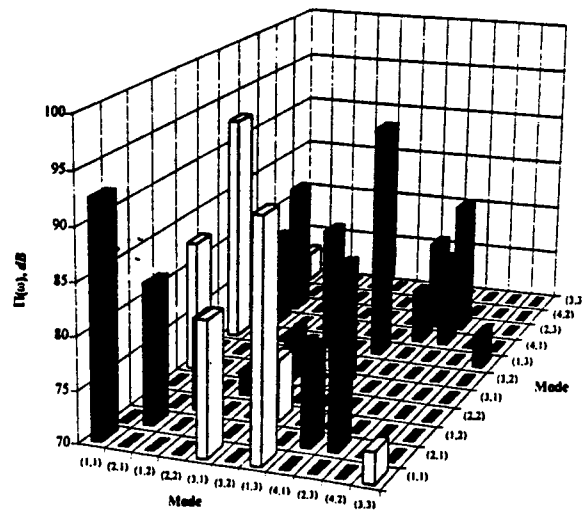


FIG. 3. Modal contributions to controlled power using the 1I1O configuration and  $\lambda = 1.0$ . Total radiated power: 91.8 dB.

higher before it implies are indicated these systems by the On the (2,3) c total p the (4 terms the (2, T is suc contrc hand do not radiate comp distur This i (10). : this e constr chang u<sub>nk</sub> - tral fc power modal

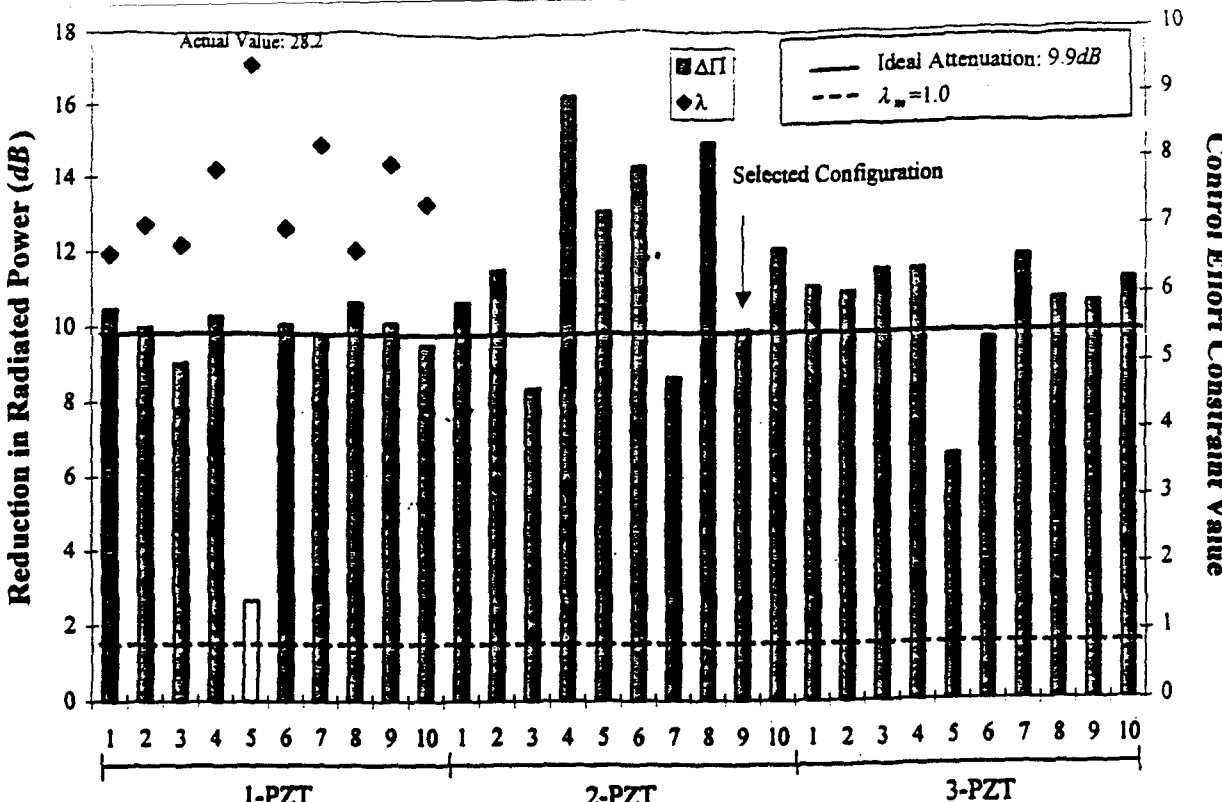


FIG. 4. Performance of optimum actuator configurations (using "ideal" sensor).

highest contributor to the uncontrolled sound field and therefore it is trivial that this mode has to be highly controlled as implied in Table I. On the other hand, modes (1,1) and (1,3) are virtually left unaffected by the control system as indicated by the low values of the unit modal control forces for these modes in Table I. This is because in the uncontrolled system the direct power radiated by these modes is canceled by their negative cross-radiation terms as shown in Fig. 1. On the other hand, Fig. 1 also shows that modes (2,1) and (2,3) do not have a significant direct term contribution to the total power. However, these modes couple acoustically with the (4,1) mode as shown by the important positive cross terms in the same figure. Thus the control system attenuates the (2,1) and (2,3) modes to reduce these cross terms.

The previous results show that the optimization process is successful in identifying only those modes that had to be controlled to reduce the total radiated power. On the other hand, the optimum modal error sensor components in Table I do not seem to observe the more important modes in the total radiated power, where the highest value of the modal error components is for mode (4,2) which is barely excited by the disturbance and do not contribute at all to the acoustic field. This is explained by looking once more at the form of Eq. (10). If the values of the control inputs  $U_k(\omega)$  are fixed in this equation, as is the case when the modal control effort constraints are active, the only control parameters that change from mode to mode are the unit modal control forces  $u_{nk}$ . Therefore, the selection of the correct unit modal control forces has a direct impact on the total radiated acoustic power. On the other hand, the relevance of the optimum modal error sensor components stands in providing the cor-

rect complex amplitudes for the control inputs and not in observing a particular mode due to its radiation characteristics. This also explains why there is no improvement in the reduction in the radiated power by simply increasing the number of error signals. Having more error signals will only provide different means to satisfy the required control effort constraints.

At this point, the major aspects of the modal domain optimization results have been covered. In a typical implementation of the proposed design approach, the designer investigates at the modal domain level many configurations, as shown in Fig. 2, and selects the one that best fits the particular situation (i.e., attenuation, number of control channels, control effort, etc.). Then, the optimum unit modal control forces and modal error sensor components of the selected configuration are used in the physical domain level to design the physical characteristics of the actuators and sensors.

## 2. Physical domain design

The first step in the lower level or physical domain design is the selection of the type of transducers to be used. One of the advantages of the present design approach is that different models of actuators and sensors can be investigated with a low computational effort. In the present work, the design formulation is demonstrated only for one type of actuator and one type of sensor. The control actuators will be PZT patches while the error sensors are assumed to be accelerometers.

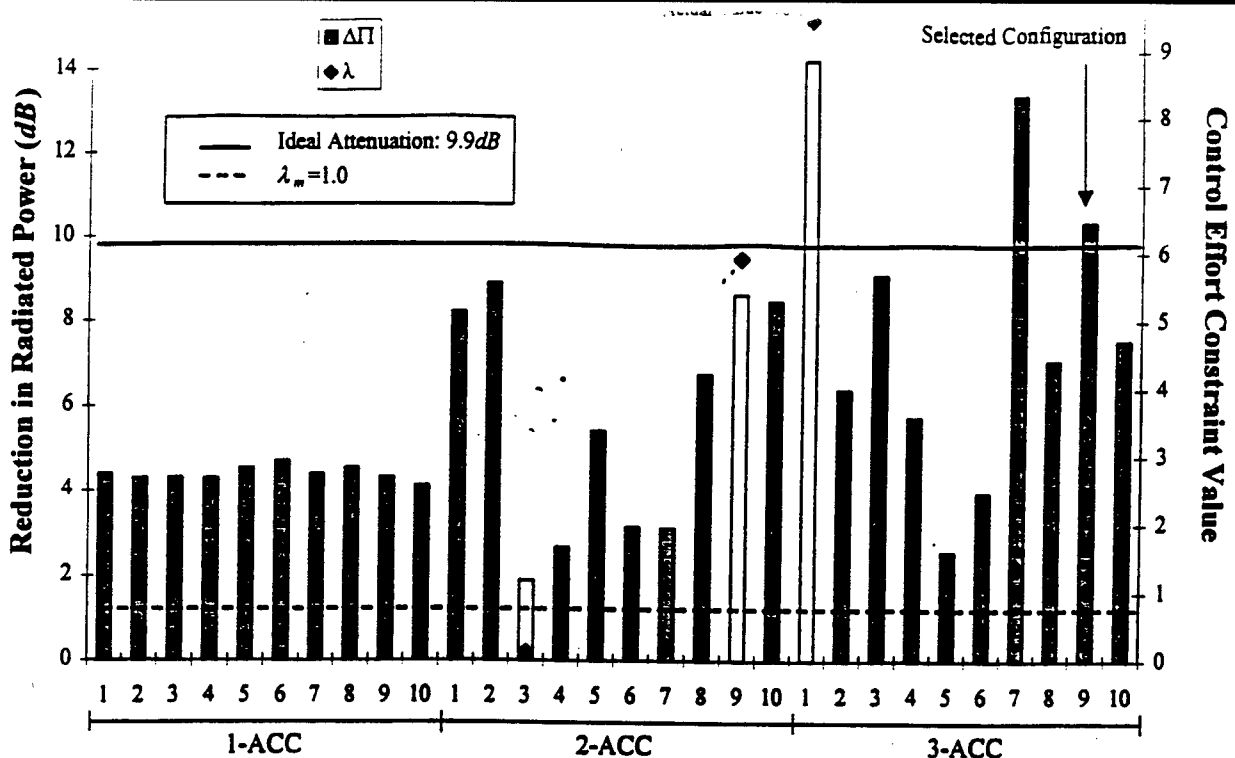


FIG. 5. Performance of optimum sensor configurations (using "ideal" control forces).

a. *Optimum actuator design.* A mechanical model for the PZT elements that relates the physical to the modal parameters is required. As shown in the literature, if two PZT patches are symmetrically bonded to both sides of the structure and wired out-of-phase, their effect can be approximated as line moments applied to the middle surface of the structure along the edges of the patches.<sup>12</sup> In the present example, this configuration (i.e., a PZT pair wired out-of-phase) is denoted as a single actuator. For the case of a simply supported plate, the line moments along the edges of the  $i$ th PZT actuator will yield an  $n$ th unit modal force in the form of<sup>14</sup>

$$\begin{aligned} \Psi_{ni}(x_{ci}, y_{ci}, l_{xi}, l_{yi}, P_i) \\ = P_i C_0 \frac{k_{xn}^2 + k_{yn}^2}{k_{xn} k_{yn}} (\cos(k_{xn}(x_{ci} - l_{xi})) \\ - \cos(k_{xn}(x_{ci} + l_{xi}))) (\cos(k_{yn}(y_{ci} - l_{yi})) \\ - \cos(k_{yn}(y_{ci} + l_{yi}))), \end{aligned} \quad (23)$$

where  $P_i = \pm 1$  is the relative phase between actuators; the constant  $C_0$  is a function of the thickness and material properties of the plate and the PZT elements;  $k_{xn} = n_x \pi / L_x$  and  $k_{yn} = n_y \pi / L_y$ ; and  $(x_{ci}, y_{ci})$  and  $(l_{xi}, l_{yi})$  are the coordinates of the central location and dimensions of the  $i$ th PZT pair, respectively. Using this configuration for the unit modal control forces, the optimum control inputs  $U_k(\omega)$  will be the voltages to be applied to the actuators. The properties of the PZT patches used in this example are: piezoelectric strain coefficient  $d_{31} = 171 \times 10^{-12}$  m/V, Poisson's ratio  $\nu_p = 0.31$ , Young's modulus  $E_p = 6.1 \times 10^{10}$  N/m<sup>2</sup>, and thickness  $h_p = 0.0002$  m. Finally, Eq. (23) is used to obtain the  $n$ th unit modal force due to  $N_A$  actuators driven in- or out-of-phase by the control input.

As implied in Eq. (23), the actuator design variables [i.e., the elements of  $\{\alpha\}_i$  in Eq. (18)] are the central location  $(x_{ci}, y_{ci})$ , the dimensions  $(l_{xi}, l_{yi})$ , and the relative phase  $P_i$  for the  $i$ th PZT pair. In the present example, up to three PZT pairs (i.e.,  $N_A = 1, 2$  or  $3$ ) were considered in the design formulation. A genetic algorithm<sup>15</sup> (GA) was used to solve this problem. Ten different GA analyses were carried out for each one of the PZT configurations. The best solution from each analysis was selected that yielded a final set of thirty possible control implementations.

The performance of these thirty control configurations is summarized in Fig. 4. The "actual" modal error sensor components are not known at this stage, therefore the results shown in this figure are obtained out using the "ideal" values of the modal error components  $\xi_{ns}$  given in Table I. In this figure, the horizontal axis represents the 30 control configurations, e.g., the first ten are the best solutions for each one of the GA analyses with a single actuator and so forth. The columns represent the power reduction achieved for each configuration. For comparison purposes, the solid horizontal line represents the predicted power attenuation from the modal domain optimization [i.e.,  $\Delta\Pi(\omega) = 9.9$  dB]. The control effort constraint given in Eq. (17b) is also plotted (dotted line) to illustrate the performance of the actuator configurations. The limit of this constraint (i.e.,  $\lambda = 1.0$ ) is indicated by the horizontal dotted line. Thus any value higher than 1.0 indicates that the constraint is violated.

The results in Fig. 4 show that good attenuation in the total radiated power is obtained even when using a single PZT. The fifth case gives an increase in the power (i.e., clear column implies negative reduction) but since there are many other alternate solutions, the designer just needs to discard that one. The good performance of the single PZT is at the

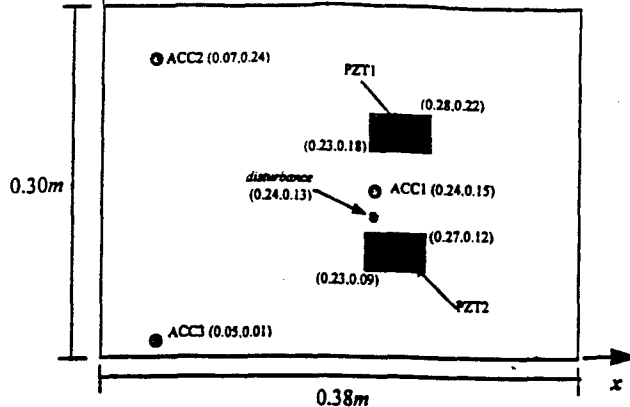


FIG. 6. Optimum actuator/sensor configuration (coordinates in meter).

expense of a significant violation in the control effort penalty. On the other hand, the control effort is reduced (i.e., the value of the constraint approaches the "ideal" value of 1.0) as the number of PZT patches is increased. This is because as the number of actuators is increased the match between the "ideal" and "actual" unit modal control forces is better and the control spillover to undesired modes is reduced.

From the 30 available solutions, the ninth configuration when using two PZTs is selected to be implemented in this example. In this configuration both actuators are driven in-phase which yields a reduction of 9.9 dB in the total radiated power and a small violation in the control effort limit of 1.5.

*b. Optimum sensor design.* The mechanical model of accelerometer sensors is simply given as the value of the mode shape at the sensor location. The design variables in this optimization problem [i.e., the elements of  $\{b\}$  in Eq. (20)] are the coordinates of the sensors  $(x_{sj}, y_{sj})$  for  $j = 1, \dots, N_E$ . The physical domain optimization problem to design the sensors is again exactly in the same form as the case of the actuator design using the GA. Results are obtained for sensing configurations consisting of one, two, and three accelerometers (i.e.,  $N_E = 1, \dots, 3$ ). The performance of the best solutions of ten GA analyses is again evaluated in the same way as for the case of the actuators. Figure 5 shows the power reduction and control effort constraint for the 30 sensing configurations. To obtain these results, the "ideal" unit modal control forces found in the modal domain optimization are used (see Table I). The results in the third figure show that using only one sensor (i.e., minimizing the error at only one location) does not yield enough amplitude to the control input  $U_k(\omega)$  to induce a significant attenuation in the total radiated power. The attenuation for this case is about 4 dB. It can also be observed that the control effort constraint is not active [i.e.,  $g_1^c(u_{nl}, \xi_{nl}) = 0.5 < 1.0$ ]. As can be seen, as the number of sensors is increased there is an increase (in the average) in the reduction of the total radiated power. On the other hand, the modal control effort is very low with one sensor and also increases with the number of sensors. Based on these results the ninth configuration with three accelerometers is selected. This configuration (in conjunction with the "ideal" control forces) yields a power reduction of 11.0 dB and again a small control effort violation [i.e.,  $g_1^c(u_{nl}, \xi_{nl}) = 1.2 > 1.0$ ].

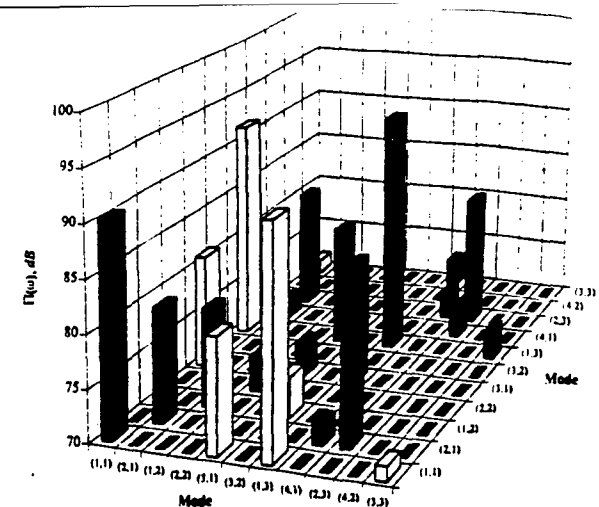


FIG. 7. Modal contributions to controlled power using the IIIO "actual" configuration. Total radiated power: 91.1 dB.

### 3. Optimum actuator/sensor configuration

A schematic of the selected actuator/sensor configuration [i.e., 2-PZT(9) and 3-ACC(9) in Figs. 10 and 11] is shown in Fig. 6. The "actual" modal control and modal error sensor components are again presented in Table I. As can be seen, the "actual" unit modal control forces show a very good agreement to the "ideal" values. The most significant discrepancy between the "actual" and "ideal" values is the change in phase in the first component. On the other hand, when compared to the "ideal" values, the "actual" modal error parameters show some differences in terms of the relative *observability* of the modes and phases. From the results in the previous section, these differences do not seem to affect the performance of the control system. Once the actuators and sensors are designed, the performance of the complete "actual" system is then compared to the performance of the "ideal" one obtained in the modal domain optimization.

The magnitude of the control input using the selected "actual" configuration is 19.1 V. This configuration yields a total reduction in the radiated power of 10.7 dB that is very close to the "ideal" attenuation predicted in the modal domain of 9.9 dB. The modal contributions to the total radiated power when implementing the "actual" control system are shown in Fig. 7. This figure can be compared to the "ideal" reductions previously shown in Fig. 3. As can be seen, both results are very similar. Note that the selected actuators/sensor configuration is only one of the 900 available combinations. In practice, the designer could check the performances of several configurations. Here, only one configuration was investigated to illustrate the method.

### IV. CONCLUSIONS

A new approach for the optimum design of actuators and error sensors to be implemented in ASAC applications has been developed. The formulation is based in a multi-level optimization procedure. The upper level is defined in the modal domain and solves for the optimum relative *controllability* and *observability* of the modes that the control system should implement in order to minimize the total radiated

problems in order to find the actuators and sensors to be implemented in the structure. The formulation allows the use of either numerical techniques or experimental results during the design process. Therefore, the proposed design approach can be readily applied for the design of control systems for complex structures with complex excitations. In this paper, the developed optimum design formulations were implemented for the case of a simply supported plate. The simply supported plate was studied because both its structural and acoustic responses are well understood which permitted to obtain a better understanding of results and the evaluation of the performance of the design method.

## ACKNOWLEDGMENTS

The authors gratefully acknowledge the support of this work by the Office of Naval Research (Grant No. ONR-N00014-92-J1170) and the State Council of Higher Education for Virginia (Commonwealth Graduate Fellowship).

<sup>1</sup>C. R. Fuller, "Apparatus and methods for global noise reduction," U.S. Patent No. 4,715,599 (1987).  
<sup>2</sup>C. R. Fuller, S. J. Elliot, and P. A. Nelson, *Active Control of Vibration* (Academic, San Diego, CA, 1996).  
<sup>3</sup>B. T. Wang, R. A. Burdisso, and C. R. Fuller, "Optimal placement of piezoelectric actuators for active control of sound radiation from elastic

<sup>4</sup>C. E. Ruckman and C. R. Fuller, "Using multiple regression and subset selection to optimize actuator locations in feedforward active control systems," *J. Acoust. Soc. Am.* **92**, 2410(A) (1992).  
<sup>5</sup>R. H. Cabell, H. C. Lester, G. P. Mathur, and B. N. Tran, "Optimization of actuator arrays for aircraft interior noise control," 15th AIAA Aeroacoustics Conference, Long Beach, California, 25-27 October 1993, 1-10 (1993).  
<sup>6</sup>R. A. Burdisso and C. R. Fuller, "Design of active structural acoustic control systems by eigenproperty assignment," *J. Acoust. Soc. Am.* **96**, 1582-1591 (1994).  
<sup>7</sup>M. T. Simpson and C. H. Hansen, "Use of genetic algorithms for optimizing vibration actuator placement for minimizing sound transmission into enclosed spaces," Proceedings of Smart Structures and Materials, San Diego, California, 26-29 February 1996.  
<sup>8</sup>H. M. Rodriguez and R. A. Burdisso, "Sensitivity analysis for feedforward control system design," *J. Acoust. Soc. Am.* **98**, 3352-3359 (1995).  
<sup>9</sup>F. Fahy, *Sound and Structural Vibration* (Academic, Orlando, FL, 1985).  
<sup>10</sup>M. C. Junger and D. Feit, *Sound, Structures and Their Interaction* (Acoustical Society of America, Woodbury, NY, 1993).  
<sup>11</sup>R. D. Ciskowski and C. A. Brebbia, *Boundary Element Methods in Acoustics* (Comp. Mechanics Publications, Boston, 1991).  
<sup>12</sup>H. M. Rodriguez, "Optimum design for feedforward structural-acoustic control of complex structural systems," Doctor of Philosophy Dissertation, Department of Mechanical Engineering, VPI&SU (1996).  
<sup>13</sup>The MathWorks, Inc., *Optimization Toolbox User's Guide* (Natick, MA, 1992).  
<sup>14</sup>E. K. Dimitriadis, C. R. Fuller, and C. R. Rogers, "Piezoelectric actuators for distributed vibration excitation of thin plates," *J. Vib. Acoust.* **113**, 100-107 (1989).  
<sup>15</sup>D. E. Goldberg, *Genetic Algorithms in Search, Optimization and Machine Learning* (Addison-Wesley, Reading, MA, 1989).

INTR

merg  
orient  
theret  
tificat  
are re  
quires  
forms  
other  
such  
could  
tional  
used  
reduc  
aspec  
difficu  
scatter  
acerba  
pende  
not kr

A  
aspec  
given  
exam  
such  
target  
energ  
Howe  
are m  
explo  
tunatu  
tures  
and a  
subse

7

# **APPENDIX 26**

Submitted to J.Acoust. Soc. Am. (1998)

Johnson, Brody D. and Fuller, Chris R.      Journal of the Acoustical Society of America

Broadband control of plate radiation using a piezoelectric, double-amplifier active-skin, part I: analytical.

Brody D. Johnson

Vibration and Acoustics Laboratories, Department of Mechanical Engineering,  
Virginia Polytechnic Institute and State University, Blacksburg, Virginia 24061.

Chris R. Fuller

Vibration and Acoustics Laboratories, Department of Mechanical Engineering,  
Virginia Polytechnic Institute and State University, Blacksburg, Virginia, 24061.

Received

Footnote Title:

Johnson and Fuller: A double-amplifier active-skin, part I.

In recent years, much work in the active control of sound has been directed towards the establishment of more practical control systems, in which compact sensor-actuator arrangements are achieved for application on generalized structures. In this work, the potential of a piezoelectric, double-amplifier active-skin is demonstrated for the reduction of broadband acoustic radiation from a vibrating panel. The active-skin is comprised of a number of independently controllable piezoelectric cells, which serve as secondary acoustic sources in the Linear Quadratic Optimal Control (LQOC) time-domain control scheme. A numerical model describing the structural-acoustic behaviour of the skin cells is sought using the Finite Element Method (FEM) in conjunction with the numerical evaluation of Rayleigh's Integral. The active-skin is applied to the control of broadband acoustic radiation from a clamped, aluminum panel. Simulation indicates that a total radiated power attenuation in excess of 10 dB may be achieved between 250 and 750 Hz with microphone error sensing. The inclusion of Structural Acoustic Sensing (SAS) is studied using the numerical model of the active-skin. For this simulation, structural sensors are used to predict the far field radiation. With SAS, the radiated acoustic power is reduced by nearly 8 dB between 250 and 750 Hz.

PACS #'s: 43.50.Ki, 43.40.At

## I. INTRODUCTION

As opposed to the common realizations of ANC and ASAC, where the control actuators comprise a relatively small portion of a system, the use of a secondary layer, or skin, for reduction of structurally radiated sound implies a complete covering of all vibrating, and hence radiating, surfaces of the offending structure. With this approach one is concerned with sound radiated from the surface of the skin rather than the primary structure. Since it is not necessary to directly modify the structural vibration, the approach is suitable for structures which have low mobility. The combined passive and active effects of the skin on the response of the net system must be considered in design. The use of an entirely passive foam layer on the surface of a radiating piston has been shown by Gentry et. al. to reduce radiated sound for high frequencies.<sup>1</sup> To take advantage of both active and passive methods, control actuators may be added to the skin for the attainment of low frequency attenuation to complement the absorptive effect of the foam at high frequencies. In these active-passive configurations, the skin may be divided into a number of independently controllable cells, whose dynamics are governed by the application of a voltage signal to a piezoelectric element contained in the active-skin cell. The inception of suitable piezoelectric materials (PZT's) has spawned much work in the area of smart-materials and smart-structures. Gentry, Guigou, and Fuller have implemented active-passive PVDF foam skins on pistons which attain global attenuation for harmonic excitations.<sup>1,2</sup> This approach takes advantage of the inherent absorptive characteristics of the foam, while also coupling with the vibration of the primary structure. Another active-skin tactic consists of the development of skin cells, which, rather than absorbing sound, prevent radiation by minimizing an acoustic cost function in terms of vibration at the surface of the skin. Thus, the control actuators provide substantial control authority over the entire bandwidth of interest. In this instance, the only passive effect is seen as a result of the mass loading of the skin cells on the primary structure. Kugel and others have developed analytical models for the characterization of PZT acoustic transducers intended for use in an active-skin of this nature.<sup>3</sup>

In this work, it is the latter skin approach that is adopted. This active-skin concept, as applied to a plate, is depicted in Figure 1. By exciting the PZT bimorphs comprising the flexible leg elements of the active-skin, an

amplified diaphragm response is obtained. The cell design employed here, shown in Figure 2, provides two means for amplification of the acoustic response. First, the use of bimorph PZT actuators, driven out-of-phase, provides an amplified flexural response of the legs of the cell. Since the cell legs are clamped at their base, the maximum leg displacement occurs at the joint between the legs and the cell diaphragm. By driving the two legs of a cell with opposite polarity, the diaphragm is forced to vibrate. Here the second stage of amplification is encountered as the response of the diaphragm tip is geometrically amplified with respect to the leg motion.

The intent of this work is to develop a numerical model describing the active-skin system, as applied to plates, for investigation of the active-skin as a viable control approach in generalized structural radiation problems. The plate geometry is chosen as it represents a building block common to many structures encountered in noise control applications, e.g. buildings, cars, machinery casings, etc.<sup>4</sup> The Finite Element Method (FEM) is used to develop a structural model of a single active-skin element. The diaphragm response is computed by application of an external loading derived for the bimorph PZT actuators. The far field acoustic response is then obtained through the discretized evaluation of the Rayleigh Integral.<sup>4</sup> By superposing the structural acoustic responses of the individual skin cells, a model of the complete active-skin is obtained. This model is then used in conjunction with Linear Quadratic Optimal Control (LQOC) theory to determine the control potential of the 6I6O active-skin control system in the time-domain. Far field microphones are used as error sensors. The performance of the system is demonstrated by comparing both the in-plane acoustic directivity and the total radiated acoustic power for the controlled and uncontrolled cases. As a preliminary investigation of a more practical error-sensing scheme, a methodology for the prediction of the radiated acoustic pressure is investigated which makes use of a number of accelerometers distributed over the radiating surface(s) of the active-skin. The use of structural error sensors in this fashion is referred to as Structural Acoustic Sensing (SAS).<sup>5</sup> Thus, SAS provides a practical technique for the computation of acoustic error signals without the use of microphones, which are a cumbersome and often unreasonable means of error sensing. This technique will be evaluated using a control configuration that parallels the one used in the microphone sensing case.

## II. THEORY

In order to simulate control with the active-skin many disciplines of engineering are required, including vibrations, acoustics, controls, and FEM. The relevant material from each of these areas is treated briefly here before being integrated into a single numerical model of the active-skin control system.

### A. Structural Modeling

The IDEAS<sup>®</sup> FEM package was used for the creation of a 180 element, 210 node, representation of a single active-skin element<sup>6</sup>. A thin-shell element type was adopted for this model, providing six degrees of freedom (DOF) for each of the four nodes comprising an element. These DOF include translational motion along and rotational motion about the three coordinate axes. The element formulation also requires definition of the element thickness, mass density, Modulus of Elasticity, and Poisson's Ratio for each element. The approximate material properties for the constituents of the active-skin cell are given below in Table 1. For the purposes of this model, the materials are assumed to behave isotropically.

Having briefly introduced the FEM approach adopted in this analysis, a discussion of important mesh features will now be undertaken which pertain to the active-skin cell. First, as shown in Fig. 2, the bimorph PZT actuators are comprised of three layers of material, in which two 0.6 mm layers of PKI550 PZT sandwich a 0.1 mm layer of brass shim. The variation of material properties across this cross-section is ignored for this model (along with the bonding layers), with PZT material properties assumed over the entire cross-section. The similarity between the brass and PZT mechanical properties, as evidenced by Table 1, suggests that such an assumption should not significantly affect the modeling results. Second, three creased-bends exist in the paper diaphragm of the active-skin cell. Two of these bends occur where the diaphragm is bonded to the flexible PZT elements, while the third occurs at the crest of the diaphragm. Two simple ways to model these bends include the assumption of either

completely rigid or completely compliant behaviour; however, another, more practical, solution may be undertaken. This consists of the inclusion of torsional springs along these bends, or hinges, to impose resistance against the free rotation of the diaphragm about these creases. With this approach, the torsional stiffness may be tuned for the best possible match with experimentally observed behaviour. Figure 3, below, depicts the complete FEM mesh for the active-skin cell, including the clamped boundary conditions imposed at the base of the PZT legs.

Once a satisfactory mesh has been created, including the appropriate boundary conditions, a numerical modal analysis is performed on the structure. The Simultaneous Vector Iteration approach is used to determine the mode shapes and resonant frequencies for the active-skin cell.<sup>6,7</sup> Each mode shape is expressed as a vector whose components represent the nodal displacements associated with a given mode. For such a multi-degree of freedom system, the response to a harmonic input may be expressed as a summation over the modes by

$$w(n, t) = \sum_{m=1}^M A_m \Phi_m(x, y) \sin(\omega t) \quad (1)$$

where  $w$  represents the displacement function,  $n$  refers to the nodal coordinate system,  $t$  is time,  $A_m$  is a complex modal amplitude,  $\Phi_m$  is the  $m^{\text{th}}$  mode shape, and  $\omega$  is the excitation frequency.<sup>7</sup> The FEM approach to modal decomposition is analogous to that of the standard lumped-parameter multi-degree of freedom system. To determine the induced modal amplitudes for an arbitrary harmonic excitation, the assumed solution of Eq. (1) must be substituted into the transformed equation of motion, which reduces to

$$[\Phi]^T [M] [\Phi] \{\ddot{\eta}(t)\} + [\Phi]^T [K] [\Phi] \{\eta(t)\} = [\Phi]^T \{f(t)\} \quad (2)$$

where  $\Phi$  is the modal matrix,  $M$  is the mass matrix,  $K$  is the stiffness matrix,  $\eta(t)$  represents the modal coordinate vector, and  $f(t)$  is the vector forcing function. Further reduction of Eq. (2) yields the modal amplitudes as

$$\{A\} = \frac{1}{m_d} [\Lambda - I\omega^2]^{-1} [\Phi]^T \{F\} \quad (3)$$

where  $A$  is the vector of modal amplitudes,  $m_d$  is the normalization constant,  $\Lambda$  is a diagonal matrix of the squares of the modal resonant frequencies,  $I$  is the identity matrix,  $\omega$  is the excitation frequency, and  $F$  is the nodal force vector.

At this stage, it remains only to discuss the determination of a nodal force vector that appropriately resembles that induced by the piezoelectric actuators of the active-skin cell. The approach applied here was first proposed by Crawley and De Luis for the representation of one-dimensional piezoelectric actuators.<sup>8</sup> In 1991, Dimitriadis, Fuller, and Rogers developed an extension to two-dimensional scenarios, such as that encountered in this work.<sup>9</sup> The goal in the implementation of this model is to determine equivalent external edge-moments to apply to the FEM models for characterization of the vibrational behaviour of the active-skin cell. This begins with an electro-mechanical relationship between the applied voltage and the induced strain of the piezoelectric actuator. For simplicity the following linear model is assumed:

$$\varepsilon = \frac{d_{31}}{t} V \quad (4)$$

where  $\varepsilon$  is the imposed strain,  $d_{31}$  is the piezoelectric strain constant,  $t$  is the thickness of the actuator, and  $V$  is the applied voltage<sup>8</sup>. It must be noted that this relationship describes the unconstrained behaviour of the actuator. This strain is developed equally in each of the two directions normal to the polarization direction, e.g. if the actuator is polarized in the  $z$ -direction, strain will be developed in both the  $x$ - and  $y$ -directions. Since the two actuators comprising the bimorph are driven out-of-phase, pure bending is developed over the portion of the plate surface within the actuator boundary. The details of this analysis lie well beyond the scope of this work, and are used here only to obtain a more realistic representation of the active-skin cell behaviour. The interested reader is referred to

the work of Dimitriadis, Fuller, and Rogers.<sup>9</sup> The final result of this model is contained in the following equations, which relate the applied voltage to the edge-moments on the actuator boundary:

$$P = -\frac{Epzt}{Eplt} \frac{(1-v_{plt}^2)}{(1-v_{pzr}^2)} K \quad (5)$$

$$C_0 = -E_{plt} \frac{1+v_{pzr}}{1-v_{plt}} \frac{P}{1+v_{plt} - (1+v_{pzr})P} \frac{2}{3} h^2 \quad (6)$$

$$K = \frac{3th(2h+t)}{2(h^3 + t^3) + 3ht^2} \quad (7)$$

$$m = C_0 \varepsilon \quad (8)$$

where  $K$  and  $P$  are non-dimensional parameters,  $C_0$  is the piezoelectric strain-plate moment coupling constant,  $m$  is the equivalent moment per unit actuator length,  $t$  is the actuator thickness,  $h$  is the plate half-thickness,  $E_{pzr}$  and  $E_{plt}$  are the Moduli of Elasticity for the actuator and plate, respectively, and  $v_{pzr}$  and  $v_{plt}$  are the respective Poisson ratios for the actuator and plate.<sup>9</sup> The moment per length,  $m$ , reflects the induced moment about the actuator boundary and is, thus, equal in each of the planar directions on the surface of the plate.

## B. Acoustic Modeling

The objective of the acoustic modeling in this work is to predict the far field radiation from the active-skin. This requires solution of the reduced-acoustic wave equation, or Helmholtz equation, under the imposed normal

velocity boundary conditions on the surface of the skin. In such an analysis, each frequency is treated separately and, therefore, the wave equation may be written in terms of a harmonic acoustic pressure field as

$$\frac{\partial^2 p}{\partial^2 x} + \frac{\partial^2 p}{\partial^2 y} + \frac{\partial^2 p}{\partial^2 z} + k^2 p = 0 \quad (9)$$

where  $p$  is the acoustic pressure,  $k$  is the acoustic wavenumber, and  $x$ ,  $y$ , and  $z$  collectively define a Cartesian coordinate system.<sup>4</sup> In order to determine the pressure throughout the acoustic medium, a solution to the Helmholtz equation must be sought which satisfies the imposed normal velocity boundary conditions on the surface of the vibrating structure. It has been shown that the combination of the wave equation and the velocity boundary conditions on the vibrating surface results in the Kirchoff-Helmholtz integral equation, given by

$$p(\bar{r}) = \int_S [p(\bar{r}_s) \frac{\partial \tilde{G}(\bar{r}, \bar{r}_s)}{\partial n} + j\omega p_0 v_n(\bar{r}_s) \tilde{G}(\bar{r}, \bar{r}_s)] dS \quad (10)$$

where  $\bar{r}$  denotes a position vector,  $\tilde{G}$  is the free-field acoustic Green's function,  $p_0$  is the density of the acoustic fluid,  $v_n$  is the normal velocity over the surface  $S$ , and  $\partial \tilde{G} / \partial n$  is the partial derivative of the acoustic Green's function with respect to the local outward normal  $n$ .<sup>4</sup> The subscripts  $s$  and  $o$  denote surface and observation position vectors, respectively. This result applies to very generalized problems, but is fairly cumbersome in practice. Fortunately, a simpler approach is possible with the active-skin. Since the skin may be effectively viewed as a baffled, planar radiator, it is the simple half-space radiation problem that requires attention. Under this limitation, Eq. (10) may be reduced to a more useful form depending only upon the normal surface velocity of the radiating structure. It will be shown that the FEM mesh of a radiating structure provides a convenient means for evaluating this reduced integral with a summation over the elements comprising the FEM mesh. Thus, each element is treated as a component source of the complex radiating structure. Furthermore, if each of these component sources is small

compared to the acoustic wavelength (maximum dimension  $\ll \lambda$ ) the analysis will appropriately model the phase variation of the radiated pressure.<sup>10</sup> Thus, for this class of radiators, the pressure radiated to a point in the acoustic medium may be written solely in terms of the normal vibration of the radiating surface. Removing the surface pressure component of the Kirchoff-Helmholtz integral equation and substituting the half-space Green's function, the radiation of a baffled, planar structure is given by Rayleigh's Integral as

$$p(\vec{r}) = \frac{j\omega\rho_0}{2\pi} \int_S \left[ v_n(\vec{r}_s) \frac{e^{-jk|\vec{r}-\vec{r}_s|}}{|\vec{r}-\vec{r}_s|} \right] dS \quad (11)$$

where,  $\vec{r}$  is the position vector of the point at which the pressure is determined and  $\vec{r}_s$  is the position vector locating a surface element of the vibrating structure.<sup>4</sup> At this point, it remains to be shown how this formulation may be used in conjunction with the vibrational results provided by the FEM approach outlined in the previous section.

From the FEM representation of a vibrating structure, the velocity of the structure at a number of defined nodal locations is known. Combining the nodal velocities with knowledge of the structure's geometry, the normal surface velocity may be computed for each element comprising the structure. This discretized normal surface velocity suggests that Rayleigh's Integral must be approximated by a summation over the elements comprising the complex structure. This discretization takes the following form:

$$p(\vec{r}) = \sum_{m=1}^N \frac{j\omega\rho_0}{2\pi} A_m v_m \frac{e^{-jkR_m}}{R_m} \quad (12)$$

where the index  $m$  identifies an element of the vibrating structure,  $N$  is the total number of elements,  $A_m$  is the area of the  $m^{th}$  element,  $v_m$  is the normal velocity of the  $m^{th}$  element, and  $R_m$  is the distance between the center of the  $m^{th}$  element and the point in acoustic medium at which the pressure is to be evaluated. So long as the maximum element

dimension satisfies the above low-frequency assumption, a discretized evaluation of Eq. (11) will yield an accurate measure of the pressure radiated to desired points in the acoustic medium. It should be noted that, in simulation, all of the information necessary for implementation of this approach is readily extracted from the FEM model already developed for the active-skin cell. In experiment, however, measurements are required for the determination of the normal surface velocity. Care must be taken in such measurements to ensure proper decoupling of potential "cross-talk" between a number of skin cells mounted to a given vibrating structure. Note further that this method is most appropriately applied to planar, baffled radiators; however, when the size of a non-planar source is small compared to the acoustic wavelength, it may also be represented in this manner.<sup>10</sup>

This modeling approach may also be modified for use in the study of Structural Acoustic Sensing (SAS) with the active-skin. The basis of the SAS technique is that, for relatively simple geometries, the acoustic radiation may be predicted from a thorough knowledge of the surface velocity over a vibrating structure. In the previous paragraphs, a *complete* knowledge of this information was available, allowing for direct determination of the radiated pressure. The idea behind SAS is to accurately predict the radiated pressure from only a *partial* knowledge of the surface velocity field. The most logical approach achieving this goal is to associate the velocity at a single point on the vibrating surface with a small area of the radiating surface neighbouring this point. As with the results in the previous paragraph, the radiated pressure is then expressed as a summation over the contributions of each component area. In general, the radiation from these areas is assumed to resemble either a monopole or a piston and the appropriate pressure relationship is applied to evaluation of the simplified form of Eq. (10). An unlimited number of alternative pressure formulations may be assumed for this discretization; however, due to the relative simplicity of these two examples one of these approaches is generally adopted.<sup>5</sup> In this work, the half-space monopole representation is exclusively applied. For this model, the pressure estimate at a point in the acoustic medium may be written, in the frequency domain, as a summation of the accelerometer signals as

$$p(\vec{r}) = \sum_{m=1}^N \frac{\rho_0}{2\pi} A_m a_m \frac{e^{-jkR_m}}{R_m} \quad (13)$$

where the index  $m$  identifies an accelerometer of the SAS array,  $N$  is the total number of SAS sensors,  $A_m$  is the area of the radiating surface associated with the  $m^{\text{th}}$  sensor,  $a_m$  is the normal acceleration at a point in the  $m^{\text{th}}$  component area, and  $R_m$  is the distance between the  $m^{\text{th}}$  sensor and the point in acoustic medium at which the pressure is to be evaluated, which is defined by the position vector  $\vec{r}$ . Note that with the monopole model presented here, the absolute locations of the sources and sensors are irrelevant as the pressure depends only upon the distance between the two points.

In order to implement SAS in real-time as a supplement to a time-domain feed forward algorithm, an array of digital filters modeling the various sensor paths is required.<sup>5</sup> The frequency response of one such filter may be expressed as

$$H_{m,n}(j\omega) = \frac{\rho_0}{2\pi} A_m \frac{e^{-jkR_{m,n}}}{R_{m,n}} \quad (14)$$

where  $H_{m,n}$  is the frequency response associated with the sensor-to-error path relating the  $m^{\text{th}}$  accelerometer to the  $n^{\text{th}}$  error signal,  $A_m$  is the elemental area associated with the  $m^{\text{th}}$  accelerometer, and  $R_{m,n}$  is the distance between the  $m^{\text{th}}$  structural sensor and the  $n^{\text{th}}$  far-field location at which the error signal is to be determined. The appropriate digital filters necessary for modeling these transfer functions must be found using a numerical curve fit with a reasonable number of FIR filter weights. Note that the number of digital filters required for implementation of an SAS system employing  $M$  accelerometers for the prediction of the acoustic pressure at  $N$  locations in the acoustic medium is  $M \times N$ . Hence, the difficulty in developing a practical SAS system lies in achieving an adequate representation of the acoustic radiation with a minimal number of structural sensors.

### C. Control Simulation

Many experiments in the active control of sound make use of adaptive feed forward algorithms implemented on powerful Digital Signal Processors (DSP's). The intent of this research is to analytically evaluate the control performance of the skin when implemented in conjunction with such an algorithm. A single-channel block diagram for a commonly used feed forward algorithm, the Filtered-X LMS algorithm, is presented in Fig. 4.<sup>11</sup> In this control scheme a measured reference signal (assumed to be coherent with the measured error signal),  $x_k$ , is fed into a digital filter that represents the behaviour of the secondary sources,  $\tilde{T}_{ce}(z)$ . This *filtered* reference signal,  $\tilde{x}_k$ , is then fed into the LMS block of the algorithm along with the current error information,  $e_k$ . The LMS block is responsible for the iterative adaptation of the control compensator, denoted by  $W(z)$ .

Execution of these types of algorithms is computationally intensive, so rather than conducting simulations that mirror such an implementation, an alternative method is chosen for this work which takes advantage of the quickness of a frequency-domain solution and the practicality of a time-domain approach. With this method, the optimal control compensator responses,  $W(z)$ , are determined using Linear Quadratic Optimal Control (LQOC) theory. Once the frequency responses have been isolated, the Matlab<sup>®</sup> function INVREQZ may be used to design digital filters for use in time-domain simulation.<sup>12</sup> This transformation uses a curve-fitting technique to provide the best possible causal representation (for a defined number of weights) of the desired complex frequency response. This transformation places a realistic limit on the performance of the control compensators, similar to that seen in experiments with feed forward algorithms such as the Filtered-X. Upon determination of the control compensators, any disturbance signal may be generated and fed through the primary and secondary control paths for evaluation of the control performance. Thus, this hybrid approach to simulation entails the design of digital filters from frequency-domain transfer functions, along with the time-domain implementation of these filters with respect to an arbitrary disturbance. With this brief overview in mind, the LQOC theory involved will be introduced for arbitrary primary and secondary control paths.

LQOC theory provides a methodology for the determination of optimal control inputs for steady-state harmonic disturbances of the primary structure. In this text, LQOC will be used for the determination of frequency responses

for each control compensator by obtaining the LQOC solution at a number of discrete frequencies spanning the desired control bandwidth of the simulation.

Consider a control system having a single disturbance,  $M$  secondary control paths, and  $N$  error sensors. Let the magnitude and phase of the  $n^{th}$  error signal be denoted by  $e_n$ , and let  $e$  represent a column vector defined by

$$e = (e_1 \quad e_2 \quad \cdots \quad e_n)^T \quad (15)$$

where the frequency dependence is suppressed. Next, an arbitrary set of disturbance and control inputs are taken, denoted by  $f_d$  and the vector  $f_c$  ( $M \times 1$ ), respectively. Representing the transfer functions (at frequency  $\omega$ ) between these inputs and the  $N$  error sensors by the vector  $D$  ( $N \times 1$ ) and the matrix  $C$  ( $M \times N$ ), respectively, the error at frequency  $\omega$  may be found by

$$e = D \cdot f_d + C \cdot f_c \quad (16)$$

Adopting a cost function defined by the sum of the square error signals, the cost function,  $J$ , may be written as

$$J = \sum_{n=1}^N |e_n|^2 = e^H e \quad (17)$$

where  $(\cdot)^H$  denotes the Hermitian operator. By substitution of equation Eq. (16) into Eq. (17), the cost function may be expressed directly in terms of the disturbance and control inputs to the system:

$$J = f_d^H D^H D f_d + f_c^H C^H D f_d + f_d^H D^H C f_c + f_c^H C^H C f_c \quad (18)$$

The cost function is now seen to be quadratic with respect to the control inputs  $f_c$ . In order to find the control inputs that minimize this quadratic function, the partial derivatives of  $J$  with respect to each of the control inputs must be constrained to zero. With this in mind, partial differentiation of  $J$ , as given in Eq. (17), with respect to each term of  $f_c$  yields a set of  $M$  simultaneous equations, the solution of which reflects the optimal control inputs,  $f_c^{opt}$ . The result may be expressed in vector form by

$$f_c^{opt} = -(C^H C)^{-1} C^H D f_d \quad (19)$$

Note that the inclusion of the Hermitian operator throughout this analysis provides solutions both for systems possessing an equal number of error sensors and control inputs ( $M = N$ ), as well as for over-determined systems ( $M < N$ ). For over-determined systems, the minimum of the cost function will not necessarily be reduced to zero, while in the first instance use of the optimal control inputs will provide complete cancellation of each error signal.

Recalling that for this work the ideal reference (the disturbance signal) is used, one may determine the optimal compensator response,  $w_c^{opt}$  ( $M \times 1$ ), directly from Eq. (19) by merely canceling the effect of the disturbance input,  $f_d$ , from each side:

$$w_c^{opt} = -(C^H C)^{-1} C^H D \quad (20)$$

Again, note that  $w_c^{opt}$  represents a vector of complex values corresponding to the optimal compensator response for a particular frequency,  $\omega$ . Application of this approach at a number of frequencies will yield the frequency-domain solution for the optimal compensator frequency responses.

Once this optimal response is known, a finite order digital filter may be created for representation of this compensator in time-domain control simulations. The INVREQZ function in the MATLAB® environment is used to perform this transformation.<sup>12</sup> For small filter sizes, the performance of the designed control compensators is

likely to be significantly worse than that of a system in which the filter weights are determined iteratively; however, as the order of the filters are increased, this effect is reduced.

### III. PLATE AND COORDINATE SYSTEMS

In the previous section, three important parts of the active-skin numerical model were isolated and discussed. The intent of this section is to explain how these parts of the model are combined for study of the control potential of the active-skin.

As mentioned earlier, in this work the active-skin is applied to a clamped, aluminum plate. The plate is rectangular, of dimensions 170 x 150 x 1.5 mm, and is mounted in a baffle. A broadband disturbance is provided to the plate through a piezoelectric actuator (38 x 30 x 0.1 mm) located for effective excitation of the first six plate modes. The location of the disturbance actuator on the plate is shown in Fig. 5. The response of the plate is determined using an FEM approach analogous to that used with the active-skin cell. For brevity this model is not presented here, but let it be noted that the acoustic response of the plate is again determined from the structural response by means of Rayleigh's Integral, which is evaluated in a discretized form. For the purposes of this work, the active-skin is mounted just above the surface of the plate, thus preventing vibrational coupling between the two structures. It is further assumed that the acoustic fields of these two structures may be determined separately and superposed for determination of the complete sound field.

In part C of the previous section, the combined frequency/time domain simulation approach was described. While a reference signal is not required for the frequency-domain determination of the optimal control compensator responses, a reference signal is necessary for the time-domain evaluation of these compensators under an arbitrary excitation. The ideal reference (the disturbance input) is assumed for this work. Furthermore, as discussed in the previous section, the error signals are sound pressure measured or predicted (in the case of SAS) at a number of far field locations. The sound pressure at a number of distinct observation points is also monitored for estimation of the global control performance. Both acoustic directivity and radiated sound power comparisons are made between the

controlled and uncontrolled responses of the system. Fig. 6 depicts the active-skin control system in an anechoic chamber from an overhead vantagepoint, including the plate, baffle, and coordinate axes. The origin of the coordinate system is taken to coincide with the center of the plate. In the next section, this coordinate system will be adopted in the location of both the secondary acoustic sources and the error sensors.

## IV. RESULTS

Three key results will be presented in this section. First, the tuned FEM model is presented and compared to experimentally measured resonant frequencies. Next, the complete active-skin model is used to demonstrate the effectiveness of this control approach in a 6I6O control system, which uses microphones as error sensors. Finally, a preliminary investigation of the effect of SAS on the active-skin is undertaken using the developed numerical model.

### A. Structural Modeling

The FEM approach to modeling the active-skin cell was outlined earlier in this paper. In order to appropriately tune the torsional springs used along the bends in the diaphragm of the active-skin cell, experiments were conducted in which the vibrational response of a single cell was observed for a broadband voltage excitation. In these experiments, a laser vibrometer was used to collect normal velocity data over the surface of the diaphragm. By computing the experimental Frequency Response Function (FRF) relating the applied voltage to the cell vibration at various positions, the experimental modes and mode shapes of the active-skin cell were obtained. Only the first two modes made significant contributions to the observed response; therefore, it is the first two modes that will be presented here. Fig. 7 displays the mode shape obtained from the FEM model for the first mode of the active-skin cell. Beneath this depiction, the FEM resonant frequency is given along with the experimentally observed value, the latter in parentheses. This mode dominates the response everywhere except near the second resonant frequency. Furthermore, this mode is desirable, as it results in the entire diaphragm moving in phase, which makes the active-

skin cell a more efficient radiator. In Fig. 8, however, the less efficient radiating second mode is depicted. Here, the upper and lower halves of the diaphragm vibrate out-of-phase, resulting in less far-field radiation for low frequencies.

### B. Microphone Error Sensing Results

The first simulation performed with the active-skin is intended to show the potential of the secondary acoustic sources, the skin cells, for application to generalized structural radiation problems. Microphone error sensing is used to meet this end, before the more compact SAS sensing scheme is employed. For this simulation, the active-skin is made up of six cells, whose distribution over the plate is depicted in Fig. 9, along with the coordinate axes used for location of the cells and error microphones in this system. Note that the origin of this coordinate system is taken to be at the center of the plate. The skin cell and microphone locations used in this configuration are given in Tables 2 and 3, respectively.

The time-domain portion of the simulation was performed with a sample rate of 1600 Hz, employing 96 coefficient FIR filters in the control path and 255 coefficient FIR filters serving as control compensators. This means that 255 FIR coefficients are used to model the optimal compensator frequency responses, as determined from LQOC theory. A target control bandwidth was chosen ranging from 250 Hz to 750 Hz, encompassing six structural modes of the clamped aluminum plate. A comparison of the uncontrolled and controlled in-plane acoustic directivity (at 1 m) is displayed in Fig. 10. Significant reduction is observed in the overall Sound Pressure Level (SPL) over the entire 180° angular range. Fig. 11 depicts the control performance in terms of the radiated sound power from the plate/skin system. An overall reduction in the acoustic power of 11.7 dB is observed between 250 and 750 Hz.

### C. SAS Error Sensing Results

In the previous section, the developed numerical model was used to demonstrate the control potential of the active-skin, as applied to plates. Here, an SAS sensing scheme will be incorporated into the model as a step towards a more practically realizable control system. This configuration, which again includes six active-skin cells distributed over the aluminum plate, is depicted in Fig. 12. The six active-skin cells remain in the positions given in Table 3; however, an accelerometer is positioned at the center of the diaphragm of each skin cell. These sensors provide the structural information necessary for prediction of the acoustic error signals.

In order to isolate the effect of SAS on the control performance of this system, the simulation parameters (sample rate, filter lengths, sensor locations, etc.) from the previous control configuration are retained here. Before presenting the results from this simulation it is useful to investigate the accuracy obtained from the six-accelerometer SAS sensing system. The accuracy of the SAS-predicted primary and secondary paths is a prime concern, as an accurate prediction of the net error is crucial to the control of sound. Figs. 13 and 14, respectively, provide a comparison between the SAS-predicted and the analytical transfer function associated with the primary and secondary paths of this system. It is evident from this comparison that the SAS system provides an adequate prediction of the radiated pressure in each case.

Implementation of this SAS active-skin system yields a 7.9 dB reduction in the overall sound power radiated from the plate-skin system. The acoustic directivity and sound power frequency spectrum for this simulation are shown in Figures 15 and 16, respectively. While the integration of the SAS error sensing scheme into the active-skin degrades the power attenuation by over 3 dB, a significant reduction is still attained. This suggests that a limited number of structural sensors can provide a reasonable approximation of the system transfer functions, which greatly simplifies the implementation of the active-skin on a generalized structure.

#### IV. CONCLUSIONS

In this work, a numerical model for the active-skin was developed and used to demonstrate the control potential of this noise control scheme. FEM techniques were used to develop a structural model of a single active-skin

element, which was, in turn, applied to the numerical determination of the acoustic radiation from this source. Integration of this structural-acoustic model into a combined frequency/time domain control approach led to the evaluation of a 6I6O active-skin system applied to a clamped, aluminum plate. Both microphone and SAS error sensing schemes were investigated. In the case of microphone error sensing, the total radiated sound power was reduced by 11.7 dB, with significant global attenuation seen over the in-plane acoustic directivity. Use of the SAS sensing approach led to nearly 8 dB reduction in the total radiated sound power, approximately 3.5 dB less than the microphone sensing case. Global attenuation was still observed over the entire in-plane directivity. This suggests that the active-skin is a suitable application of SAS, making the combined actuator/sensor system much more compact than previously developed ASAC or ANC systems.

The main conclusion drawn from this work is that the piezoelectric, double-amplifier active-skin system shows potential for application to broadband structural radiation problems, including those where far field microphone sensing would represent a impractical error sensing scheme and when the radiating structure is relatively massive.

## V. ACKNOWLEDGEMENTS

The authors gratefully acknowledge the funding of this research under Grant Number N00014-94-1-1140 by the Office of Naval Research, Dr. Kam Ng, Technical Monitor.

## VI. REFERENCES

<sup>1</sup> Gentry, C.A., Guigou, C., and Fuller, C.R., "Smart Foam for Applications in Passive/Active Noise Radiation Control," J. Acoust. Soc. Am., **101** (4), pp 1771-1778, April 1997 (selected research article.)

<sup>2</sup> Gentry, C.A., Guigou, C., and Fuller, C.R., "Foam-PVDF Smart Skin for Active Control of Sound," Proceedings of the 1996 Smart Structures and Materials Symposium, Industrial and Commercial Applications of Smart Structures Technologies, San Diego California, Vol. 2721, pp 26-37, February 1996.

<sup>3</sup> Xu, B., Zhang, Q.M., Kugel, V.D., Qingming Wang, and Cross, L.E., "Optimization of Bimorph Based Double Amplifier Actuator Under Quasistatic Situation," ISAF '96, Proceedings of the Tenth IEEE International Symposium on Applications of Ferroelectrics, p. 2, Vol. 1034, 217-20 vol. 1, 1996.

<sup>4</sup> Fahy, F., *Sound and Structural Vibration*, Academic Press, Inc., London, 1985, Chapter 2, pp. 60-72.

<sup>5</sup> Maillard, J., and Fuller, C.R. "Advanced Time Domain Wave-number Sensing for Structural Acoustic Systems, Part III: Experiments on Active Broadband Radiation Control of a Simply-Supported Plate," *J. Acoust. Soc. Am.*, Vol. 98, No. 6, Pt. 1, pp 2613-2621, November 1995.

<sup>6</sup> Structural Dynamics Research Corporation, *I-DEAS Master Series User Guide Level 4: Model Solution and Optimization*, Structural Dynamics Research Corporation, Milford, Ohio, 1988, Chapter 6, pp 6-7.

<sup>7</sup> Meirovitch, L., *Elements of Vibration Analysis*, McGraw-Hill, Inc., New York, 1975, Second Ed., Chapter 4, pp.178-185.

<sup>8</sup> Crawley, E.F., and de Luis, Javier, "Use of Piezoelectric Actuators as Elements of Intelligent Structures," AIAA Paper 86-0878, pp. 1373-1385, October 1987.

<sup>9</sup> Dimitriadis, E.K., Fuller, C.R., and Rogers, C.A., "Piezoelectric Actuators for Distributed Vibration Excitation of Thin Plates," *J. Vib. Acoust.* **113**, pp 100-107 1989.

<sup>10</sup> Kinsler, L.E., Frey, A.R., Coppens, A.B., and Sanders, J.V., *Fundamentals of Acoustics*, John Wiley & Sons, Inc., New York, 1982 Third Ed., Chapter 8, pp. 167-169.

<sup>11</sup> Widrow, B.J., and Stearns, S.D., *Adaptive Signal Processing*, Prentice-Hall, Englewood Cliffs, New Jersey, 1985, Chapter 6, pp. 99-116.

<sup>12</sup> Mathworks, Inc., *MATLAB Signal Processing Manual*, Prentice-Hall, Inc., New York, 1995, Chapter 6, pp 180-182.

Figure 1: The active-skin concept

Figure 2: The active-skin cell (dimensions in mm)

Figure 3: The active-skin cell FEM mesh

Figure 4: Block diagram of the single-channel filtered-x LMS feed forward algorithm

Figure 5: The piezoelectric disturbance actuator

Figure 6: Top-view of the Plate-Baffle System

Figure 7: Displacement magnitude for the first active-skin cell mode: 246 Hz (250 Hz)

Figure 8: Displacement magnitude for the second active-skin cell mode: 374 Hz (390 Hz)

Figure 9: 6I6O active-skin cell configuration

Figure 10: Total in-plane acoustic directivity before and after control (250 to 750 Hz)

Figure 11: Radiated acoustic power before and after control

Figure 12: 6I6O active-skin configuration including structural acoustic sensing

Figure 13: Structural acoustic sensing and analytical disturbance path models

Figure 14: Structural acoustic sensing and analytical control path models

Figure 15: Total in-plane acoustic directivity before and after control with structural acoustic sensing (250 to 750 Hz)

Figure 16: Radiated acoustic power before and after control with structural acoustic sensing

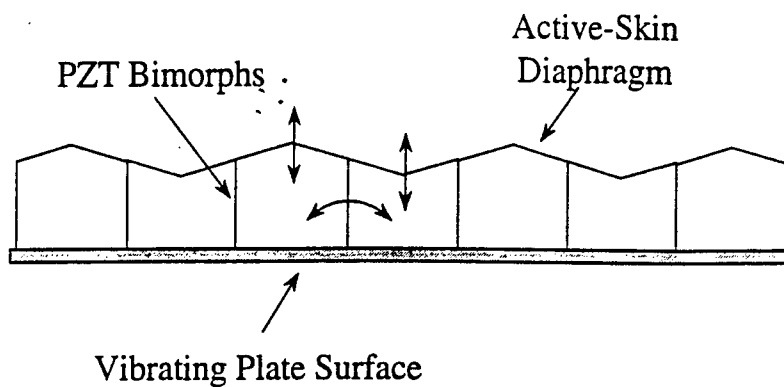


Figure 1

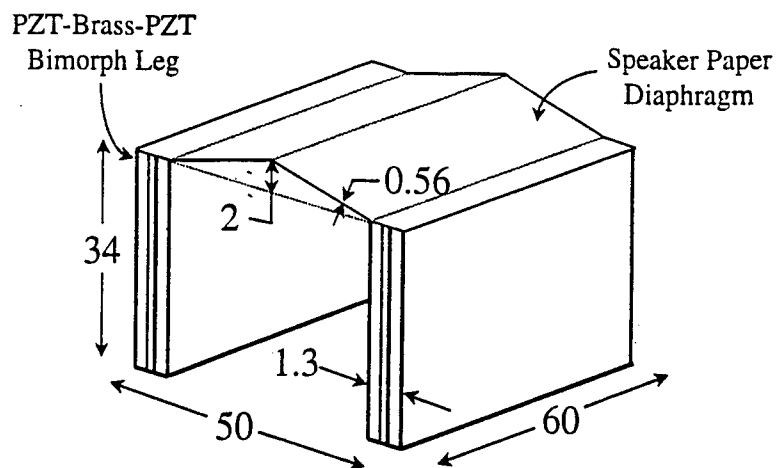


Figure 2

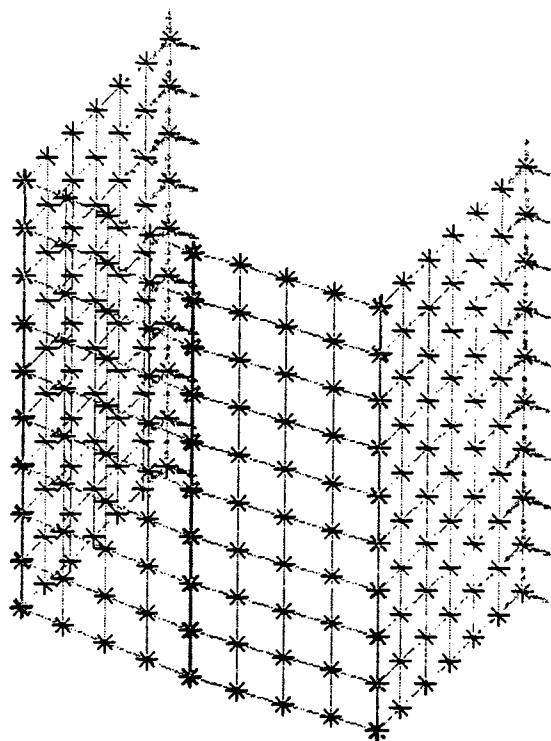


Figure 3

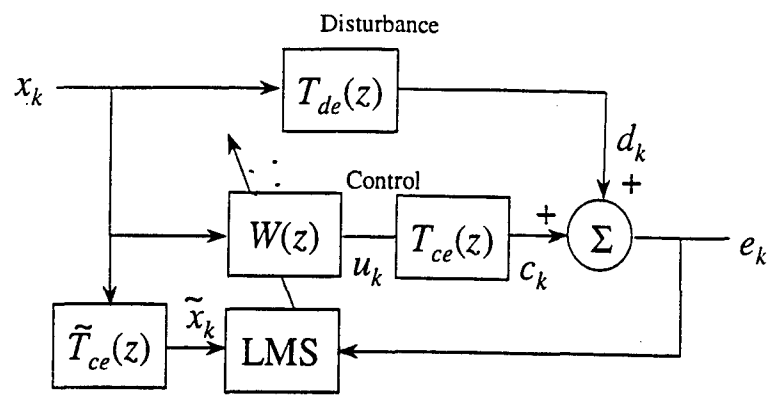


Figure 4

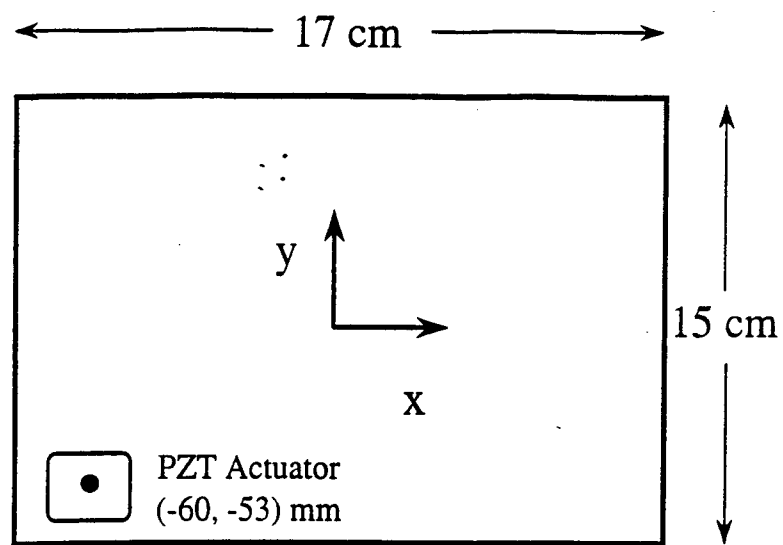


Figure 5

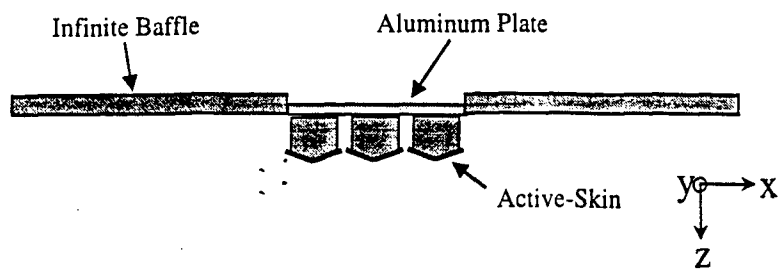


Figure 6

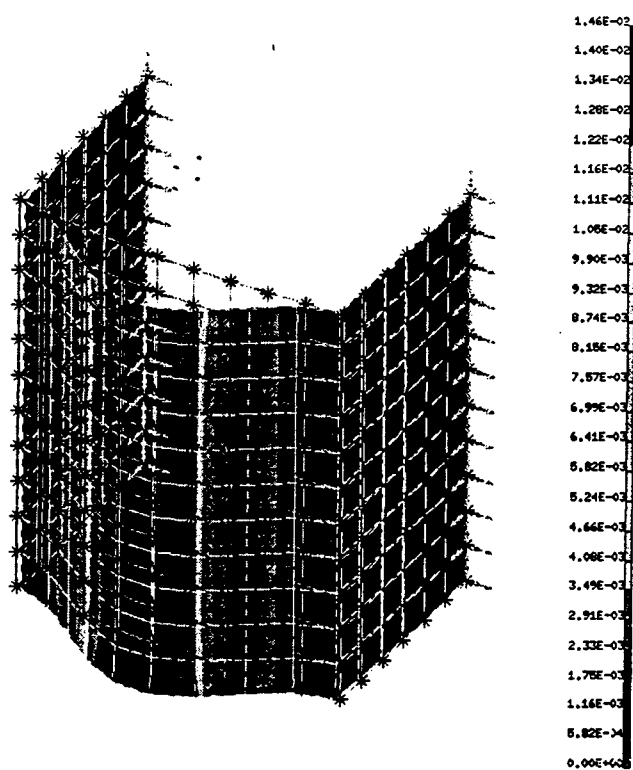


Figure 7

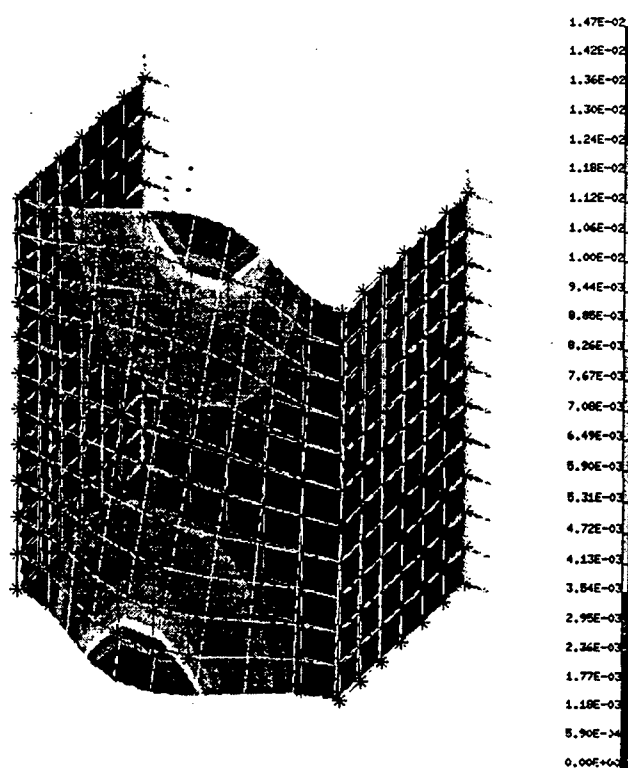


Figure 8

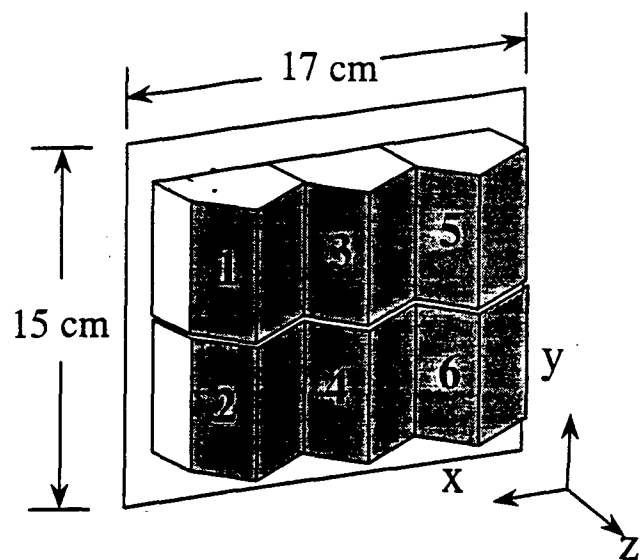


Figure 9

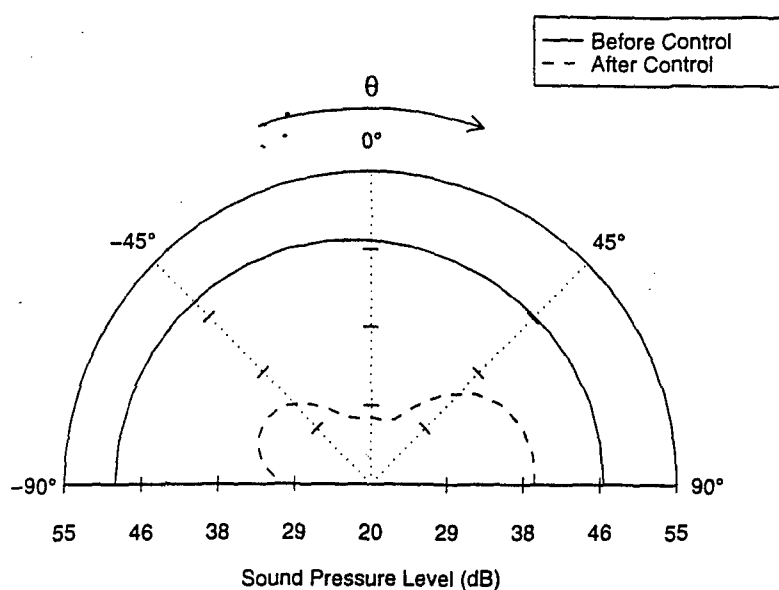


Figure 10

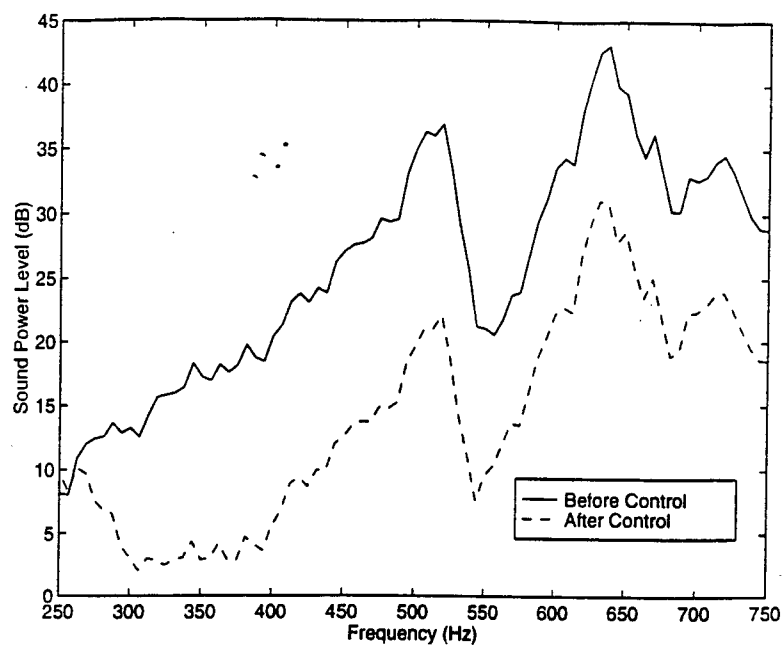


Figure 11

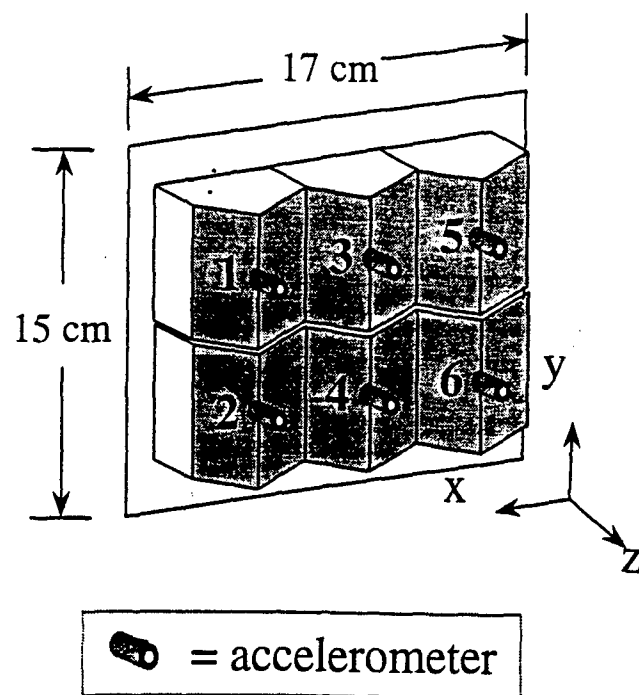


Figure 12

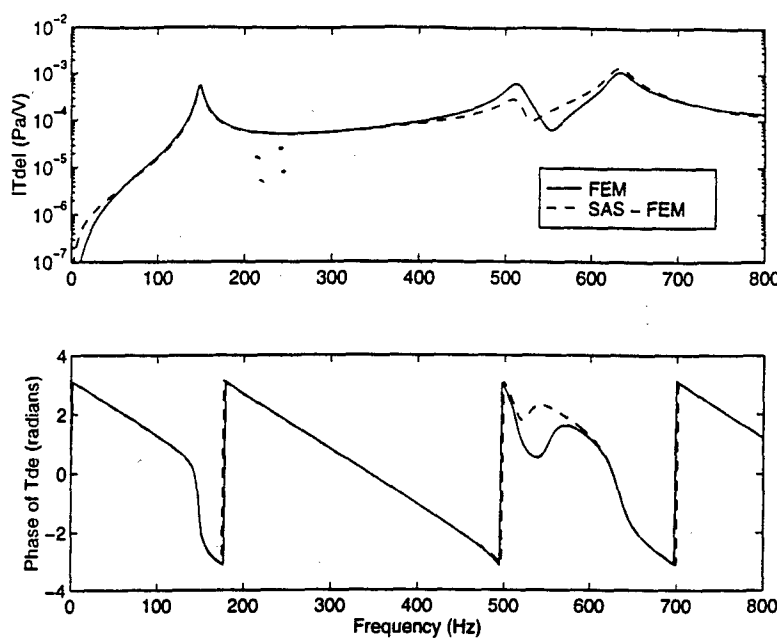


Figure 13

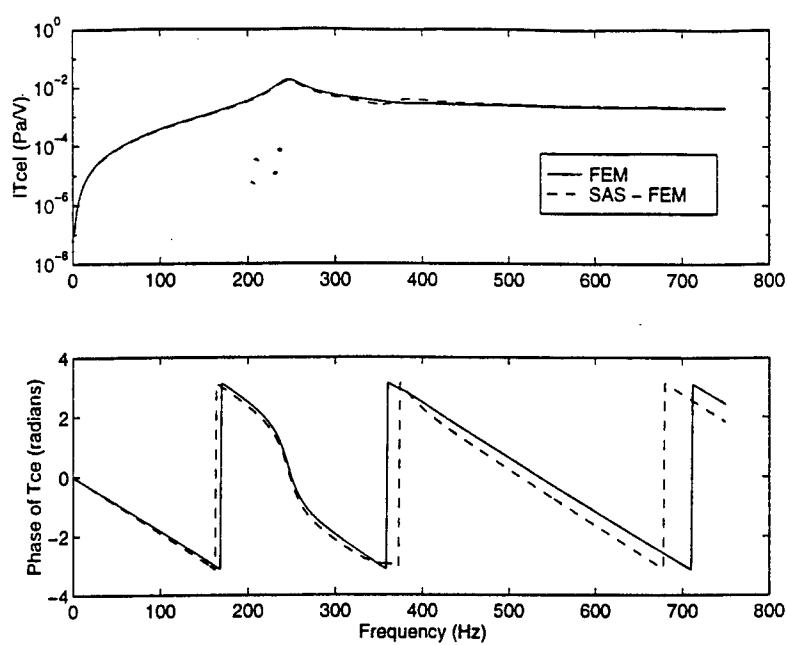


Figure 14

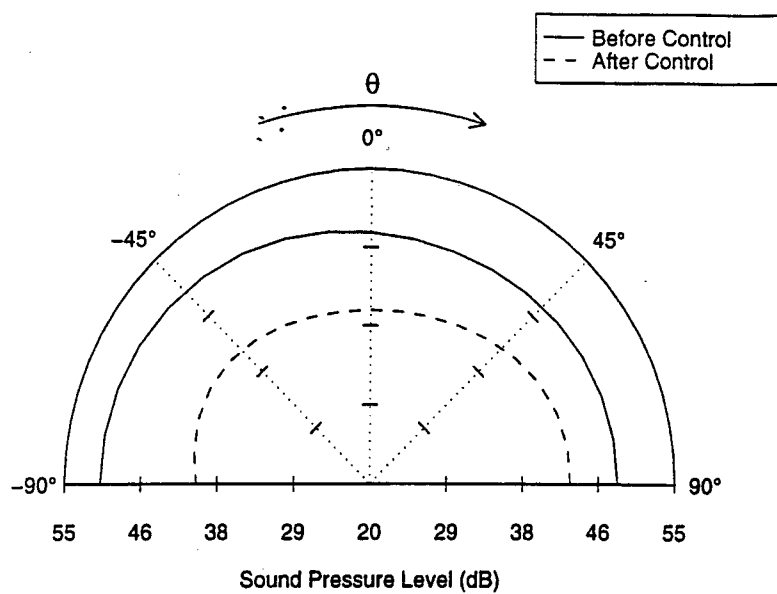


Figure 15

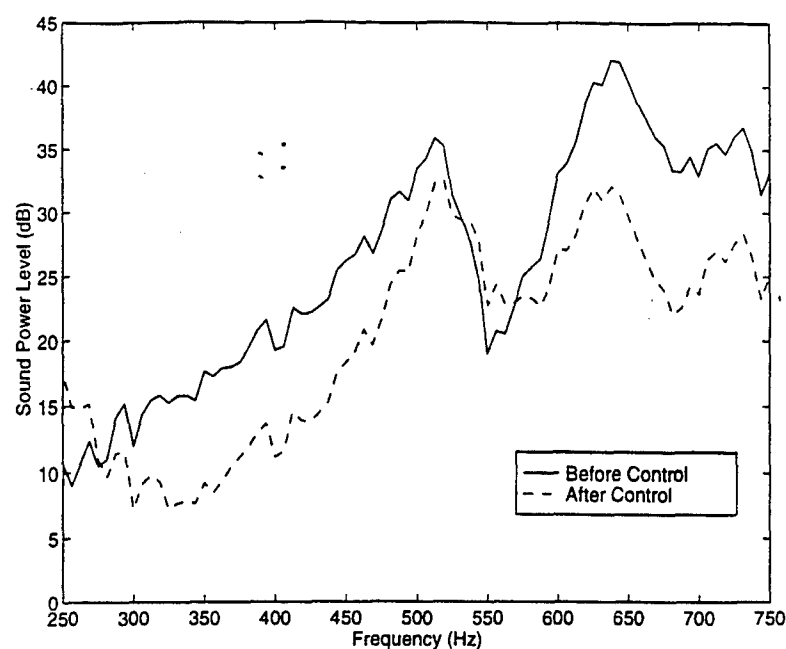


Figure 16

*Table I – Mechanical Properties of Active-Skin Cell Materials*

Material	Mass Density (kg/m <sup>3</sup> )	Modulus of Elasticity (Pa)	Modulus of Rigidity (Pa)	Poisson's Ratio
Speaker Paper	545	7.84 x 10 <sup>+8</sup>	3.04 x 10 <sup>+8</sup>	0.29
PKI550 PZT	7500	6.3 x 10 <sup>+10</sup>	2.44 x 10 <sup>+10</sup>	0.29
Brass	8700	11.0 x 10 <sup>+10</sup>	4.26 x 10 <sup>+10</sup>	0.29

*Table II – Active-Skin Cell Locations*

Cell Number	x (mm)	y (mm)	z (mm)
1	-51	45	2.5
2	-51	-45	2.5
3	0	45	2.5
4	0	-45	2.5
5	51	45	2.5
6	51	-45	2.5

*Table III – Error Microphone Locations*

Mic. Number	x (cm)	y (cm)	z (cm)
1	-20	33	39
2	0	0	65
3	-43	-15	44
4	0	-36	40
5	48	0	41
6	32	38	30

## **APPENDIX 27**

Submitted to the J. Acoust. Soc. Am. (1998)

Johnson, Brody D. and Fuller, Chris R.      Journal of the Acoustical Society of America

Broadband control of plate radiation using a piezoelectric, double-amplifier active-skin, part II: experimental.

Brody D. Johnson

Vibration and Acoustics Laboratories, Department of Mechanical Engineering,  
Virginia Polytechnic Institute and State University, Blacksburg, Virginia 24061.

Chris R. Fuller

Vibration and Acoustics Laboratories, Department of Mechanical Engineering,  
Virginia Polytechnic Institute and State University, Blacksburg, Virginia, 24061.

Received

Footnote Title:

Johnson and Fuller: A double-amplifier active-skin, part II.

The search for more practical active control systems has lead to the development of many alternate approaches to actuator-sensor arrangements. This research push is directed towards the creation of compact, robust control systems for implementation in general noise control environments. The intent of this work is to experimentally demonstrate the potential of a piezoelectric, double-amplifier active-skin in satisfying the aforementioned goals in the control of structural-acoustic radiation from a plate. The active-skin consists of a complete covering of the vibrating portions of a structure with active piezoelectric elements. These elements serve as secondary sources in the control system. The adaptive feed forward filtered-x LMS algorithm, implemented on a TI C40 DSP, was used in conjunction with the 6I6O control system. Initial experimentation was conducted using microphone error sensing; however, as a more compact sensing scheme, Structural Acoustic Sensing was adopted for further experimentation with the active-skin. With microphone error sensing 11.8 dB attenuation was achieved in the overall radiated acoustic power between 175 and 600 Hz, with significant reduction observed over the entire in-plane acoustic directivity. Inclusion of SAS resulted in a 7.3 dB overall power reduction in this frequency band, again providing substantial reduction throughout the in-plane acoustic directivity.

PACS #'s: 43.50.Ki, 43.40.At

## I. INTRODUCTION

Much of the initial work in Active Noise Control (ANC) was directed toward the demonstration of the feasibility of this noise suppression concept in the context of a limited number of suitable applications, e.g. one-dimensional harmonic duct noise.<sup>1</sup> From this meager beginning, ANC has been applied to a wide variety of noise control problems, including jet engine exhaust noise,<sup>2</sup> interior cabin noise (aircraft and automobiles),<sup>3</sup> and external structural-acoustic radiation.<sup>4</sup> This research has been paralleled by much growth in the area of Active Structural Acoustic Control (ASAC), in which the acoustic radiation of a given structure is modified by control actuators mounted directly on the offending structure.<sup>5,6</sup> Recent work in these areas has shared a common trend: the pursuit of practical active control systems that may be applied in more generalized noise control environments. For instance, due to space constraints, it is often impractical to locate microphone error sensors in the target area of the acoustic control. The use of alternate error sensing schemes, such as Structural Acoustic Sensing (SAS), has proven to be an effective solution to this problem. SAS consists of the prediction of acoustic error from vibration information taken from a number of structurally mounted sensors. Maillard has shown, both analytically and experimentally, that SAS is an effective technique for the estimation of an acoustic cost function in multi-channel ASAC systems.<sup>7</sup> The greatest asset of this technique is its versatility, as, with some work, SAS may be applied in many control systems which have previously depended on microphone error sensing.

Another important consideration in the design of a practical control system lies in an objective assessment of the effect of the necessary hardware on the primary structure. Characteristics such as the weight and size of the control system must be evaluated, as well as any potential deterioration in the performance of the primary structure under the influence of the secondary system(s). Obvious examples are automotive and aeronautical applications where each of these effects is of prime concern. In order to satisfy the constraints imposed in these and other applications, lightweight, compact control systems must be devised. This motive has lead to the investigation of a wide variety of control approaches, one simply consisting of the complete covering of the radiating surface of a structure with a specially designed skin. This skin may exhibit both passive and active characteristics and in many

cases is comprised of a number of individual skin elements that make use of one or both of these tactics. As suspected, the use of a foam layer on the surface of a vibrating piston has provided attenuation of high frequency sound.<sup>8</sup> As a supplement to an ordinary foam layer, Gentry, Guigou, and Fuller have included PVDF actuators inside the foam layer that increases the low frequency performance of the skin while still taking advantage of the passive properties of the foam.<sup>8,9</sup> Ross and Burdisso have taken another approach to the skin concept, by designing what is essentially a single degree of freedom (DOF) skin element.<sup>10</sup> When this passive device is applied to a vibrating surface, the mass component of the single DOF element is forced to vibrate at one level, while the base surrounding the mass element shares the original vibration level of the primary structure. Thus, for frequencies above the resonance of this single DOF system, the mass and base elements vibrate out of phase. By determining the appropriate areas for the base and mass surfaces of the skin element, an acoustic dipole is created. A previous companion paper has analytically investigated the use of a piezoelectric double amplifier active skin for sound radiation control.<sup>11</sup> In this paper the analytical work is experimentally verified.

A number of examples of the skin concept in the control of sound were discussed in the previous paragraph. In each of these examples the goal lies in the development of a compact noise suppression system, albeit passive or active, that allows for application to a wider variety of noise control problems. It is such a system that will be evaluated here. This work is a continuation of a previous *analytical* investigation of a piezoelectric, double-amplifier active-skin in which an *experimental* metric of the concept is sought as applied to a clamped, aluminum plate. The reader is referred to this previous work for a complete treatment of the skin concept; however, a brief description of the slightly different skin design used in this work is necessary before presenting experimental results.<sup>12</sup> The active-skin employed here consists of a number of independently controllable piezoelectric elements, which serve as secondary acoustic sources in the control scheme. These elements, or skin cells, are designed to provide a high level of diaphragm vibration with only a small space requirement. A rough schematic of this skin cell design is given in Fig. 1. In this sketch, the dashed lines depict an exaggerated motion of the skin cell frame, while solid black lines represent the motion of the diaphragm. This improved cell design includes piezoelectric material inside the frame, with an outer covering of steel for protection of the piezoelectric material. A stiff,

lightweight carbon-graphite material is used for the diaphragm, preventing high order diaphragm modes from dominating the response of the device. The actual devices used for this experimentation were designed and fabricated by the Material Research Laboratory at the Pennsylvania State University at State College, Pennsylvania.<sup>13</sup> One such device, which is approximately 55 x 55 x 20 mm in size, is shown in Fig. 2. Two stages of vibrational amplification are present in this skin cell design. Piezoelectric material contained in the sides and bottom of the skin cell provides the first stage, while the second stage results directly from the geometric design of the cell. In this most recent design, the additional piezoelectric material employed on the bottom of the skin cell allows for even greater displacement of the cell diaphragm.

The results presented here correspond to the application of a six-cell active-skin on a clamped, aluminum plate. A multi-channel formulation of the adaptive feed forward filtered-x Least Mean Square (LMS) control algorithm is used, in conjunction with either far field microphone or SAS error sensing schemes. These results are intended to demonstrate the feasibility of the active-skin in conjunction with SAS and, thus, a comparison of microphone and SAS sensing cases for a given cell configuration must be drawn to measure the utility of both the SAS sensing system and the active-skin sources. The effect of the SAS sensors (accelerometers) on the behaviour of the active-skin is studied by conducting experiments for two structural sensor configurations. In the first case, an accelerometer is mounted to the flexible leg of each active-skin cell, with an additional sensor located on the plate. Due to the relative stiffness of the legs with respect to the diaphragm of the skin cell, and correspondingly lower levels of vibration, the sensor is not expected to mass load the skin cell. Hence, the diaphragm vibration for this case should essentially match that observed when the sensor is not present. The second configuration, on the other hand, consists of locating the cell accelerometers directly on the diaphragm surface. In this case, a mass loading of the diaphragm is expected as the mass of a sensor is significant when compared to the mass of the diaphragm. Again, an additional sensor is located on the plate. The performance of the control system in each case is studied in two ways. First, the in-plane acoustic directivity is measured over the 180° span of the baffle for both the controlled and uncontrolled cases. Second, the effect of the skin on the radiated acoustic power is estimated from Sound Pressure Level (SPL) measurements using a ten-point approximation.

## II. CONTROL APPROACH

The successful implementation of the active-skin relies on two key components. The first is the control algorithm, the adaptive feed forward filtered-x LMS in this case, which is performed via a digital signal processor (DSP) for the iterative determination of appropriate control voltages issued to the various active-skin cells. The filtered-x LMS adaptive algorithm is well established in the control of both sound and vibration.<sup>2,14</sup> The second system of importance here is the SAS sensing system used in the absence of far field microphone error sensing. Previous work with SAS has relied on the known radiation behaviour of specialized geometries, while in this work a convenient experimental technique is used to determine relationships between the measured structural vibration and the desired far field acoustic response. In either case, transfer functions relating the structural sensors to each of the desired acoustic error estimates must be determined. Once these transfer functions are known, Finite Impulse Response (FIR) filters must be designed for the real time representation of these acoustic paths on a DSP. The following sections are devoted to a concise treatment of these two components.

### A. Control Algorithm

In this work, a brief survey of the important aspects of the filtered-x LMS algorithm is given using a single-reference multi-channel formulation. Fig. 3 contains a generalized block diagram representation of the general multi-channel filtered-x sequencing algorithm. In this depiction,  $x$  is the reference signal,  $e_n$  represents the total error signal due to the combined effects of the disturbance and control inputs on the  $n^{th}$  error sensor,  $u_m$  is the input to the  $m^{th}$  secondary path, and  $\hat{x}_{mn}$  is the filtered-x signal relating the  $m^{th}$  secondary path to the  $n^{th}$  error sensor. The primary structure is represented by the  $z$ -domain transfer functions  $T_{de}(z)$ , while  $T_{ce}(z)$  represents the control path transfer functions relating the excitation of a particular control source and each of the  $n$  error sensors. A digital filter model of each control path transfer function, denoted by  $\tilde{T}_{ce}(z)$ , is required represented for adaptation of the control

compensators. These models are found through system identification, in which the actual control-to-error paths are directly modeled using digital filters in conjunction with a standard LMS gradient approach.<sup>15,16</sup> The intent of these models is to provide knowledge of the effect that the secondary path has on the error signals and, thus, accurate modeling of these paths is crucial. The control compensators, denoted by  $W_m(z)$ , are responsible for the filtering of the reference signal,  $x$ , in such a way that appropriate control voltages,  $u_m$ , are applied to the secondary sources. A quadratic cost function was used in this work corresponding to the sum of the squared error for each time step.

Practical limitations exist in the performance of the algorithm which are governed by many parameters, including the coherence between the reference and disturbance signals, the accuracy of system identification, the sample rate, the FIR filter orders, the convergence parameter, and the number of control channels. A six-channel formulation was employed with the active-skin in this work. This significantly taxes the memory resident in the DSP, providing upper limits on the sample rate as well as the lengths of compensator and system identification filters. A sample rate of 2000 Hz was adopted in combination with 175 coefficient compensators and 64 coefficient system identification filters. The ideal reference signal, the disturbance signal, was used in each experiment.

## B. Structural Acoustic Sensing

As an introduction to a more practical error-sensing scheme, this section is devoted to the development of an experimental methodology for the prediction of the radiated acoustic pressure using a number of accelerometers, which are distributed over the radiating surfaces of the active-skin. The signals provided by these accelerometers are used in conjunction with an array of specially designed digital filters to construct signals that correspond to the acoustic pressure at desired points in the far field. For accurate prediction of the acoustic error, the influence of a given structural sensor at a desired error location must be known. This relationship between the structural sensors and the error locations may be found in a number of ways. A limited number of geometries admit a theoretical solution, while geometries of slightly greater complexity may be studied using numerical methods such as the Boundary Element Method (BEM). For a description of the theory governing this technique, the reader is referred

to previous analytical work with the active-skin.<sup>11,12</sup> If the geometry of the system is very complex, it is difficult to determine the proper influence functions with either of these approaches, necessitating another means for relating these vibration and acoustic quantities. In some instances it may be possible to excite isolated areas of a structure. Assuming this is possible for the time being, the radiation sensed by a microphone at a given far field location depends only on the vibration of the isolated surface vibration. In this case, the appropriate influence function is given by the transfer function between the vibration of this isolated surface and the measured acoustic pressure at the desired location in the acoustic medium. Fortunately, the individual skin cells of the active-skin provide a convenient means for the isolation of these influence functions. Thus, the desired influence relationships are determined by the exciting a single skin cell and directly measuring the transfer functions between an accelerometer mounted on the cell to each of the far field microphones. This process yields the necessary information for relating the skin vibration to the measured acoustic response in the far field, but fails to characterize the relationship between the plate vibration and the associated far field acoustic disturbance. By placing a single additional accelerometer on the plate and issuing a disturbance to the plate via a shaker, a similar set of measurements may be made which characterizes the effect of the plate vibration on the net error. It is important to note that any "cross-talk" between the structural sensors would serve to dissolve the validity of this approach. This coupling is eliminated by mounting the skin cells on a perforate sheet slightly above the surface of the plate. Once the influence functions have been determined, they must be incorporated into a real time DSP code. Thus, an array of digital filters modeling the various sensor paths is required. The appropriate digital filters necessary for modeling these transfer functions must be found using a numerical curve fit with a reasonable number of FIR filter weights. Note that the number of digital filters that are required for implementation of an SAS system employing  $M$  accelerometers for the prediction of the acoustic pressure at  $N$  locations in the acoustic medium is  $M \times N$ . Hence, the difficulty in developing a practical SAS system lies in achieving an adequate representation of the acoustic radiation with a minimal number of structural sensors.

### III. EXPERIMENTAL SETUP

As previously mentioned, the active-skin is implemented here on a clamped, aluminum plate. The plate is of dimensions 170 x 150 x 1.5 mm and is situated in a baffle which divides the surrounding anechoic chamber. Fig. 4 is a side view of the anechoic chamber (4.2 x 2.5 x 2.2 m) revealing the location of the plate in the baffle, a tubular hemisphere used to support a number of microphones, and a traverse boom used to acquire in-plane acoustic directivity data over the 180° space on the front side of the baffle. A total of sixteen microphones are mounted on the hemisphere, six for use as error sensors in microphone sensing configurations and an additional ten to provide a picture of the total radiated acoustic power. A schematic of the experimental setup is given in Fig. 5. Dashed lines are used with the microphones to indicate that either microphone or SAS sensing is adopted for a particular control configuration. As depicted in Fig. 5, a shaker mounted to the plate from the backside of the baffle disturbs the plate. A photograph of this shaker, as mounted to the plate during experiment, is presented in Fig. 6. The skin cells are mounted to a perforated aluminum support plate approximately 5 mm in front of the surface of the plate. The perforated plate is necessary for the prevention of coupling between the plate and skin cell vibrations. Such coupling would greatly complicate the SAS approach. An accelerometer is mounted to each radiating structure, one on each of the six skin cells and another on the backside of the plate. The signals from each accelerometer are passed along to the filter controller, see Fig. 5, where the SAS filtering is performed on a TI-C30 DSP. 30 coefficients are employed in each of the forty-two SAS paths at a 1300 Hz sample rate. The SAS filter controller constructs estimates of the radiated acoustic pressure at each of the desired error sensor locations before passing along this error information to the filtered-x controller. A TI-C40 DSP is used to implement the filtered-x control algorithm at a sample rate of 2000 Hz. With this sample rate, the control compensators and system identification filters may possess up to 175 and 96 FIR coefficients, respectively. The ideal reference (the disturbance input) is used in this work. The maximum filter length is applied in each control configuration. The limiting factor in the controllable bandwidth of this application of the active-skin is the 1300 Hz sample rate of the SAS sensing. Hence,

all control experiments are conducted for a band limited random disturbance between 175 and 600 Hz to ensure accurate prediction of the far field acoustic error.

#### IV. RESULTS

The primary objective of this work is to show the potential of the active-skin in the control of structural radiation; however, a secondary objective is to evaluate the SAS sensor configuration in search of the most functional error sensing arrangement. Thus, the skin is employed in two configurations, the first corresponding to the side mounting of the SAS accelerometers on the active-skin cells and the second constituting the top-mounting of the SAS accelerometers. With each of the mounting configurations, results are presented first for the microphone sensing array and second for the SAS system.

##### A. Side Mounting SAS Scheme

For a first experiment with the SAS sensing approach, a side-mounting scheme was chosen for the attachment of accelerometers to each of the six active-skin cells. Note that in this and the following mounting scheme a seventh sensor is located on the backside of the aluminum plate. Due to the relative mass and stiffness of the leg in comparison to that of the diaphragm, side mounting the SAS sensors is suspected to induce less mass loading of the diaphragm response than top mounting. However, the vibration of the cell legs creates virtually no acoustic response, and seems an unlikely location for the placement of a structural acoustic sensor. Fortunately, the diaphragm vibration is due entirely to the excitation provided by the legs, which indicates that a linear relationship exists between these motions. The six-cell active-skin, mounted to a perforated aluminum sheet, is depicted in Fig. 7, showing the accelerometers mounted on the sides of the individual skin cells. The following paragraphs summarize the results obtained for this mounting configuration under the aid of microphone and SAS sensing systems.

To set the pace for the SAS system, the microphone sensing setup is adopted first. For this 6I6O control system, the error microphones were distributed evenly over the tubular hemisphere shown in Fig. 4. The shaker attached to the plate was driven with band-limited random noise between 175 and 600 Hz. While several plate modes are present in the frequency range investigated, the response of the plate is dominated by two modes due to the nature of the shaker loading. The filtered-x algorithm was run with a sample rate of 2000 Hz and 175 coefficients were used in each of the six adaptive FIR control compensators. Following a three-minute period of system identification, the control compensators were allowed to adapt for two minutes. Fig. 8 depicts the in-plane acoustic directivity, in SPL, for the controlled and uncontrolled cases, illustrating global reduction in the acoustic radiation from the plate-skin system. An estimate of the radiated sound power is given in Fig. 9 for the controllable bandwidth, which reveals significant attenuation around each resonant frequency of the aluminum plate. This power estimate was formulated from SPL measurements made at ten points distributed evenly over the hemisphere. Note that each of these ten locations is distinct from the microphone error sensor locations. An 10.9 dB reduction is achieved in the controlled power radiation from the plate-skin system in the 175 to 600 Hz bandwidth.

Having established a base-line performance for the active-skin, the primary objective of this work, as discussed above, is satisfied. However, in an attempt to produce a more practical control system, the search for a more compact error-sensing scheme is undertaken. Thus, a second set of experiments were conducted, in which the side mounted accelerometers are employed in an SAS system for the prediction of the acoustic error at each microphone location adopted for the previous set of results. The forty-two influence paths, relating the seven structural signals to each of the six error estimates, were obtained using the experimental procedure outlined in section II.B of this work. Once these paths have been identified a straightforward application of the control algorithm is made. Again, a sample rate of 2000 Hz was used, in conjunction with 175 coefficient adaptive control compensators. A 1300 Hz sampling frequency was adopted with the SAS controller, using 30 coefficients in each of the SAS influence paths. Fig. 10 depicts the in-plane acoustic directivity data obtained for this experiment, which reflects reduction levels slightly less than that observed for the microphone sensing case. A total radiated power reduction of 6.6 dB was

attained over the 175 to 600 Hz bandwidth, while the corresponding frequency spectrum is given in Fig. 11. Thus, as one might expect, the practical advantage of the compact SAS system comes at a small performance cost.

### B. Top Mounting SAS Scheme

Having already obtained good control performance with both microphone and SAS sensing arrangements, another step is taken to determine the best configuration for the active-skin SAS system. Here, the six SAS accelerometers on the skin cells are repositioned to the center of the diaphragm of each cell. This configuration is depicted in Fig. 12. Other than the accelerometer locations, this configuration is identical to that used in the previous section. As with the previous case, the microphone-sensing scheme is investigated before examining the system under the influence of SAS.

With this experiment, the effect of the accelerometers on the response of the skin cell diaphragms is to be studied. It is expected that the extra mass damping of the accelerometers will reduce the control authority of the skin cells and correspondingly reduce the overall performance of the control system. To ensure isolation of this effect, the sample frequency (2000 Hz) and compensator length (175 coefficients) from the previous experiment are assumed. The in-plane directivity result for this test is depicted in Fig. 13. Comparing this data with that of Fig. 8, it is evident that the accelerometers play a role in the control authority of the skin cells. The radiated acoustic power for the controlled and uncontrolled scenarios is presented in Fig. 14. This data indicates that the low frequency performance of the system is affected most by the presence of the accelerometers on the cell diaphragm, while an overall power reduction of 9.5 dB was still observed.

Finally, the SAS sensing system was implemented for the top mounted accelerometer setup. The 2000 Hz sampling frequency and 175 coefficient compensator lengths of the previous systems are preserved for this test. The SAS controller again operates at 1300 Hz, making use of 30 coefficients in each of the forty-two SAS influence paths. Surprisingly, the results obtained with this configuration surpassed that of the side-mounted SAS arrangement, albeit by a relatively small amount. Fig. 15 reveals an in-plane directivity response quite similar to

that observed in the previous SAS test, described above. The overall radiated power was reduced by 7.3 dB in the control bandwidth, as depicted by Fig. 16. The low frequency performance deterioration observed in the side-mounted sensing case is not present here. One possible explanation for this anomaly would be increased accuracy in the SAS estimate for these frequencies, acting to counteract the loss of control authority. Since the side-mounted scheme depends on an *assumed* linear relationship between the leg and diaphragm vibrations, this line of reasoning becomes more plausible. At any rate, a slightly better control performance is obtained with this configuration.

Before concluding, it is worth pausing briefly to contrast the experimental results obtained here to the analytical conclusions offered in the companion paper.<sup>11</sup> It is necessary, at this point, to note that in simulation a piezoelectric patch was assumed for the disturbance input, while in experiment the piezoelectric actuator was replaced with a shaker. The shaker acts to lower the resonant frequencies of the aluminum plate, leading to a difference in control bandwidths between the two sets of results. This disparity aside, the radiation characteristics of the plate under either of the two loadings is expected to be similar. In simulation, nearly a 12 dB reduction in radiated acoustic power was observed over a bandwidth from 250 to 750 Hz. As with the experimental results, two modes of the plate were present in the control bandwidth with between 10 and 15 dB attenuation observed at each resonant peak. With the SAS system, simulation predicted just under 8 dB reduction in the radiated acoustic power between 250 and 750 Hz. This is quite similar to the results presented here, in which the SAS results are between 2 and 5 dB lower than the associated microphone-sensing case.

#### IV. CONCLUSIONS

In this work, experiments were conducted with a piezoelectric double-amplifier active-skin in conjunction with a number of microphone and SAS sensing arrangements in order to validate the active-skin approach. An experimental technique for the determination of SAS influence relationships was described and validated through use in control experiments. Significant attenuation in radiated sound power was achieved with each active-skin

configuration, along with global reduction of the SPL observed over the in-plane acoustic directivity. While SAS configurations resulted in a lessened control performance with respect to the corresponding microphone sensing result, substantial reduction was still obtained. This degradation of control performance is suspected to depend on the maximum sample rate and filter lengths attainable with the SAS DSP controller. These results further suggest that the active-skin system is conducive to the inclusion of SAS, which makes the actuator-sensor system more compact and, hence, more practical than many previously developed ASAC or ANC systems. Lastly, the active-skin system was shown to be another successful application of feed forward control.

The work presented here leads to the conclusion that the piezoelectric, double-amplifier active-skin, combined with SAS error estimation, represents a viable control approach for application to generalized broadband structural radiation problems.

## V. ACKNOWLEDGEMENTS

The authors gratefully acknowledge the support of this work under Grant Number N00014-94-1-1140 by the Office of Naval Research, Dr. Kam Ng, Technical Monitor.

## VI. REFERENCES

- <sup>1</sup> Warnaka, G.E., "Active Attenuation of Noise - The State of the Art," *Noise Control Eng.* 18(3), pp 100-110, 1982.
- <sup>2</sup> Smith, J.P., Burdisso, R.A., Fuller, C.R., and Gibson, R.G., "Active Control of Low-Frequency Broadband Jet Engine Exhaust Noise," *Noise Control Eng. J.*, 44(1), pp 45-52, 1996.

<sup>3</sup> Elliot, S.J., Nelson, P.A., Stothers, I.M., and Boucher, C.C., "In-Flight Experiments on the Active Control of Propeller-Induced Cabin Noise," *J. Sound Vib.*, **140**(2), 219-238, 1990.

<sup>4</sup> Deffayet, C., and Nelson, P.A., "Active Control of Low Frequency Harmonic Sound Radiated by a Finite Panel," *J. Acoust. Soc. Am.* **84**(6), pp 2192-2199 1988.

<sup>5</sup> Fuller, C.R., "Apparatus and Method for Global Noise Reduction," U.S. Patent No. 4,715,599, 1987.

<sup>6</sup> Clark, R.L., and Fuller, C.R., "Optimal Placement of Piezoelectric Actuators and Polyvinylidene Fluoride (PVDF) Error Sensors in Active Structural Acoustic Control Approaches," *J. Acoust. Soc. Am.*, **92**(3), pp 1489-1498, 1992.

<sup>7</sup> Maillard, J., and Fuller, C.R. "Advanced Time Domain Wave-number Sensing for Structural Acoustic Systems, Part III: Experiments on Active Broadband Radiation Control of a Simply-Supported Plate," *J. Acoust. Soc. Am.*, Vol. 98, No. 6, Pt. 1, pp 2613-2621, November 1995.

<sup>8</sup> Gentry, C.A., Guigou, C., and Fuller, C.R., "Smart Foam for Applications in Passive/Active Noise Radiation Control," *J. Acoust. Soc. Am.*, **101** (4), pp 1771-1778, April 1997 (selected research article.)

<sup>9</sup> Gentry, C.A., Guigou, C., and Fuller, C.R., "Foam-PVDF Smart Skin for Active Control of Sound," Proceedings of the 1996 Smart Structures and Materials Symposium, Industrial and Commercial Applications of Smart Structures Technologies, San Diego, California, Vol. 2721, pp 26-37, February 1996.

<sup>10</sup> Ross, B.W., and Burdisso, R. A., "Control of Low Frequency Structurally Radiated Noise with an Array of Weak Radiating Cells: An Experimental Study," submitted to the Journal of the Acoustical Society of America, 1997.

<sup>11</sup> Johnson, B.D. and Fuller, C.R., "Broadband Control of Plate Radiation Using a Piezoelectric, Double-Amplifier Active-Skin, Part I: Analytical," submitted to the Journal of the Acoustical Society of America, 1998.

<sup>12</sup> Johnson, B.D., "Control of Broadband Structural Radiation from Structures Using a Piezoelectric Double-Amplifier Active-Skin," *Master of Science Thesis*, Department of Mechanical Engineering, VPI&SU 1997.

<sup>13</sup> Xu, B., Zhang, Q.M., Kugel, V.D., Qingming Wang, and Cross, L.E., "Optimization of Bimorph Based Double Amplifier Actuator Under Quasistatic Situation," ISAF '96, Proceedings of the Tenth IEEE International Symposium on Applications of Ferroelectrics, p. 2, Vol. 1034, 217-20 vol. 1, 1996.

<sup>14</sup> Vipperman, J.S., Burdisso, R.A., and Fuller, C.R., "Active Control of Broadband Structural Vibration Using the LMS Adaptive Algorithm," *J. Sound Vib.*, **166**(2), pp 283-299, 1993.

<sup>15</sup> Elliot, S.J., Nelson, P.A., and Stothers, I.M., "A Multiple Error LMS Algorithm and Its Application to the Active Control of Sound and Vibration," *IEEE Trans. Acoust., Speech, Signal Processing*, **ASSP-35**, pp 1423-1434, 1987.

<sup>16</sup> Widrow, B.J., and Stearns, S.D., *Adaptive Signal Processing*, Prentice-Hall, Englewood Cliffs, New Jersey, 1985, Chapter 6, pp. 99-116.

Figure 1: The active-skin cell design

Figure 2: A single active-skin cell

Figure 3: Block diagram of the MIMO filtered-x LMS algorithm

Figure 4: The anechoic chamber, showing the baffle, shaker, and microphone locations

Figure 5: The active-skin experimental setup

Figure 6: A close-up of the shaker/plate system

Figure 7: The active-skin in a side-mounted structural acoustic sensing configuration

Figure 8: Total in-plane acoustic directivity (SPL), side-mounted accelerometer configuration with microphone error sensing

Figure 9: Radiated sound power spectra, side-mounted accelerometer configuration with microphone error sensing

Figure 10: Total in-plane acoustic directivity (SPL), side-mounted accelerometer configuration with structural acoustic sensing

Figure 11: Radiated sound power spectra, side-mounted accelerometer configuration with structural acoustic sensing

Figure 12: The active-skin in a top-mounted structural acoustic sensing configuration

Figure 13: Total in-plane acoustic directivity (SPL), top-mounted accelerometer configuration with microphone error sensing

Figure 14: Radiated sound power spectra, top-mounted accelerometer configuration with microphone sensing

Figure 15: Total in-plane acoustic directivity (SPL), top-mounted accelerometer configuration with structural acoustic sensing

Figure 16: Radiated sound power spectra, top-mounted accelerometer configuration with structural acoustic sensing

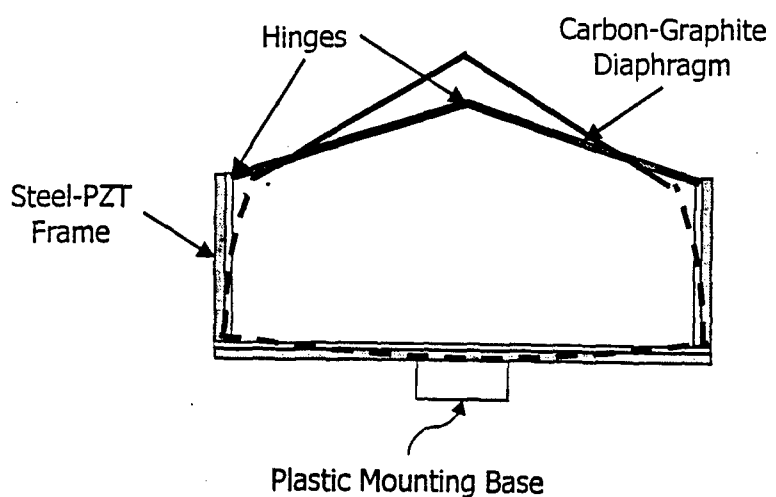


Figure 1

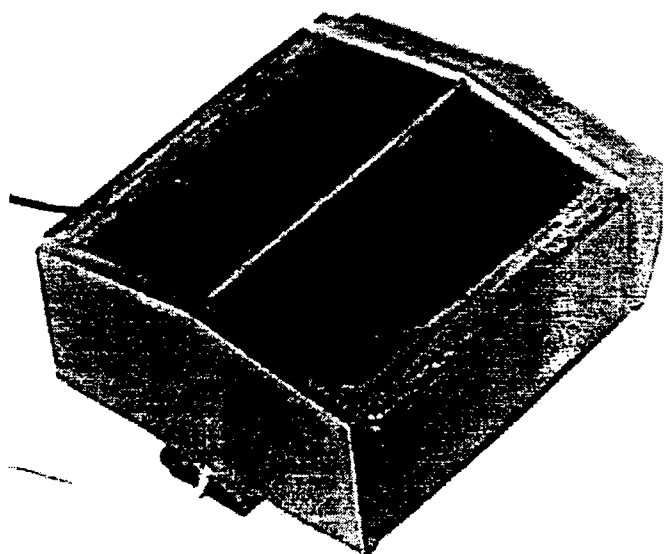


Figure 2

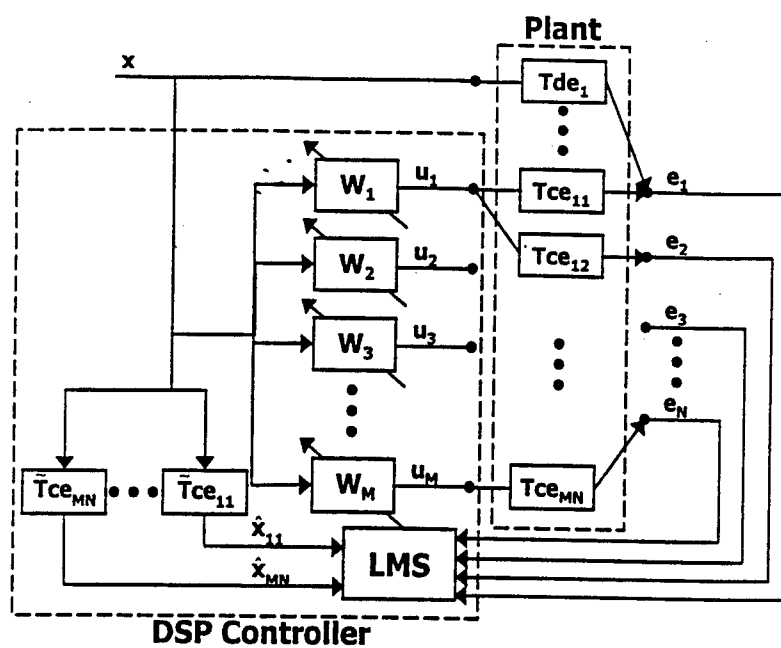


Figure 3

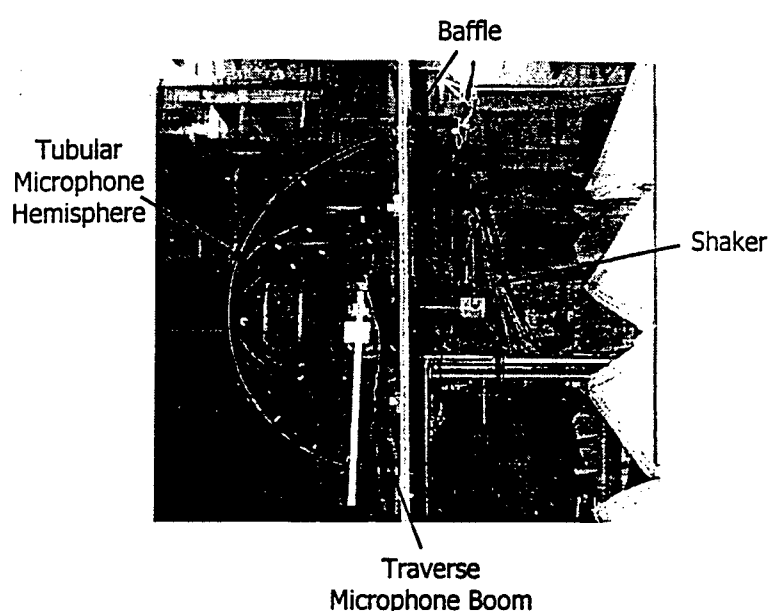


Figure 4

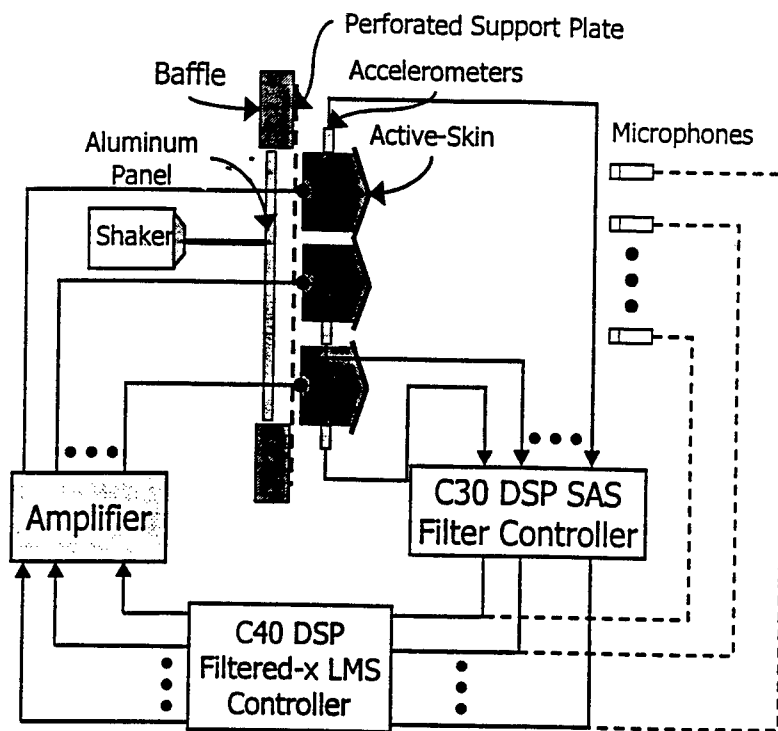


Figure 5

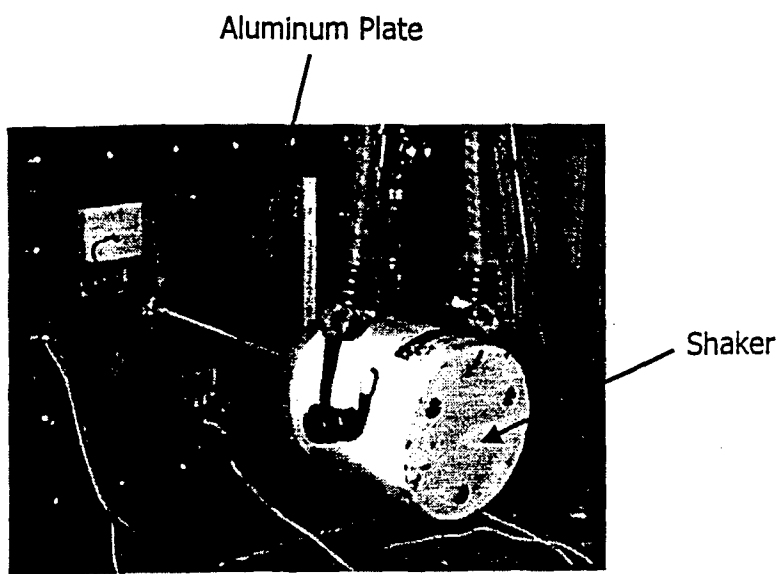


Figure 6

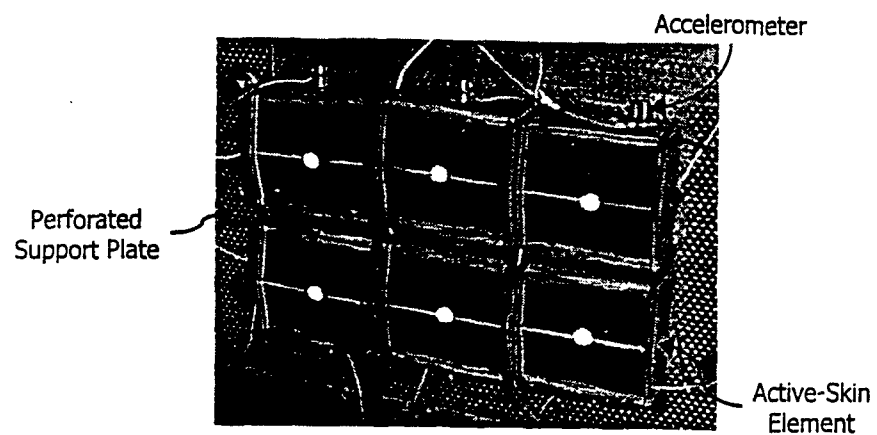


Figure 7

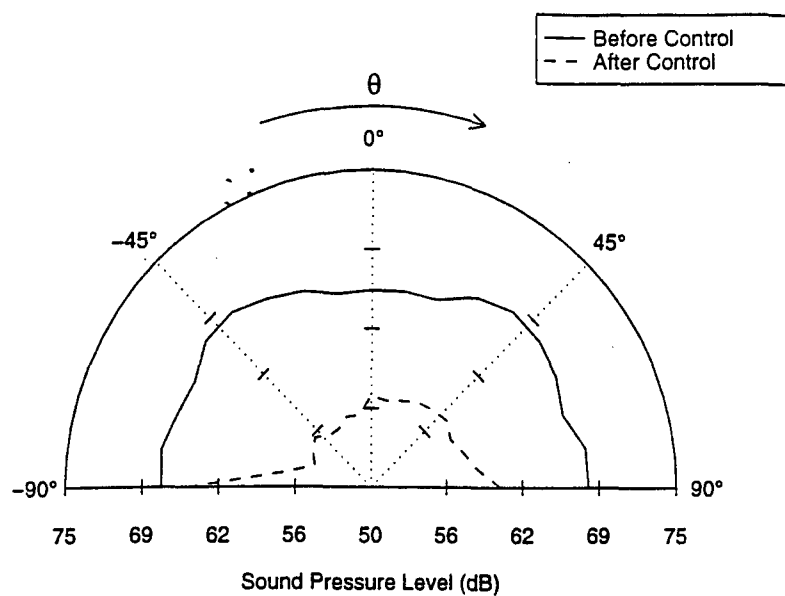


Figure 8

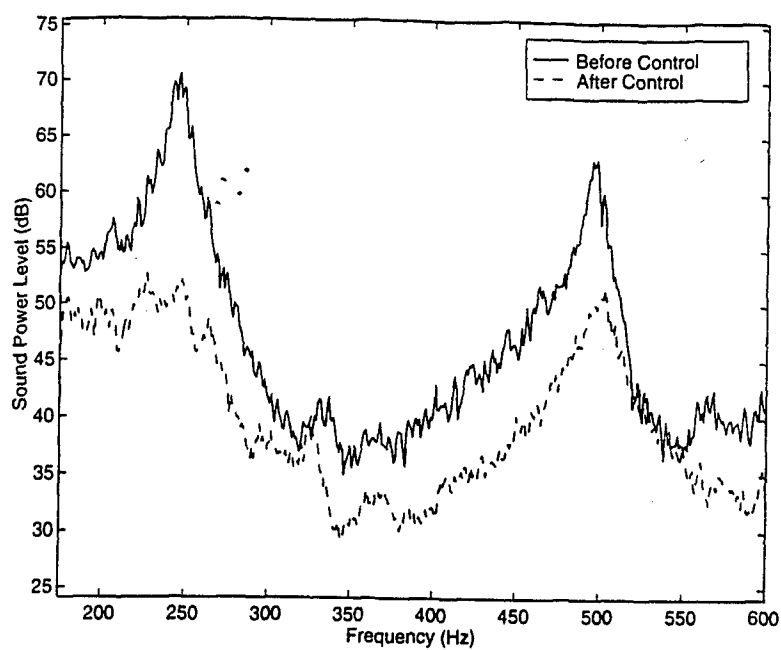


Figure 9

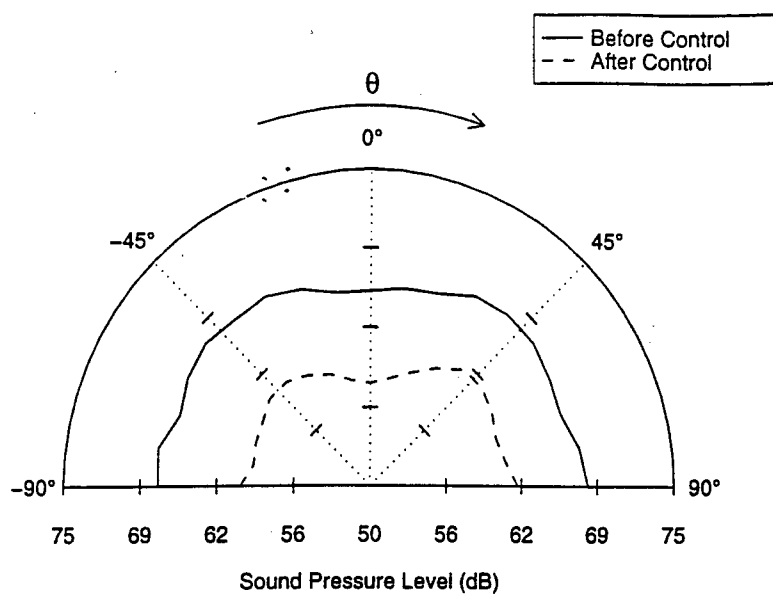


Figure 10

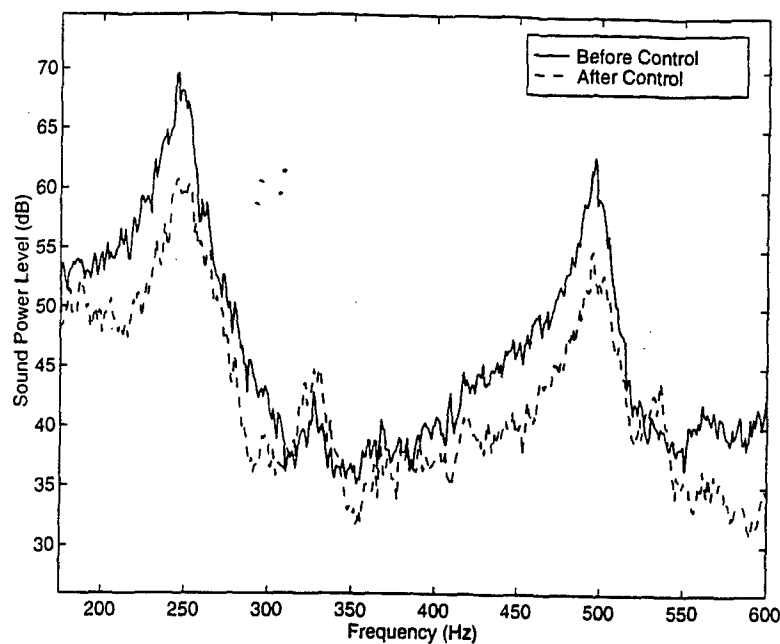


Figure 11

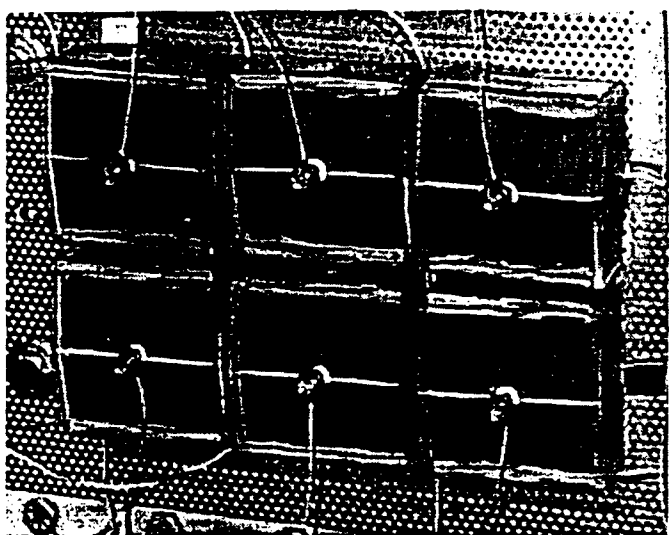


Figure 12

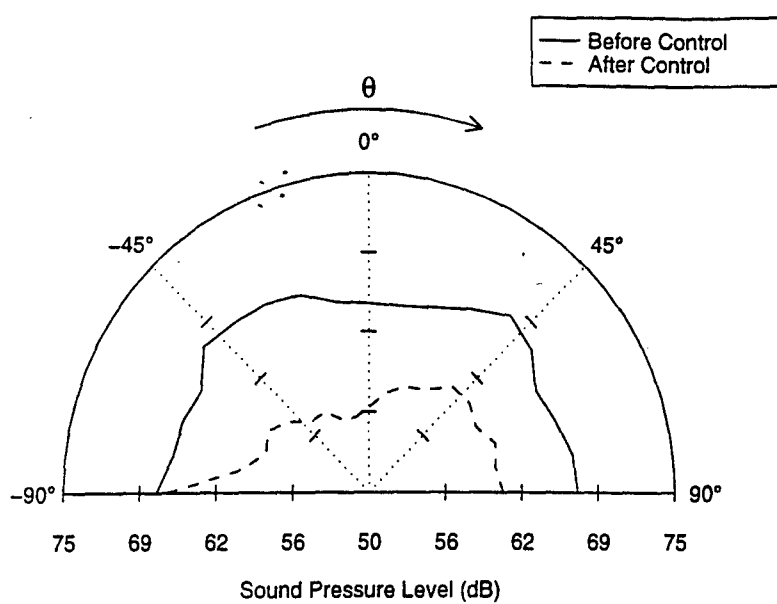


Figure 13

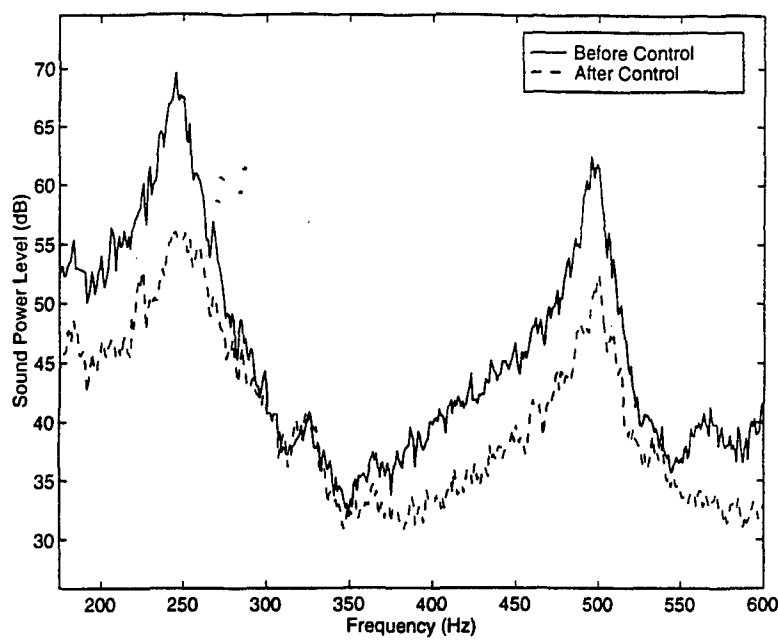


Figure 14

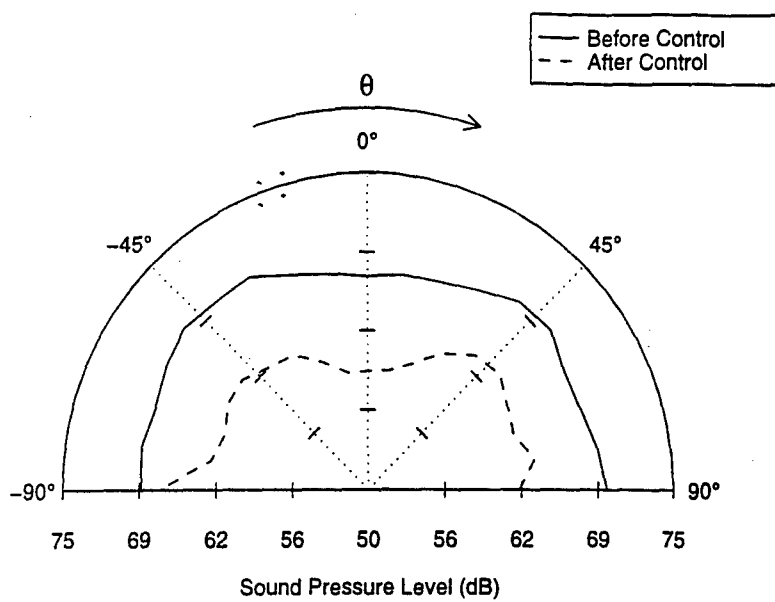


Figure 15

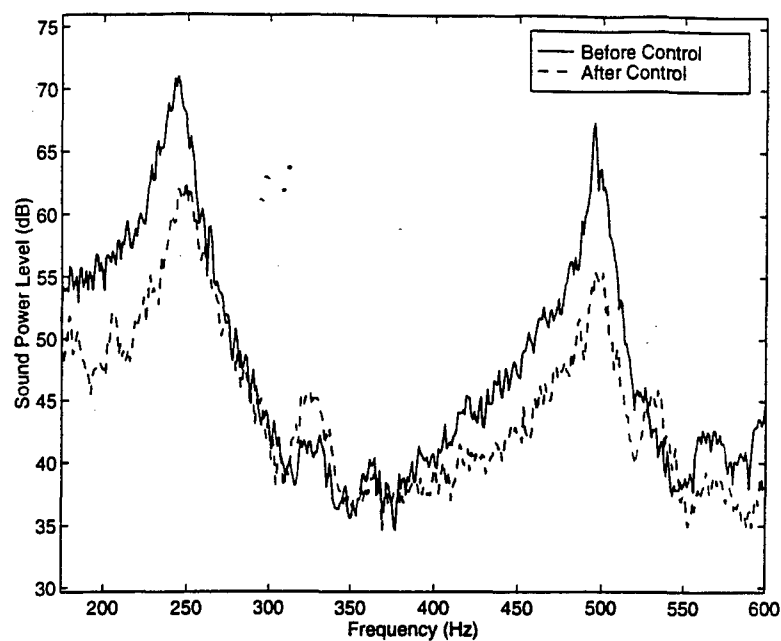


Figure 16

## **APPENDIX 28**

# NOISE-CON 97

The Pennsylvania State University  
University Park, Pennsylvania  
1997 June 15-17

## SIMULTANEOUS ACTIVE/PASSIVE CONTROL OF EXTENSIONAL AND FLEXURAL POWER FLOWS IN THIN BEAMS

F. L. Deneufve, C. Guigou and C. R. Fuller

Vibration and Acoustic Laboratories,  
Department of Mechanical Engineering  
Virginia Polytechnic Institute and State University  
Blacksburg, Virginia 24061-0238

### INTRODUCTION

Passive control techniques are the traditional methods of reducing structural vibrations and are mainly based on absorption and reflection of waves. They include vibration isolation using mass-spring systems and the addition of passive damping using viscoelastic materials. Dimensions or material changes, i.e., impedance changes, can also be used to achieve passive control of structure-borne vibrations. The addition of damping through a passive material discontinuity of high loss factor can considerably attenuate vibration amplitudes. Cremer et al. [1] developed a model of an infinite concrete beam with a finite length viscoelastic insert. They demonstrated that a 3 cm cork insert results in attenuation of both extensional and flexural wave amplitudes. A similar system is used for the passive approach considered in this paper. However, such passive approach usually implies a significant mass and/or length increase of the insert to achieve satisfactory results at low frequencies. Passive control techniques are therefore more effective in the high frequency range.

Active control approaches are complementary to passive control approaches since they are more suited to low frequency applications. This explains the increasing interest of combining passive and active control techniques to reduce structural vibrations [2]. The passive system usually applies the primary control action, while the active system is used to reinforce the action of the passive system or to overcome its limitations.

Fuller et al. [3] and Gibbs [4] recently studied the active control of extensional and flexural power flows in beams. First, they demonstrated that a single asymmetric piezoceramic element bonded on the surface of a thin beam simultaneously excites extensional and flexural waves. Then, they experimentally verified that two co-located independent actuators bonded on each side of the beam could generate any desired combination of extensional and flexural vibrations. They finally successfully achieved active control of extensional and flexural power flows in beams with two co-located independently driven piezoceramic actuators (i.e., one input per wave type).

This work investigates, both analytically and experimentally, the potential of a hybrid active/passive control technique to simultaneously attenuate the vibrational power flows due to extensional and flexural waves traveling along infinite or semi-infinite thin beams. The passive component consists of a passive stiff insert of high damping (such as PVC material) placed between

two identical beams. The active component consists of two co-located independently driven piezoceramic actuators. The combination of passive and active control methods is then studied for the actuators at three locations: upstream, downstream or on the passive insert. Analytical results are obtained for a broad range of harmonic excitation and presented in terms of extensional and flexural power flow attenuations and voltage control effort required by the control actuators. Results demonstrate the advantage of bonding the piezoceramic actuators on the passive insert. Indeed, this active/passive configuration has great potential for reducing both the flexural and extensional power flows as well as the voltage control effort. This is explained in terms of impedance matching between the piezoceramic actuators and the passive insert. Experimental results are presented and corroborate the analytical predictions.

## THEORETICAL DEVELOPMENTS

For the sake of brevity, details about the theoretical analysis are not presented; they can be found in [4,5]. The solutions of the equations of motion will be given in terms of propagating and decaying waves with positive waves travelling from right to left.

### Extensional Equation of Motion and Power Flow

The extensional displacement  $u(x,t)$  in a section of beam between two interfaces in  $x_1$  and  $x_2$  is expressed as follows

$$u(x,t) = (E_1 e^{-ik_e(x-x_1)} + F_1 e^{ik_e(x-x_2)}) e^{i\omega t} \quad (1)$$

where  $k_e$  is the extensional wavenumber,  $\omega$  is the angular frequency.  $E_1$  and  $F_1$  represent the complex amplitudes of the wave travelling in the  $x$  positive and negative direction respectively (see Figure 1(a)). The associated net extensional power flow in that finite section of beam is given by

$$P_e(\omega) = \frac{ESk_e\omega}{2} (|E_1|^2 - |F_1|^2) \quad (2)$$

where  $E$  and  $S$  are respectively the elasticity modulus and the cross-sectional area of the beam. Then, the net extensional power flow in a finite beam section is proportional to the difference of the squares of the positive and negative travelling wave magnitudes. Note that, for a semi-infinite section of beam, the negative travelling wave is zero (i.e.,  $F_1=0$ ).

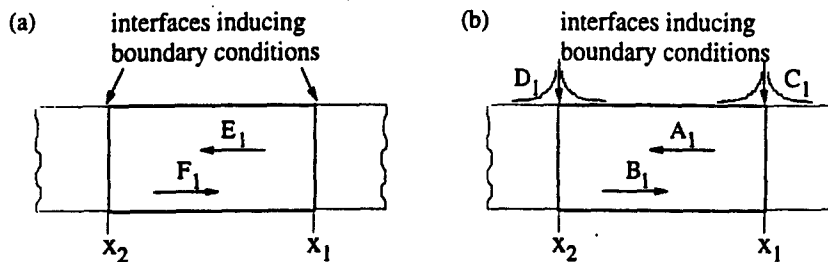


Figure 1: (a) Extensional and (b) flexural waves propagating in a finite section of beam.

### Flexural Equation of Motion and Power flow

Following Bernoulli-Euler's theory, the flexural or out-of-plane displacement  $w(x,t)$  in a finite section of beam between  $x_1$  and  $x_2$  is composed of four waves

$$w(x,t) = (A_1 e^{-ik_f(x-x_1)} + B_1 e^{ik_f(x-x_2)} + C_1 e^{-k_f(x-x_1)} + D_1 e^{k_f(x-x_2)}) e^{i\omega t} \quad (3)$$

where  $k_f$  is the flexural wavenumber.  $A_1$  and  $B_1$  represent the positive and negative travelling waves respectively, and  $C_1$  and  $D_1$  the positive and negative decaying waves respectively (see Figure 1(b)). The associated net flexural power flow is expressed as

$$P_f(\omega) = E I k_f^3 \omega \left( |A_1|^2 - |B_1|^2 - 2e^{k_f(x_1-x_2)} \operatorname{Im}(C_1 D_1^*) \right) \quad (4)$$

where  $I$  is the area moment of inertia, and the superscript '\*' refers to the complex conjugate. In Equation (4), the last term in brackets represents the flexural power flow associated with the near-field waves interaction. For a semi-infinite section of beam, the negative propagating and negative near-field waves are zero.

### Point Force Excitation

In order to excite both extensional and flexural motions, a point force  $F$  at an angle  $\theta=10^\circ$  with the neutral axis is applied to the beam at  $x=0$  (see Figure 2(a)). The point force  $F$  can be decomposed into in-plane force and normal forces. The normal component of the force ( $F \sin\theta$ ) is considered to drive the flexural waves while the in-plane component ( $F \cos\theta$ ) drives the extensional waves [6]. Varying the angle  $\theta$  allows variation of the relative amplitude of the resultant extensional and flexural disturbances.

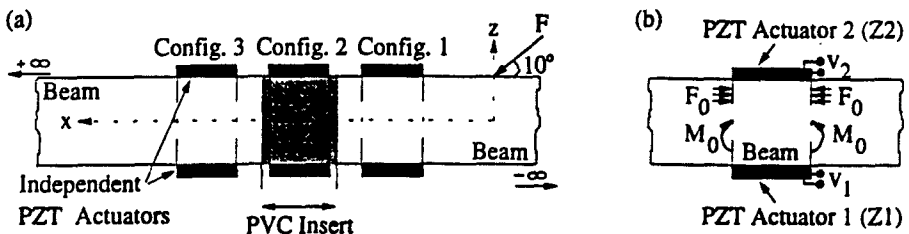


Figure 2: Schematic of (a) the 3 active/passive configurations and (b) the extensional and flexural loading induced by 2 co-located independent PZT actuators.

### Piezoceramic Actuator Excitation

Two co-located independent piezoceramic (PZT) actuators are used to simultaneously control extensional and flexural power flows [4]. Figure 2(b) presents the extensional and flexural loading induced by such actuators. The upper PZT (Z2) is assumed to be driven by a complex voltage  $v_2$ , and the lower PZT (Z1) by a complex voltage  $v_1$ . The stress induced by the two independent actuators is considered equivalent to two equal and opposite forces for extensional excitation and two equal and opposite moments for flexural excitation. The induced forces and moments can be expressed as

$$F_0 = \frac{ESK^e d_{31}}{T_a} (v_1 + v_2) = \frac{ESK^e d_{31}}{T_a} v_e \quad (5)$$

$$M_0 = \frac{EIK^f d_{31}}{T_a} (v_1 - v_2) = \frac{EIK^f d_{31}}{T_a} v_f \quad (6)$$

where  $K^e$  and  $K^f$  are defined in [4], and  $d_{31}$  and  $T_a$  represent respectively the strain sensitivity and the thickness of the PZT actuator. In Equations (5) and (6),  $v_e$  and  $v_f$  are the complex voltage required to minimize the extensional and flexural power flows respectively. Throughout this paper,  $v_1$  and  $v_2$  are the applied voltages, while  $v_e$  and  $v_f$  are the control voltages. The energy required by the PZT actuators to minimize both the extensional and the flexural power flows is investigated in terms of the voltage control effort  $V_{\text{eff}}$  defined as

$$V_{\text{eff}} = \sqrt{|V_1|^2 + |V_2|^2} \quad (7)$$

## ANALYTICAL RESULTS AND DISCUSSIONS

### Description of the Analytical Systems

Passive control obtained using a stiff material insert of high damping, and active control achieved with two co-located independent PZT actuators are combined in order to minimize the total (i.e., extensional and flexural) power flow. The beam system is considered to be infinite. Indeed, the passive insert is located between two identical semi-infinite beams as depicted in Figure 2(a). The beams are considered made of aluminum with characteristics given in Table I. The passive insert is made of PVC material characterized by a high loss factor. Its characteristics [7,8] are also presented in Table I. The length of the insert primarily dictates the amount of passive attenuation obtained. A length of 5 cm was chosen since it could be experimentally implemented. The active control actuators are G-1195 piezoceramic patches, which properties are in Table I.

Table I. Mechanical properties and dimensions of system components.

	Beams	PZT Actuator	PVC Insert
Density ( $\text{kg/m}^3$ )	2700	7650	1370
Young Modulus ( $\text{N/m}^2$ )	$7.1 \times 10^{10}$	$6.3 \times 10^{10}$	$0.25 \times 10^{10}$
Loss Factor	0	0.1%	1
Poisson Ratio	0.33	0.28	0.33
Thickness (m)	$3.2 \times 10^{-3}$	$0.178 \times 10^{-3}$	$3.2 \times 10^{-3}$
Width (m)	$76 \times 10^{-3}$	$63.5 \times 10^{-3}$	$76 \times 10^{-3}$
Length (m)		$38.1 \times 10^{-3}$	$50.8 \times 10^{-3}$
Strain Sensitivity (m/V)		$166 \times 10^{-12}$	

Three configurations of active/passive control systems are investigated as shown in Figure 2(a). The PZT actuators are located upstream of the passive insert for Configuration 1. In Configuration 2, the actuators are directly bonded on the PVC insert. The actuators are symmetrically located with respect to the center of the passive insert. Configuration 3 corresponds to the actuators placed downstream of the passive insert. The disturbance point force has a constant magnitude  $F$  equal to 1 N, applied at the angle of  $10^\circ$  with the beam neutral axis. That angle was chosen since it results in induced extensional and flexural power flows of approximately equivalent magnitude.

### Analytical Control Procedure

In this study, the cost function to be minimized is the total power flow transmitted downstream of the active/passive control location. Note that the total power flow is equal to the nett power flow since that beam section is semi-infinite (i.e., the reflected waves in the x-negative direction are zero). It can be written as (using Equations (2) and (4) for a semi-infinite beam)

$$P_t = P_e + P_f = \frac{ESk_e\omega}{2} |E_1|^2 + EIk_i^3\omega |A_1|^2 \quad (8)$$

Equation (8) can be shown to be a quadratic function of the actuator applied voltages  $v_1$  and  $v_2$ , which has a unique minimum [5]. Indeed, minimizing the cost function as defined by Equation (8) results in driving both travelling waves  $E_1$  (extensional) and  $A_1$  (flexural) to zero. Then, for the

three active/passive configurations, the analytical control procedure involves (i) expressing the flexural and extensional displacements downstream of the insert in terms of the applied voltages, (ii) setting the corresponding extensional and flexural positive travelling waves to zero, and (iii) solving for the unique applied voltages  $v_e$  and  $v_f$ .

### Analytical Results and Discussion

Upon minimizing the cost function as defined previously, the control effort  $V_{eff}$ , and control voltages  $v_e$  and  $v_f$  are determined for each active/passive configuration. Figure 3(a) presents the control effort for the three active/passive configurations. Configurations 1 and 3 require about the same control effort  $V_{eff}$  to minimize the cost function. A significant reduction in the required control effort is achieved, over the entire frequency range, for Configuration 2, i.e., when the actuators are bonded to the passive insert. Since this configuration requires less energy to drive the PZT actuators, it is more effective than the other two (1 and 3). To investigate this result, the control voltages  $v_e$  and  $v_f$  are presented in Figure 3(b-c). Indeed, Configurations 1 and 3 correspond to about the same control voltage  $v_e$ . However, using Configuration 2, the control voltage  $v_e$  (see Figure 3(c)) appears to be much smaller, for all three configurations, than the control voltage  $v_e$ . This is due to the fact that beams are much stiffer in extension than flexure. The three configurations result in approximately the same amount of energy required to cancel the flexural power flow (see Figure 3(c)). Thus, the low control effort obtained for Configuration 2 is related to the low control voltage  $v_e$  required by the PZT actuators when located on the passive insert. Configuration 2 is then the optimal active/passive configuration.

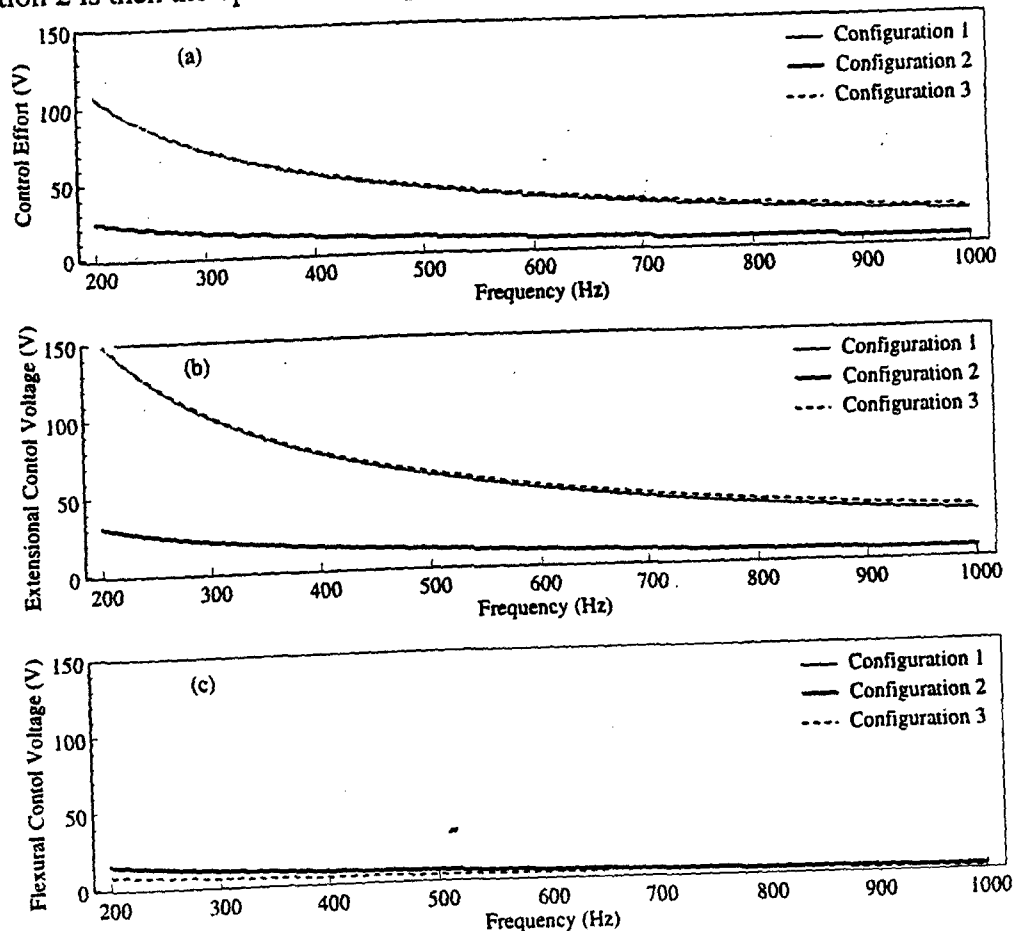


Figure 3: (a) Control effort  $V_{eff}$ , (b) extensional  $v_e$  and (c) flexural  $v_f$  control voltage.

The ability of an actuator to transfer power to its host structure at any frequency depends on the mechanical impedances of the actuator and the structure. Indeed, an actuator provides the maximum input power when the structural mechanical impedance matches the actuator mechanical impedance. The control effort required by that actuator is minimized when the power transferred from an actuator to a structure is maximized. The actuator's mechanical impedance and the structure impedances for the aluminum and PVC beams are calculated according to [9]. The mechanical impedance  $Z_a$  of two co-located identical PZT actuators is defined as the ratio of the actuation force to the velocity, i.e.,

$$Z_a = 2i \frac{-K_a(1+i\eta_a)}{\omega} \frac{k_a L_a}{\tan(k_a L_a)} \quad (9)$$

where  $K_a$  and  $k_a$  are respectively the static stiffness (given by  $E_a w_a T_a / L_a$ ) and the extensional wavenumber of the piezoceramic. The actuators located on the beam between  $x_1$  and  $x_2$  result in forces and moments applied at the actuator ends. The extensional beam mechanical impedance  $Z_e$  is expressed as the ratio of the actuators induced force to the difference of the in-plane velocities at the actuator ends, i.e.,

$$Z_e = \frac{F_0}{v_u(x_2) - v_u(x_1)} \quad (10)$$

The flexural beam mechanical impedance  $Z_f$  is proportional to the ratio of the actuators induced moment to the difference of the angular velocities at the actuator ends, i.e.,

$$Z_f = \frac{2}{(2h + T_a)^2} \frac{M_0}{\Theta_w(x_2) - \Theta_w(x_1)} \quad (11)$$

For more detail about the actuators and beam mechanical impedances, see reference [5]. The PZT actuators, aluminum beam and PVC beam mechanical impedance magnitudes are compared in Figure 4, for the structure in extension and flexure. Note that for the beam in extension, the impedance of the actuators is much closer to the PVC beam impedance than the aluminum beam impedance (see Figure 4(a)). On the other hand, for the beam in bending, the actuators impedance is found to be slightly closer to the aluminum beam impedance (see Figure 4(b)). This demonstrates that for extensional motion, considerably better impedance matching exists between the PZT actuators and the PVC material than between the PZT actuators and the aluminum material. This is the reason why the control voltage  $v_e$  and the control effort are low when the PZT actuators are bonded to the PVC insert (Configuration 2).

## EXPERIMENTAL SYSTEMS, RESULTS AND DISCUSSIONS

### Experimental Setup

A schematic of the experimental arrangement is presented in Figure 5. The thin beams are again made of aluminum and each is 2.4 m long, 76 mm wide and 3.2 mm thick. The PVC insert located between the two aluminum beams has the same properties and dimensions as in the analytical study (see Table I). The beam structure is fitted at the left end with an anechoic termination, which consists of a diverging pyramid shaped box filled with sand. This termination was tested to have a flexural power reflection coefficient less than 0.1 for frequencies greater than 200 Hz. Thus, above 200 Hz, the termination is anechoic for flexural waves simulating a semi-infinite beam structure. However, the termination was not found to be anechoic for extensional waves due to their long wavelengths. The disturbance was generated by a 25 lb. shaker mounted at the free end of the beam with a 10° angle. The point force had to be applied at the free end of the

beam in order to have such a small angle. Three sets of two co-located actuators were bonded to the system at 10 cm before the insert ( $Z_1$  and  $Z_2$  for Config.1), in the center of the insert ( $Z_3$  and  $Z_4$  for Config.2), and at 10 cm after the insert ( $Z_5$  and  $Z_6$  for Config.3). The beam is also equipped with a total of 6 PVDF sensors that are used with a digital filter network in order to provide real time estimates of the positive and negative extensional and flexural travelling waves in the beam. This method of real time narrowband and broadband estimation of extensional and flexural power flows from 6 independent PVDF strain measurements was developed by Gibbs [4], and is briefly discussed in the following section.

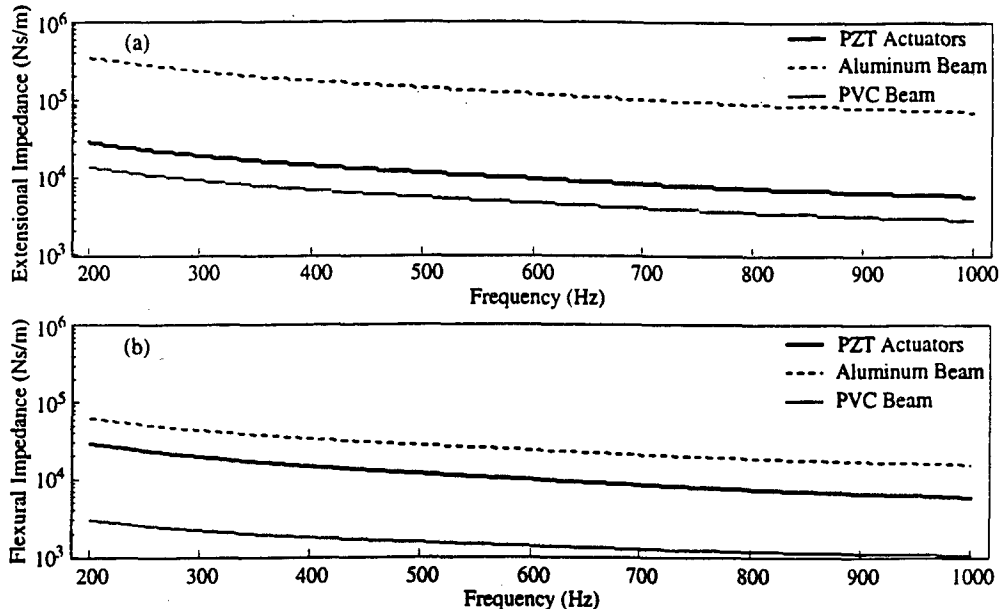


Figure 4: Mechanical impedance for system in (a) extension and (b) flexure.

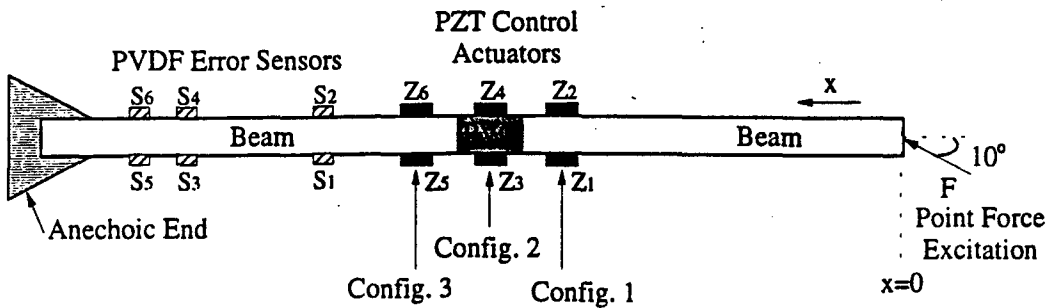


Figure 5: Schematic of the experimental arrangement.

### Experimental Control Procedure

A block diagram of the adaptive control system used in this experiment is shown in Figure 6. The active control was experimentally implemented using a Filtered-x LMS algorithm [10]. This algorithm has been modified using the extensional and flexural wave filters [4]. Sensors S1 and S2, as well as sensors S5 and S6, are summed to provide a response proportional to the extensional motion only, which is then passed through the extensional wave filter to provide information about the propagating waves  $E_1$  and  $F_1$ . Similarly, sensors S3 and S4, as well as sensors S5 and S6, are subtracted to provide a response proportional to the flexural motion only, which is then passed through the flexural wave filter to provide information about the propagating waves  $A_1$  and  $B_1$ . Such a wave vector filtering network results in good estimate of the positive and negative extensional and flexural travelling waves in the region of the beam downstream of the passive insert [4]. The estimated positive extensional and flexural travelling waves ( $E_1$  and  $A_1$ ) are the error

signals for the filtered-x LMS algorithm. Similarly to the analytical control procedure, the experimental control algorithm consists of minimizing both the extensional and flexural waves travelling towards the anechoic termination (the reflected waves should be minimized as a result). The magnitude of the different waves ( $E_1$ ,  $F_1$ ,  $A_1$  and  $B_1$ ) was measured before and after control was implemented and then the resulting nett extensional power flow was calculated as

$$P_e = \frac{ESk_e \omega}{2} (|E_1|^2 - |F_1|^2) \quad (12)$$

while the resulting nett flexural power flow was determined as

$$P_f = EI k_f^3 \omega (|A_1|^2 - |B_1|^2) \quad (13)$$

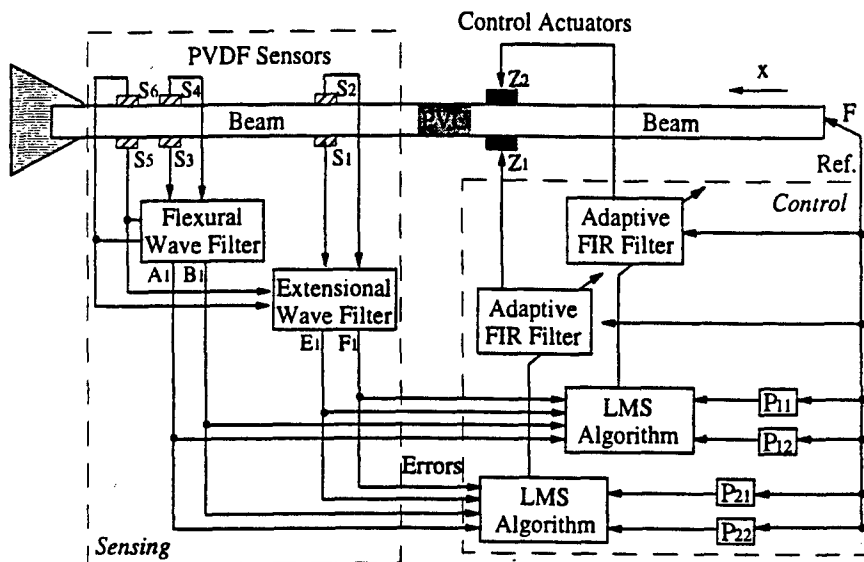


Figure 6: Block diagram of adaptive control system with wave vector filters.

### Experimental Results and Discussion

Control was implemented for five different frequencies of excitation, 440 Hz, 580 Hz, 680 Hz, 790 Hz and 900 Hz. The associated results are presented in Figures 7 to 11 for each control actuators configuration, in terms of the achieved nett extensional and flexural power flow attenuation and the control effort as well as the extensional ( $v_e$ ) and flexural ( $v_f$ ) voltages necessary to drive the control actuators. First, it can be seen that Config. 2 (PZT actuators on passive PVC insert) led to the largest extensional power flow reduction. The three configurations resulted in important attenuation of the flexural power flow. Note the attenuation of extensional power flow is lower than that of the flexural one. As expected from the analytical study, for each of the excitation frequencies, the control effort associated with Config. 2 is the lowest and in general less than half that associated with Config. 1 and 3. The control effort for Config. 1 and 3 is for most cases of the same level. The results also show that, even though the flexural power flow is the most reduced, the flexural control voltage is much smaller than the extensional one. Indeed, the extensional control voltage is very high for Config. 1 and 3, which yielded the low extensional power flow reduction. On the other hand, extensional control voltage corresponding to Config. 2 is very low and much smaller than that for Config. 1 and 3. This is the reason why Config. 2 is the most effective configuration (lowest control effort and largest power flow attenuation). Thus, these preliminary experimental results corroborate very well the analytical prediction. Indeed, bonding the control actuators to the passive PVC insert provide the most compact and the most effective active/passive system.

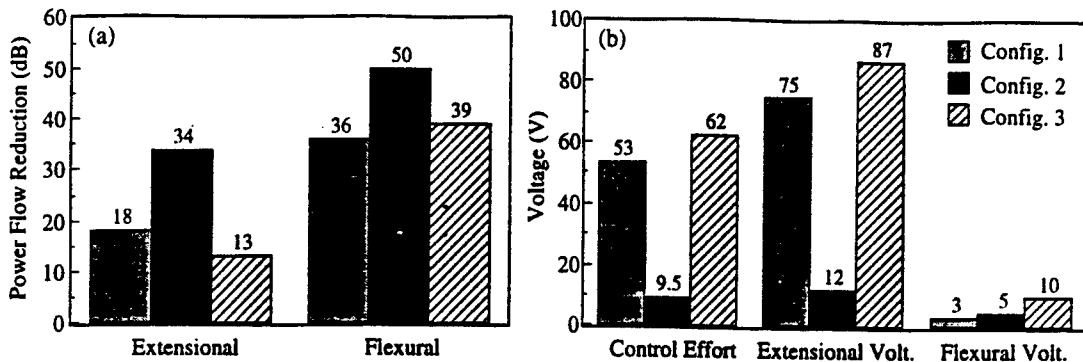


Figure 8: Control Results at 440 Hz; (a) power flow reduction and (b) control voltages.

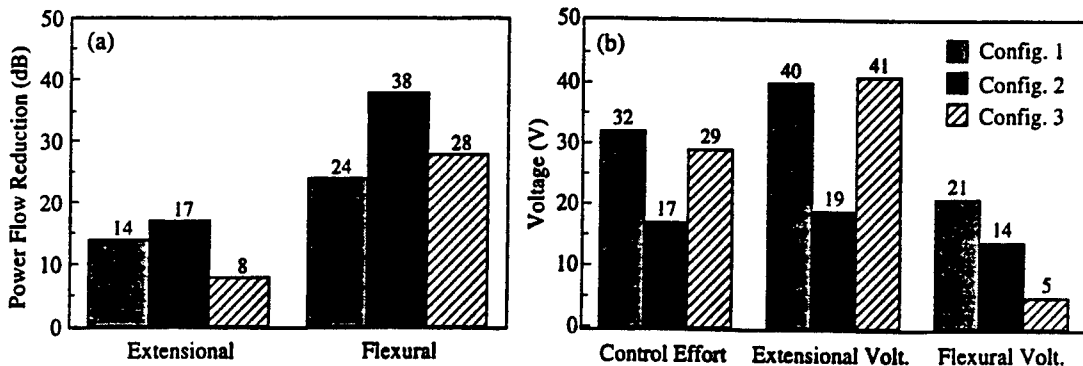


Figure 9: Control Results at 580 Hz; (a) power flow reduction and (b) control voltages.

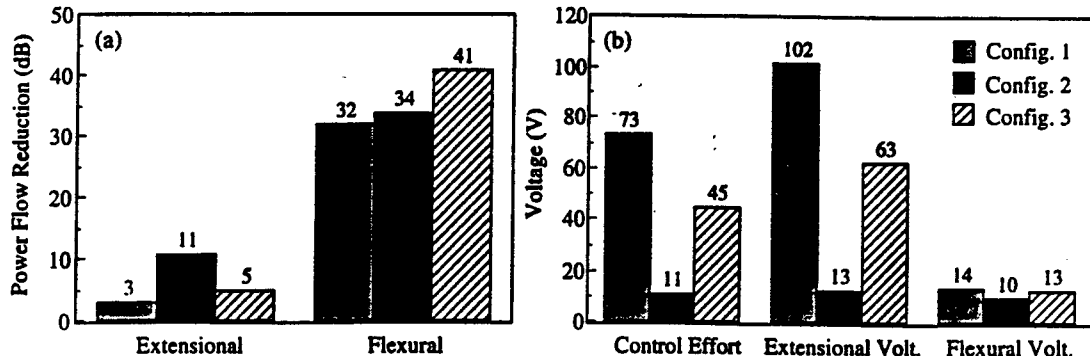


Figure 10: Control Results at 680 Hz; (a) power flow reduction and (b) control voltages.

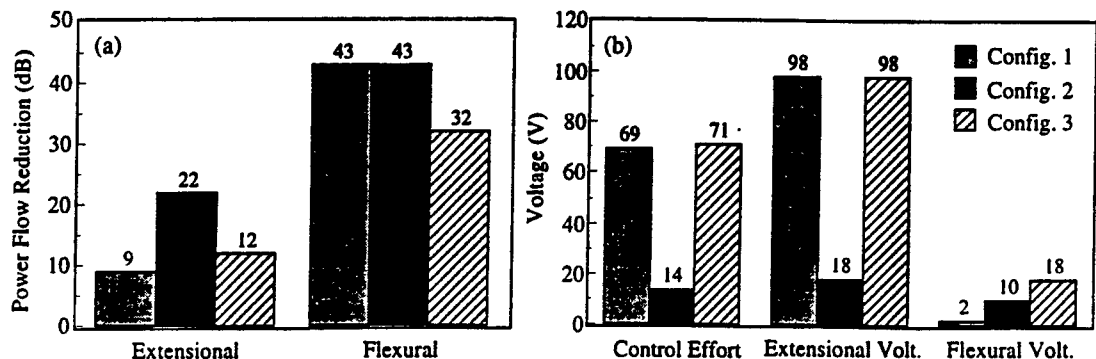


Figure 11: Control Results at 790 Hz; (a) power flow reduction and (b) control voltages.

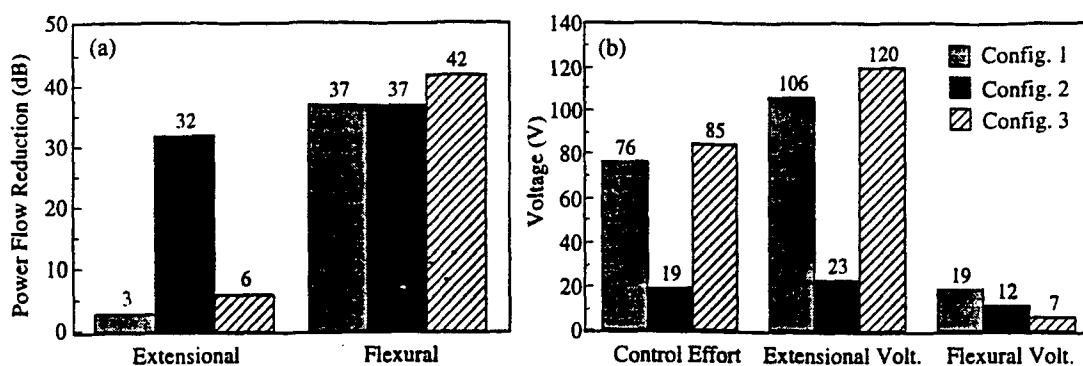


Figure 12: Control Results at 900 Hz; (a) power flow reduction and (b) control voltages.

## SUMMARY AND CONCLUSIONS

Passive and active control methods were combined to attenuate both extensional and flexural power flow in beams. The passive element consist of a stiff insert with high damping (PVC) while the active component is provided by co-located independent PZT actuators. The objective was to find the optimal active/passive configuration, with respect to minimum voltage control effort. Three different active/passive configurations were studied. Configuration 1 had the PZT actuators upstream of the passive insert, Configuration 2 consisted of the actuators directly bonded to the insert, and Configuration 3 located the actuators downstream of the insert. For both analytical and experimental systems, the most effective active/passive combination (lower control effort for largest power flow attenuation) was obtained when the actuators were bonded directly to the passive insert. The low control effort associated with this configuration was related to the low control voltage required to minimize the extensional power flow. Indeed, it was found that for extensional motion, better impedance matching exists between the PZT actuators and the PVC material than between the actuators and the aluminum material. Therefore, bonding the control actuators to the passive PVC insert provide the most compact and the most effective active/passive system. Further work will involve measuring the flexural and extensional displacement along the beam with a laser vibrometer as well as investigating control for broadband excitation.

The authors gratefully acknowledge the support of this work by the Office of Naval Research under the Grant ONR N00014-92-J-470, Dr. Kam Ng Technical Monitor.

## REFERENCES

- [1] L. Cremer, M. Heckl, and E. E. Ungar, *Structure-Borne Sound: Structural Vibrations and Sound Radiation*, Springer Verlag, Berlin, 1973.
- [2] K. W. Ng, "Applications of Active Control", The 1995 International Symposium on Active Control of Sound and Vibration, Active 95, Newport Beach, CA, 1995.
- [3] C. R. Fuller, G. P. Gibbs, and R. J. Silcox, "Simultaneous Active Control of Flexural and Extensional Power Flows in Beams", *Journal of Intelligent Materials Systems and Structures*, 1(2), 235-247, 1989.
- [4] G. Gibbs, "Simultaneous Active Control of Flexural and Extensional Power Flow in Thin Beams", Ph.D. Dissertation, Virginia Polytechnic Institute and State University, 1993.
- [5] F. L. Deneufve, "Simultaneous Active/Passive Control of Extensional and Flexural Power Flows in Infinite Thin Beams", Ms. Thesis, Virginia Polytechnic Institute and State University, 1996.
- [6] J. Pan and C. H. Hansen, "Active Control of Total Power Flow Along a Beam", *Proceedings of the International Congress on Recent Developments in Air and Structure-Borne Sound and Vibration*, Auburn University, AL, 1990.
- [7] L. I. Nass, *Encyclopedia of PVC (2nd Edition V. 1, V. 2 and V. 3)*, M. Dekker, Inc., New York, 1986.
- [8] B. J. Lazan, *Damping of Materials and Members in Structural Mechanics*, Pergamon Press, New York, 1968.
- [9] C. Liang, F. P. Sun, and C. A. Rogers, "An Impedance Method for Dynamic Analysis of Active Material Systems", *34th AIAA Structures, Structural Dynamics and Materials Conference*, La Jolla, CA, 3587-3599, 1993.
- [10] S. J. Elliot, I. M. Strothers, and P. A. Nelson, "A Multiple Error LMS Algorithm and its Application to the Active Control of Sound and Vibration", *IEEE Transaction on Acoustic Speech and Signal Processing*, ASSP-35, 1, 1423-1434, 1987.

## **APPENDIX 29**

Submitted to the J. Acoust. Soc. Am. (1997)

**SIMULTANEOUS ACTIVE/PASSIVE CONTROL OF EXTENSIONAL  
AND FLEXURAL POWER FLOWS IN THIN BEAMS**

F. L. Deneufve

C. Guigou

C. R. Fuller

Vibration and Acoustic Laboratories

Department of Mechanical Engineering

Virginia Polytechnic Institute and State University

Blacksburg, Virginia 24061-0238

Received

## **ABSTRACT**

Passive control techniques can be used to minimize structural vibrations but are limited with respect to the amount of attenuation obtained, especially in the low frequency region. Active control methods are very effective for reducing structural vibrations, especially at low frequencies, but may require adding significant amount of energy (to drive the control sources). The complementary nature of passive and active control methods is a natural approach and their combination has been of increasing interest in the last few years. This work investigates the potential of a hybrid active/passive control technique to simultaneously attenuate the vibrational power flows due to extensional and flexural waves traveling along infinite or semi-infinite thin beams. The passive component consists of a passive insert of high damping (such as PVC material) placed between two identical long thin beam sections. The active component consists of two co-located independently driven piezoceramic actuators. The combination of passive and active control methods is then studied for the actuators in three locations: upstream, downstream or on the passive insert. Analytical results are obtained for a wide range of harmonic excitation and presented in terms of extensional and flexural power flow attenuations and voltage control effort required by the actuators. An experimental setup was implemented to verify the analytical predictions. Analytical and experimental results both demonstrate the advantage of bonding the actuators on the passive insert. Indeed, this active/passive configuration has great potential for reducing both the flexural and extensional power flows as well as the voltage control effort. This effect is explained in terms of impedance matching between the piezoceramic actuators and the passive insert.

PACS numbers: 43.40.Vn, 43.40.Tm

## I. INTRODUCTION

Many mechanical structures are equipped with beams as the primary elements of support. These beams can be subjected to forces which produce structure-borne vibrational waves propagating along them. It is then essential to control these unwanted vibrations in order to guarantee the reliability and acceptance of these systems. Two kinds of control approaches are then possible, passive control approaches and active control techniques.

Passive control techniques are the traditional methods of reducing structural vibrations and are mainly based on absorption and reflection of waves. A first type of passive control method consists of barriers, mufflers, and enclosures, which are relatively well established techniques [1,2]. A second type of passive control approach includes vibration isolation using mass-spring systems and the addition of passive damping using viscoelastic materials. Structure-borne vibrations can also be passively controlled by introducing dimensions or material changes in the vibrating structure (i.e. impedance changes) [3]. The addition of damping through a passive material discontinuity of high loss factor can considerably attenuate vibration amplitudes. Cremer et al. [3] developed a model of an infinite concrete beam with a viscoelastic interlayer of finite length. They demonstrated that a 3 cm cork interlayer results in attenuation of both extensional and flexural wave amplitudes. A similar model will be used for the passive approach considered in this paper. However, passive control techniques usually imply a significant mass increase to achieve satisfactory results at low frequencies. Passive control techniques are therefore more effective in the high frequency range.

Active control approaches are complementary to passive control approaches since they are more suited to low frequency applications. This explains the increasing interest of combining

passive and active control techniques to reduce structural vibrations. Essentially two types of active/passive control systems exist: adaptive/passive techniques and active/passive hybrid techniques [4]. The adaptive/passive systems are mainly passive mechanisms whose performance is optimized by adaptations or changes of the passive system properties. The active/passive hybrid systems combine both active and passive elements in series or parallel. The passive system usually applies the primary control action, while the active system is used to reinforce the action of the passive system or to overcome its limitations [4]. The use of active/passive hybrid systems started with an experimental investigation by Guicking et al. in 1984 [5].

Many authors investigated the wave control approach considering the minimization of power flow (i.e. travelling energy) in beams. Redman-White et al. [6] investigated an active system to experimentally control the flexural power flow in an infinite beam. Also, Gonidou and Fuller [7] demonstrated that active forces applied to beam-like structures could attenuate the flexural power flow. In these previous studies, active control of vibrations was achieved considering only flexural waves travelling along the beam. Cremer et al [3] showed that three wave forms known as extensional, flexural and torsional can propagate vibrational energy and are coupled at discontinuity points. Thus, all wave forms should be considered in vibrating structures with structural junctions and discontinuities. Fuller et al. [8] and Gibbs [9] recently studied the simultaneous active control of extensional and flexural power flows in beams. They demonstrated that extensional and flexural power flows leaving finite beams through the boundaries could be efficiently controlled using one control input per wave type.

The development and implementation of smart materials such as piezoelectric actuators and PVDF sensors has made active vibration control possible. Many studies have been pursued

concerning excitation and control of vibrations in beams using piezoceramic actuators. Fanson and Chen [10] demonstrated that driving two co-located actuators with the same complex voltage but  $180^\circ$  out-of-phase signal, results in a forcing function equivalent to two equal and opposite induced moments in the beam. Crawley and de Luis [11] showed that the induced moments generated by the actuators can be assumed to be located at the ends of the actuators. Also, Crawley and Anderson [12] established that two co-located actuators driven in-phase with the same amplitude of voltage result in two equal and opposite in-plane forces located at the ends of the actuators. Recently, Fuller et al. [8] demonstrated that a single asymmetric piezoelectric element bonded on the surface of a thin beam simultaneously excites extensional and flexural waves. Subsequently, they experimentally showed that two co-located independent actuators bonded on each side of the beam can create and control any combination of extensional and flexural vibrations.

This work investigates, both analytically and experimentally, the potential of a hybrid active/passive control technique to simultaneously attenuate the vibrational power flows due to extensional and flexural waves traveling along infinite or semi-infinite thin beams. The passive component consists of a passive insert of high damping (such as PVC material) placed between two identical beams. Note that such passive insert is relatively stiff but not as much as the beam. The active component consists of two co-located independently driven piezoceramic actuators. The combination of passive and active control methods is then studied for the actuators at three locations: upstream, downstream or on the passive insert. Analytical results are obtained for a wide range of harmonic excitation and presented in terms of extensional and flexural power flow attenuations and voltage control effort required by the control actuators. Results demonstrate the advantage of bonding the piezoceramic actuators on the passive insert. Indeed, this active/passive

configuration has great potential for reducing both the flexural and extensional power flows as well as the voltage control effort. This is explained in terms of impedance matching between the piezoceramic actuators and the passive insert. Experimental results are presented and corroborate the analytical predictions.

## II. THEORETICAL DEVELOPMENTS

Most of the following derivations have been based upon fundamental vibration theories developed by Cremer et al. [3], Meirovitch [13], and Junger and Feit [14]. The solutions of the equations of motion will be given in terms of propagating and decaying waves with positive waves travelling from right to left, corresponding to the experimental setup.

### A. Extensional Equation of Motion and Power Flow

The extensional or longitudinal displacement  $u(x,t)$  in a section of beam between two interfaces in  $x_1$  and  $x_2$  is expressed as follows [3]

$$u(x,t) = (E_1 e^{-ik_e(x-x_1)} + F_1 e^{ik_e(x-x_2)}) e^{i\omega t} \quad (1)$$

where  $k_e$  is the extensional wavenumber and  $\omega$  is the angular frequency.  $E_1$  and  $F_1$  are the complex magnitudes of the waves travelling in the  $x$  positive and negative direction respectively (see Figure 1(a)). The associated net extensional power flow in that finite section of beam is then determined as [15]

$$P_e(\omega) = \frac{ESk_e\omega}{2} (|E_1|^2 - |F_1|^2) \quad (2)$$

where  $E$  and  $S$  are respectively the elasticity modulus and the cross-sectional area of the beam. Then, the net extensional power flow in a finite beam section is proportional to the difference of the squares of the positive and negative travelling wave magnitudes. Note that, for a semi-infinite section of beam, the negative travelling wave is zero (i.e.  $F_1=0$ ).

## B. Flexural Equation of Motion and Power flow

Following Bernouilli-Euler's theory, the flexural or out-of-plane displacement  $w(x,t)$  in a finite section of beam between  $x_1$  and  $x_2$  is composed of four waves and can be written as [3]

$$w(x,t) = (A_1 e^{-ik_f(x-x_1)} + B_1 e^{ik_f(x-x_2)} + C_1 e^{-k_f(x-x_1)} + D_1 e^{k_f(x-x_2)}) e^{i\omega t} \quad (3)$$

where  $k_f$  is the flexural wavenumber.  $A_1$  and  $B_1$  are the complex magnitudes of the positive and negative travelling waves respectively, and  $C_1$  and  $D_1$  are the complex magnitudes of the positive and negative decaying waves respectively (see Figure 1(b)). The associated net flexural power flow in that finite section of beam is expressed as [15]

$$P_f(\omega) = EI k_f^3 \omega \left( |A_1|^2 - |B_1|^2 - 2e^{k_f(x_1-x_2)} \text{Im}(C_1 D_1^*) \right) \quad (4)$$

where  $I$  is the area moment of inertia, and the superscript '\*' refers to the complex conjugate. The net flexural power flow is proportional to the positive and negative travelling waves, and to the complex product of the positive and negative near-field waves (or near-field interaction). Note that when  $C_1$  and  $D_1$  are in-phase or  $180^\circ$  out-of-phase, the imaginary term is equal to zero. For a semi-infinite section of beam, the negative propagating and near-field waves do not exist. More detailed discussion can be found in [16].

## C. Point Force Excitation

The vibrational responses to be minimized are those associated with the power flows induced by a point force excitation. In order to excite both extensional and flexural motions, a point force  $F$  is applied at the origin of the beam at an angle  $\theta=10^\circ$  with the neutral axis (see Figure 2(a)). The point force  $F$  can be decomposed into an in-plane and normal forces. The normal component of the force ( $F \sin\theta$ ) is considered to drive the flexural waves while the in-plane component ( $F \cos\theta$ )

drives the extensional waves [17]. Varying the angle  $\theta$  allows variation of the relative amplitude of the resultant extensional and flexural disturbances. Away from the point force excitation, the extensional and flexural waves are assumed to travel uncoupled, which is a reasonable assumption for a thin beam characterized by a width to thickness ratio of at least ten [9].

#### D. Piezoelectric Excitation

To simultaneously control extensional and flexural power flows requires the ability to precisely induce extensional and flexural motions at different ratios using piezoelectric actuators. Figure 2(b) presents the extensional and flexural loading induced by two co-located independently driven PZT actuators, based upon the work by Gibbs [9]. The upper PZT (Z2) is assumed to be driven by a complex voltage  $v_2$ , and the lower PZT (Z1) by a complex voltage  $v_1$ . The stress induced by the two independent actuators is considered equivalent to two equal and opposite forces for extensional excitation and two equal and opposite moments for flexural excitation [15]. The relative magnitude of the induced extensional and flexural waves is precisely determined by the varying relative magnitude and phase of the two complex voltages. The expressions for the induced forces and moments are [16]

$$F_0 = \frac{ESK^e d_{31}}{T_a} (v_1 + v_2) = \frac{ESK^e d_{31}}{T_a} v_e \quad (5)$$

$$M_0 = \frac{EIK^f d_{31}}{T_a} (v_1 - v_2) = \frac{EIK^f d_{31}}{T_a} v_f \quad (6)$$

where  $K^e$  and  $K^f$  are defined in [9], and  $d_{31}$  and  $T_a$  represent respectively the strain sensitivity and the thickness of the PZT actuators. In Equations (5) and (6),  $v_e$  and  $v_f$  are the complex voltage required to minimize the extensional and flexural power flows respectively. The voltage  $v_e$  is the sum of  $v_1$  and  $v_2$  since purely extensional motion corresponds to voltages in-phase. Also,  $v_f$  is the

difference of  $v_1$  and  $v_2$  since purely flexural motion is associated with voltages out-of-phase. Throughout this paper,  $v_1$  and  $v_2$  are the applied voltages, while  $v_e$  and  $v_f$  are the control voltages. The energy required by the PZT actuators to minimize both the extensional and the flexural power flows (given by Equations (2) and (4) respectively) is investigated in terms of the voltage control effort  $V_{\text{eff}}$  defined as

$$V_{\text{eff}} = \sqrt{|v_1|^2 + |v_2|^2} \quad (7)$$

### III. ANALYTICAL SYSTEMS, RESULTS AND DISCUSSIONS

#### A. Description of the Analytical Systems

Passive control obtained using a material insert of high damping, and active control achieved with two co-located independent actuators are combined here, in order to minimize the far-field total (i.e. extensional and flexural) power flow. At this stage, no attempt was made to optimally choose the passive insert properties. In the analytical models, the beam system is considered to be infinite, which means that the passive insert is located between two identical long thin semi-infinite beams as depicted in Figure 2(a). The beams are considered made of aluminum with characteristics given in Table I [18]. The passive insert is made of PVC material characterized by a high loss factor. Its characteristics [19,20] are also presented in Table I. The length of the insert primarily dictates the amount of passive attenuation obtained. A practical length of 5 cm was considered primarily due to the requirements of the experimental rig. The active control actuators are G-1195 piezoceramic patches made of Lead Zirconate Titanate material, which properties are in Table I [15].

Three configurations of active/passive control systems are investigated as shown in Figure 2(a). The PZT actuators are located upstream of the passive insert for Configuration 1. In

Configuration 2, the actuators are directly bonded on the PVC insert. The actuators are symmetrically located with respect to the center of the passive insert. Configuration 3 corresponds to the actuators placed downstream of the passive insert. Then, Configuration 2 corresponds to the most compact active/passive configuration. The disturbance point force has a constant magnitude  $F$  equal to 1 N, applied at the angle of  $10^\circ$  with the beam neutral axis. That angle was chosen since it results in induced extensional and flexural power flows of approximately equivalent magnitude.

## B. Analytical Control Procedure

In any active control method, the purpose is to minimize a cost function representing the unwanted vibration or noise. In this study, the cost function to be minimized is the total power flow transmitted downstream of the active/passive control location. Note that in the analytical models, the section downstream of the control location is infinite. Once active control is applied, the resulting extensional and flexural displacements downstream of the control location are linear combinations of the displacements due to the primary and secondary sources. The associated total power flow in the far-field (using Equations (2) and (4) for semi-infinite beam) is

$$P_t = P_e + P_f = \frac{ESk_e\omega}{2} |E_1|^2 + EIk_f^3\omega |A_1|^2 \quad (8)$$

Equation (8) can be shown to be quadratic of the actuator applied voltages  $v_1$  and  $v_2$  [16] and therefore has a unique minimum [15]. The beam, being a two dimensional system with only one travelling wave solution per wave type, a secondary source can be created to produce zero far-field power flow when superimposed with the primary source [9]. Thus, two co-located independently driven actuators can analytically provide complete control of the total far-field power flow (i.e. minimum of the cost function equal to zero). Indeed, minimizing the cost function as defined by Equation (8) results in driving both travelling waves  $E_1$  (extensional) and  $A_1$  (flexural) to zero.

Then, for the three active/passive configurations, the analytical control procedure involves (i) expressing the flexural and extensional displacements downstream of the insert in terms of the applied voltages, (ii) setting the corresponding extensional and flexural positive travelling waves to zero, and (iii) solving for the unique applied voltages  $v_1$  and  $v_2$ .

### C. Analytical Results

Upon minimizing the cost function as defined previously, the control effort  $V_{\text{eff}}$ , and control voltages  $v_e$  and  $v_f$  are determined for each active/passive configuration. Figure 3(a) presents the control effort for the three active/passive configurations. Configurations 1 and 3 require about the same control effort  $V_{\text{eff}}$  to minimize the cost function. A significant reduction in the required control effort is achieved, over the entire frequency range, for Configuration 2, i.e., when the actuators are bonded to the passive insert. Since this configuration requires less energy to drive the PZT actuators, it is more effective than the other two (1 and 3). To investigate this result, the control voltages  $v_e$  and  $v_f$  are presented in Figure 3(b) and (c) respectively. Indeed, Configurations 1 and 3 correspond to about the same control voltage  $v_e$  required to cancel the extensional power flow. However, using Configuration 2, the control voltage  $v_e$  is reduced by a factor of more than 3 over the entire frequency range. The control voltage  $v_f$  required to cancel the extensional power flow (see Figure 3(c)) appears to be much smaller, for all three configurations, than the control voltage  $v_e$ . This is due to the fact that beams are much stiffer in extension than flexure. The three configurations result in approximately the same amount of energy required to cancel the flexural power flow (see Figure 3(c)). Thus, the low control effort obtained for Configuration 2 is related to the low control voltage  $v_e$  required by the PZT actuators when located on the passive insert. Configuration 2 is found to be the optimal active/passive configuration out of those arrangements.

considered here.

#### D. Discussion of Analytical Results

In the previous section, it was shown that the lowest control voltage required to cancel the extensional power flow and consequently the lowest control effort, are obtained for the actuators located on the passive PVC insert. The purpose here is to first verify that for a given actuator input, more extensional power flow is induced by PZT actuators located on PVC material than on aluminum material. Then, to explain the physics of this phenomenon from an impedance point of view, the mechanical impedance of the PZT actuators is compared to that of the aluminum and PVC beam sections.

Consider the case of a pair of PZT actuators on an infinite beam excited by a given control effort equal to +141 V, while no primary disturbance is apply to the beam. One infinite beam is made of aluminum and the other is made of PVC. Extensional power flow is induced in the beams by driving the PZT actuators with the same complex voltage, and flexural power flow is induced by driving the PZT actuators with voltages of same magnitude but  $180^\circ$  out-of-phase. The resulting extensional and flexural power flows are presented in Figure 4 for both aluminum and PVC beams. Figure 4(a) shows that, over the entire frequency range, the extensional power flow induced by the PZT actuators on the PVC beam is greater than that on the aluminum beam. On the other hand, Figure 4(b) indicates that the flexural power flow induced by the PZT actuators is almost the same for both beams. Therefore, it appears that the PZT actuators are able to transfer more extensional power flow or power when located on PVC material rather than on aluminum material. This result will be discussed below in terms of mechanical impedance.

The ability of an actuator to transfer power to its host structure at any frequency depends on

the relative mechanical impedances of the actuator and the structure. Indeed, an actuator provides the maximum input power when the structural mechanical impedance matches the actuator mechanical impedance [21]. For a constant response, the control effort required by that actuator is minimized when the power transferred from an actuator to a structure is maximized. The actuator's mechanical impedance and the structure impedances for the aluminum and PVC beams are calculated according to the theory of [22]. The mechanical impedance  $Z_a$  of two co-located identical PZT actuators is defined as the ratio of the actuation force to the velocity, i.e.,

$$Z_a = 2i \frac{-K_a(1+i\eta_a)}{\omega} \frac{k_a L_a}{\tan(k_a L_a)} \quad (9)$$

where  $K_a$  and  $k_a$  are respectively the static stiffness (given by  $E_a w_a T_a / L_a$ ) and the extensional wavenumber of the piezoceramic. The actuators located on the beam between  $x_1$  and  $x_2$  result in forces and moments applied at the actuator ends. The extensional beam mechanical impedance  $Z_e$  is expressed as the ratio of the actuators induced force to the difference of the in-plane velocities at the actuator ends, i.e.,

$$Z_e = \frac{F_0}{v_u(x_2) - v_u(x_1)} \quad (10)$$

The flexural beam mechanical impedance  $Z_f$  is proportional to the ratio of the actuators induced moment to the difference of the angular velocities at the actuator ends, i.e.,

$$Z_f = \frac{2}{(2h + T_a)^2} \frac{M_0}{\Theta_w(x_2) - \Theta_w(x_1)} \quad (11)$$

For more detail about the actuators and beam mechanical impedances, see reference [16]. The PZT actuators, aluminum beam and PVC beam mechanical impedance magnitudes are compared in Figure 5, for the structure in extension and flexure. Note that for the beam in extension, the

impedance of the actuators is much closer to the PVC beam impedance than the aluminum beam impedance (see Figure 5(a)). On the other hand, for the beam in bending, the actuators impedance is found to be slightly closer to the aluminum beam impedance (see Figure 5(b)). This demonstrates that for extensional motion, considerably better impedance matching exists between the PZT actuators and the PVC material than between the PZT actuators and the aluminum material. This is the reason why the control voltage  $v_e$  and the control effort are low when the PZT actuators are bonded to the PVC insert (Configuration 2). Note that these results are only for the specific physical system studied here, and they may vary for different beam or actuator thicknesses as well as insert properties for instance. However, they do illustrate the importance of impedance matching in lowering the control power.

#### **IV. EXPERIMENTAL SYSTEMS, RESULTS AND DISCUSSIONS**

##### **A. Experimental Setup**

A schematic of the arrangement considered for the experimental testing is presented in Figure 6. The thin beams are again made of aluminum and each have the dimensions of 2.4 m long by 76 mm wide by 3.2 mm thick. The PVC insert located between the two aluminum beams has the same properties and dimensions as in the analytical study (see Table I). In order to model a perfect junction, the PVC insert and the aluminum beams are bonded at the interfaces with high strength glue along with three small steel pins for extra interlocking support. PVC material was chosen for its combination of relatively high damping and structural stability. The beam structure is fitted at the left end with an anechoic termination, which consists of a diverging pyramid shaped box filled with sand. This termination has been tested to have a flexural power reflection coefficient less than 0.1 for frequencies greater than 200 Hz. Thus, for the frequency range of concern, the termination is

anechoic for flexural waves simulating a semi-infinite beam structure. However, the anechoic termination is found to be highly reflective for extensional waves due to their long wavelengths, and thus for extensional waves, the beam structure can be considered finite. The primary noise source is generated by a 25 lb. shaker exciting the beam at the free end with a  $10^\circ$  angle. The 25 lb. point force shaker had to be applied at a free end of the beam in order to have such a small angle of  $10^\circ$  due to its large size. Three sets of two co-located actuators were bonded to the system at 10 cm before the insert ( $Z_1$  and  $Z_2$  for Config.1), in the center of the insert ( $Z_3$  and  $Z_4$  for Config.2), and at 10 cm after the insert ( $Z_5$  and  $Z_6$  for Config.3). The beam is also equipped with a total of 6 PVDF sensors that are used with a digital filter network in order to provide real time estimates of the positive and negative extensional and flexural travelling waves in the beam. This method of real time narrowband and broadband estimation of extensional and flexural power flows from 6 independent PVDF strain measurements was developed by Gibbs [9], and is discussed in the following section.

## B. Experimental Control Procedure

A block diagram of the adaptive control system used in this experiment is shown in Figure 7. The active control was experimentally implemented using the Filtered x-LMS (FXLMS) algorithm described by Elliot et al. [23]. This algorithm was modified using the extensional and flexural wave filters presented in Figure 7. Sensors S1 and S2, as well as sensors S5 and S6, are summed to provide a response proportional to the extensional motion only, which is then passed through the extensional wave filter to provide information about the propagating waves  $E_1$  and  $F_1$ . Similarly, sensors S3 and S4, as well as sensors S5 and S6, are subtracted to provide a response proportional to the flexural motion only, which is then passed through the flexural wave filter to

provide information about the propagating waves  $A_1$  and  $B_1$ . Such a wave vector filtering network results in good estimate of the positive and negative extensional and flexural travelling waves in the region of the beam downstream of the passive insert [9]. The estimated positive extensional and flexural travelling waves ( $E_1$  and  $F_1$ ) are the error signals for the FXLMS algorithm. Similarly to the analytical control procedure, the experimental control algorithm consists of minimizing both the extensional and flexural waves travelling towards the anechoic termination (the reflected waves from the termination should be also minimized as a result). The magnitude of the different waves ( $E_1$ ,  $F_1$ ,  $A_1$  and  $B_1$ ) was measured before and after control was implemented and then the resulting nett extensional power flow was calculated as

$$P_e = \frac{ESk_e\omega}{2} (|E_1|^2 - |F_1|^2) \quad (12)$$

while the resulting nett flexural power flow was determined as

$$P_f = EIk_f^3\omega (|A_1|^2 - |B_1|^2) \quad (13)$$

## B. Experimental Results and Discussion

Control was implemented for five different frequencies of excitation, 440 Hz, 580 Hz, 680 Hz, 790 Hz and 900 Hz. The associated results are presented in Figures 8 to 12 for each control actuators configuration, in terms of the achieved nett extensional and flexural power flow attenuation and the control effort as well as the extensional ( $v_e$ ) and flexural ( $v_f$ ) voltages necessary to drive the control actuators. First, it can be seen that Config. 2 (PZT actuators on passive PVC insert) led to the largest extensional power flow reduction. The three configurations resulted in important attenuation of the flexural power flow. Note the attenuation of extensional power flow is lower than that of the flexural one. As expected from the analytical study, for each of the excitation

frequencies, the control effort associated with Config. 2 is the lowest and in general less than half that associated with Config. 1 and 3. The control effort for Config. 1 and 3 is for most cases of the same level. The results also show that, even though the flexural power flow is the most reduced, the flexural control voltage is much smaller than the extensional one. Indeed, the extensional control voltage is very high for Config. 1 and 3, which yielded the low extensional power flow reduction. On the other hand, extensional control voltage corresponding to Config. 2 is very low and much smaller than that for Config. 1 and 3. This is the reason why Config. 2 is the most effective configuration (lowest control effort and largest power flow attenuation). Thus, these preliminary experimental results corroborate very well the analytical prediction. In addition, bonding the control actuators to the passive PVC insert provide the most compact and the most effective active/passive system.

## V. SUMMARY AND CONCLUSIONS

The goal of this work was to analytically and experimentally demonstrate the advantages of combining passive and active control methods to attenuate the total far-field vibrational power flow in infinite beams subjected to a point force excitation. The objective was also to find the optimal active/passive configuration, with respect to minimum control effort required, by comparing the control results for 3 different active/passive systems. Control was examined over a wide range of harmonic excitation from 200 Hz to 1000 Hz. The point force was applied at an angle  $\theta=10^\circ$  with the neutral axis of the beam in order to simultaneously induce extensional and flexural motion. The passive approach and active control technique were combined and studied for three different configurations: the actuators upstream, downstream or on the passive insert. Configuration 1 had the actuators upstream of the insert, configuration 2 consisted of the actuators directly bonded to the

insert, and configuration 3 located the actuators downstream of the insert. The purpose was to evaluate which of the piezoelectric actuator locations was the most effective, in terms of the lowest control effort required. The control effort was defined as proportional to the sum of the complex voltages  $v_1$  and  $v_2$  respectively applied to the upper and lower actuators. For both analytical and experimental systems, the most effective active/passive combination was obtained when the actuators were bonded directly to the passive insert. The optimal active/passive configuration resulted in less control voltage required to cancel the extensional power flow than with the purely active system. Consequently, the control effort was significantly reduced. This was associated with the fact that the actuators were found to induce ten times more extensional power flow when located on the PVC material than on an aluminum material. A physical explanation was that for extensional motion, better impedance matching exists between the actuators and the PVC material than between the actuators and the aluminum material. Thus, the extensional power flow is more effectively induced and controlled in the PVC material than in the aluminum material for this arrangement.

## VI. ACKNOWLEDGEMENTS

The authors gratefully acknowledge the support of this work by the Office of Naval Research under the Grant ONR N00014-92-J-470, Dr. Kam Ng Technical Monitor.

## VII. REFERENCES

- [1] C.E. Wilson, *Noise Control: Measurement, Analysis, and Control of Sound and Vibration*, Harper and Row Inc., New York, 1989.
- [2] L.L. Beranek and I.L. Vér, *Noise and Vibration Control Engineering: Principles and Applications*, John Wiley & Sons, Inc., New York, 1992.

[3] L. Cremer, M. Heckl, and E.E. Ungar, *Structure-Borne Sound: Structural Vibrations and Sound Radiation*, Springer Verlag, Berlin, 1973.

[4] K.W. Ng, "Applications of Active Control", The 1995 International Symposium on Active Control of Sound and Vibration, Active 95, Newport Beach, CA, 1995.

[5] D. Guicking and E. Lorenz, "An Active Sound Absorber with Porous Plate", *Journal of Vibration, Acoustics, Stress and Reliability in Design*, **106**, 389-392, 1984.

[6] W. Redman-White, P.A. Nelson and A.R.D. Curits, "Experiments on the Active Control of Flexural Wave Power", *Journal of Sound and Vibration*, **112**(1), 187-192, 1987.

[7] L.O. Gonidou and C.R. Fuller, "Further Research on Active Control of Flexural Power Flow in Elastic Thin Beams", *Journal of the Acoustical Society of America*, **85**(S1), 573, 1989.

[8] C.R. Fuller, G.P. Gibbs, and R.J. Silcox, "Simultaneous Active Control of Flexural and Extensional Power Flows in Beams", *Journal of Intelligent Materials Systems and Structures*, **1**(2), 235-247, 1990.

[9] G. Gibbs, "Simultaneous Active Control of Flexural and Extensional Power Flow in Thin Beams", Ph.D. Dissertation, Virginia Polytechnic Institute and State University, 1993.

[10] J.L. Fanson and J.C. Chen, "Structural Control by the Use of Piezoelectric Active Members," *Proceedings of NASA-DOD Control-Structures Interaction Conference*, NASA CP-2447, Part II, 1986.

[11] E.E. Crawley and J. de Luis, "The Use of Piezoelectric Actuators as Elements of Intelligent Structures," *AIAA Journal*, **25**(10), 137-1385, 1987.

[12] E.E. Crawley and E.H. Anderson, "Detailed Models for Piezoelectric Actuation of Beams," *Journal of Intelligent Materials Systems and Structures*, **1**(1), 4-25, 1990.

- [13] L. Meirovitch, *Elements of Vibration Analysis*, Mc Graw-Hill, New York, 2<sup>nd</sup> Edition, 1986.
- [14] M.C. Junger and D. Feit, *Sound, Structures, and Their Interaction*, The MIT Press, Cambridge, 2<sup>nd</sup> Edition, 1986.
- [15] C.R. Fuller, S.J. Elliott and P.A. Nelson, *Active Control of Vibration*, Academic Press, London, 1996.
- [16] F.L. Deneuve, "Simultaneous Active/Passive Control of Extensional and Flexural Power Flows in Infinite Thin Beams", Ms. Thesis, Virginia Polytechnic Institute and State University, 1996.
- [17] J. Pan and C.H. Hansen, "Active Control of Total Power Flow Along a Beam", *Proceedings of the International Congress on Recent Developments in Air and Structure-Borne Sound and Vibration*, Auburn University, AL, 1990.
- [18] L.E. Kinsler, A.R. Frey, A.B. Coppens and J.V. Sanders, *Fundamentals of Acoustics*, John Wiley & Sons, Inc., New York, 1982.
- [19] L.I. Nass, *Encyclopedia of PVC (2nd Edition V. 1, V. 2 and V. 3)*, M. Dekker, Inc., New York, 1986.
- [20] B.J. Lazan, *Damping of Materials and Members in Structural Mechanics*, Pergamon Press, New York, 1968.
- [21] R.A. Lomenzo, H. Sumali and H.H. Cudney, "Maximizing mechanical power transfer from piezoceramic stacked actuators to structures", *Proceedings of the ASME Adaptive Structures and Material Systems Conference*, AD-Vol. 35, 229-235, 1993.
- [22] C. Liang, F.P. Sun, and C.A. Rogers, "An Impedance Method for Dynamic Analysis of Active Material Systems", *34th AIAA Structures, Structural Dynamics and Materials Conference*, La Jolla,

CA, 3587-3599, 1993.

[23] P.A. Nelson and S.J. Elliot, *Active Control of Sound*, Academic Press, London, 1992.

Table I. Mechanical properties and dimensions of system components.

	Beams	PZT Actuator	PVC Insert
Density (kg/m <sup>3</sup> )	2700	7650	1370
Young Modulus (N/m <sup>2</sup> )	$7.1 \times 10^{10}$	$6.3 \times 10^{10}$	$0.25 \times 10^{10}$
Loss Factor	0	0.1%	1
Poisson Ratio	0.33	0.28	0.33
Thickness (m)	$3.2 \times 10^{-3}$	$0.178 \times 10^{-3}$	$3.2 \times 10^{-3}$
Width (m)	$76 \times 10^{-3}$	$63.5 \times 10^{-3}$	$76 \times 10^{-3}$
Length (m)		$38.1 \times 10^{-3}$	$50.8 \times 10^{-3}$
Strain Sensitivity (m/V)		$166 \times 10^{-12}$	

## LIST OF FIGURE CAPTIONS

Figure 1: (a) Extensional and (b) flexural waves propagating in a finite section of beam.

Figure 2: Schematic of (a) the 3 active/passive configurations and (b) the extensional and flexural loading induced by 2 co-located independent PZT actuators.

Figure 3: (a) Control effort  $V_{eff}$ , (b) control voltage  $v_e$  and (c) control voltage  $v_f$ .

Figure 4: Comparison of (a) the extensional and (b) flexural power flows induced by the two co-located PZTs in infinite aluminum and PVC beams.

Figure 5: Mechanical impedance for system in (a) extension and (b) flexure.

Figure 6: Schematic of the experimental arrangement.

Figure 7: Block diagram of adaptive control system with wave vector filters.

Figure 8: Control results at 440 Hz; (a) power flow reduction and (b) control voltages.

Figure 9: Control results at 580 Hz; (a) power flow reduction and (b) control voltages.

Figure 10: Control results at 680 Hz; (a) power flow reduction and (b) control voltages.

Figure 11: Control results at 790 Hz; (a) power flow reduction and (b) control voltages.

Figure 12: Control results at 900 Hz; (a) power flow reduction and (b) control voltages.

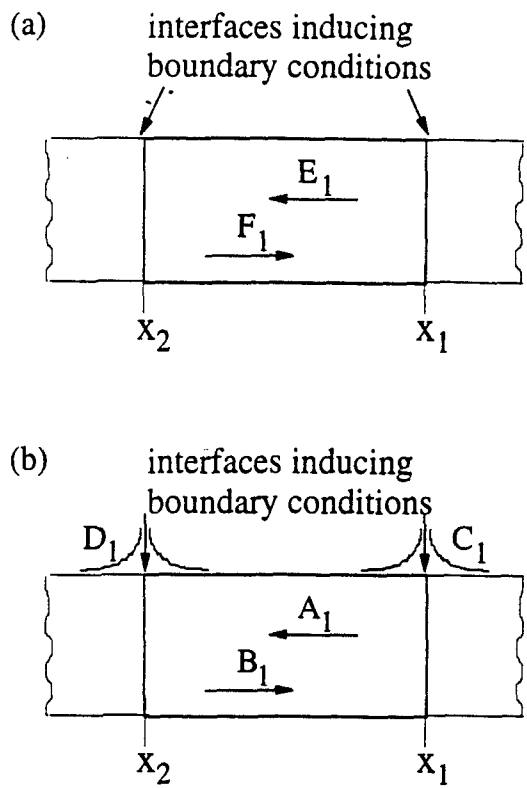


Figure 1: (a) Extensional and (b) flexural waves propagating in a finite section of beam.

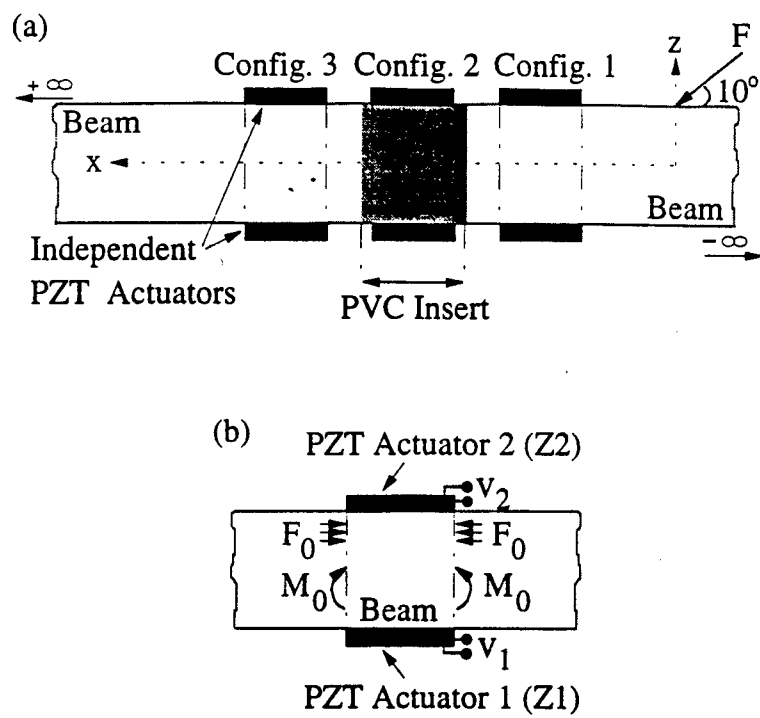


Figure 2: Schematic of (a) the 3 active/passive configurations and (b) the extensional and flexural loading induced by 2 co-located independent PZT actuators.

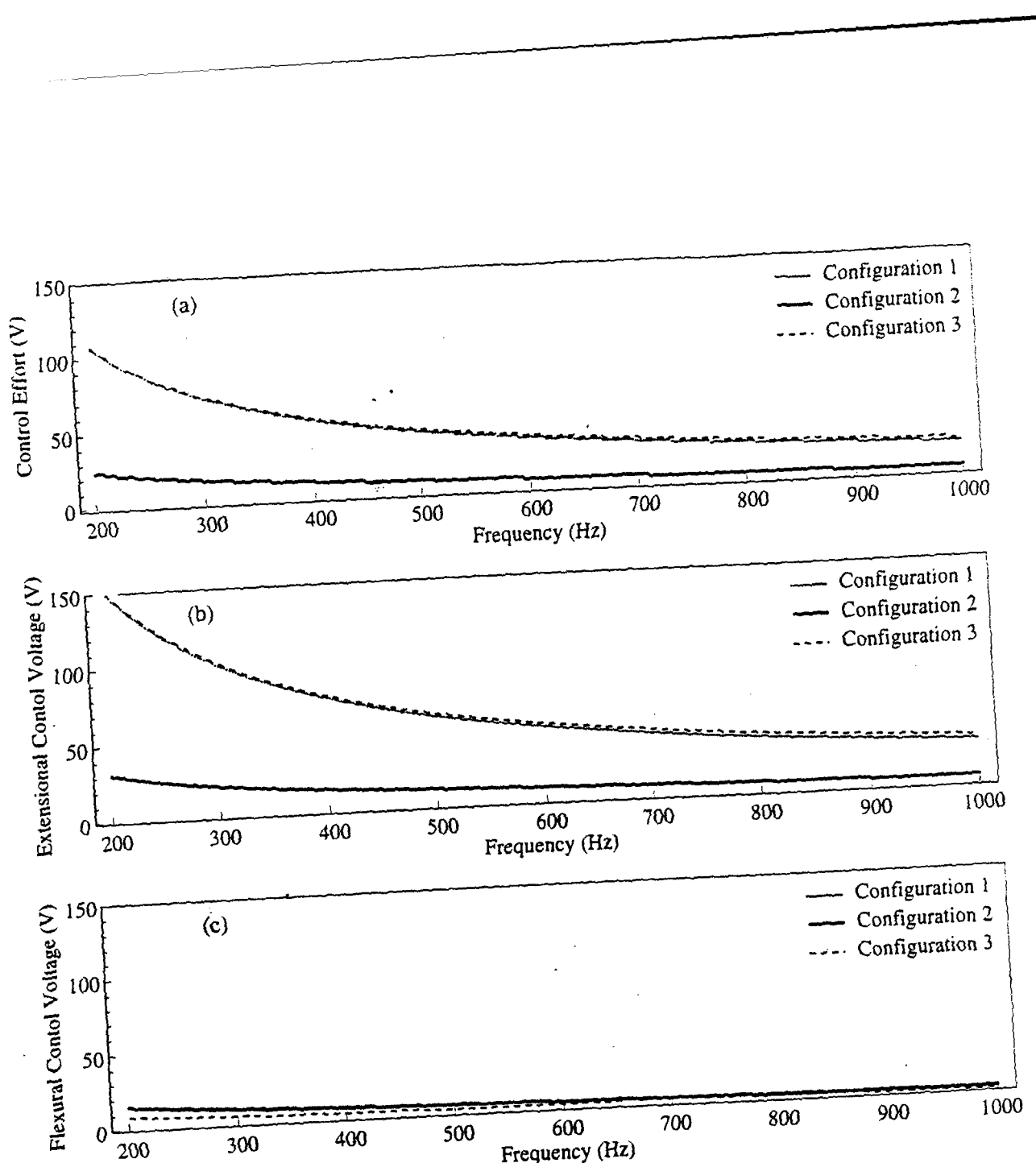


Figure 3: (a) Control effort  $V_{eff}$ , (b) control voltage  $v_e$  and (c) control voltage  $v_f$ .

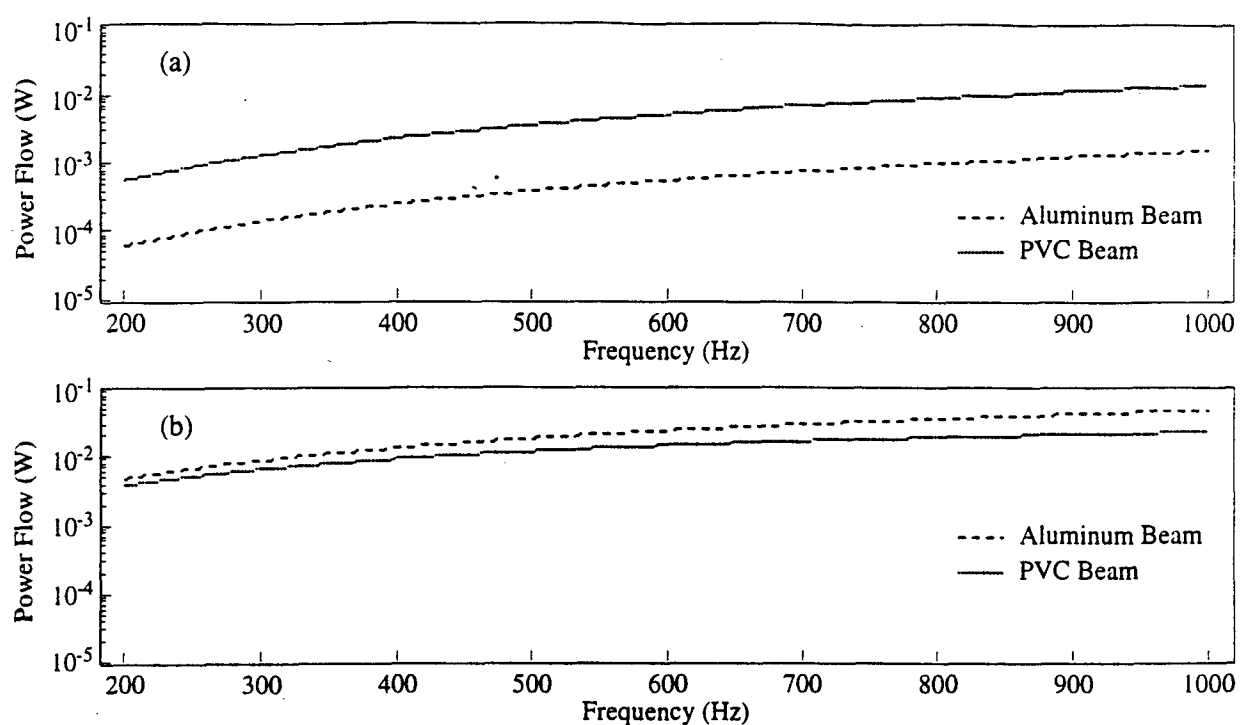


Figure 4: Comparison of (a) the extensional and (b) flexural power flows induced by the two co-located PZTs in infinite aluminum and PVC beams.

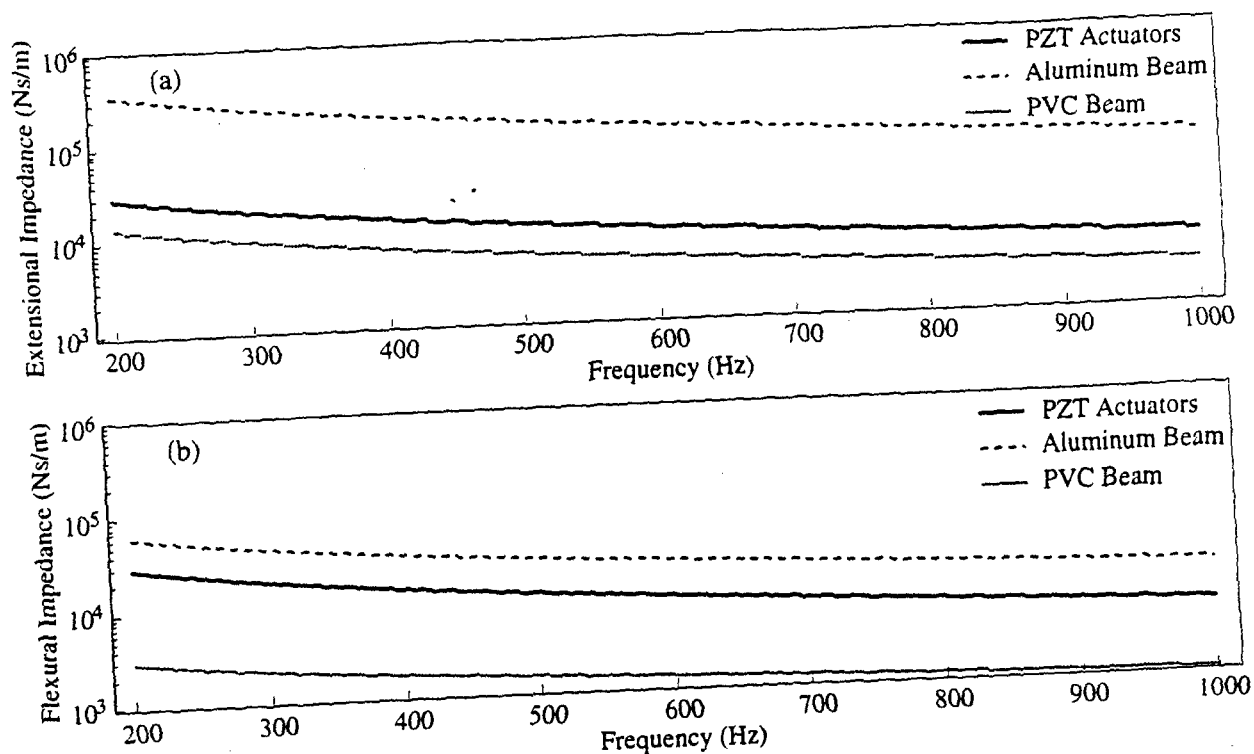


Figure 5: Mechanical impedance for system in (a) extension and (b) flexure.

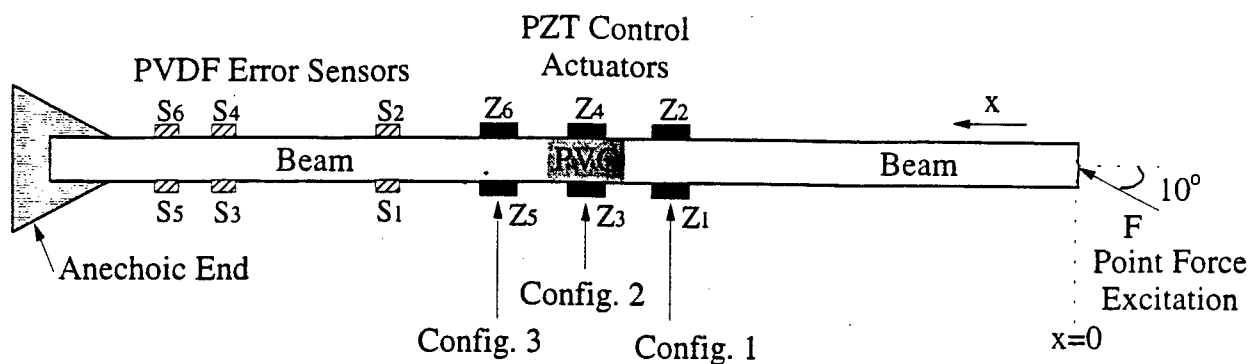


Figure 6: Schematic of the experimental arrangement.

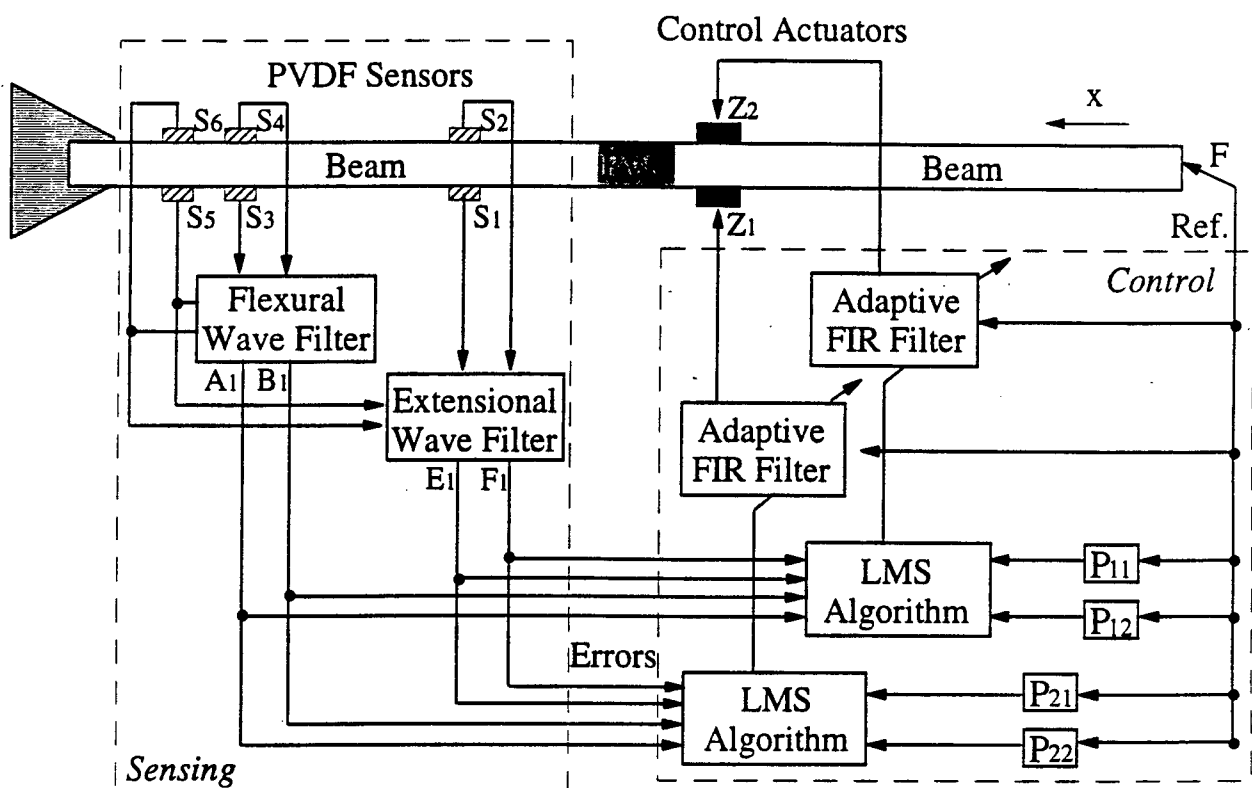


Figure 7: Block diagram of adaptive control system with wave vector filters.

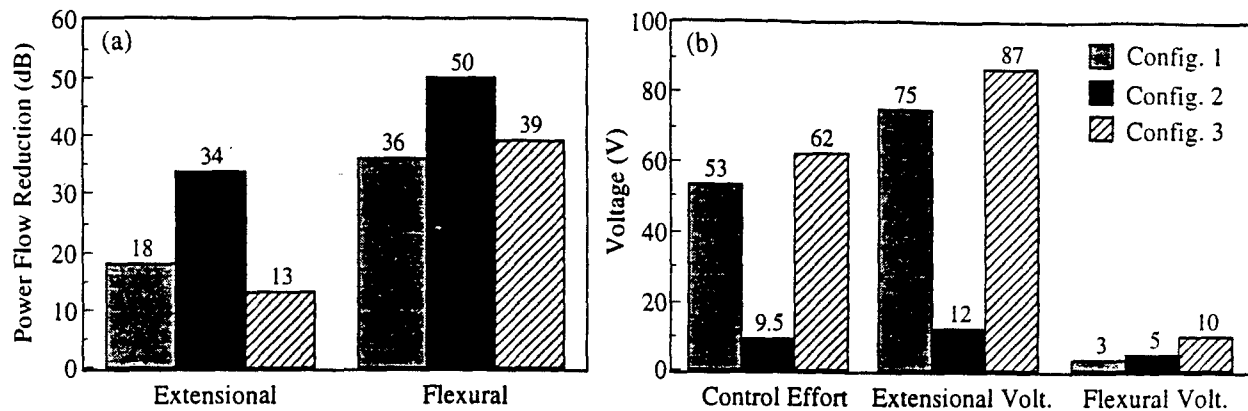


Figure 8: Control results at 440 Hz; (a) power flow reduction and (b) control voltages.

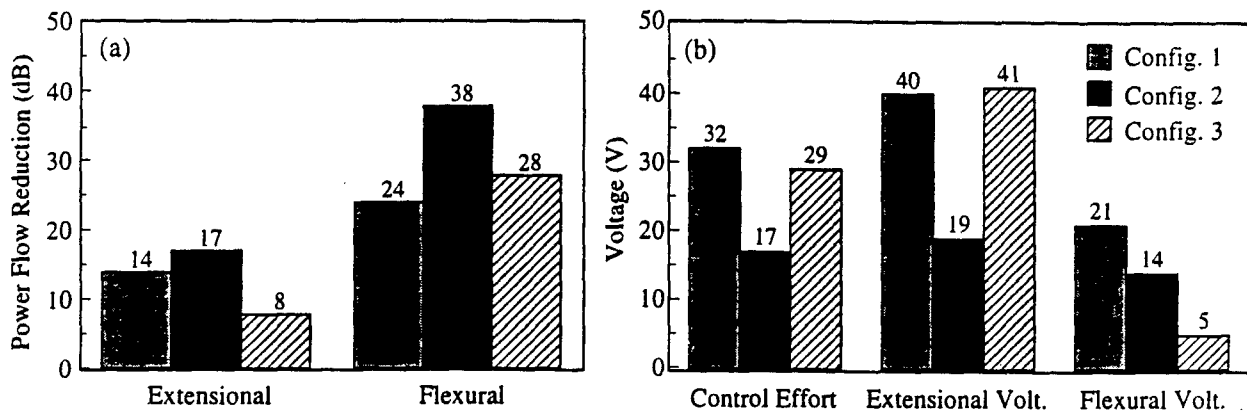


Figure 9: Control results at 580 Hz; (a) power flow reduction and (b) control voltages.

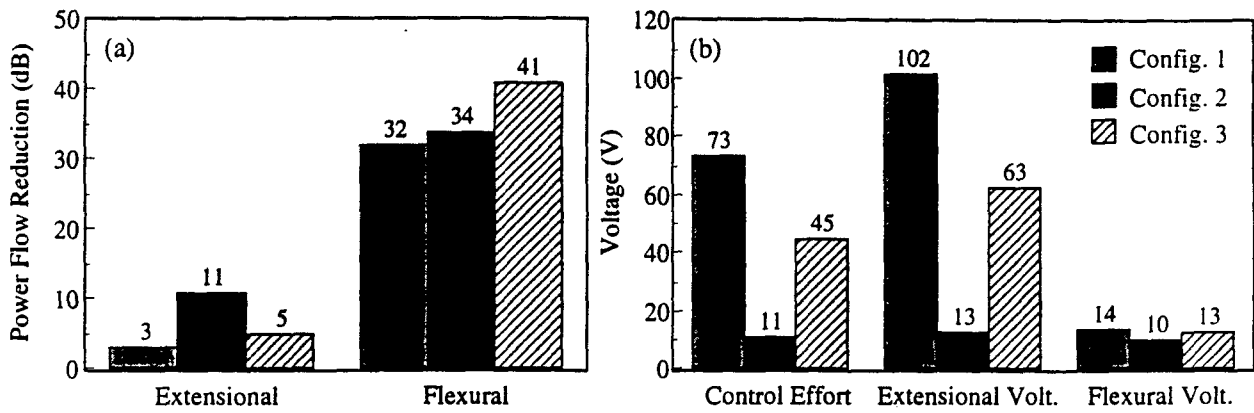


Figure 10: Control results at 680 Hz; (a) power flow reduction and (b) control voltages.

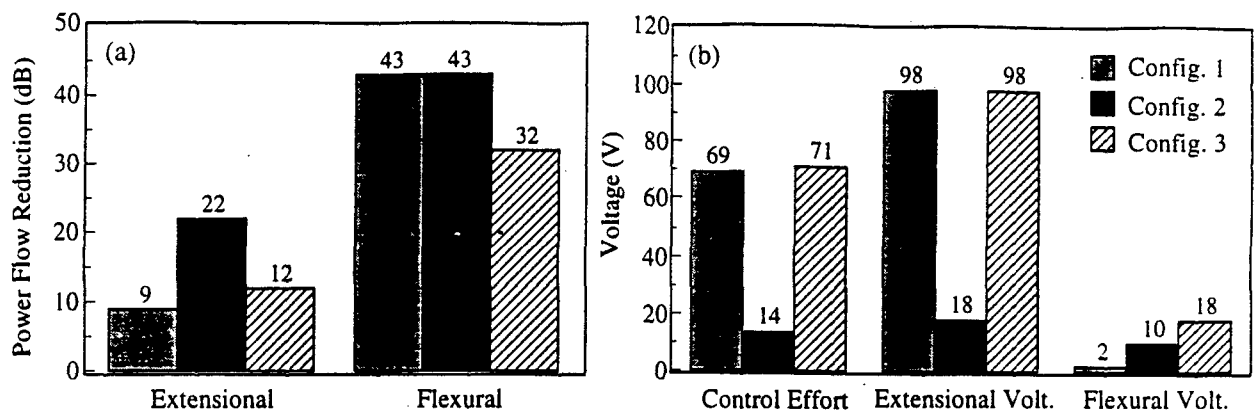


Figure 11: Control results at 790 Hz; (a) power flow reduction and (b) control voltages.

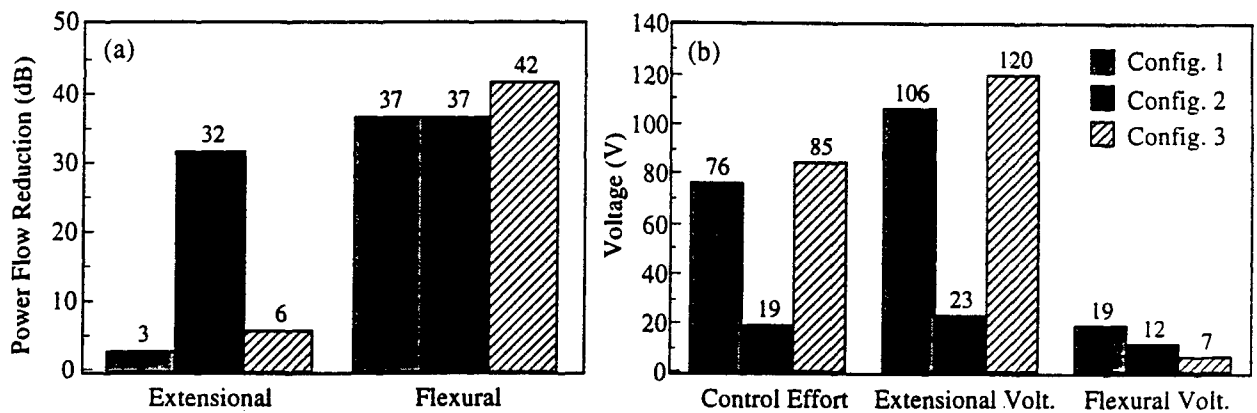


Figure 12: Control results at 900 Hz; (a) power flow reduction and (b) control voltages.

# **APPENDIX 30**



FOURTH INTERNATIONAL CONGRESS  
ON SOUND AND VIBRATION  
JUNE 24-27, 1996  
ST. PETERSBURG, RUSSIA

STUDY OF GLOBALLY DETUNED ABSORBERS FOR CONTROLLING  
AIRCRAFT INTERIOR NOISE

C. Guigou, J.P. Maillard and C.R. Fuller

Virginia Polytechnic Institute and State University, Mechanical Engineering Department  
Vibration and Acoustics Laboratories, Blacksburg, VA 24061-0238

ABSTRACT

The potential of tunable mechanical vibration absorbers to reduce aircraft interior noise is discussed. First, a simplified analytical model describing the vibrational and acoustic fields for a propeller aircraft is developed. The system then consists of introducing multiple vibration absorbers whose properties can be electronically adjusted, attached to the cylindrical structure representative of the aircraft fuselage. These adaptive absorbers are configured to have resonances on or very close to the disturbance frequency and thus can exert significant reactive force with a low system mass and a very low power consumption. The properties of the absorbers are globally adapted in order to minimize a cost function based upon interior acoustic levels. This ensures that the absorbers minimize the structural cylinder modes well coupled to the interior acoustic field. Previous work has shown that such globally detuned absorbers out perform tuned absorbers in which the base motion is directly minimized. The paper concentrates on further studying the effects of the detuning factor and mechanical impedance as well as the absorbers number and position, on the interior noise attenuation. Two disturbance frequencies, i.e. the first and second propeller blade passage frequency, are investigated. The results show that, for properly configured absorbers, large global attenuation of aircraft interior noise can be achieved and confirm that the detuned absorbers provide more sound attenuation than the tuned.

INTRODUCTION

The reduction of interior noise in turboprop aircraft still remains an important design challenge. A typical turboprop aircraft is configured with two wing-mounted propellers, with small distance between the propellers blades and the fuselage. In the area where the blades approach the closest to the fuselage, exterior pressure levels are typically around 130 dB at the blade passage frequency (BPF), while significant but lower levels exist at the harmonics of the BPF. The propellers pressure loading causes the fuselage to vibrate. These structural vibrations couple with the air of the enclosed space resulting in large interior sound levels. In the recent years, several passive and active techniques have been considered to reduce aircraft interior noise.

A simple approach, known as synchrophasing, consists of controlling the relative phase angle of the propellers so the interior cabin sound fields of the individual propellers destructively interfere [1,2]. For this strategy, the weight and cost penalties are minimal but sound attenuation is limited. Various active control techniques have also been considered. Recent flight tests have demonstrated the potential of Active Noise Control (ANC), which involves acoustic sources and error microphones distributed throughout the cabin space [3,4]. Such systems using 24 up to 36 optimally located loudspeakers in conjunction with 48 to 72 error microphones, have been installed in aircraft such as the SAAB 340 or SAAB 2000. However, the total weight is about 70 kg for a 10 dB attenuation in the propeller fundamental frequency. This approach generally requires a large number of control transducers. Furthermore, performance is decreased at the higher harmonics of the propeller noise. An alternative active approach termed Active Structural Acoustic Control (ASAC) uses fuselage mounted vibration actuators in conjunction with interior microphones [5,6]. This technique shows potential to

significantly reduce the number of required control transducers. It can be estimated that a 12 actuator / 24 sensor system could provide around 25 dB of attenuation with a weight of 18 kg (using inertial shakers). However, important disadvantages compared to ANC are a requirement for larger control authority (or force/stroke output of the control actuator) and a possible increase in the fuselage vibration. Active control techniques shows great potential to reduce interior noise but are in general very expensive and require significant amount of energy. Tuned mechanical vibration absorbers designed to reduce the vibration of the aircraft fuselage, and hence its interior noise, have been tested by several aircraft companies [7-10] and are presently in use. Sound reductions of 8 to 10 dB have been reported at the fundamental blade passing frequency under cruise conditions. In that case, the weight penalty is only about 25 kg. This technique suffers from a loss in performance when the absorbers are off-resonance, i.e. when the propeller speeds vary from the design point. A suggested solution to this problem is to use absorbers whose properties could be adapted in order to track the varying disturbance frequency [11].

This work analytically investigates the potential of a system which is configured to combine some of the advantages of the above approaches. Such a system was previously introduced in [12] and consists of multiple vibration absorbers whose properties can be electronically adjusted (adaptive absorber) mounted on an elastic cylindrical structure representative of an aircraft fuselage. The adaptive absorbers are configured to have resonance on or very near the disturbance frequency and thus can exert significant reactive force with a low system mass. Designing the individual absorbers to resonate at the disturbance frequency results in large decrease of the cylinder motion at their attachment point. Previous studies on interior sound control in aircraft have shown that minimizing the fuselage vibration does not perform as well as directly minimizing the coupled interior acoustic field for low frequency disturbances [13,14]. Therefore, the properties of the absorbers are globally adapted in order to minimize either the fuselage vibrational kinetic energy or the interior acoustic potential energy. Note that the present study takes into account the external pressure loading from both propellers in contrast to the work presented in [12] and uses multiple (more than 4) absorbers.

## ANALYSIS

In this section, the analytical model representative of an aircraft fuselage is outlined to evaluate the vibrational field and the coupled interior sound field. However, a brief review of mechanical absorbers and approximate design formula are first presented

### Mechanical absorbers

A mechanical absorber, as shown in Figure 1, can be decomposed into a mass ( $M$ ) mounted on a moving base through a spring/dash-pot (stiffness  $K$  / damping  $C$ ) mechanism. Note that the system is assumed to move in the direction whose motion has to be suppressed. The mechanical impedance  $Z_a$  of such a vibrational absorber is

$$Z_a = jM\omega \left[ \frac{1 + j\alpha/Q}{1 - \alpha^2 + j\alpha/Q} \right], \quad (1)$$

where  $\alpha$  is the detuning factor defined by the ratio between the disturbance frequency  $\omega$  and the natural frequency of the absorber  $\omega_a = \sqrt{K/M}$ , i.e.  $\alpha = \omega/\omega_a$ . The sharpness of the absorber response at resonance is represented by the quality factor  $Q = M\omega_a/C$ . For large  $Q$  absorbers and near resonance, the mechanical impedance is reduced to  $Z_a = MQ\omega$ , which is  $Q$  times that resulting from the same mass rigidly attached to the base. Therefore, at resonance, the increase of  $Q$  is a convenient low-mass method for gaining mechanical impedance. However, off-resonance, the absorber impedance is strictly proportional to its mass. As observed in Figure 2, given two absorbers having the same dynamic impedance at resonance, the one with a lower  $Q$  and a larger mass is more effective off-resonance. As for aircraft applications low weight is an important concern, absorbers should in that case have the highest possible quality factors (which implies low damping).

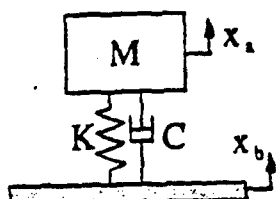


Figure 1: Schematic of mechanical vibration absorber.

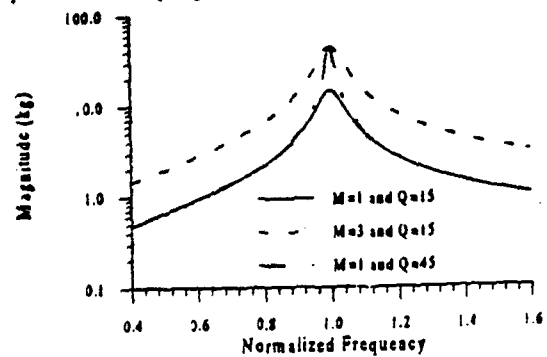


Figure 2: Normalized absorber impedance.

### Vibrational field of the fuselage

A simply supported cylinder (length  $L$ , radius  $a$  and thickness  $h$ ) is used to model an aircraft fuselage as shown in Figure 3. The analysis follows that presented by Thomas et al. [13,14] and Fuller et al [12]. Note that the cylinder is assumed to have rigid shear-diaphragm end caps. The elastic modulus, density, Poisson ratio and structural damping factor of the cylinder material are respectively denoted by  $E$ ,  $\rho$ ,  $v$  and  $\eta$ .

The disturbance associated to the propellers is represented by an external pressure loading  $p_e(x, \theta)e^{j\omega t}$  acting on the exterior of the cylinder. The external pressure loading is maximum where the propellers blades approach the closest to the fuselage, i.e. at the locations  $x=3.5$  m,  $\theta=85^\circ$  and  $275^\circ$  [13]. Measurements [13] also showed that the external pressure loading decays exponentially along the  $x$ -axis and linearly in the angular direction and is as well convected around the fuselage. Therefore, the external pressure distribution associated to one propeller is assumed to be of the form

$$p_{ext}(x, \theta) = \begin{cases} p_{ext} e^{-d|x-x_0|} \frac{\theta - \theta_1}{\theta_0 - \theta_1} e^{jk_a \theta} & \text{for } \theta_1 \leq \theta \leq \theta_0, \\ p_{ext} e^{-d|x-x_0|} \frac{\theta - \theta_2}{\theta_2 - \theta_0} e^{jk_a \theta} & \text{for } \theta_0 < \theta \leq \theta_2, \\ 0 & \text{elsewhere} \end{cases} \quad (2)$$

where  $x_0$  and  $\theta_0$  define the position of maximum pressure,  $\theta_1$  and  $\theta_2$  are the upper and lower limits of the circumferential pressure distribution;  $k_a$  corresponds to the convection speed of the pressure around the fuselage and  $d$  is the axial decay constant. The total pressure loading on the fuselage is then the contribution from the port ( $\theta_0=275^\circ$ ) and the starboard ( $\theta_0=85^\circ$ ) propellers, i.e.

$$p_e(x, \theta) = p_p(x, \theta) + p_s(x, \theta)e^{j\theta}, \quad (3)$$

where  $p_p$  and  $p_s$  are given by Eq. (2). In Eq. (3), it is assumed that the propellers rotate at the same constant speed and with a fixed relative phase  $\theta$ , usually called the synchrophase angle.

Vibration absorbers are mounted on the cylinder in order to alter the primary structural response due to external pressure field. Each absorber is modeled by a radially acting point force. For the  $i^{\text{th}}$  absorbers attached at  $(x_i, \theta_i)$ , this force is written as

$$F_i = j\omega Z_i w(x_i, \theta_i), \quad (4)$$

where  $Z_i$  represents the mechanical impedance (as given in Eq. (1)) and  $w(x_i, \theta_i)$  the fuselage normal displacement at the absorber mounting location. The contribution from a number of  $N_a$  absorbers is expressed as a pressure input distribution as

$$F(x, \theta) = \sum_{i=1}^{N_a} F_i \delta(x - x_i) \frac{\delta(\theta - \theta_i)}{a}, \quad (5)$$

where  $\delta$  represents the Dirac delta function. Note that with respect to ANC and ASAC approaches, Eq. (5) corresponds to the forcing distribution associated with the "control" sources while the external pressure field (Eq. (3)) represents the primary "disturbance" source.

Following standard thin shell theory [14], the normal displacement of the cylinder can be written as

$$w(x, \theta, t) = \left\{ \sum_{m=1}^{\infty} \sum_{n=0}^{\infty} W_m^n \Phi_m^n(x, \theta) + \sum_{m=1}^{\infty} \sum_{n=0}^{\infty} W_m^n \Phi_{mn}^n(x, \theta) \right\} e^{j\omega t}, \quad (6)$$

where the vibrational modal functions are defined by

$$\begin{cases} \Phi_m^n(x, \theta) = \sin(k_m x) \cos(n\theta) \\ \Phi_{mn}^n(x, \theta) = \sin(k_m x) \sin(n\theta) \end{cases}, \quad (7)$$

and  $W_m^n$  are the complex amplitude of the cylinder response in the  $(m,n)^{\text{th}}$  vibrational mode and  $k_m = m\pi/L$  verifies the simply-supported boundary conditions. Note that  $m$  and  $n$  correspond to the modal order in the axial and circumferential direction respectively. The modal displacement amplitude can be expressed by

$$W_m^n = H_{mn}(\omega)(p_{mn}^{sh} + F_{mn}^{sh}), \quad (8)$$

where the modal amplitudes of the forcing distribution are

$$p_{mn}^{sh} = \frac{2}{\pi L a \epsilon_n} \int_S p_e(x, \theta) \Phi_m^n(x, \theta) dS, \quad (9a)$$

$$F_{mn}^{sh} = \frac{2}{\pi L a \epsilon_n} \int_S F(x, \theta) \Phi_{mn}^n(x, \theta) dS, \quad (9b)$$

where  $\varepsilon_n=2$  if  $n=0$  and  $\varepsilon_n=1$  otherwise. The modal frequency response is defined as

$$H_{nn}(\omega) = \gamma \left( \frac{L_{11}L_{22} - L_{12}L_{21}}{\det(L)} \right) \quad (10)$$

where  $\gamma = -(1-v^2)a^2/Eh$  and the matrix  $L$  is given by

$$\begin{cases} L_{11} = \Omega^2 - (k_m a)^2 - n^2(1-v)/2 \\ L_{12} = L_{21} = n(k_m a)(1+v)/2 \\ L_{13} = L_{31} = v(k_m a) \\ L_{22} = \Omega^2 - n^2 - (k_m a)^2(1-v)/2 \\ L_{23} = L_{32} = -n \\ L_{33} = \Omega^2 - 1 - \beta^2(\mu_1(k_m a)^4 + \mu_2 n^4 + 2\mu_1 n^2(k_m a)^2) \end{cases} \quad (11)$$

where  $\beta^2 = h^2/12a^2$  and  $\Omega$  is the non-dimensional disturbance frequency defined by  $\Omega = \omega a/c_L$ . The longitudinal phase speed of the shell material is  $c_L = \sqrt{E_s/\rho\mu_m(1-v^2)}$ , where  $E_s = E(1+j\eta)$ . Note that the mass, the bending and torsional stiffness due to the stringers and frames are taken into account by introducing the corrections factors  $\mu_1$ ,  $\mu_2$ ,  $\mu_3$  and  $\mu_4$  defined in Table I [16]. These additional effects significantly decrease the input compliance of the cylinder to a value close to that characterizing the dynamics of a real fuselage. They also result in lower modal density at the frequencies of interest.

A compact matrix notation is used to solve for the coupled response of the system with absorbers. In Eq. (6), the summations are truncated to the first  $N_r$  circumferential modes and the first  $N_z$  longitudinal modes corresponding to a total number of  $N_{modes}=2*N_r*N_z$ . The column vector of modal displacement amplitudes  $\underline{W}^{st}$  is denoted  $\underline{q}$ . Then, the modal displacement amplitudes of the coupled cylinder-absorber system can be found by solving the following linear system

$$(I - j\omega H \Psi^* Z \Phi^*) \underline{q} = H \underline{p}_s \quad (12)$$

where  $I$  is the  $N_{modes}$  by  $N_{modes}$  identity matrix;  $Z$  is a  $N_r$  by  $N_r$  diagonal matrix containing the mechanical impedance  $Z_i$  ( $i=1, \dots, N_r$ );  $\Phi^*$  is a  $N_z$  by  $N_{modes}$  matrix relating the modal displacement amplitudes to the normal displacement at the absorbers mounting locations  $w(x_i, \theta_i)$ ;  $\Psi^*$  is a  $N_{modes}$  by  $N_z$  matrix relating the modal forcing function to the location of the absorbers;  $H$  is a diagonal matrix containing the modal transfer functions  $H_{nn}(\omega)$  and  $\underline{p}_s$  is the column vector of the external pressure modal component,  $\underline{p}_s^{st}$ . Note that the matrix  $(I - j\omega H \Psi^* Z \Phi^*)$  is not diagonal as the system is coupled due to the presence of the absorbers. The cylinder displacement modal amplitudes for the cylinder with no absorbers are simply obtained by setting the absorber mechanical impedance matrix  $Z$  to zero.

#### Interior sound field of the fuselage

A Green function technique is used to evaluate the interior acoustic pressure of the fuselage. It is assumed that the end caps of the finite cylinder are rigid and that the loading effect of the enclosed fluid can be neglected. The Green function chosen for the modeling of the interior pressure distribution corresponds to that used for characterization of sound field in a hard-walled cylindrical room [17], i.e.

$$G(x, r, \theta; x_0, r_0, \theta_0) = \sum_{m=0}^{\infty} \sum_{n=0}^{\infty} \sum_{l=1}^{\infty} \frac{\Theta_m^*(x, r, \theta) \Theta_{ml}^*(x_0, r_0, \theta_0)}{\Lambda_{ml}^*(k_m^2 - k_0^2 + 2jc_{ml}k_{ml})} + \sum_{m=0}^{\infty} \sum_{n=0}^{\infty} \sum_{l=1}^{\infty} \frac{\Theta_{ml}^*(x, r, \theta) \Theta_m^*(x_0, r_0, \theta_0)}{\Lambda_{ml}^*(k_m^2 - k_0^2 + 2jc_{ml}k_{ml})} \quad (13)$$

where the acoustic modal functions are defined by

$$\begin{cases} \Theta_{ml}^*(x, r, \theta) = \cos(k_m x) \cos(n\theta) J(k_m r) \\ \Theta_m^*(x, r, \theta) = \cos(k_m x) \sin(n\theta) J(k_m r) \end{cases} \quad (14)$$

and  $k_{ml}$  is the radial wavenumber verifying the hard-wall boundary conditions  $\partial J(k_m r)/\partial r = 0$ . The normalizing factor  $\Lambda_{ml}^{st}$  is given by

$$\Lambda_{ml}^{st} = \int_V [\Theta_{ml}^{st}]^2 dV \quad (15)$$

The wavenumber  $k_{ml}$  verifies  $k_{ml} = \sqrt{k_m^2 + k_n^2}$ , while  $k_0 = \omega/c_0$  where  $c_0$  is the speed of sound in the enclosed medium. The modal damping constant  $c_{ml}$  in the interior space is related to the surface averaged absorption coefficient by

$$c_{ml} = \frac{1}{16(\pi a^2 L)} \left[ \frac{\alpha_s S_s}{1 - (n/k_m a)^2} + \frac{4\alpha_s S_s}{\varepsilon_m} \right] \quad (16)$$

where  $\alpha_s$  and  $S_s$  represent the surface averaged absorption coefficient and the surface of the curved walls, while  $\alpha_e$  and  $S_e$  are the equivalent quantities for the end walls. Note that the distribution of the absorbing material over the curved and end walls is assumed to be equal (i.e.,  $\alpha_s = \alpha_e = \alpha_a$ ).

Then, the acoustic pressure within the cylinder can be written in terms of the Green function given in Eq. (13) and the normal displacement of the cylinder walls expressed in Eq. (6) as

$$p(x, r, \theta) = p_0 \omega^2 \int_S G(x, r, \theta; x_0, r_0, \theta_0) w(x_0, r_0, \theta_0) dS_0 \quad (17)$$

where  $p_0$  is the density of the enclosed medium. Performing the surface integral in Eq. (17) leads to

$$p(x, r, \theta) = \sum_{n=0}^{\infty} \sum_{m=0}^{\infty} \sum_{l=1}^{\infty} P_{nml}^e \Theta_{nml}^e(x, r, \theta) + \sum_{n=0}^{\infty} \sum_{m=0}^{\infty} \sum_{l=1}^{\infty} P_{nml}^i \Theta_{nml}^i(x, r, \theta) \quad (18)$$

where  $P_{nml}^{e/i}$  are the interior pressure modal amplitudes. Note that the infinite summations in Eq. (18) are truncated and only the first  $N_c$  circumferential modes,  $N_l$  longitudinal modes and  $N_r$  radial modes are taken into account.

Table I: Density and stiffness correction factors

Density	$\mu_n = 1 + \frac{A_p}{hS_p} + \frac{A_t}{hS_t}$
Torsion	$\mu_t = \frac{3D_t^3}{h^3 S_t}$
Axial Bending	$\mu_a = 1 + \frac{1}{I_p S_t} \left( I_p + \frac{D_p^2}{4} \frac{hS_p A_t}{hS_t + A_t} \right)$
Hoop Bending	$\mu_h = 1 + \frac{1}{I_p S_p} \left( I_p + \frac{D_p^2}{4} \frac{hS_p A_p}{hS_t + A_p} \right)$

where  $A_p, A_t$ : frame and longeron cross-section area;  $D_p, D_t$ : frame and longeron height;  $S_p, S_t$ : frame and longeron spacing;  $I_p, I_t$ : frame and longeron area moment of inertia about neutral axis;  $I_p$ : skin area moment of inertia per unit length about neutral axis.

#### Optimization of the absorbers detuning factor

As mentioned previously, the absorbers can be detuned by selecting a natural frequency  $\omega_i$  different from the disturbance frequency  $\omega$ . The  $i^{th}$  absorber is then tuned when  $\alpha_i=1$  and detuned otherwise. Note that tuning or detuning the absorber can be achieved by modifying its stiffness. The detuning factors  $\alpha_i$  ( $i=1, \dots, N_a$ ) are determined such that some cost function is minimized. In this paper, two different cost functions are considered. The first cost function consists of the kinetic energy associated with the normal vibrational field of the cylinder and is expressed as

$$J_{\text{kin}} = \omega^2 q^T q \quad (19)$$

The second cost function is directly related to the average pressure fluctuations throughout the interior volume of the cylinder and is defined as the acoustic potential energy

$$J_{\text{acous}} = \frac{1}{4p_0 c_0} \mathbf{p}^T \mathbf{A} \mathbf{p} \quad (20)$$

where  $\mathbf{p}$  is the column vector of modal pressure amplitudes  $P_{nml}^{e/i}$  and  $\mathbf{A}$  is a diagonal matrix which elements are the normalizing factors given in Eq. (15).

These two cost functions are non-linear functions of the detuning ratio  $\alpha_i$ , which requires implementing a non-linear optimization procedure. The optimization algorithm used in these calculations is the same as that used in [12] and is based on a constrained quasi-Newton approach. Note that the search for the cost function minimum is constrained by a set of upper and lower bounds on the detuning factors.

#### RESULTS AND DISCUSSION

The characteristics of the fuselage are presented in Table II and correspond to that of a BAe 748 propeller aircraft modeled [13]. The effects of frames and stringers have also been included as outlined in [12]. The following results were obtained using  $N_c=7$  circumferential modes,  $N_l=15$  axial modes and  $N_r=3$  radial modes. This modal truncation was shown to converge sufficiently accurately at the frequencies of interest. The propellers induced excitation characteristics as shown in Table III were also deduced from [13]. Two single

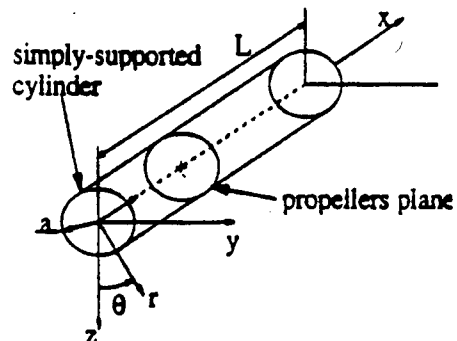


Figure 3: Cylinder coordinate system.

frequencies are investigated; the cruise blade passage frequency (BPF) of the BAe 748 at 88 Hz and twice the BPF at 176 Hz. The amplitude of the external pressure loading due to each propeller was taken to be 50 Pa or 130 dB at the BPF and 20 Pa or 120 dB at twice the BPF which are representative pressure loads from turboprop aircraft [10]. In the following analysis, a number of 16 absorbers ( $N_a=16$ ) are assumed to be mounted on the fuselage positioned in the propeller plane as suggested by previous results [7-9,12]. The angular position of the absorbers was not determined by the dominant mode at the frequency of interest as in [12] but rather by the external pressure loading distribution. These angular positions are  $\theta=5^\circ, 25^\circ, 45^\circ, 65^\circ, 85^\circ, 105^\circ, 125^\circ, 145^\circ, 215^\circ, 235^\circ, 255^\circ, 275^\circ, 295^\circ, 315^\circ, 335^\circ$  and  $355^\circ$ . For most of the calculations, the mass of each absorber is chosen to be 2 kg, which is more physically realizable than the work in [12]. This gives a total control moving mass of 32 kg (with respect to cylinder weight of about 645 kg). The quality factor of the absorbers was selected to be 15. Therefore, the MQ of the system is 480 kg. The stiffness of the detuned absorbers was then adapted in order to optimize the cost functions defined previously. The detuning factors are constrained such that the absorbers natural frequency stay between  $0.2\omega$  and  $1.8\omega$ , i.e.  $0.56 < \alpha_a < 5$ . Note that modal amplitudes are presented for either the fuselage vibrational field or interior acoustic field in the case without absorbers, with tuned absorbers and with detuned absorbers. Since the vibrational and acoustic fields consist of both a  $\cos(n\theta)$  and  $\sin(n\theta)$  component (see Eqs. (6) and (18)), the modal amplitudes are obtained from the square root of the sum of each component squared (i.e. represent the amplitude of a  $\cos(n\theta)$  rotated to the maximum displacement). First, the relative phase between the propellers  $\theta_0$  is considered to be zero and the vibrational and acoustical reduction induced by the tuned and detuned absorbers are investigated as a function of the frequency. In the last section, the absorbers performance to reduce the interior sound field is studied as a function of the synchrophase angle  $\theta_s$ .

Table II: Fuselage model characteristics.

Cylinder Length L	16 m	Frame spacing $S_F$	0.40 m
Cylinder radius a	1.3 m	Frame height $D_F$	0.09 m
Cylinder thickness h	$1.2 \cdot 10^{-3}$ m	Frame area $A_F$	$1.8 \cdot 10^{-4}$ m <sup>2</sup>
Material density $\rho_c$	$2700 \text{ kg/m}^3$	Frame moment of inertia $I_F$	$8.7 \cdot 10^{-7}$ m <sup>4</sup>
Young modulus E	$7.1 \cdot 10^{10}$ N/m <sup>2</sup>	Longeron spacing $S_P$	0.4 m
Poisson ratio $\nu$	0.31	Longeron height $D_P$	0.015 m
Damping ratio $\eta_s$	0.1	Longeron area $A_P$	$0.7 \cdot 10^{-4}$ m <sup>2</sup>
Speed of sound $c_0$	343 m/s	Longeron moment of inertia $I_P$	$2.7 \cdot 10^{-9}$ m <sup>4</sup>
Density of air $\rho_0$	$1.21 \text{ kg/m}^3$	Walls absorption coefficient $\alpha$	0.008 $\pi f$

Table III: Excitation characteristics.

Propellers plane location $x_0$	3.5 m
Axial decay constant d	2.0
Angle of maximum pressure $\theta_0$	$85^\circ$ $275^\circ$
Lower circumferential limit $\theta_L$	$0^\circ$ $190^\circ$
Upper circumferential limit $\theta_U$	$150^\circ$ $340^\circ$
Convection speed $k_c$	1.5

#### Frequency of 88 Hz (BPF) and synchrophase angle of $\theta_s=0^\circ$

The first studied frequency corresponds to the first propeller blade passage frequency, i.e. 88 Hz. Figures 4 and 5 present the modal amplitudes of the fuselage vibrational field and the interior pressure field respectively. The results show that the fuselage vibrational response is dominated by the  $n=1, 2$  and  $3$  circumferential modes, while the acoustic response is dominated by the  $n=1$  and  $2$  modes. Note that only the acoustic modal amplitude are presented only for the first radial mode ( $k=1$ ) as it was found to be the dominant one. When the tuned absorbers are mounted on the fuselage, all modes are seen to be attenuated to some extent. The vibrational kinetic energy and the acoustic potential energy are reduced by 8.5 and 7.5 dB respectively. It should be noticed that the vibrational amplitudes at the absorbers mounting location were attenuated by 10 to 18 dB. Then, the absorbers are detuned to first minimize the kinetic energy. It can be seen in Figure 4 that the  $n=2$  modes have been reduced in contrast to the tuned absorber, while the  $n=1$  and  $n=3$  modes have been increased. The vibrational levels at the absorbers attachment points has been decreased by 8 to 15 dB. Indeed, the attenuation of kinetic energy has been increased to 12.3 dB; however, the acoustic potential energy is again attenuated by 7.5 dB. In that case, the globally detuned absorbers do not out perform the tuned ones in terms of interior sound reduction. Then, the acoustic potential energy is used as a cost function to determine the absorbers detuning factors. This results in 8.2 dB reduction in kinetic energy and 16.3 dB attenuation of the interior sound levels. It can be observed in Figure 4 that the detuned absorbers largely decrease the vibrational amplitudes of the  $n=1$  modes which are well coupled to the interior sound field. Note that the vibration levels under each absorbers are reduced by only 5 dB in average. It is also worth mentioning that the detuning factors vary only between the values  $\alpha_{min}=0.92$  and  $\alpha_{max}=1.3$  (which can be translated into a change in absorber stiffness using the expression

$K=M\omega^2=M\omega^2/\alpha$ ). In fact, previous work considering 4 absorbers [12] resulted in a very large span of the detuning factors (0.56 up to 5) which would be hard to obtain with actual adaptive absorbers. Then, one advantage of having multiple (more than 4) absorbers is that the adaptive absorbers are more physically realizable. The results are summarized in Table IV. It is then evident that globally detuning the absorbers leads to a significant improvement in reduction of the interior field over the tuned absorbers.

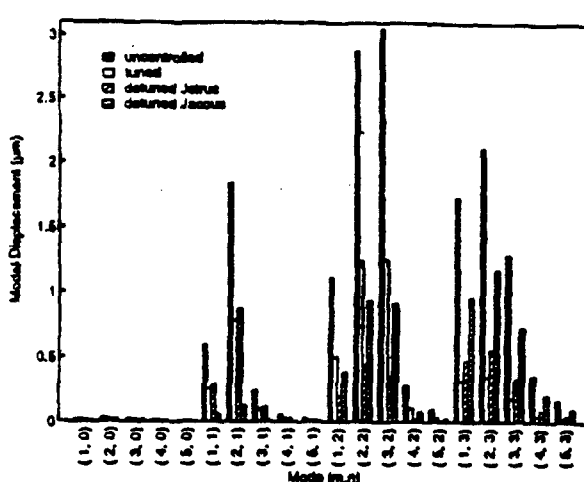


Figure 4: Structural response at 88 Hz.

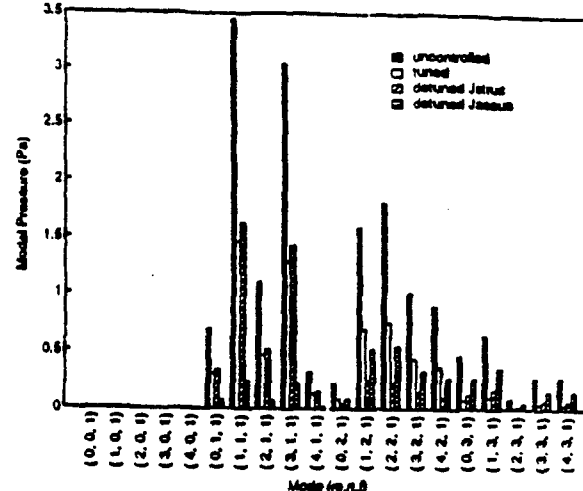


Figure 5: Interior acoustic response at 88 Hz.

#### Frequency of 176 Hz (BPF) and synchrophase angle of $\theta=0^\circ$

The same simulation is then performed at twice the blade passage frequency, i.e. 176 Hz. Figure 6 and 7 show the modal amplitudes of the fuselage vibrational field and the interior pressure field respectively. The results in terms of attenuation obtained are presented in Table V. In Figure 6, it can be seen that a larger number of modes contribute to the vibrational response of the fuselage. However, the acoustic field is mainly associated to the  $n=3$  modes. The tuned absorbers are able to reduce the vibrational kinetic energy and the acoustic potential energy by 10.6 and 11 dB respectively. Note that the vibrational amplitudes at the absorbers mounting location were attenuated by 15 to 30 dB. When the absorbers are detuned to minimize the kinetic energy, they further decrease the vibrational and acoustical modal amplitudes. This leads to an attenuation of about 15 dB for both the kinetic energy and the acoustic potential energy. In that case, the globally detuned absorbers outperform the tuned ones by an increase of 6 dB in interior sound reduction. At last, the acoustic potential energy is used as a cost function. In that case, the  $n=3$  modal amplitudes of the interior pressure is further attenuated. This results in 12.6 dB reduction in kinetic energy and 16.6 dB attenuation of the interior sound levels. Thus, at twice the BPF, the use of globally detuned absorbers also leads to a significant improvement in reduction of the interior field over tuned absorbers. It should also be noticed that the absorbers detuning factors are laying between  $\alpha_{min}=0.72$  and  $\alpha_{max}=1.3$ . These values correspond to more physically realizable adaptive absorbers than that obtained in [12].

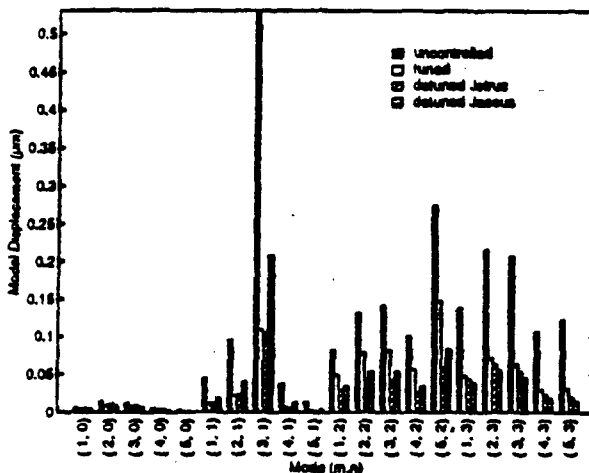


Figure 6: Structural response at 176 Hz.

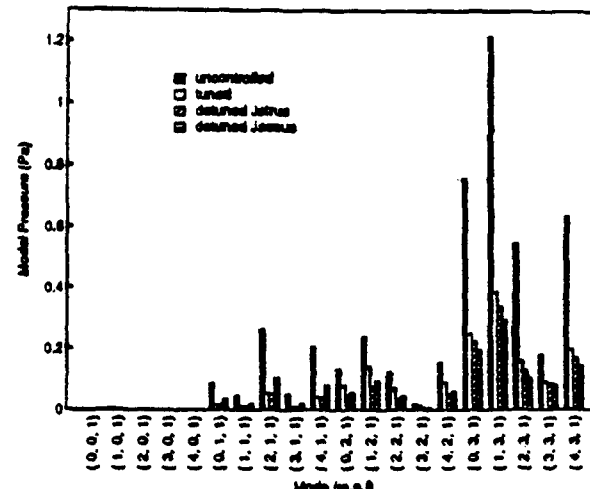


Figure 7: Interior acoustic response at 176 Hz.

### Absorbers with reduced mass MQ=240kg

The mass of each individual absorber is reduced from 2 kg to 1 kg, i.e. the MQ of the system is then divided by two. The attenuation results for the tuned and detuned absorbers are presented in Table VI at 88 Hz (BPF) and a synchrophase angle of  $\theta_s=0^\circ$ . The lighter absorbers do not perform as well as the heavier ones considered previously. This was expected as the mechanical absorbers impedance is directly proportional to its mass (see Figure 2) off-resonance (i.e. detuned). However, a decrease of 10 dB of the interior sound field is obtained using globally detuned absorbers, which is 6 dB over the reduction obtained with tuned absorbers.

Table IV: Results at 88 Hz (BPF)  
and for  $\theta_s=0$ .

	$\Delta J_{\text{redu}}$	$\Delta J_{\text{redu}}$
Tuned	8.7 dB	7.5 dB
Detuned ( $J_{\text{redu}}$ )	12.3 dB	7.5 dB
Detuned ( $J_{\text{redu}}$ )	8.2 dB	16.3 dB

Table V: Results at 176 Hz  
(2BPF) and  $\theta_s=0$ .

	$\Delta J_{\text{redu}}$	$\Delta J_{\text{redu}}$
Tuned	10.6 dB	11.1 dB
Detuned ( $J_{\text{redu}}$ )	15.0 dB	15.8 dB
Detuned ( $J_{\text{redu}}$ )	12.8 dB	16.6 dB

Table VI: Results with reduced mass at 88 Hz (BPF) and for  $\theta_s=0$ .

	$\Delta J_{\text{redu}}$	$\Delta J_{\text{redu}}$
Tuned	6.2 dB	4.3 dB
Detuned ( $J_{\text{redu}}$ )	8.9 dB	4.1 dB
Detuned ( $J_{\text{redu}}$ )	4.6 dB	10.1 dB

### Variation of the synchrophase angle $\theta_s$

The last tests are concerned with the variation of the synchrophase angle  $\theta_s$ , representing the relative phase between the two propellers. Figure 8 and 9 present the attenuation results as a function of  $\theta_s$ , obtained without, with the tuned and with the detuned absorbers, at 88 Hz (BPF) and at 176 Hz (2 BPF) respectively. Note that the MQ of the system is 480 kg and that the absorbers detuning factors are obtained by minimizing the acoustic potential energy  $J_{\text{redu}}$ . It can be seen that when no absorbers are mounted on the fuselage, there exists some optimum synchrophase angles for which the interior noise reduction is important (about 13 dB). They correspond to  $\theta_s=30^\circ$  and  $90^\circ$  at 88 Hz and  $\theta_s=120^\circ$  at 176 Hz. This phenomenon has been used to experimentally reduce cabin noise [2]. The attenuation obtained by adding tuned absorbers to the fuselage is only slightly dependent on the synchrophase angle and is in the order of 7.5 dB at the BPF and 10 dB at twice the BPF. The detuned absorbers perform in average 6 dB better than the tuned absorbers for both studied frequencies. Note that at the first BPF, the attenuation obtained with the globally detuned absorbers depends on the synchrophase angle, and the reductions are slightly more important for large  $\theta_s$  (see Figure 8).

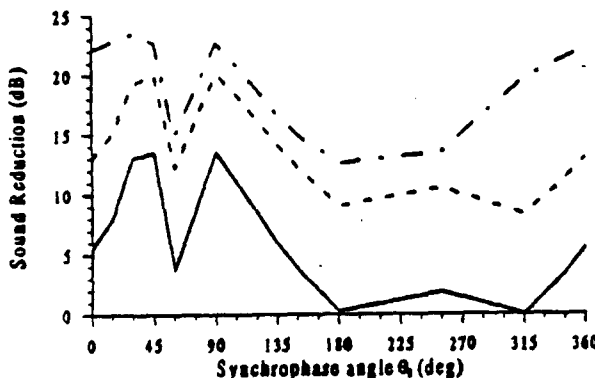


Figure 8: Sound reduction as function of  $\theta_s$ : — without absorbers, ..... with tuned absorbers, - - - with detuned absorbers  $J_{\text{redu}}$ , at 88 Hz (BPF).

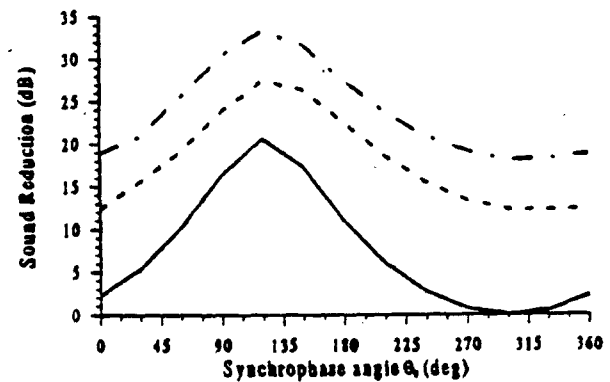


Figure 9: Sound reduction as function of  $\theta_s$ : — without absorbers, ..... with tuned absorbers, - - - with detuned absorbers  $J_{\text{redu}}$ , at 176 Hz (2BPF).

### CONCLUSIONS

An analytical model of the structural acoustic behavior of a propeller aircraft including vibrational absorbers attached to the fuselage has been developed. It was then used to study the potential of multiple tuned and detuned absorbers for reducing interior noise. A set of 16 absorbers of 2 kg each (more realistic than the work in [12]), was located in the propeller plane. The results demonstrate that the absorbers can provide an attenuation of 10-16 dB in the acoustic potential energy. Globally detuning the absorbers to minimize the acoustic potential energy was also demonstrated to give improved attenuation over tuned absorbers. The results also show that the values of detuning factors were more feasible to obtain with actual adaptive absorbers than that in [12]. Thus, an important advantage of having multiple (more than 4) absorbers is that the adaptive

absorbers are more physically realizable. Further analysis indicated that the attenuations are only slightly sensitive to the synchrophase angle (representative of the relative phase between the two propellers) at the first blade passage frequency of 88 Hz.

#### ACKNOWLEDGMENTS

The authors gratefully acknowledge the support of this work by the Office of Naval Research under Contract N00014-94-C-0026; Dr. Kam Ng, Technical Monitor.

#### REFERENCES

- [1] C.R. Fuller, "Analytical model for investigation of interior noise characteristics in aircraft with multiple propellers including synchrophasing," *Journal of Sound and Vibration*, 109(1), 1986, 141-156.
- [2] B. Magliozi, "Synchrophasing for cabin noise reduction of propeller-driven airplanes," AIAA-83-0717, 1983.
- [3] S.J. Elliott, P.A. Nelson, I.M. Stothers and C.C. Boucher, "Preliminary results of in-flight experiments on the active control of propeller-induced cabin noise," *Journal of Sound and Vibration*, 128(2), 1989, 355-357.
- [4] C.M. Dorling, G.P. Eatwell, S.M. Hutchins, C.F. Ross and S.G.C. Sutcliff, "A demonstration of active noise reduction in an aircraft cabin," *Journal of Sound and Vibration*, 128(2), 1989, 358-360.
- [5] C.R. Fuller and J.D. Jones, "Experiments on reduction of propeller induced interior noise by active control of cylinder vibration," *Journal of Sound and Vibration*, 112(2), 1987, 389-395.
- [6] M.A. Simpson, T.M. Luong, C.R. Fuller and J.D. Jones, "Full-scale demonstration tests on cabin noise reduction using active vibration control," *AIAA Paper 89-1074*, 1989.
- [7] W.G. Halvorsen and U. Emborg, "Interior Noise control of the SAAB 340 Aircraft," *Proceedings of the Business Aircraft Meeting and Exposition*, Wichita, Kansas, SAE Paper 89-1080, April 11-13 1989.
- [8] E.H. Waterman, D. Kaptein and S.L. Sarin, "Fokker's activities in cabin noise control for propeller aircraft," *Proceedings of the Business Aircraft Meeting and Exposition*, Wichita, Kansas, SAE Paper 89-0736, April 11-13 1989.
- [9] H.J. Hackstein, I.U. Borchers, K. Renger and K. Vogt, "The Dornier 32B Acoustics Test Cell (ATC) for interior noise tests and selected test results," *Proceedings of the DGLR/AIAA 14th Aeroacoustics Conference*, Aachen, Germany, DGLR/AIAA Paper 92-02-164, May 11-14 1992.
- [10] B. Leigh and R. Garcia, "The use of tuned vibration absorbers to reduce cabin noise in regional turboprop aircraft," *Canadian Aeroacoustics and Space Journal*, Vol 40, No. 2, June 1994, 62-67.
- [11] A.H. von Flotow, A. Beard and Don Bailey, "Adaptive tuned vibration absorbers: tuning laws, tracking agility, sizing, and physical implementations," *Proceedings of Noise-Con 94*, Ft. Lauderdale, FL, May 1994, 437-454.
- [12] C.R. Fuller, J.P. Maillard, M. Mercadal and A.H. von Flotow, "Control of aircraft interior noise using globally detuned vibration absorbers," *Proceedings of First Joint CEAS/AIAA Aeroacoustics Conference*, Germany, Volume 1, 1995, pp. 615-624.
- [13] D.R. Thomas, P.A. Nelson and S.J. Elliott, "Active control of the transmission of sound through a thin cylindrical shell, Part I: The minimization of vibrational energy," *Journal of Sound and Vibration*, 167(1), 1993, 91-111.
- [14] D.R. Thomas, P.A. Nelson and S.J. Elliott, "Active control of the transmission of sound through a thin cylindrical shell, Part II: The minimization of acoustic potential energy," *Journal of Sound and Vibration*, 167(1), 1993, 113-128.
- [15] A.W. Leissa, "Vibration of Shells," *NASA SP-288*, 1973.
- [16] H.C. Nelson, B. Zapotowski and M. Bernstein, "Vibration analysis of orthogonally stiffened circular fuselage and comparison with experiment," *National Specialist Meeting on Dynamics and Aeroelasticity*, November 1958.
- [17] P.M. Morse and K.U. Ingard, *Theoretical Acoustics*, Princeton University Press, Princeton, New Jersey, Second edition, 1986.

## **APPENDIX 31**

ADAPTIVE VIBRATION ABSORBERS FOR CONTROL OF SOUND RADIATION FROM PANELS.

By

Francois Charette  
Chris R. Fuller  
James P. Carneal

Vibration and Acoustics Laboratories  
Mechanical Engineering Department  
Virginia Polytechnic Institute & State University  
Blacksburg, Virginia, U.S. VA 24061-0238

**ABSTRACT**

Vibration absorbers are typically used to minimize the vibration of structures at localized points. The focus of the work presented here is to use adaptive tunable vibration absorbers (ATVA) for sound minimization instead of vibration minimization. New and original ATVA's were developed and implemented experimentally. Two types of excitation are considered; harmonic and band pass (i.e. broadband over a certain frequency range). Results obtained when the plate is excited harmonically show that a certain level of sound attenuation can generally be realized when the absorber resonance frequency corresponds to the excitation frequency, i.e., absorber is tuned. The results also show that an increase in sound reduction is achieved when the absorber resonance frequency is not equal to the excitation frequency, i.e. absorber is detuned. Furthermore, although tunable vibration absorbers can be viewed as a single frequency device, the band pass results suggest that an acoustic cost function (e.g. radiated power) over a certain frequency range can be used in order to obtain a global sound reduction over that frequency range.

**INTRODUCTION**

Sound radiation generated by structural vibrations is present in our everyday life and has always been a subject of great interest. Historically, passive approaches for control have been the most popular one due to their low cost and availability. There is a great variety of passive approaches. Usually they minimize sound by adding some sort of damping on or around the structure. These approaches are generally not efficient at low frequencies and for transportation applications (e.g. airplanes, cars, etc.) the added weight is not desirable.

In the last 10 to 15 years, active control has become an interesting alternative for applications where passive control approaches were difficult to implement. The development of active control has become possible mainly due to the advances in DSP chips that are constantly becoming faster and cheaper. The application of active control to efficiently minimize sound radiation from structure has been demonstrated by many authors <sup>1,2,3,4,5</sup>, just to name a few. Unfortunately, active control typically requires significant electrical power for the control transducers and a high computational overhead for the control calculations (especially for broadband control).

Active-passive control (or adaptive control) is becoming increasingly popular. The idea is to take advantage of the complementary nature of simultaneous active and passive control to expand the bandwidth and stability of the control. It offers the possibility of designing new approaches that have increased noise control performance with a much lower control authority/power requirement. The passive part will always insure a certain amount of sound minimization while the active part will be present to enhance this minimization. The computational requirement is typically very low since there is no "real" time control signal needed as in active control. Unfortunately, compact and efficient adaptive transducers are not readily available.

The present work discusses the development and use of new ATVA's for sound reduction of panels. The basic idea of an ATVA is to be able to change (adjust according to the condition of operation) the characteristics of the absorber (i.e. resonance frequency). Such transducers consume very little electrical power and have a very low computational overhead. The only electrical power needed is during the adjustment of the characteristics.

## 1. THEORY: S-S PLATE MODEL WITH ATVA'S

The analytical model for a simply supported (s-s) plate with tunable vibration absorbers is presented in this section. The ATVA basic equations are presented first.

### 1.1 Adaptive Tunable Vibration Absorber (ATVA)

A single degree of freedom ATVA is generally modeled as a rigid mass mounted on a spring/dash-pot mechanism (see Figure 1). The term "tunable" implies that the resonance frequency of the absorber can be changed. This can be achieved by changing the mass and/or stiffness. Generally, it is easier and more convenient to change the stiffness rather than the mass. A survey of possible concepts that can be used to build a tunable vibration absorber has been presented previously by Sun *et al.*<sup>6</sup>.

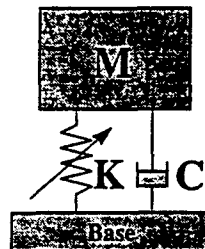


Figure 1: Schematic of a single degree of freedom ATVA.

The dynamics of absorbers (lumped mass-spring system) can be found in many books and articles of vibrations and dynamics<sup>7,8</sup>. Recently, Fuller *et al.*<sup>9</sup> have presented an overview on the dynamics of adaptive tunable vibration absorbers and their use for the reduction of sound pressure level. In order to be concise, the basic equations of ATVA (in terms of impedance) and the definition of certain constants used throughout the present article are recalled in what follows.

The mechanical impedance of an absorber attached to a moving base is given by,

$$Z^{abs} = j \cdot M^{abs} \cdot \alpha \cdot \omega^{abs} \cdot \left[ \frac{1 + j \cdot \alpha/Q}{1 - \alpha^2 + j \cdot \alpha/Q} \right] \quad (1)$$

where  $M^{abs}$  is the rigid mass of the absorber,  $\omega^{abs}$  is the resonance (i.e. natural) frequency of the absorber, 'Q' is the quality factor and  $\alpha$  the ratio between the disturbance frequency and resonance frequency of the absorber. In the present article,  $\alpha$  is called the tune ratio and is given by,

$$\alpha = \frac{\omega}{\omega^{abs}}. \quad (2)$$

Note, for harmonic excitation, this ratio is equal to 1 when the absorber resonance frequency is equal to the excitation frequency. In this case, the absorber is "tuned".

The resonance frequency of the absorber is simply,

$$\omega^{abs} = \sqrt{\frac{K^{abs}}{M^{abs}}}. \quad (3)$$

The quality factor 'Q' is an indicator of the sharpness of the absorber resonance peak and is related to damping as

$$Q = \frac{M^{abs} \cdot \omega^{abs}}{C^{abs}}, \quad (4)$$

Figure 2 presents the normalized impedance of a ATVA as a function of the normalized frequency  $\alpha$ . Three curves are presented in order to show the effects of the mass and quality factor 'Q' on the impedance values. An increase or decrease of the ATVA mass ( $M^{abs}$ ) simply translates the curve up and down, while the quality factor, 'Q', changes the sharpness of the peak (i.e. damping).

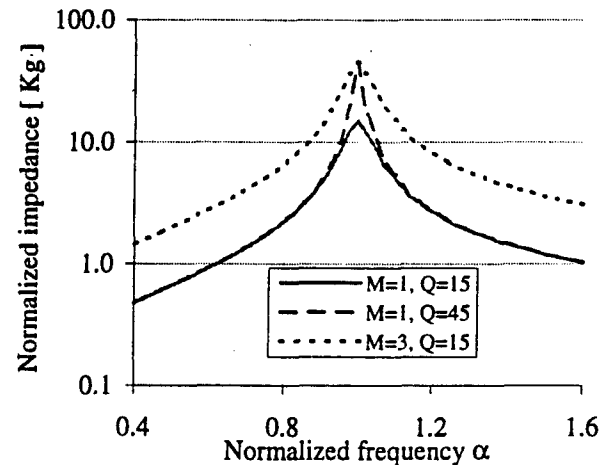


Figure 2: Normalized impedance of an ATVA

### 1.2 Plate transversal displacement

The approach used for the plate-ATVA model developed here is similar to that used by Fuller *et al.*<sup>9</sup> for their cylinder model. The system studied is shown in Figure 3. It consists of a simply supported plate with a piezoelectric actuator used for disturbance excitation. A piezoelectric actuator is composed of two identical

collocated piezoceramic patches on each face of the plate. The piezoceramic patches are assumed to be perfectly bonded to the plate surface. A symmetric actuation (pure flexure) is induced in the plate when the two piezoceramic patches are driven 180° out of phase<sup>1</sup>. Under these conditions, the piezoelectric actuator excitation corresponds to line moments applied on the periphery of the actuator itself. The transverse displacement of a simply supported rectangular plate excited by piezoelectric actuators has been studied previously by Dimitriadis *et al.*<sup>10</sup>, Crawley *et al.*<sup>11</sup>, Kim *et al.*<sup>12</sup> and Charette *et al.*<sup>13</sup>.

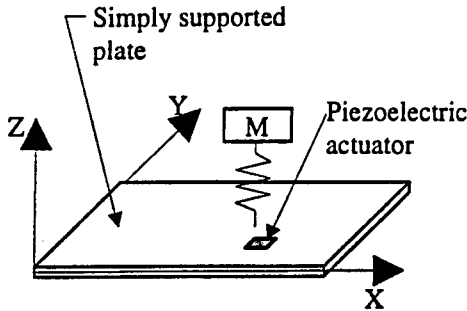


Figure 3: Schematic of the simply supported plate.

Using the classical modal approach, the simply supported plate displacement can be written as a sum of modal contributions of the form,

$$w(x, y) = \sum_{p=1}^P \sum_{q=1}^Q \hat{W}_{pq} \cdot \sin\left(\frac{p \cdot \pi \cdot x}{L_x^{pl}}\right) \cdot \sin\left(\frac{q \cdot \pi \cdot y}{L_y^{pl}}\right). \quad (5)$$

In this last equation, 'p' and 'q' are the modal order in the x and y direction, respectively,  $\hat{W}_{pq}$  are the modal amplitudes associated with the piezoelectric actuation and the absorbers forces. This equation can be written in matrix form,

$$w(x, y) = \langle B_{PQ} \rangle \hat{W}_{PQ}. \quad (6)$$

where '{ }' represents a column vector while the '< >' bracket represents a line vector. The line vector terms are given by

$$B_{pq} = \sin\left(\frac{p \cdot \pi \cdot x}{L_x^{pl}}\right) \cdot \sin\left(\frac{q \cdot \pi \cdot y}{L_y^{pl}}\right) \quad (7)$$

The difficulty in equations (5) and (6) is the fact that the modal amplitudes depends on the plate displacement at the position of the absorbers. Since the absorber forces are coupled to the plate response, one has to build a system of linear equations to determine the modal amplitudes. In order to build this system of equations, the absorber forces and piezoelectric moments have to be expressed as modal contributions. This is presented in the next sections.

### 1.3 Absorber modal force

The action of the absorbers on the plate can be modeled as point forces. If there is a total of 'K' absorbers on the plate, then the force of the k<sup>th</sup> absorber mounted on the plate is given by,

$$F_k^{abs} = -Z_k^{abs} \cdot (j \cdot \omega \cdot w(x_k^{abs}, y_k^{abs})) \quad (8)$$

where the term ' $j \cdot \omega \cdot w(x_k^{abs}, y_k^{abs})$ ' represents the velocity of the plate at the position of the absorber, 'j' being the complex number  $\sqrt{-1}$ . The coupling between the forces of the absorbers and the plate displacement is clearly shown in this equation. The forces of all the absorbers can be written in matrix form as follows,

$$\{F_K^{abs}\} = -j \cdot \omega \cdot [Z]_{K,K} \cdot [B_{K,PQ}] \cdot \{\hat{W}_{PQ}\}. \quad (9)$$

Here, [Z] is a diagonal matrix whose terms contains the impedance of each absorbers (equation (1)) and matrix [B] is a rectangular matrix whose terms are given by,

$$B_{k,pq} = \sin\left(\frac{p \cdot \pi \cdot x_k^{abs}}{L_x^{pl}}\right) \cdot \sin\left(\frac{q \cdot \pi \cdot y_k^{abs}}{L_y^{pl}}\right) \quad (10)$$

The contribution of the 'K' absorbers can be written as a distributed function of the form,

$$f^{abs}(x, y) = \sum_{k=1}^K F_k^{abs} \cdot \delta(x - x_k^{abs}) \cdot \delta(y - y_k^{abs}) \quad (11)$$

where  $\delta$  is the Dirac function.

In order to find the response of the plate, it is convenient to write the force input function of the absorbers as modal contributions,

$$f^{abs}(x, y) = \sum_{p=1}^P \sum_{q=1}^Q \hat{F}_{pq}^{abs} \cdot \sin\left(\frac{p \cdot \pi \cdot x}{L_x^{pl}}\right) \cdot \sin\left(\frac{q \cdot \pi \cdot y}{L_y^{pl}}\right), \quad (12)$$

where  $\hat{F}_{pq}^{abs}$  corresponds to the modal forces of the absorbers.

Equation (11) and (12) leads to,

$$\begin{aligned} & \sum_{p=1}^P \sum_{q=1}^Q \hat{F}_{pq}^{abs} \cdot \sin\left(\frac{p \cdot \pi \cdot x}{L_x^{pl}}\right) \cdot \sin\left(\frac{q \cdot \pi \cdot y}{L_y^{pl}}\right) \\ & = \sum_{k=1}^K F_k^{abs} \cdot \delta(x - x_k^{abs}) \cdot \delta(y - y_k^{abs}) \end{aligned} \quad (13)$$

Then, using the orthogonality properties of the plate mode shape on this last equation, the absorbers modal forces written in matrix form are found to be,

$$\{\hat{F}_{PQ}^{abs}\} = \frac{4}{L_x^{pl} \cdot L_y^{pl}} \cdot [B_{PQ,K}] \cdot \{F_K^{abs}\}. \quad (14)$$

In this equation, the vector  $\{F_k^{abs}\}$  is given by equation (9) and the matrix corresponds to the transpose matrix of equation (9).

#### 1.4 Piezoelectric actuator modal moments

The piezoelectric moments of 'N' actuators can be expressed as

$$m^{pz}(x, y) = \sum_{n=1}^N M_n^{pz} \cdot \left( \begin{array}{l} (\delta'(x - x_n^{pz})) - \delta'(x - x_n^{pz})) \\ \cdot (h(y - y_n^{pz})) - h(y - y_n^{pz})) \\ + (h(x - x_n^{pz})) - h(x - x_n^{pz})) \\ \cdot (\delta'(y - y_n^{pz})) - \delta'(y - y_n^{pz})) \end{array} \right) \quad (15)$$

where 'h' is the unit step function and the equations needed to calculate  $M_n^{pz}$  are given in Dimitriadis *et al.*<sup>10</sup>. The value of the variable  $M_n^{pz}$  depends on the mechanical and piezoelectric properties of the actuator and plate. This variable  $M_n^{pz}$  represents the amplitude of the line moment applied at the edges of the piezoelectric actuator. The expression of  $M_n^{pz}$  is obtained from a static analysis, equilibrium of forces and moments.

Using the same development as for the absorbers, one can arrive at the modal moments of the piezoelectric actuators,

$$\{\hat{M}_{PQ}^{pz}\} = \frac{4}{L_x^{pl} \cdot L_y^{pl}} \cdot [D_{PQ,N}] \cdot \{M_N^{pz}\}, \quad (16)$$

where

$$D_{pq,n} = -\frac{(p \cdot L_y^{pl})^2 + (q \cdot L_x^{pl})^2}{p \cdot q \cdot L_y^{pl} \cdot L_x^{pl}} \cdot \left( \cos\left(\frac{p \cdot \pi \cdot x_n^{pz}}{L_x^{pl}}\right) - \cos\left(\frac{p \cdot \pi \cdot x_n^{pz}}{L_x^{pl}}\right) \right) \cdot \left( \cos\left(\frac{q \cdot \pi \cdot y_n^{pz}}{L_y^{pl}}\right) - \cos\left(\frac{q \cdot \pi \cdot y_n^{pz}}{L_y^{pl}}\right) \right) \quad (17)$$

#### 1.5 Plate modal amplitudes

Solving the standard differential equation of motion for thin plates leads to the plate modal amplitudes, which are,

$$\hat{W}_{pq} = \frac{1}{\rho^{pl} \cdot L_z^{pl} \cdot (\omega_{pq}^2 - \omega^2)} \cdot (\hat{F}_{pq}^{abs} + \hat{M}_{pq}^{pz}). \quad (18)$$

This last equation written in matrix form for all the modes considered is,

$$\{\hat{W}_{PQ}\} = [H_{PQ,PQ}] \cdot \{\hat{F}_{PQ}^{abs}\} + [H_{PQ,PQ}] \cdot \{\hat{M}_{PQ}^{pz}\}, \quad (19)$$

where '[H]' is a diagonal matrix whose  $(pq,pq)^{th}$  term is given by,

$$H_{pq,pq} = \frac{1}{\rho^{pl} \cdot L_z^{pl} \cdot (\omega_{pq}^2 - \omega^2)} \cdot (\hat{F}_{pq}^{abs} + \hat{M}_{pq}^{pz}). \quad (20)$$

Substituting equations (14) and (16) into (19) leads to,

$$\begin{aligned} \{\hat{W}_{PQ}\} &= \frac{4}{L_x^{pl} \cdot L_y^{pl}} \cdot ([H_{PQ,PQ}] \cdot [B_{PQ,K}] \cdot \{F_K^{abs}\} \\ &\quad + [H_{PQ,PQ}] \cdot [D_{PQ,N}] \cdot \{M_N^{pz}\}) \end{aligned} \quad (21)$$

Then, replacing equation (9) in this last equation and rearranging, the following system of linear equations is obtained,

$$\begin{aligned} &\left[ [I_{PQ,PQ}] - \frac{j \cdot 4 \cdot \omega}{L_x^{pl} \cdot L_y^{pl}} [H_{PQ,PQ}] [B_{PQ,K}] [Z_{K,K}^{abs}] [B_{K,PQ}] \right] [\hat{W}_{PQ}] \\ &= \frac{4}{L_x^{pl} \cdot L_y^{pl}} \cdot [H_{PQ,PQ}] [D_{PQ,N}] \cdot \{M_N^{pz}\} \end{aligned} \quad (22)$$

where [I] is the identity matrix. The solution of this system of linear equations yields the modal amplitudes of the plate. Once these modal amplitudes are known, equation (6) can be used to calculate the displacement of the plate.

Once the displacement of the plate is known, it is possible to determine the radiated power and the mean square velocity of the plate. The radiated power is obtained by integrating the far-field intensity over a hemisphere<sup>1,14</sup> and can be calculated as<sup>5</sup>,

$$\begin{aligned} \Pi &= \frac{\omega^4 \rho_0}{8\pi^2 c_0} \\ &\times \int_0^{2\pi} \int_{\pi/2}^{\pi} \left| \tilde{w} \left( \frac{\omega}{c_0} \cdot \sin\theta \cdot \cos\phi, \frac{\omega}{c_0} \cdot \sin\theta \cdot \sin\phi \right) \right|^2 \\ &\cdot \sin\theta d\theta d\phi \end{aligned} \quad (23)$$

where  $\tilde{w}$  is the double spatial Fourier transform of the displacement and  $c_0$ ,  $\rho_0$  are respectively the sound speed and density of the surrounding medium. The mean square velocity is defined as the spatial and temporal average of the squared transversal plate velocities, i.e.,

$$\dot{v}^2 = \frac{1}{L_z^{pl} \cdot L_y^{pl}} \cdot \int_0^{L_z^{pl}} \int_0^{L_y^{pl}} \frac{1}{2} \left| \frac{\partial w}{\partial t} \right|^2 dy dx. \quad (24)$$

## 2. THEORETICAL RESULTS

Results obtained using the model developed in the first section of this paper are presented here. The idea is to use the model to optimize the position and/or resonance frequency of the ATVA in order to minimize the radiated power of a simply supported plate. Two types of disturbance are studied; single frequency and band pass (i.e. broadband over a certain frequency range). The single frequency case is presented first and is the typical application for a ATVA. The band pass case is studied to see what kind of results is possible to obtain with simple transducers such as a ATVA. The result presented in this section are valid for one ATVA having a mass of 0.16 kg (=10% the total mass of the plate) and a quality factor 'Q' of 50. The simply supported plate characteristics considered are given in Table I, while the piezoelectric actuator characteristics and position are given in Table II.

Table I: Simply supported plate characteristics

Length	38.0 cm
Width	30.0 cm
Thickness	2.1 mm
Young modulus.	$2.0 \times 10^{11}$ Pa
Density	7750 Kg/m <sup>3</sup>

Table II: Piezoelectric actuator characteristics

Length	3.79 cm
Width	3.16 cm
Thickness	0.27 mm
Pos. of the center along the X axis	26.6 cm
Pos. of the center along the Y axis	9.0 cm
Young modulus	$6.3 \times 10^{10}$ Pa
$d_{31}$	$2.1 \times 10^{-10}$ m/V

The Brent optimization algorithm is used here<sup>15</sup>. Given a specified position of the ATVA, the optimization algorithm finds the ATVA resonance frequency that yields the greatest reduction in radiated power.

### 2.1 Single frequency disturbance

The optimal tune ratios  $\alpha$  (i.e. resonance frequency), to reduce the sound radiated from the plate-ATVA system at a given frequency, for all the frequencies between 50Hz and 300 Hz are given in Figure 4. Note that the position of the ATVA is given by  $X/L_x = 0.65$  and  $Y/L_y = 0.45$ . Values of  $\alpha$  equal to 0.4 indicate that

the optimization algorithm could not converge for those frequencies since the tune range was limited to  $0.4 \leq \alpha \leq 2.0$ .

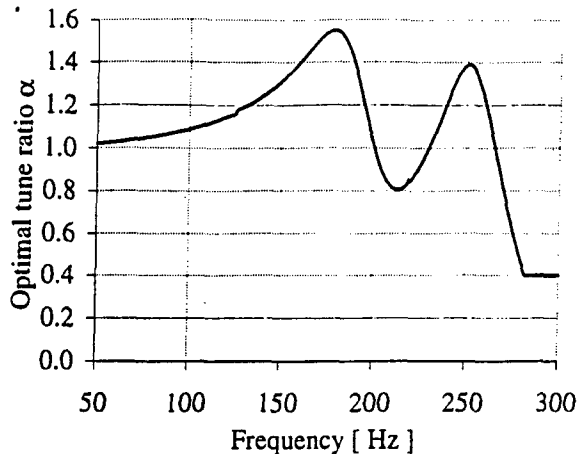


Figure 4: Optimal tune ratio  $\alpha$  for frequencies between 50Hz and 300Hz.

Two frequencies are studied in this section; i) 91Hz, which correspond to the first resonance frequency of the plate alone and ii) 150Hz, which is an off resonance frequency of the plate alone. Table III presents the results. At 91Hz, tuning the absorber to the excitation frequency (i.e.  $f_{res}^{abs}=91$ Hz) leads to radiated power reduction of 44.6dB, while detuning the absorber using the optimal tune ratio  $\alpha=1.07$  (i.e.  $f_{res}^{abs}=85$ Hz) allows to obtain a further 14.9dB attenuation (for a total reduction of 59.5dB). In contrast, the results for the 150Hz case shows that the tuned ATVA actually increases the radiated power by 25.1dB, while the detuned case  $\alpha=1.31$  (i.e.  $f_{res}^{abs}=114.5$ Hz) reduces the radiated power by 12.5dB. This represents a difference of 37.6dB between the tuned and detuned case for the frequency of 150Hz. This demonstrate the advantage of detuning the ATVA.

Table III: Harmonic results, theoretical radiated power reductions

	Opt. $\alpha$	Reduction (dB) Detuned case (optimal $\alpha$ )	Reduction (dB) Tuned case ( $\alpha = 1.0$ )
91 Hz (ON res.)	1.07	59.5	44.6
150 Hz (OFF res.)	1.31	12.5	-25.1

These results are explained in the following discussion. Installing an ATVA on a plate completely changes the dynamics of the plate; one ends up with a new mechanical system consisting of the "plate-ATVA" (coupled system). The resonance frequencies of this new plate-ATVA system depend on the

properties of the ATVA (e.g. resonance frequency, position, etc.). This means that for each resonance frequency of the ATVA, the dynamics of the plate-ATVA system changes. Therefore, simply tuning the ATVA to the excitation frequency may or may not lead to a resonance frequency of the system plate-ATVA. The results presented demonstrate this effect. In the case of the 91Hz, tuning the ATVA leads to an off-resonance of the plate-ATVA system, while the 150Hz case did the opposite and led to a resonance of the plate-ATVA system. Adjusting (i.e. detuning) the ATVA resonance frequency such that the radiated power of the plate is minimized, will always try to change the coupled dynamics to an off-resonance of the plate-ATVA system. In some instance, depending on the ATVA characteristics, it may not be possible to detune the ATVA in order to approach an off-resonance condition of the plate-ATVA system. This is exactly what is shown in Figure 4 for frequencies greater than 280Hz when the optimization algorithm could not converge. For these frequencies, other positions of ATVA should be tested.

## 2.2 Band pass disturbance

The frequency band considered here is  $50\text{Hz} < f < 300\text{Hz}$ . The first three modes of the plate are within this frequency band.

Given a position of the absorber, the optimization algorithm finds the resonance frequency that yields the greatest reduction in radiated power between  $50\text{Hz} < f < 300\text{Hz}$ . Figure 5 shows the maximum reduction possible as a function of the absorber position on the plate. The reduction varies between 0dB and 3.8dB. The resonance frequencies needed to obtain these reductions are given in Figure 6. Positions where the resonance frequencies are equal or greater to 300Hz indicates that the algorithm could not converge since 300Hz is the high limit of the frequency band considered here. Therefore, the only relevant positions for the ATVA are approximately situated between  $0.4 < X/L_x < 0.9$  and  $0.15 < Y/L_y < 0.9$  in the present study.

The maximum global reduction possible with the ATVA considered here, in the frequency band of interest, is 3.84dB. The position associated with this reduction is  $X/L_x=0.7$  and  $Y/L_y=0.35$ . This is almost directly over the excitation actuator. In order to not physically damage the piezoelectric actuator by putting the ATVA directly on it (i.e. in the experimental setup), the position chosen to be used here is  $X/L_x = 0.65$  and  $Y/L_y = 0.45$ . This is slightly away from the excitation actuator. The expected reduction at that position is 3.2dB for an ATVA resonance frequency of 109Hz.

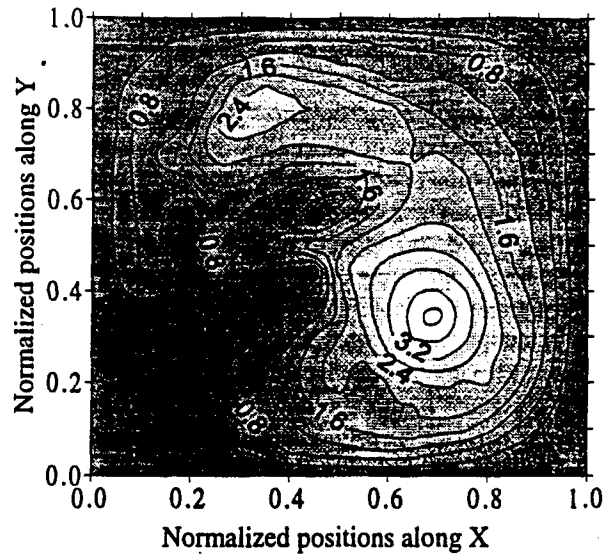


Figure 5: Reductions (dB) of radiated power between  $50\text{Hz} < f < 300\text{Hz}$  as a function of the ATVA position.

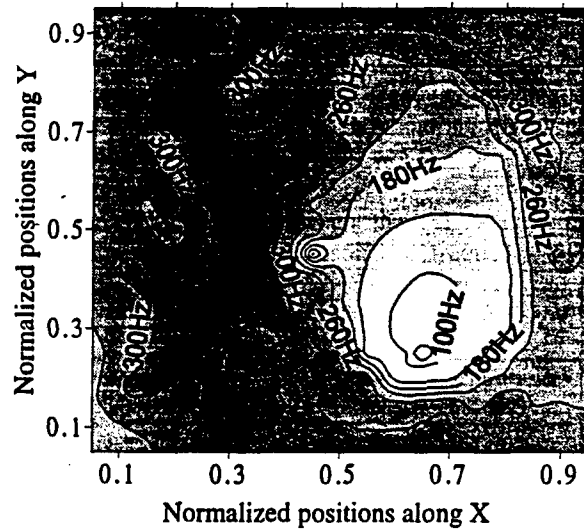


Figure 6: Resonance frequency of the ATVA needed to obtain the reductions shown in Figure 5.

Figure 7 presents the radiated power of the plate alone and that obtained when an ATVA is installed on the plate. The radiated power for three different values of resonance frequencies of the ATVA are presented for discussion purposes. The effects of the ATVA on the plate dynamics are concentrated between 50Hz and 235Hz for the ATVA resonance frequencies considered here (i.e., 85Hz, 91Hz and 109Hz) and are discussed in what follows.

Figure 7 shows that when the ATVA resonance frequency is equal to the resonance frequency of the

plate first mode, a new resonance and anti-resonance appears in the radiated power (i.e., curve 'ATVA  $f_r=91\text{Hz}$ '). In order for this new anti-resonance to coincide with the resonance of the plate first mode (i.e. 91Hz) the ATVA resonance frequency has to be 85Hz (i.e., curve 'ATVA  $f_r=85\text{Hz}$ '). This yields the largest reduction possible for harmonic excitation at 91Hz. Note that this ATVA resonance frequency ( $f_r=85\text{Hz}$ ) was determined as the optimal one by the optimization algorithm as presented in the previous section.

Figure 7 also depicts that by changing the resonance frequency of the ATVA from 85Hz to 91Hz, the anti-resonance frequency is shifted up by 9Hz. On the other hand, the second resonance frequency of the coupled system is shifted up by only 3Hz. Therefore, as the ATVA resonance frequency is increased, the anti-resonance frequency increases faster than the second resonance frequency. This indicates the possibility that the anti-resonance (zero) frequency could coincide with the second resonance (pole) frequency. In other words, the zero would cancel the pole. This is exactly what the optimization algorithm for the band pass case is trying to achieve. The resonance for the ATVA found by the optimization algorithm is 109Hz and the curve of radiated power associated with this resonance frequency is also shown in Figure 7.

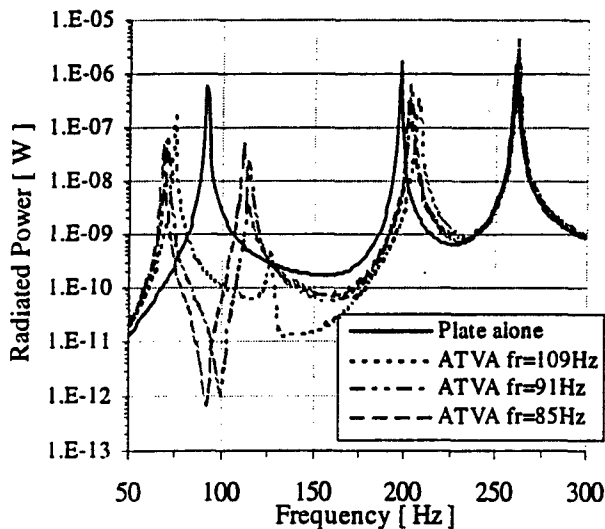


Figure 7: Theoretical radiated power of the plate alone and with the ATVA ( $X/L_x=0.65$ ,  $Y/L_y=0.45$ ) having different resonance frequency.

The peak at 125Hz shown in Figure 7 (i.e., curve 'ATVA  $f_r=109\text{Hz}$ ') is due to the fact that the resonance (pole) and anti-resonance (zero) do not perfectly coincide. In this simulation, it was assumed that the ATVA resonance frequency could be adjusted by step of 1.0 Hz. Indeed, to achieve perfect cancellation the

ATVA resonance frequency should be precisely 109.523Hz. Such high resolution in frequency is presently impossible to reach in experiments. Therefore, using a frequency resolution of 1.0Hz leads a small resonance peak at 125Hz (see Figure 7) as the zero-pole cancellation is not perfect.

### 3. EXPERIMENTAL RESULTS

As mentioned in section 1.1 of this work, there are many different ways to implement an ATVA. Two new types of ATVA were developed and implemented experimentally in this study. One is called the "V" type ATVA while the other is called the "I" type ATVA. These ATVA's were implemented on two different simply supported plates because they have different mass. Multiple "V" type ATVA (i.e. two in the present study) for a total active mass of 400g were tested on a plate of 8.4kg giving a ratio 'mass absorber/mass plate' of around 0.05. A single "I" type absorber having an active mass of 157g was tested on a plate of 1.86kg, which represents a ratio 'mass absorber/mass plate' of around 0.09. The idea is to keep the ratio 'mass absorber/mass plate' as low as possible since it is desired to mainly use the dynamics of the ATVA, not the added mass effects.

#### 3.1 Experimental "V" type ATVA

A picture of the new "V" type ATVA is shown in Figure 8.

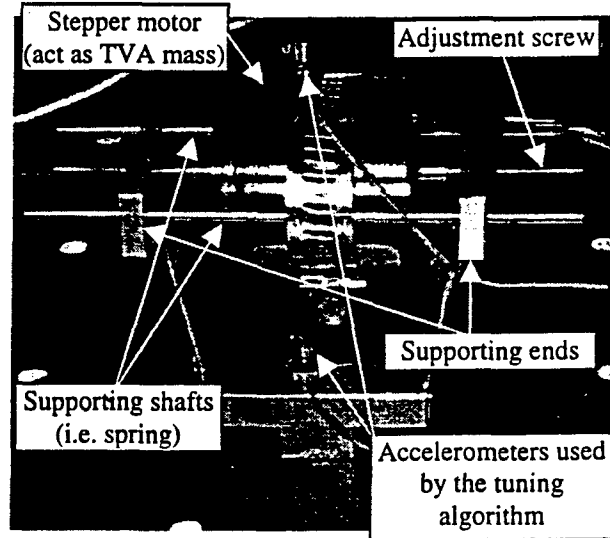


Figure 8: "V" type ATVA.

The basic principle of this new type of ATVA is to use a stepper motor to move back and forth the

supporting ends. This changes the length of the supporting shafts which effectively changes their stiffness. Therefore, the resonance frequency of the ATVA is changed. Note, in this design, the stepper motor also acts as the ATVA active mass. Figure 9 presents the frequency response of the "V" type ATVA for different length of shaft. A 25mm separation distance yields a resonance frequency of about 170Hz, while a 3mm separation distance corresponds to a resonance frequency of 310Hz.

The "V" type ATVA can be adjusted electronically by a controller. Two "V" type ATVA's were fixed on the simply supported described in Table IV. Tests to compare the results obtained when the ATVA's are tuned to those obtained with the ATVA's detuned were performed. The experimental setup used is shown in Figure 10. Seven monitoring microphones were positioned above the plate. The sum of the square of the amplitude of the signals from the seven microphones gives an estimate of the radiated power of the plate.

The following experimental procedure was used for each frequency tested. First, each ATVA is set to its high tune limit and a measurement of the microphone signals is made. When the ATVA are set to their high limit they simply act as added masses. This high limit measurement is used as reference to compare the tuned results to the detuned ones. Once the high limit measurement is finished, then each ATVA is electronically tuned to the excitation frequency and a second measurement is performed. Finally, the third measurement is made once the ATVA's are electronically detuned in order to minimize the sum of the square of the amplitudes of the microphone signals using the global detuning algorithm.

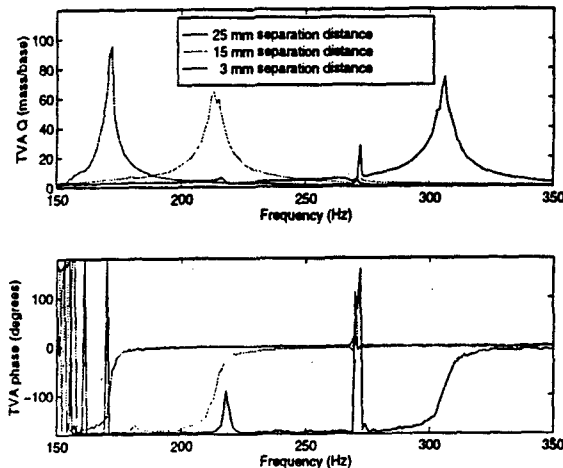


Figure 9: Different FRF of the "V" type ATVA.

The global detuning algorithm used is based upon the least mean squares (LMS) steepest descent gradient algorithm and was programmed on a TMS320C30 digital signal processor (DSP) mounted in a Personal Computer (PC). To increase the maximum sampling rate, the number of operations performed by the DSP was minimized. Therefore, the data acquisition and the single frequency Fourier transform calculations were performed on the DSP, while the controller logic and output signals to control the ATVA were performed on the PC. The sample rate for the controller was set at approximately ten times the excitation frequency with each error signal consisting of 100 time sample points. This leads to an update for the output approximately every 0.1 seconds at a sampling frequency of 1000 Hz. In order to tune the ATVA's, the signals from two accelerometers on the ATVA's (see Figure 8) were driven to be in quadrature (i.e., 90° out of phase).

Table IV: Simply supported plate characteristics used with the "V" type ATVA.

Length	60.0 cm
Width	42.5 cm
Thickness	4.2 mm
Young modulus.	$2.0 \times 10^{11}$ Pa
Density	7750 Kg/m <sup>3</sup>

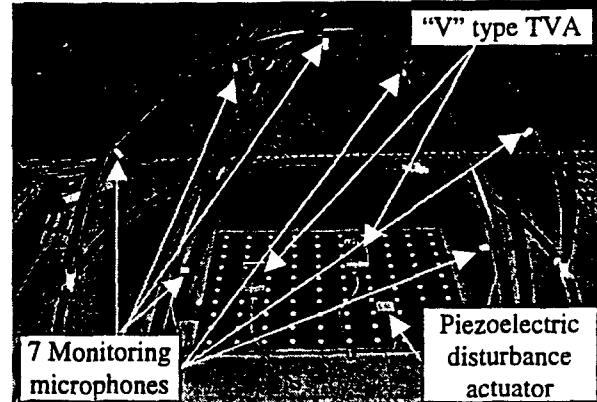


Figure 10: "V" type ATVA experimental setup.

Two frequencies were tested, 118Hz and 183Hz. The radiated power reductions for each frequency are presented in Table V. Figure 11 and 12 present the modal amplitude distribution for each frequency.

Table V: Harmonic results, experimental radiated power reductions

	Reduction (dB) Detuned case (optimal $\alpha$ )	Reduction (dB) Tuned case ( $\alpha = 1.0$ )
118 Hz	8.1	4.7
183 Hz	18.7	-1.2

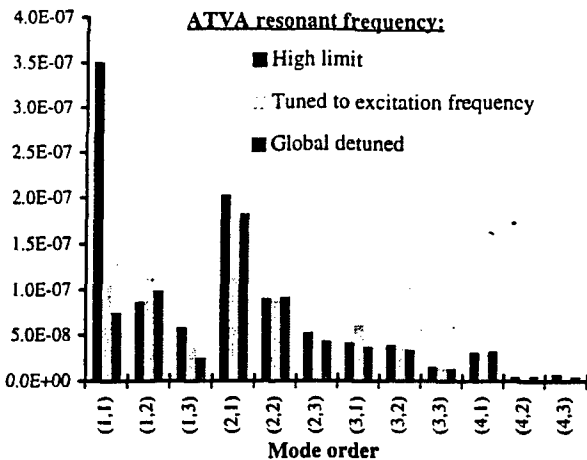


Figure 11: Modal amplitude distribution at 118Hz.

In the case of 118Hz, a reduction of around 4.7dB was achieved by tuning the ATVA but the global detuning algorithm obtained 8.1 dB. This represents an increased reduction of 3.4dB compared to the tuned case. Figure 11 shows that the increase in reduction can be associated with modal restructuring<sup>1</sup>. The 183Hz case shows that simply tuning the ATVA to the excitation frequency can actually increase the radiated power of the plate (by 1.2dB in the present case). The global detuning algorithm can reduce the radiated power by about 18.7dB for that same frequency of 183Hz. This represents a total difference of 19.9dB between the tuned and detuned case for the 183Hz frequency and supports the trend of the theoretical results. Figure 12 shows that the tuned case actually increases the contribution of the strong radiator modes<sup>1</sup> (i.e. odd-odd order modes) while the detuned case decreased the contribution of these modes, especially the (1,1) which is a strong radiator at that frequency<sup>1</sup>.

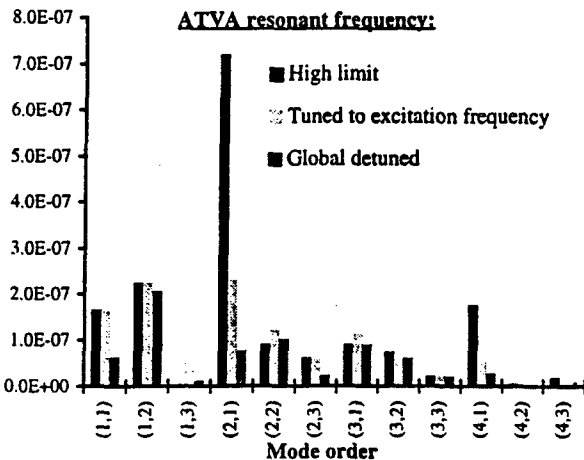


Figure 12: Modal amplitudes distribution at 183Hz.

The experimental results show that the tendency predicted by the model in section I are good and clearly validate that the detuned ATVA's yield much larger sound attenuation than the tuned ones.

### 3.2 Experimental "I" type ATVA

In order to verify the predicted global reduction by the model for the band pass disturbance, the simply supported plate described in Table I with the piezoelectric actuator (Table II) was implemented experimentally. One "I" type ATVA was fixed on the plate. The transversal velocities of the plate were measured at 100 points using a laser vibrometer, mounted on a traverse.

A photo of the "I" type ATVA is shown in Figure 13. The principle of this new type of ATVA is simple. A mass is mounted on a threaded shaft. The shaft screw pitch is equal to that of the spring. Therefore, the shaft can be screwed in and out of the spring. By screwing the shaft in and out, the number of active coils change, thus altering the stiffness and resonance frequency of the ATVA.

This type of absorber is very compact. The total moving mass of the absorber is the top mass and the mass of the shaft. There is no added mass due to any mounting system. At this stage the absorber is not adjustable electronically, but the "electronic" version of this absorber is presently being designed and built. For the objectives of the present section, a "manual" ATVA, such as the one presented in Figure 13, can be used. Figure 14 compares the frequency response measured experimentally to the theoretical one.

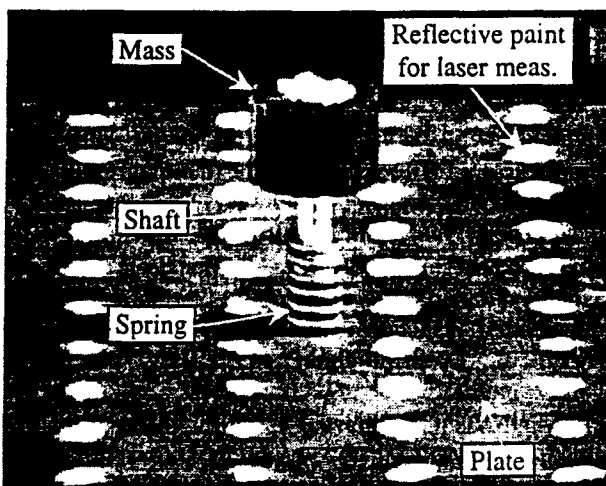


Figure 13: "I" type ATVA.

The radiated power of the plate with and without the ATVA ( $M^{\text{abs}} = 157\text{g}$ ,  $X/L_x = 0.65$ ,  $Y/L_y = 0.45$  and  $f_{\text{res}}^{\text{abs}} = 114\text{Hz}$ ) obtained experimentally are compared in Figure 15. The radiated power is calculated from the experimental measurements of the transversal velocities using equation (23) with the discrete double spatial Fourier transform given by,

$$\hat{w} \left( \frac{\omega}{c_0} \cdot \sin \theta \cdot \cos \phi, \frac{\omega}{c_0} \cdot \sin \theta \cdot \sin \phi \right) = \frac{L_x^{\text{pl}} : L_y^{\text{pl}}}{R \cdot S} . \quad (25)$$

$$\times \sum_{r=1}^R \sum_{s=1}^S w(x_r, y_s) \cdot e^{j \frac{\omega}{c_0} (\sin \theta \cdot \cos \phi \cdot x_r + \sin \theta \cdot \sin \phi \cdot y_s)}$$

In equation (25), the measuring points indices in the  $x$  and  $y$  direction are "r" and "s" respectively, for a total number of points in each directions given by "R" and "S".  $R=S=10$  points in the present study. The parameters  $x_r$  and  $y_s$  give the position of a measuring point, while  $w(x_r, y_s)$  is the measured displacement (i.e. velocity) of that point.

The theoretical results presented in section 2 were obtained using a resonance frequency for the ATVA of 109Hz while the resonance frequency used for the experimental results presented here was around 114Hz. The difference between the resonance frequency of the actual ATVA with the one considered theoretically results from the fact that there are always some discrepancy between assumed theoretical conditions and real experimental conditions (e.g. boundary conditions, plate mechanical and dynamical properties etc.).

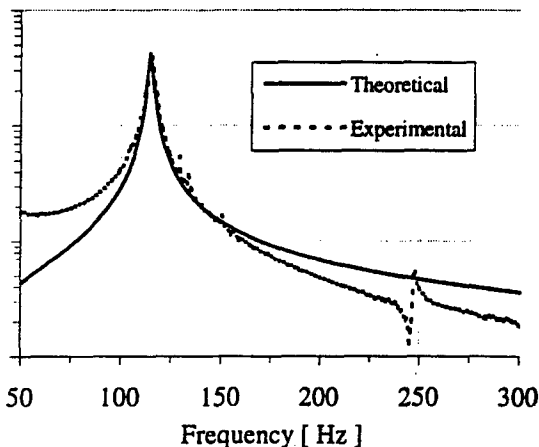


Figure 14: ATVA frequency response for  $f_{\text{res}}^{\text{abs}} = 114\text{Hz}$ .

From Figure 15, the reduction of radiated power obtained experimentally can be seen to be about 3.0dB. This is close to the 3.2dB predicted by the analytical model. Comparing Figure 7 (looking at the curves

'plate alone' and 'ATVA  $f_r=109\text{Hz}$ ' in that figure) with Figure 15, one can see that the difference in reduction between theoretical and experimental results comes mainly from the unpredicted small peak at 155Hz that appears in the experimental results (Figure 15). This small peak is probably due to sideways motion of the absorber in the experimental setup. Theoretically, the absorber should only be able to move up and down. Unfortunately in the experimental setup, the flexural stiffness of the spring used may not have been sufficient to insure no side motion of the ATVA. Except for the peak at 155Hz, Figure 7 (curves 'plate alone' and 'ATVA  $f_r=109\text{Hz}$ ') and Figure 15 are practically identical, which shows that the theoretical modeling of the plate-ATVA system is correct and confirms that global reduction of radiated power over a certain frequency band can be obtained using an ATVA.

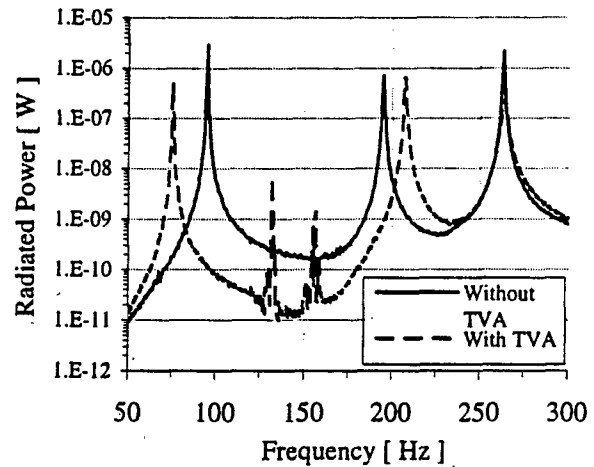


Figure 15: Experimental radiated power of the plate with and without the ATVA ( $M=0.157\text{Kg}$ ,  $f_{\text{res}}^{\text{abs}} = 114\text{Hz}$ ).

## CONCLUSIONS

A theoretical model for simply supported plates with tunable vibration absorbers (ATVA) was presented. New and original ATVA's were developed and implemented experimentally. The model was used to optimize the resonance frequency and/or position of a ATVA in order to minimize the radiated power of the plate. Two types of excitation, harmonic and band pass, were considered.

The harmonic case clearly demonstrated that the best sound attenuation, for a given position, is generally obtained with a "detuned" ATVA. Both the theoretical

and experimental results show that it is not sufficient to use a vibration cost function for the ATVA (i.e. resonance frequency of the ATVA is equal to the excitation frequency, tune ratio  $\alpha=1$ ), since it does not necessarily leads to the best reduction of sound radiation. Actually, in some cases, it can lead to an increase of sound radiation. It is much better to use an acoustic cost function, such as the minimization of the radiated power, in order to "detune" the ATVA.

In the case of the band pass disturbance, the results of the present paper show that radiated power reduction can be achieved over a frequency band, i.e.  $50\text{Hz} < f < 300\text{Hz}$ . A global reduction of radiated power of around 3.0dB was obtained theoretically and experimentally. This reduction may seem modest, but it is obtained with an extremely simple transducer that does not need any outside source of power once it is adjusted at the right resonance frequency. Use of multiple ATVA's is likely to improve the band pass performance.

The results thus suggest that active-passive transducers such as ATVA, which requires much lower electrical power than conventional transducers (e.g. PZT, shakers, etc.), can be used to efficiently minimize sound radiation from structures.

## ACKNOWLEDGEMENTS

This work is supported by NASA Langley Research Center and the ONR.

## REFERENCES

- 1) C.R. Fuller, S.J. Elliott and P.A. Nelson "Active control of vibration," Academic Press Limited, London (1996).
- 2) P.A. Nelson and S.J. Elliott, "Active control of sound," Academic Press Limited, London (1992).
- 3) C.R. Fuller, "Active control of sound transmission/radiation from elastic plates by vibrational inputs: I. Analysis," Journal of Sound and Vibration **136**, 1-15 (1990).
- 4) R.L. Clark and C.R. Fuller, "Experiments on active control of structurally radiated sound using multiple piezoelectric actuators," Journal of the Acoustical Society of America **91**(6), 3313-3320 (1992).
- 5) C. Guigou, A. Berry, F. Charette, and J. Nicolas "Active control of finite beam volume velocity using shaped PVDF sensor," Acta Acustica Journal **82**(5), 772-783 (1996).
- 6) J.Q. Sun, M.R. Jolly and M.A. Norris "Passive, Adaptive and Active Tuned Vibration Absorbers - A Survey," Transactions of the ASME **117**, 234-242 (1995).
- 7) J.P. Den Hartog, "Mechanical vibrations," 4<sup>th</sup> Edition McGraw-Hill, New York (1956).
- 8) W.T. Thomson, "Theory of vibration with applications," 2<sup>nd</sup> Edition Prentice-Hall, New Jersey (1981).
- 9) C.R. Fuller, J.P. Maillard, M. Mercadal and A.H. von Flotow, "Control of aircraft interior noise using globally detuned vibration absorbers," Proceedings of the First Joint CEAS/AIAA Aeroacoustics Conference, Germany, Volume 1, 615-624 (1995).
- 10) E.K. Dimitriadis, C.R. Fuller and C.A. Rogers "Piezoelectric actuators for distributed vibration excitation of thin plates," Journal of Vibration and Acoustics. **113**, 100-107 (1991).
- 11) E.F. Crawley and J. de Luis "Use of piezoelectric actuators as elements of intelligent structures," AIAA Journal **25** (10), 1373-1385 (1987).
- 12) S.J. Kim and J.D. Jones "Optimal design of piezoactuators for active noise and vibration control," AIAA Journal **29**, 2047-2053 (1991).
- 13) F. Charette, A. Berry and C. Guigou "Dynamical effects of piezoelectric actuators and sensors on plate response," accepted for publication in the Journal of Intelligent Material and Structures.
- 14) M.C. Junger and D. Feit, "Sound, Structures and their interactions," The MIT Press, Cambridge (1972), re-issued (1986).
- 15) W.H. Press, B.P. Flannery, S.A. Teukolsky and W.T. Vetterling, "Numerical Recipes in C; The Art of Scientific Computing," Cambridge University Press, Cambridge (1988).

## **APPENDIX 32**

## Bimorph and Pseudo Shear Mode Actuation

L. Eric Cross

Intercollege Materials Research Laboratory  
The Pennsylvania State University  
University Park, PA 16802-4800 USA

In an earlier meeting we reported preliminary results on a piezoelectric double amplifier concept to provide a light weight high amplitude acoustic source for air acoustic noise control. The continuing development is part of a cooperative program with Dr. Christopher Fuller's group at Virginia Polytechnic Institute (VPI) and Materials Systems Inc (MSI). The original concept (fig. 1) was to used amplified response from two vertical bimorph generators to drive a flexing diaphragm in the orthogonal direction. For the simple unconstrained bimorph the amplification factor over the linear bar displacement

$$A_B = \frac{3}{2} \left( \frac{L}{t} \right) \quad (1)$$

where L is the length and t the thickness. For the flexing element

$$A_F = \frac{w}{h} \quad (2)$$

so that the total amplification

$$A_T = \frac{3}{2} \left( \frac{L}{t} \right) \left( \frac{w}{h} \right) \quad (3)$$

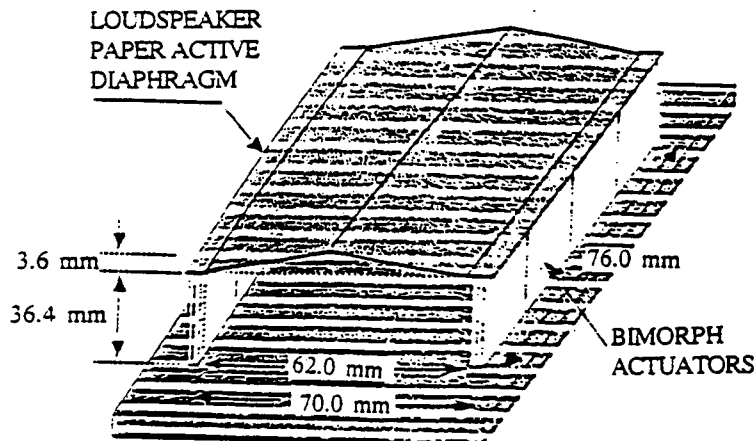


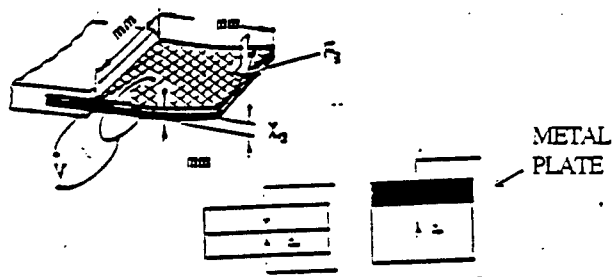
Fig. 1. Bimorph Driven Double Amplifier

some 254 times for the dimensions in Fig. 1 adequate to develop near field sound pressure of 135 dB at 600 Hz with an acoustic impedance -2000 Rayls.

To improve performance a broad ranging study of the performance of short, end clamped bending mode actuators was undertaken. The configuration used is shown in Fig. 2a, and the simple measuring setup in Fig. 2b. To permit direct comparison all actuators were fabricated from the same piezoceramic, thickness t, length h, and width w of the active ceramic plate was the same, and all were driven by the same electric field. As a figure of merit we chose for our application

$$(Tip displacement \times Blocking Force)/Admittance. \quad (4)$$

Bending Effect



BIMORPH      UNIMORPH

(a)

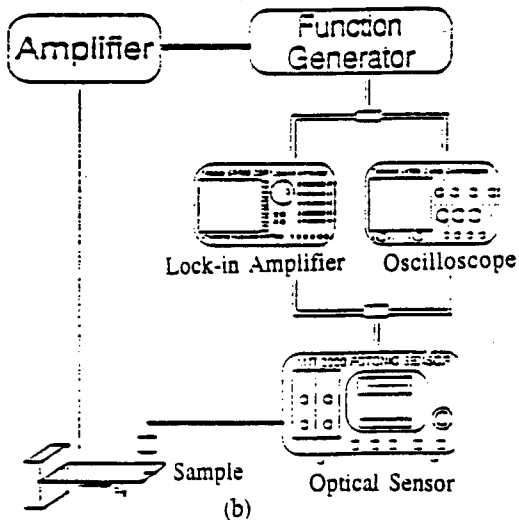


Fig. 2 (a). Typical Bending Mode Actuators.

Fig. 2 (b). Measuring System.

Results for a wide range of bending mode systems are summarized in Table 1 where performance is scaled to that of a simple bimorph taken as 1 in each category (blocking force, displacement, admittance).

Only the  $d_{33}$  driven systems, as expected show significant advantage, although there is a modest improvement with the L-shaped system which is important for the envisaged amplifier configuration.

It should be stressed that the figure of merit chosen does not speak to the robustness of the system or the advantages of slow and benign degradation in performance which are significant advantages for Thunder, Crescent, and Rainbow types.

TABLE I  
FIGURE OF MERIT FOR  
SEVERAL TYPES OF ACTUATORS

TYPE OF PIEZOELEMENT	Displa-cement	Blocking Force	Admit-tance	Figure of Merit
$d_{33}$ Bimorph (PK1550)	1	1	1	1
$d_{33}$ Unimorph (SS301 PK1550)	0.41	1.3	1.0	0.74
L-Shape $d_{33}$ Bimorph ( $A_1/A_2=0.50$ )	0.75	1.5	1.0	1.13
L-Shape $d_{33}$ Unimorph (SS301 PK1550)	0.31	2.7	1.0	0.84
RAINBOW Auto Ceramic (C3900 C)	0.19-0.22	0.1-1.2	0.66	0.03-0.40
CRESCENT -25°C (SS301 PK1550)	0.44	1.75	0.91	0.35
THUNDER -60°C (GA1P155A, A2)	0.12	0.36-1.0	0.90	0.05-0.13
Shear-mode $d_{31}$ (3003HD)	<0.1	?	1	-
$d_{33}$ Bimorph (PK1550)	2.5	1.52	-1	3.80
$d_{33}$ Unimorph (SS301 PK1550)	0.72	3.5	-1	2.52

Based on the L shaped monomorph a new PANEL design has been fabricated using more robust carbon fiber reinforced composite diaphragm (Fig. 3). The expected performance is shown in Fig. 4.

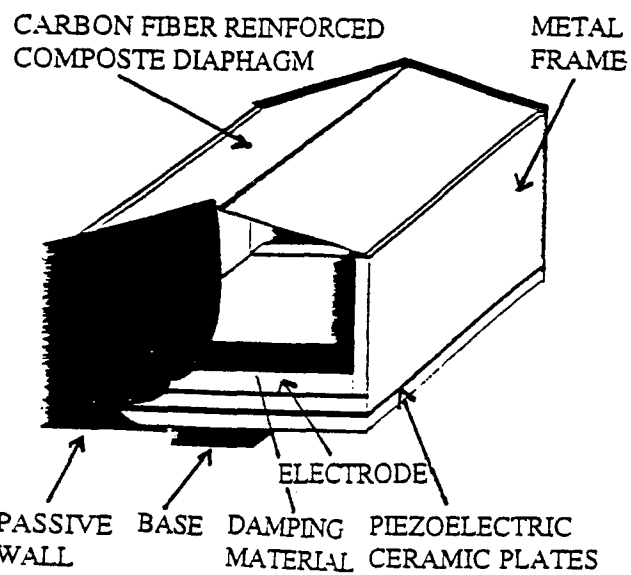


Fig. 3. PANEL: L-shaped Unimorph Driven Double Amplifier

PANEL: Calculated sound pressure of single device based on model of baffled piston

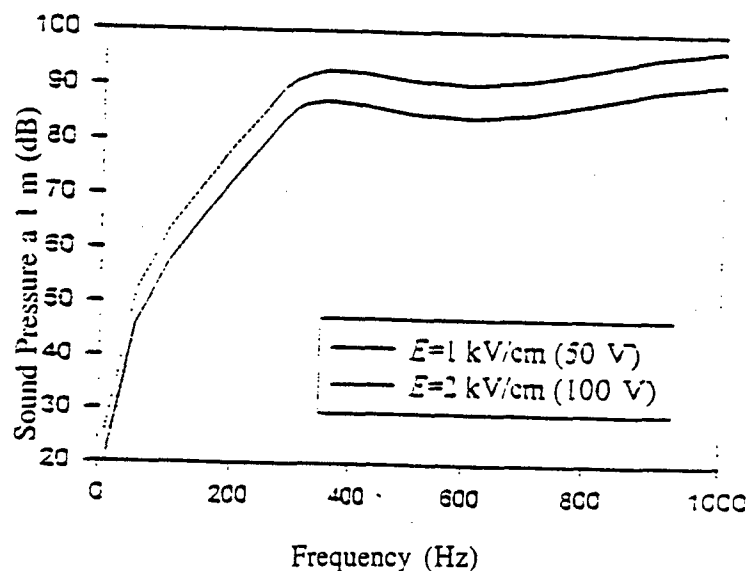
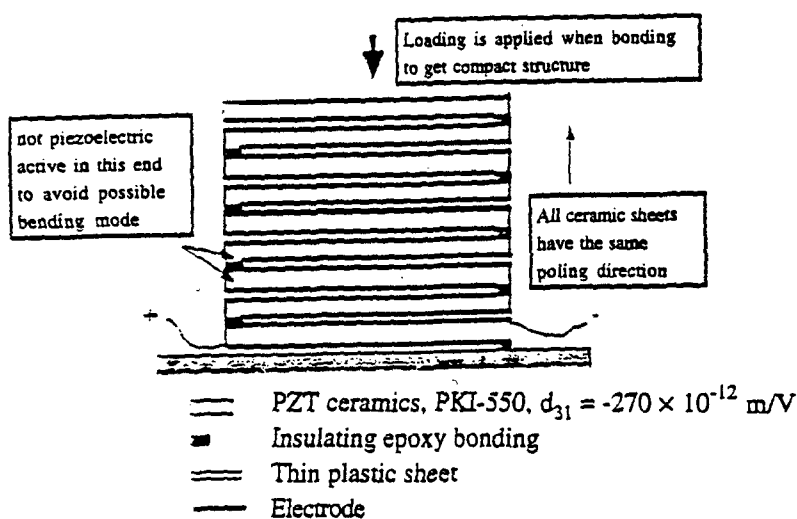


Fig. 4. Expected Performance for PANEL Sound Source.

To enhance lower frequency performance a new type of pseudo shear mode actuator is being explored. The device is essentially a folded  $d_{31}$  driven linear actuator (Fig. 5) which develops translation of the upper platen with respect to the base and thus a shearing motion. Performance for a 40 layer structure in PZT5H is given in Fig. 6.

Performance figures for a low frequency sound generator based on the pseudo-shear actuator will be presented.



#### ADVANTAGES:

1. Only need two connection wires.
2. Eliminate the undesirable low resonance bending modes.
3. Easy fabrication.
4. Blocking force could be larger than bending actuators.
5. Displacement increases with the number of PZT layers.

Fig. 5. Construction of Pseudo-Shear Mode Actuator.

Top Layer Displacement vs. Driving Electric Field for  
40 Layers PSEUDO-SHEAR Actuator  
(Layer dimensions: 30×10×0.45 mm)

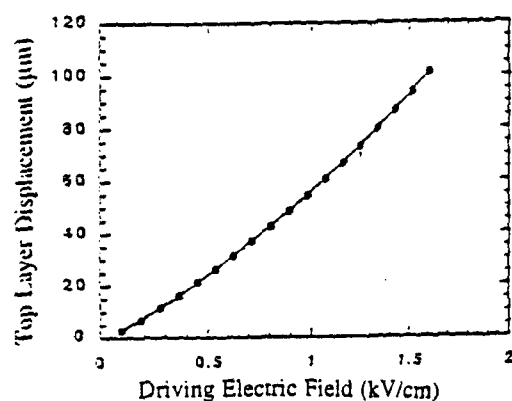


Fig. 6. Transverse Static Displacement for a 40 Layer Pseudo-Shear Device in Soft PZT.

# **APPENDIX 33**

## Piezoelectric Double Amplifier Systems for Air Acoustic Noise Control

L. Eric Cross

Intercollage Materials Research Laboratory

The Pennsylvania State University

University Park, Pennsylvania 16802-4800 USA

**Abstract.** The piezoelectric bimorph is a very well known amplifying structure, and more recently the "cymbal" modification of the "moonie" structure has also been shown to provide gain. In this work the two concepts have been combined to develop a thin diaphragm structure driven by a U-shaped configuration of piezoelectric bimorph and unimorph actuators, to act as an effective acoustic source which is both lighter and more compact than the equivalent electromagnetic transducer. The role of the diaphragm is two-fold: it amplifies the tip displacement of the piezoelectrics by a factor of 5-20 and also increases the source emitting area. Amplitude of vibration and useable frequency range depend on the dimensions and materials. In the current design, the overall dimensions of the device are  $52 \times 50 \times 24$  mm. The U-shaped frame of the device is made of 0.2 mm thick stainless steel, with soft PZT ceramic as the active driving elements. The diaphragm is of 0.2 mm thick light carbon fiber reinforced composite. Experiments have demonstrated diaphragm amplitude exceeding 0.5 mm in the range well below resonance ( $v_r \sim 300\text{-}400$  Hz) and useable response up to 1.5 kHz. Mechanical quality factor of the system is adjusted between 2 and 50 by a suitable choice of damping layer.

The transducer developed was tested as a sound control element in the integrated system for active noise control at Virginia Polytechnic Institute (Christopher Fuller). Six independently controlled PANELs were mounted over the vibrating aluminum plate forming an effective active skin. The adaptive feed forward Filters-x Least-Mean-Square (LMS) Algorithm was employed in the six input, six output control scheme. Far field microphones were used for each of the six error sensors, while ten additional far field microphones enabled estimation of the sound power radiated before and after the implementation of control. Experiments revealed that attenuation of more than 10 dB is attainable over the frequency range of interest.

A brief report will also be given of a new pseudo-shear mode driven diaphragm source which is being implemented for lower frequency higher amplitude control.

### 1. Introduction

Monolithic piezoelectric transducers are well known as generating massive stress ( $\sim$ tons/in $^2$ ) but only minuscule strain ( $\sim 10^{-3}$ ). What is however most frequently needed for air acoustic control are very much larger displacements from a compact source (much higher strain) but only relatively weak force (stress). In this study, two conventional piezoelectric strain amplifier, the bimorph and the flexensional cymbal are combined in a unique orthogonal arrangement to provide gain  $\sim 250$  times in the strain generated in a compact PANEL (Piezoelectric Acoustic Noise Eliminating) structure [1]. The PANEL generator is approximately  $50 \times 50 \times 24$  mm with the  $50 \times 50$  surface being the radiating plane. The square panels can

be assembled into a sheet only ~1" thick in which local surface displacement amplitudes exceeding 0.5 mm can be generated over the frequency range 300 to 1.5 kHz and controlled in both amplitude and phase [2].

An array of six independently controlled PANEL generators have been tested in a system for active noise control at Virginia Polytechnic Institute (Christopher Fuller). The PANELs form an active skin over a vibrating aluminum plate and using adaptive feed-forward control were shown to provide attenuation of more than 10 dB for the far field noise in the frequency range of interest.

A very broad ranging study of the many new bending mode amplifier configurations showed that none were capable of the force/displacement required at lower frequencies. A new type of pseudo-shear mode stacked actuator has been designed and shown to have many promising performance characteristics in larger area very thin low frequency panels.

## 2. Amplifier Development

The load line for a typical monolithic soft PZT 5H is shown schematically in figure 1a, and is clearly completely unsuitable for air acoustics where what is needed is as in figure 1b. To achieve the needed surface displacements ~mms for a plate only 1" (2.5 cm) thick requires strain levels ~10%, i.e. gain in an amplifier structure of order 100. Two strain amplification structures are well known, the simple bending mode bimorph (figure 2a) and the more recent cymbal (figure 2b). Clearly, the gains of these two systems could be multiplied together by mounting them orthogonally as in figure 2c, which could be simplified to an arrangement as in figure 2d.

For the end clamped bimorph, the tip displacement  $\Delta B$  is given by

$$\Delta B = \frac{3}{2} d_{31} E_3 \left( \frac{L^2}{t} \right) \quad (1)$$

Where  $d_{31}$  is the transverse piezoconstant,  $E_3$  the applied electric field,  $L$  the unclamped length, and  $t$  the bimorph thickness.

In the pure transversely deforming ceramic

$$\Delta l = d_{31} E_3 L \quad (2)$$

so that the effective amplification

$$\Delta B / \Delta l = \frac{3}{2} \left( \frac{L}{t} \right). \quad (3)$$

In the simplified flexing hinged element of figure 2d the flexextensional gain  $A$  is

$$A = W/h. \quad (4)$$

Where  $W$  is the width to mid point and  $h$  is the apex height.

Thus the total gain for the two orthogonal amplifier  $A_T$  will be

$$A_T = \frac{3}{2} \left( \frac{L}{t} \right) \left( \frac{W}{h} \right) \quad (5)$$

which for reasonable values of  $L, t, W, h$  is in the range required.

For a PZT 5H bimorph 1.8 cm unclamped length, 1 mm width driving a light diaphragm of half width 2.5 cm apex height 1.5 mm, for an applied field to the bimorph of 150 volts peak at 500 Hz gives  $\Delta B = 39 \mu\text{m}$  bimorph tip displacement,  $\Delta h = 0.55 \text{ mm}$  amplified apex displacement,  $A_T = 254$  total amplifier gain, predicted sound pressure level  $SPL = 136 \text{ dB}$  at an acoustic efficiency of 4.5%.

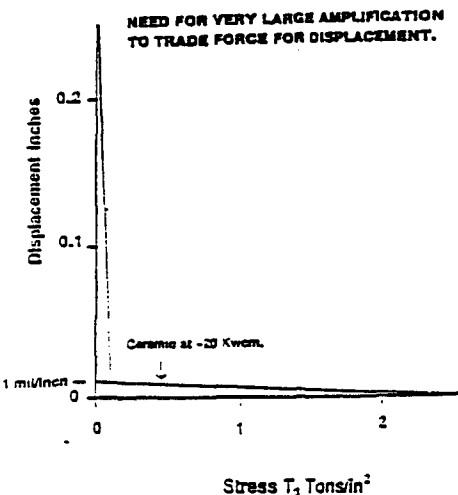


Figure 1

- (a) Load Line for Monolithic PZT 5H Actuator (High Stress Low Strain).
- (b) Required Load Line for Air Acoustic Transducer (Low Stress High Strain).

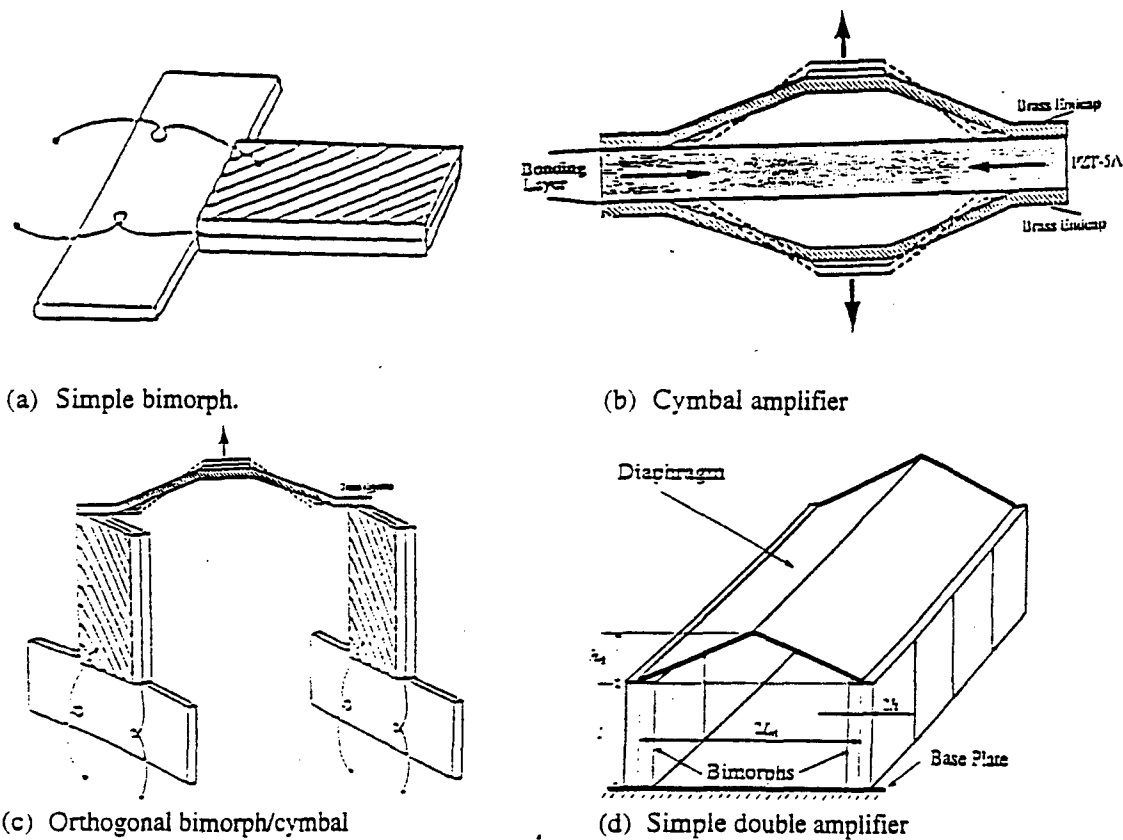


Figure 2  
Evolution of the orthogonal double amplifier

### 3 . Transducer Selection

In recent years there has been a very marked upsurge of interest in bending mode transducers, leading to the development of RAINBOW, CRESCENT (CERAMBOW), THUNDER, and  $d_{33}$  configured unimorph and bimorph transducers. For the rather short (2.5 cm) end clamped configuration needed for the double amplifier structures, it was desirable to examine the possible alternative bending mode systems to select the optimum configuration for this geometry. A very broad ranging study was made of all types, applied to the specific requirement of the double amplifier, i.e. a short single end clamped situation, and these results have already been published [3].

A compact summary of the results is presented in Table 1. All transducers were fabricated from soft PZT piezoceramic with regular rectangular cross section and the dimensions length 15-35 mm, width 5-15 mm, thickness 0.4 to 2.5 mm. For each of the studied systems results were reduced to identical equivalent dimensions of ceramic element.

Characterization was in terms of tip displacement  $f_m^{\eta}$  blocking force  $f_m^F$ , admittance  $f_m^Y$  and an overall performance figure of merit  $f_m$  derived from

$$f_m = f_m^{\eta} \times f_m^F / f_m^Y \quad (6)$$

For convenience the  $d_{31}$  driven bimorph was selected as a standard and assigned the figure 1 in each category, in other cases the ratio of the performance to that of the equivalent bimorph is given.

A quick scan of the Table 1 shows that the  $d_{33}$  driven actuator has major advantage, however complexity and cost of manufacture are not attractive. For the additional robustness associated with the metal schim in the  $d_{31}$  driven unimorph, the small performance penalty in tip displacement is compensated by the larger blocking force and higher resonant frequency.

The special circumstance of the orthogonal amplifier structure suggested the possible advantage of an active base, in the L shaped structure shown schematically in figure 3 with performance delineated in Table 2. Two contra-mounted L shaped unimorph actuators were the configuration chosen for PANEL.

### 4 . PANEL Design

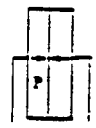
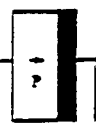
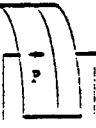
Initial studies focused upon a simple configuration using bimorph actuators to drive a fragile diaphragm made from loudspeaker paper. This system proved to have excellent acoustic characteristics, but was difficult to fabricate and too fragile for normal experimental abuse. For noise control studies the PANEL system depicted in figure 4 was developed using a pair of L shaped unimorph/bimorph transducers fabricated on a stainless steel metal frame.

The bimorphs fixed along the mid plane provide the active base, with the diaphragm now constructed of carbon fiber reinforced composite. To lower the mechanical Q for broad band application, sheet damping material (SOUND COAT GP-3) was applied to the inner surfaces.

Diaphragm vibration as function of frequencies stimulated at driving levels up to 1 KV/cm (50 volts) are shown in figure 5, indicating a mechanical Q ~2.2 at 310 Hz. Expected sound pressure levels based on a baffled piston model are shown in figure 6 for driving levels of 1 and 2 KV/cm, well within the acceptable field range of the PZT.

**Table 1**

Figures of Merit for Different Bending Mode Elements Compared to a simple  $d_{31}$  Driven Bimorph

TYPE OF PIEZOELEMENT	Displacement	Blocking Force	Admittance	Figure of Merit
$d_{31}$ Bimorph (PKI550)		1	1	1
$d_{31}$ Unimorph (SS302/PKI550)		0.41	1.8	1.0
RAINBOW Aura Ceramics (C3900?)		0.19- 0.22	0.1-1.2	0.66
CRESENT 250°C (SS302/PKI550)		0.44	1.75	0.91
THUNDER ~300°C (3Al/PZT5A/Al)		0.12	0.36-1.0	0.90
Shear-mode ( $d_{15}$ ) (3203HD)		<0.1	?	1
$d_{33}$ Bimorph (PKI550)		2.5	1.52	-1
$d_{33}$ Unimorph (SS302/PKI550)		0.72	3.5	-1

**Table 2**

Comparison Between Straight and L Shaped Actuators in the Configuration of Figure 3

ACTUATOR	tip displacement	blocking force	resonant frequency
STRAIGHT BIMORPH OR UNIMORPH	1	1	1
L-SHAPE BIMORPH OR UNIMORPH	0.75	1.5	1.32

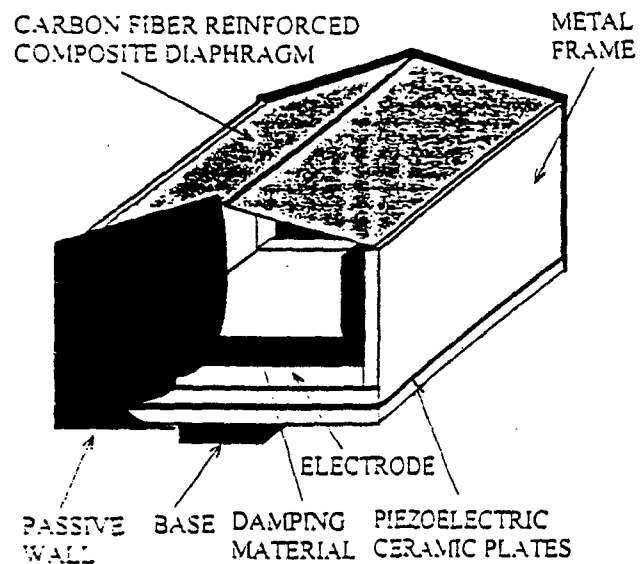
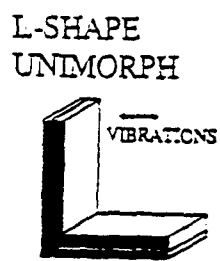
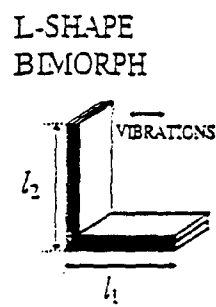


**Figure 3**  
L-Shaped Unimorph and Bimorph Actuators

**Figure 4**  
PANEL Noise Control Element

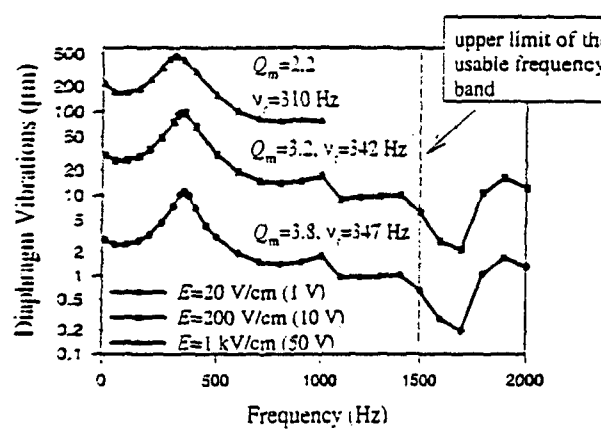


**Figure 5**  
Diaphragm Apex  
Displacement vs Frequency and Field

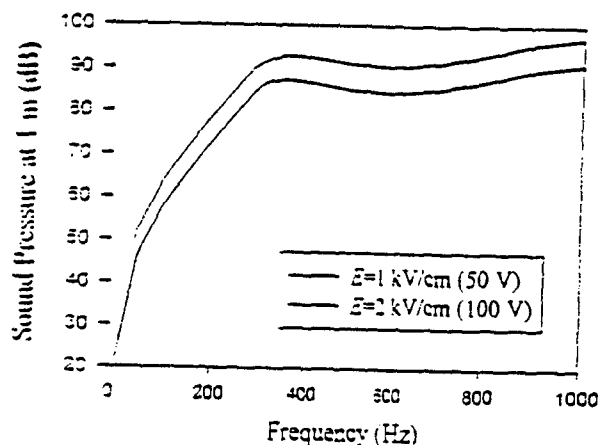


**Figure 6**  
Calculated Sound  
Pressure vs Frequency and Field

## 5. Active Noise Control

For an initial experiment in active noise control, six PANEL devices of the design discussed above were supplied to Dr. Christopher Fuller at VPI. In Fuller's experiment the PANELs were mounted over an aluminum plate driven by an electromagnetic shaker to provide a broad band noise source.

The arrangement is shown in figure 7a, and the adaptive feed forward control system schematically in figure 7b. Active control results for the frequency band 200 to 600 Hz are shown in figure 8, for microphone sensing. Filtered-x LMS parameters were  $f_s = 1000$  Hz 255 Coefficient FIR Compensator; 64 Coefficient System IP. With microphone sensing sound power level reduction of 10.9 dB was achieved.

## 6. Pseudo-Shear Mode Actuation

To enhance lower frequency response in the frequency range below 300 Hz where the performance of PANEL falls markedly, a new type of pseudo-shear mode actuator is being explored. This device is essentially a folded  $d_{31}$  driven actuator (figure 9), in which the poling is such that alternate platens expand and contract to develop translation of the upper platen equivalent to that which would be produced by the full length of the unfolded unipolar transducer. Performance for a forty layer stack of  $30 \times 10 \times 0.45$  mm plates is given in figure 10. Comparison to the simple bimorph shows that for equivalent displacements under similar driving field, the pseudo shear mode system generates ten times the blocking force of the bimorph.

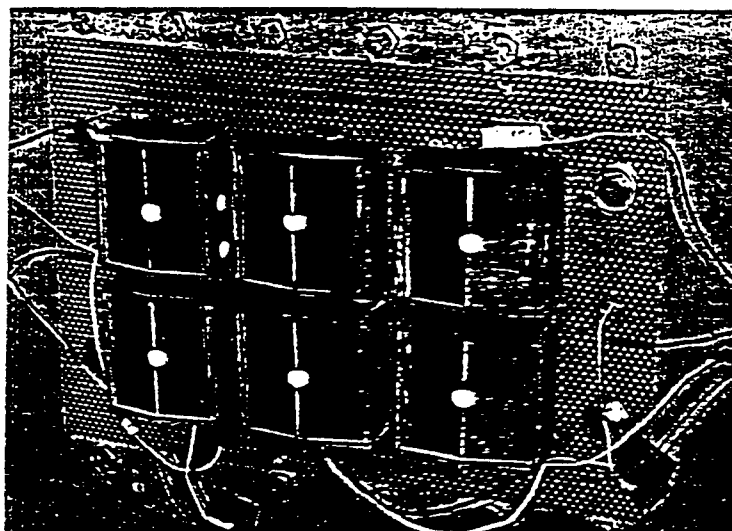
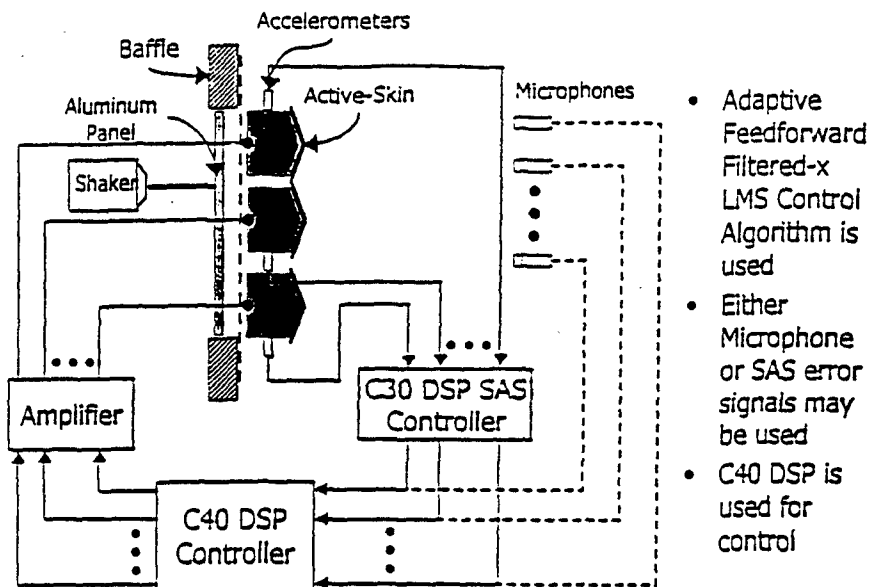
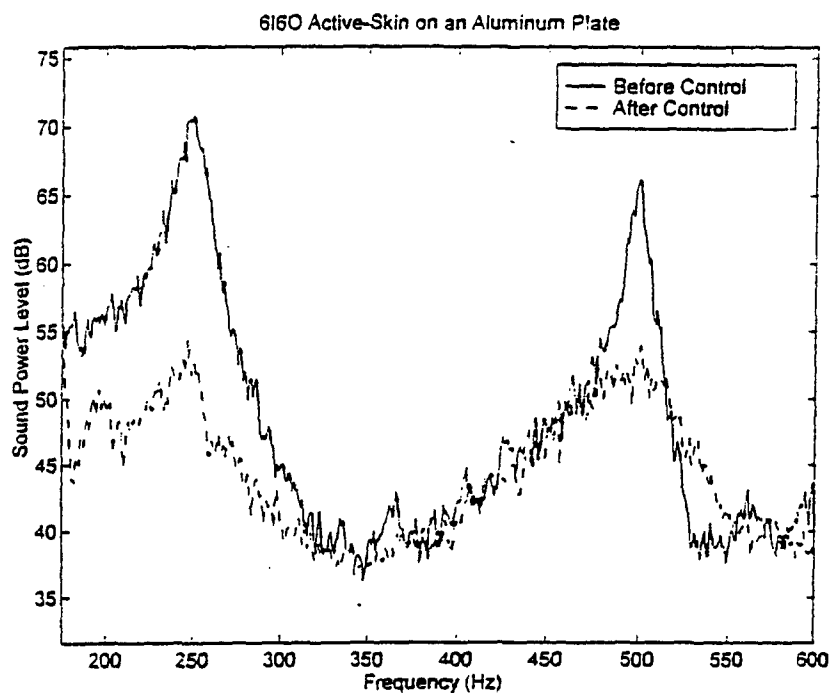


Figure 7a  
PANEL Arrangement for Active Control Experiment



**Figure 7b**  
Schematic Diagram of the Feed Forward Control System



**Figure 8**  
Sound Power Level Over the Range 200 to 600 Hz With and Without Active Control

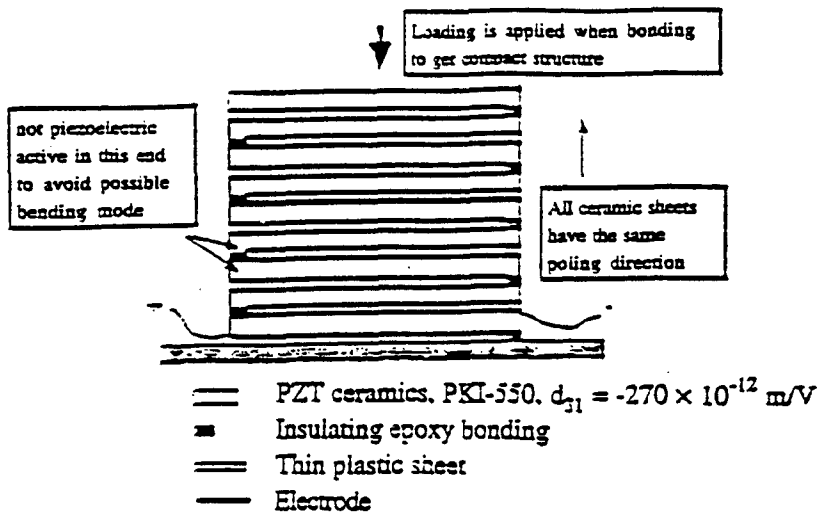


**Figure 9**  
Pseudo-Shear Mode Actuator

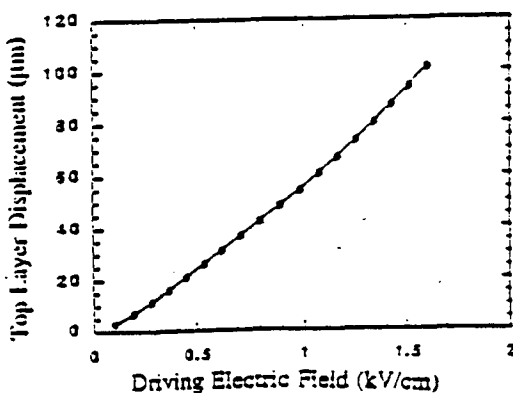


**Figure 10**  
Displacement vs Driving field at 5 Hz for a 40 Layer Stack of  $30 \times 10 \times 0.45$  mm Plates

## References

- [1] Kugel V D 1997 *Proceedings of Engineering Foundation Conference* Banff Canada.
- [2] Xu B, Q M Zhang, V D Kugel, Q Wang, L E Cross 1996 *Proceedings ISAF 96* Vol 1 217
- [3] Kugel V D, S Chandran, L.E. Cross 1996 *SPIE Proceedings "Smart Structures and Materials"*

## Acknowledgement

This work was accomplished under a joint program with Virginia Polytechnic Institute funded under a University Research Initiative (URI) Contract No. N00014-91-1-1140 from the Office of Naval Research.

## **APPENDIX 34**

**Piezoelectric Pseudo-Shear Mode Actuator  
Made by L-Shape Joint Bonding**

Ruabin Liu, Qingming Wang, Qiming Zhang, L. E. Cross

187 Materials Research Laboratory  
The Pennsylvania State University, University Park, PA 16802

## **Abstract**

A new type of Pseudo-Shear mode piezoelectric actuator is described which uses a particular bonding design on a multilayer piezoelectric ceramic stack. In this actuator, long thin rectangular surface electroded PZT piezoelectric sheets are stacked and epoxy bonded at alternate ends. The poling directions in the sheets are selected such that a common potential difference applied to the plates produces alternate lengthening and contraction through the action of  $d_{31}$ , and thus a cumulative displacement over the whole length of the effectively 'folded' ceramic. The rectangular stack of plates thus 'shears' over to produce a substantial shear angle, hence the title of pseudo-shear mode actuator. In this paper, a new higher strength bonding for the anchoring of the alternate ends is discussed, and shown to permit the generation of large unloaded surface displacements and a high blocking force.

**Keyword:** Piezoelectric actuator, pseudo-shear mode actuator

## **1. Introduction**

A new type of multilayer piezoceramic pseudo-shear mode actuator is under study at the Materials Research Laboratory in Penn State [1][2]. In this design, alternate ends of thin rectangular surface electroded PZT sheets are bonded together in a cyclic manner as shown in Fig. 1. If alternate sheets are poled in opposition, application of a common potential difference to the electrodes produces alternate lengthening and contraction leading to a cumulative layer displacement, so that the equivalent strain is equal to the strain from a very long ceramic sheet.

Earlier studies by Wang and Cross [2] demonstrated large displacement capability of this device, but evidence of undesirable bending modes at lower frequency indicated by impedance analysis gave rise to the need for this more detailed study. It was found that the joint bonding between sheets plays an important role in determining device performance. Because of opposing strains in alternate sheets, direct bonding of the sheets leads to shear deformation at the bond, uneven contact and associated undesirable bending.

In the L shaped bonding design discussed, the advantages are delineated and lead to a model 24 layer device with  $23 \mu\text{m}$  displacement and a blocking force of 6.2 N at a drive level of only  $1.4 \text{ kV/cm}$ .

## **2. L-shape joint bonding and experimental procedures**

The configuration of L-shape joint bonding is shown in Fig. 2. Firstly, a 2 mm length small rectangular ceramic piece with the same thickness and width as the ceramic plate was bonded to the one side of ceramic plate. Then the ceramic plates were laminated with the bonding part on the cross section of the surface. Vacuum grease was coated on the contacting surfaces before stacking and cross section bonding.

L-shape joint bonding provides the following side effect:

- The flat and complete contact between the neighboring plates makes it possible to apply grease or lubricate agent as the coating of the contacting surfaces. The grease can perform the two functions: 1. Protect the sample electrode from wearing off during the vibration; 2. Transverse lubrication effect and vertical vacuum adhesion effect could strengthen the desired transverse vibration and prevent the undesired bending vibration in the normal direction.
- Avoid the uncontrollable horizontal diffusion of epoxy, which leads to undesirable long bonded regions.
- The bonded part on the cross section will have less deformation during vibration in comparison with the direct bonding since the normal strain elastic modulus is larger than the shear strain elastic modulus.

A 24 layers prototype actuator was fabricated. Single ceramic plate with a dimension 30 mm × 10 mm × 0.5 mm (l×w×t) was cut from the Motorola commercial soft PZT (3203 HD) block ceramic. The surface of ceramic plate was polished by 3 μm grinding paper.

Au electrodes were sputtered on both major surfaces with 2 mm width margin at opposite edge in the top and bottom surface. The samples were poled by 18 kV/cm electric field at 80°C applied for 1 min. Small ceramic bars with the dimension 2 mm × 10 mm × 0.5 mm were cut and pre-bonded to the end edges of the top surface (positive polarization surface). Then the bar-side of the ceramic plate was bonded to the bar-free side of another plate. Before bonding, two contacting surfaces were coated with grease. This process was repeated until the desired number of layers was achieved. The grease used was DOW CORNING high vacuum grease (Dow Corning Corporation). Mechanical bonding epoxy was J-B Weld (JB WELD CO). Silver epoxy for electric connection among the ceramic plates was E-solder No 3021 conductive adhesives (IMI Insulation Materials Incorporated).

Device characterization was mainly concentrated on the displacement and generative force. Displacement of the top layer of device was measured by Fontonic Sensor MTI 2000 (MTI Instruments). The sensor probe was mounted on a three dimensional movable micro-positioner (Ealing Electro-Optic, Inc.). The generative force was measured by a load cell ELF-TC500 (Entran Devices, Inc.). A T-shape metal head was used to connect the load cell and the top layer area of the device for test. The load cell was driven by a power supply PS-15 (Entran Devices, Inc.). Function Generator DS 345 (Stanford Research Systems) was used to supply signal to a power amplifier (790 series, PCB Piezotronics, Inc.) to obtain device operation power. The output signals were measured by a lock-in amplifier (SR 830 DSP, Stanford Research Systems, Inc.) which is synchronized with the Function Generator. The experimental set up is shown in Fig. 3.

Vibration mode was analyzed by its impedance spectrum on a HP 4194A impedance/gain phase analyzer (Hewlett Packard Co.).

The maximum generative force is the blocking force of the device which is defined as the generative force when the displacement (or strain) is zero. It is very difficult to clamp the device completely. Usually we measure the generative force versus the displacement at a different load levels then plot the generative force Vs displacement coordinate. The device should have a linear relationship between generative force and displacement, we can apply linear curve fitting on the established points and extrapolate the curve to the point of zero displacement. Thus, the corresponding point at the generative force axis is the theoretical blocking force.

### **3. Experimental Results**

#### **3.1 Quasistatic displacement**

Displacement at quasistatic condition (10 Hz) for the unloaded device (24 layers) was measured as a function of driving electric field. The result is shown in the Fig. 4. An obvious nonlinearity is seen. The curve fitting equation is  $y=13.6 E + 5.74 E^2 + 0.9 E^3$ .

#### **3.2 Blocking force**

In order to establish the curve for extrapolating the blocking force, at least two points at generative force vs displacement coordinate are needed for curve fitting. The simplest way to determine the curve is using the following two points. One point is free

displacement with zero generative force; another point is the direct contact between device test area and metal head of the load cell, corresponding to a certain generative force and a less displacement. Two points curve fitting were performed at the DC and AC (10 Hz) drive conditions. See Fig. 5 (a) and (b). More points will make the curve fitting more accurate. In the DC condition, a wood bar was sandwiched between the metal head and the device test area. Because the wood has a less elastic modulus than the metal, it will have some intermediate restraining effect. Thus, an intermediate point will be obtained in addition to the other two specific points for the curve fitting (see Fig. 5 (c)).

From the curve fitting equations, we can calculate the blocking force at zero displacement. The relationships between derived blocking force and the DC and AC driving electric field are shown in the Fig. 6.

The blocking forces derived from the two and three point DC conditions agree very well at the measuring electric field range. The blocking forces obtained from the AC condition have very good agreement with those obtained from DC condition at low driving electric field, but there is a deviation from the blocking forces derived from DC condition at higher driving electric field.

#### **4. Discussions and summary**

From Fig. 4, we can see the relationship of displacement and electric field exhibits nonlinearity when the electric field exceeds the 0.6 kV/cm. The reason for this nonlinear property results from the nonlinear piezoelectric coefficient  $d_{31}$ , which increases with the

increasing of electric field. The nonlinear property of  $d_{31}$  was confirmed by Wang in previous work on the same material. [2] The nonlinear contribution to the piezoelectric response is attributed to the non-180 ° domain wall motion.

Introducing the vacuum grease between the contacting surfaces has a significant effect on eliminating the bending vibration at the frequency around 1 kHz. The impedance spectrum of 24 layers device shown in Fig. 7 (a) indicates that the first resonant vibration mode occurs at 1.6 kHz, which is very weak. In order to understand the vibration mode behavior, the impedance spectrum of 12 layer from the same device was measured and is shown in Fig. 7 (b). The first resonant vibration mode frequency moves to 3 kHz, almost double the first resonant vibration frequency of the 24 Layers device. So the first resonant vibration mode is strongly dependent on the total length of the device. The bending vibration mode around 1 kHz was not observed after introducing the vacuum grease. Although we can eliminate the bending vibration mode, the transverse vibration mode related with the total length needs to be considered. Considering the total length of the device as a whole ceramic piece, the theoretical resonant frequency  $f_r$  for the first transverse resonant mode is determined by the equation:[3]

$$f_r = v/2l$$

Where the  $v$  is the transverse sound speed in ceramic, which is about 2850 m/s for soft PZT ceramics.  $l$  is the total length of the device.

For 24 layers device, with a total length 0.624 m, the first transverse resonant vibration frequency is 2.3 kHz; for 12 layers device, with a total length 0.312 m, resonant frequency for first transverse vibration mode is 4.5 kHz. These are the theoretical cases.

The real situation in this device is that the total length is not composed by a whole piece. The joint bonding parts make the whole structure softer, which will decrease the resonant frequency. Thus, the measured frequencies are reasonable for the two devices and are the transverse modes of the compound structure.

In summary, a pseudo shear mode actuator was fabricated by a L-shape joint bonding structure. The lubricating grease can be coated at the contacting surface, which effectively eliminates the bending vibration and makes the structure more rigid. Blocking forces of a 24-layer pseudo-shear mode actuator were evaluated at DC and AC driving electric field. The blocking force of this model can be 6.2 N at the 1.4 kV/cm driving electric field. The vibration mode for this compound structure is still a length extension mode.

## **Acknowledgment**

This work was supported by the Office of Naval Research under the contract N00014-94-1-1140.

## **References**

1. L. E. CROSS and Q. M. WANG, U.S. Patent has been applied for.
2. Q. M. WANG, L. E. CROSS, Appl. Phys. Lett, 72 (18)(1998).
3. T. IKEDA, in "Fundamentals of piezoelectricity" (Oxford University Press, 1990), chapter 5,

## **FIGURE LEGENDS**

Fig. 1 Basic configuration and operation principle for Pseudo-Shear mode actuator

Fig. 2 Configuration of L-shape joint bonding Pseudo-Shear mode actuator

Fig. 3 Experimental set-up for displacement and generative force measurement

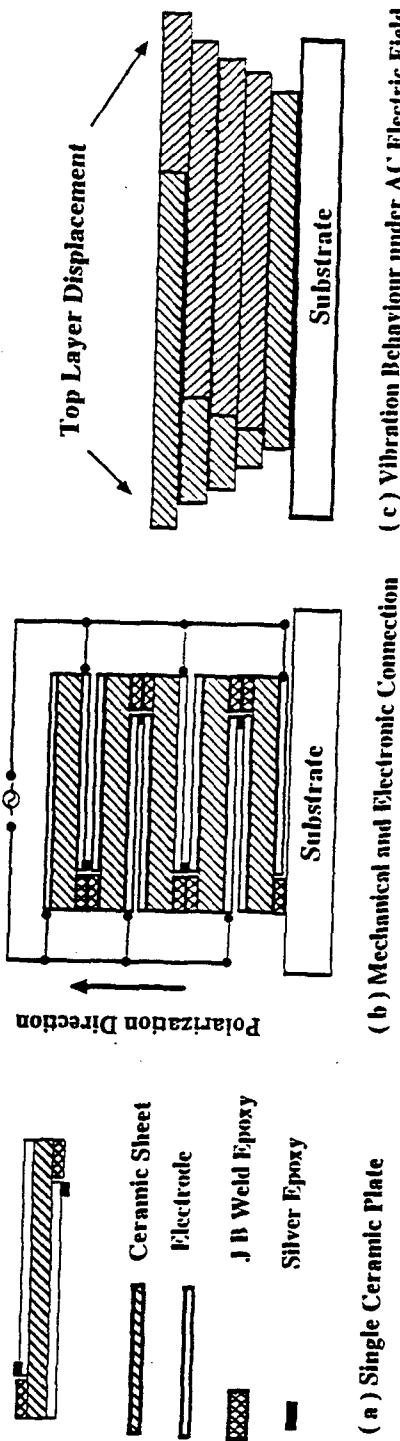
Fig. 4 Top layer displacement of unloaded device as a function of electric field at 10 Hz frequency

Fig. 5 Curve fitting at different situations and different electric field: (a) two points DC, (b) two points AC (c) three points DC.

Fig. 6 Derived blocking force as a function of DC and AC driving electric field

Fig. 7 Impedance spectrum of 24 layers (a) and 12 layers (b) device

**Fig.1**



(a) Single Ceramic Plate      (b) Mechanical and Electronic Connection      (c) Vibration Behaviour under AC Electric Field

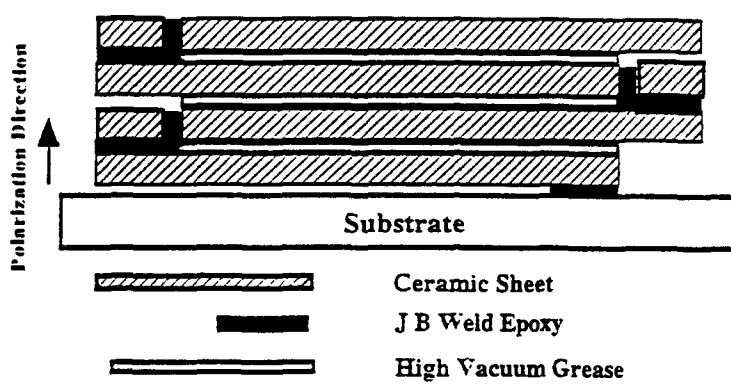


Fig.2

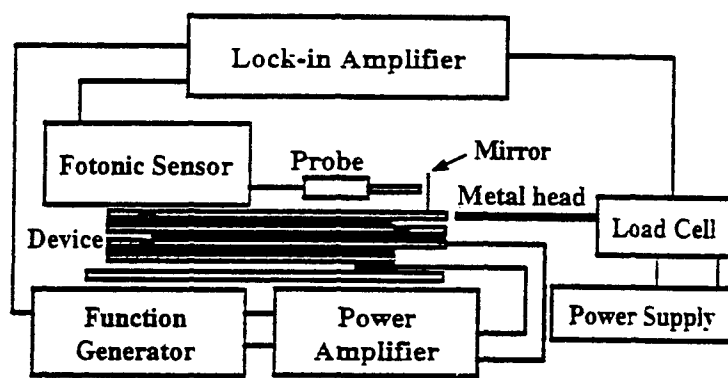
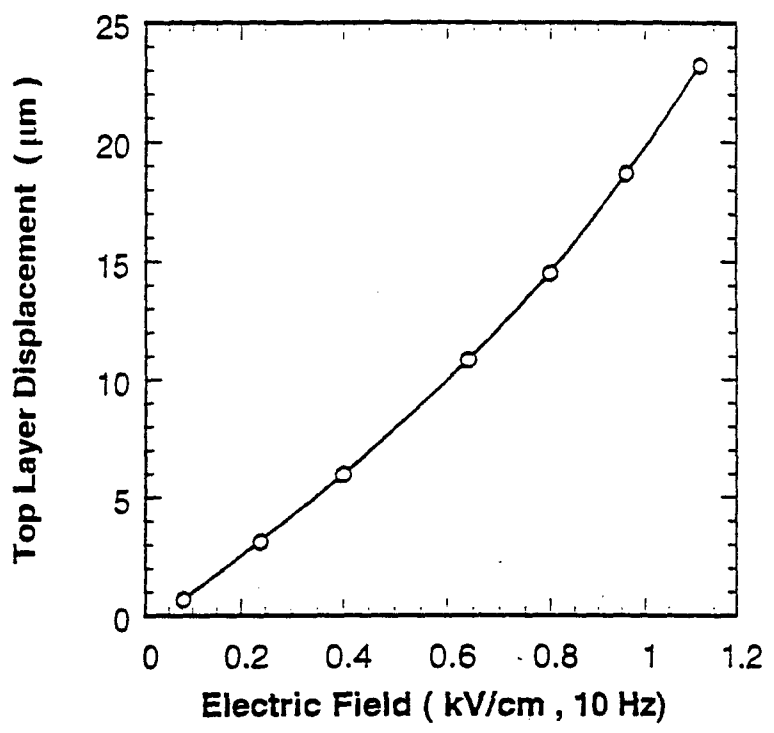
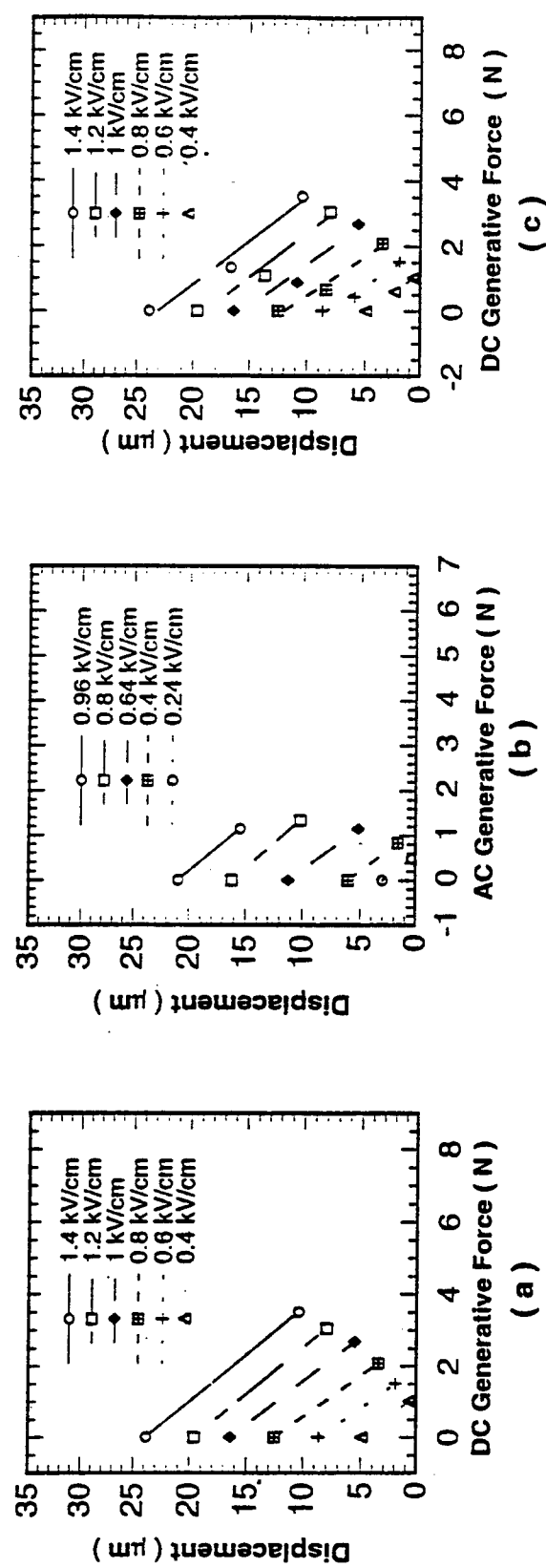


Fig.3



**Fig. 4**

Fig.5



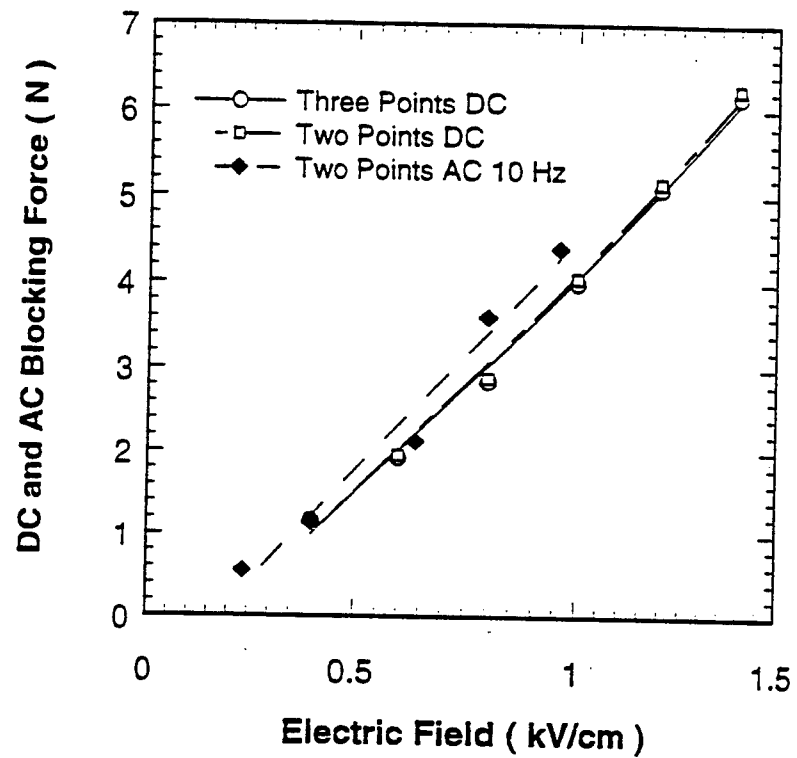
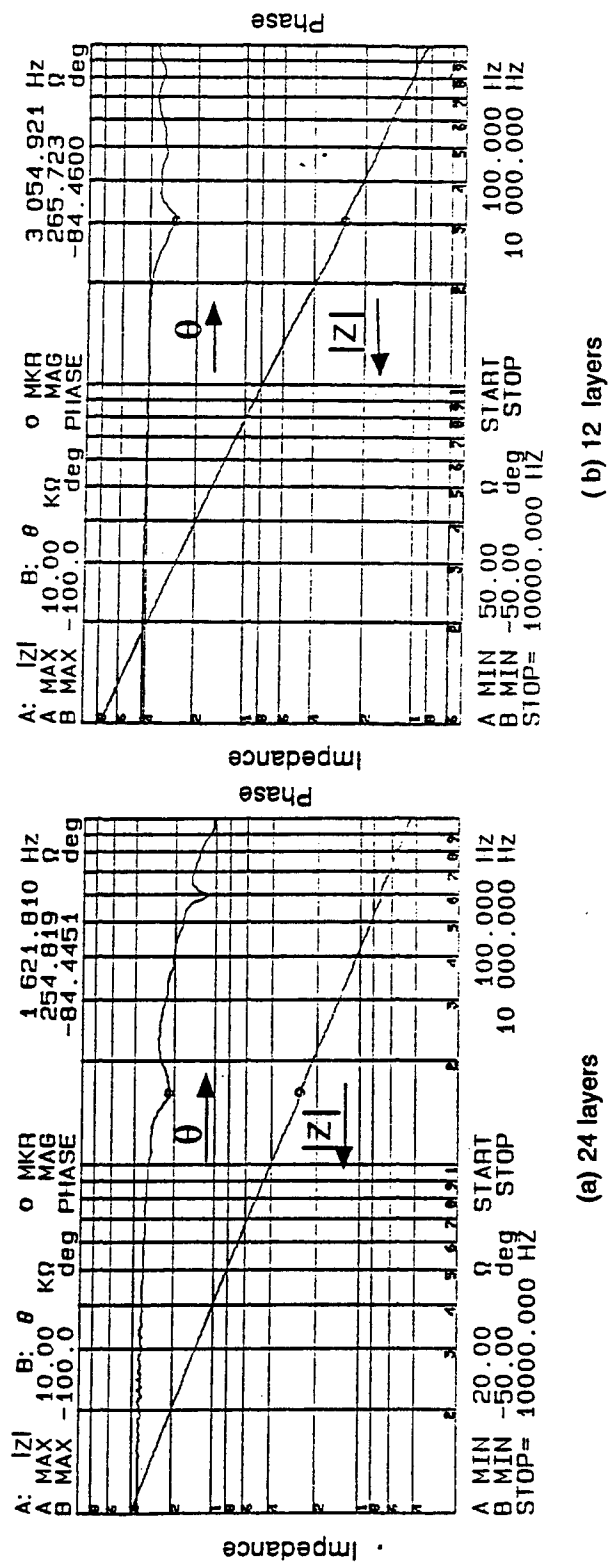


Fig.6

Fig.7



# **APPENDIX 35**

## RECENT ADVANCES IN THE ACTIVE CONTROL OF STRUCTURALLY RADIATED SOUND

by

C. R. Fuller

Vibration and Acoustics Laboratories

Department of Mechanical Engineering

Virginia Polytechnic Institute & State University

Blacksburg, Virginia, USA 24061-0238

website:<http://www.VAL.me.vt.edu/>

### ABSTRACT

Recent research and applications in the field of Active Structural Acoustic Control (ASAC), a technique for reducing low frequency sound radiation from structures, are discussed. The paper overviews some new advances in the ASAC component and system areas of actuators, sensors, controllers, analysis and optimization. Recent commercial applications of ASAC as well as some promising new uses are briefly outlined.

### INTRODUCTION

The technique of Active Structural Acoustic Control (ASAC) in which sound radiation from vibrating structures is controlled by the use of active structural inputs used in conjunction with radiation error sensors has passed a decade of investigation [1]. In the last few years there has been a much increased interest in ASAC with the result that there has been significant advances in ASAC systems and some commercial applications. This paper will review some of the advances and applications. This paper is not intended to be comprehensive, rather, give a flavor of recent developments and directions. For introductory material on ASAC and a description of previous work, the reader is referred to Ref. 1.

The talk is broken up into a discussion of recent work in the main components of an ASAC system (actuators, sensor and controllers). Some discussion is given to the important areas of system analysis and optimization and finally recent commercial applications of ASAC are described.

## ACTUATORS

In general, most of the recent work in actuators for ASAC has been based upon piezoelectric thin plate or wafer devices, which can be directly attached or embedded in the structure. These devices tend to be high force, low strain while low frequency active control applications usually require significant displacements from the actuators. Much effort has thus been directed towards increasing the control authority (the strain) of the actuators and directly integrating the sensor into the actuator system. In general, motion amplification is achieved by attaching the piezoelectric wafer to another wafer element or inactive structure as in a bimorph or unimorph configuration [1]. Tip bending then occurs due to differential expansion or off-axis traction loads respectively. More recently, two unique methods of manufacturing such actuators have appeared; the "Rainbow" [2] and the "Thunder" [3]. The Rainbow actuators are manufactured by selectively reducing one surface of the piezoelectric wafer while the Thunder actuators are laminated under heat and pressure. Both actuators are essentially unimorphs, although the manufacturing process results in a domed shape, which also gives some amplification. Another related actuator is a "Moonie" shown in diagrammatic form in Figure 1 [4]. This actuator consists of a piezoelectric stack actuator (PZT) with two half moon shaped metal caps attached to each end of the stack. As the stack shrinks when an electrical voltage is applied, the metal caps are squeezed upwards and because of their curvature, the transverse deflection is greater than the stack. Amplifications of 20:1 over the stack displacement are achievable [4].

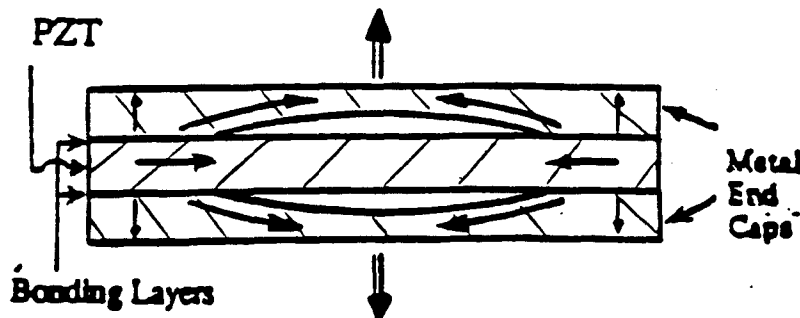


Figure 1. Configuration of a Moonie Acutator [4]

Vipperman and Clark [5] have recently developed a practical piezoelectric element which can simultaneously apply traction loads to a structure while sensing its response (termed a "sensoriaactuator"). In this approach an adaptive filter is used to estimate the feedthrough capacitance of the piezoelectric device. The mechanical response of the piezoelectric element is resolved from the total electrical response of the element by standard adaptive signal processing techniques. Vipperman and Clark have demonstrated the use of the sensoriaactuator on rate feedback control of vibration of a beam [5] and more recently on ASAC applied to a plate (see later).

Effort has been directed towards developing active skins for use in ASAC. In this arrangement the active skin is used to directly change the radiation impedance of the structure in order to control the sound radiation in contrast to the standard approach of altering the structural response. Guigou and Fuller have developed a smart foam in which sheets of the piezoelectric polymer, PVDF, are embedded into passive acoustic foam as shown in Figure 2 [6]. The PVDF can be seen to be curved to achieve motion amplification as discussed above

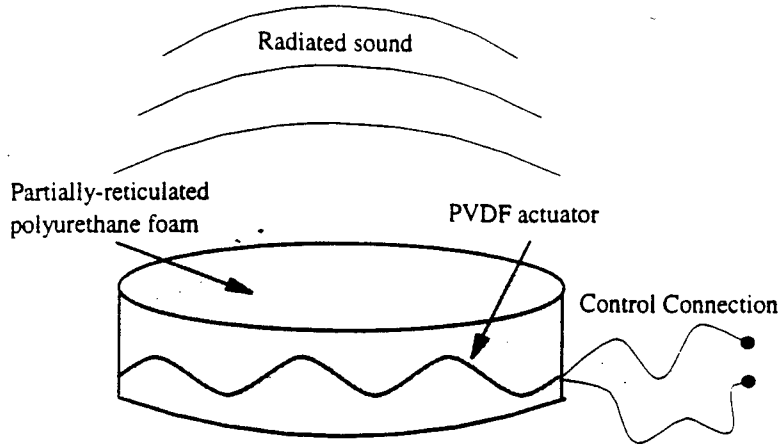
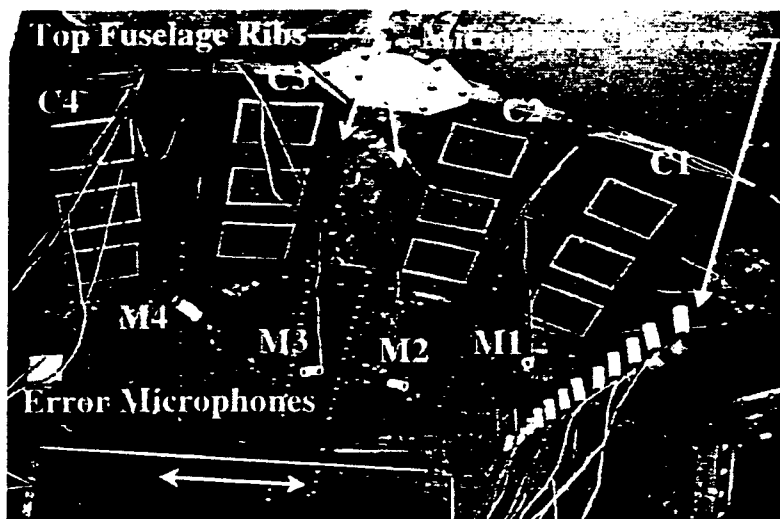
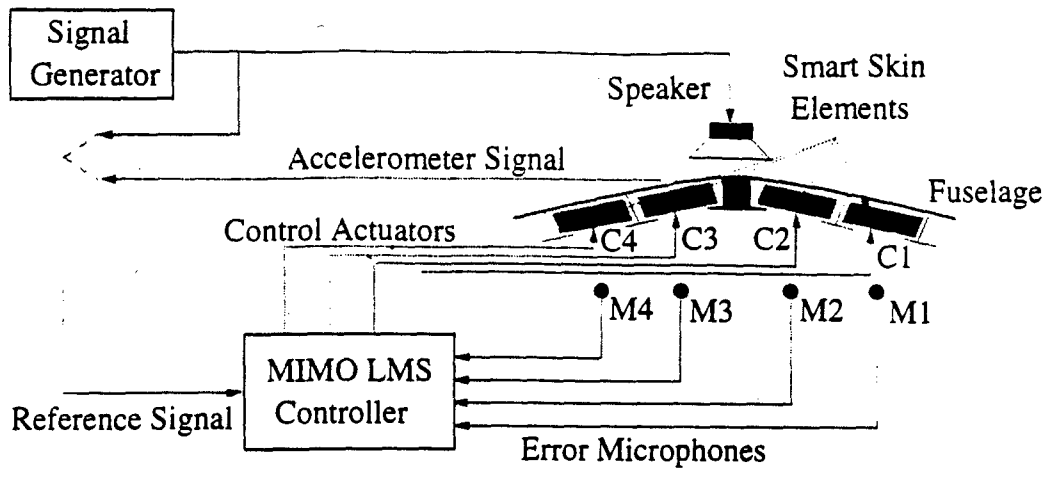


Figure 2. Configuration of smart foam [6]

and alternating sections are wired out-of phase to increase the sound radiation. The radiating structure is covered with the smart foam and control signals are applied to the PVDF in order to minimize sound radiation. The foam also provides structural support for the PVDF and gives significant passive attenuation of sound and vibration. Experiments on using the smart foam for broad band sound radiation into aircraft cabins has shown much potential with attenuations of random noise of 8-10 dB achieved over a 300 Hz bandwidth. The experimental arrangement and control system are shown in Figure 3. In another active skin configuration developed at PSU and shown in Figure 4, unimorph or bimorph piezoelectric actuators are mounted to a base or directly on the structure and are connected with a top cover plate (a double amplification of motion). Thus the small in-plane motor of the piezoelectric wafer actuator is converted into a much larger normal displacement of the cover plate by geometric amplification as discussed above. Amplifications of 25:1 and cover plate displacements of approximately  $30 \mu\text{m}$  at 100 Hz have been measured and a continuous array of the devices (i.e. an active skin) has been used in laboratory experiments to control broadband sound radiation from structures [7].



(a)



(b)

Figure 3. Smart Foam installed in an aircraft cabin for interior noise reduction [6].  
 (a) Configuration (b) Control System

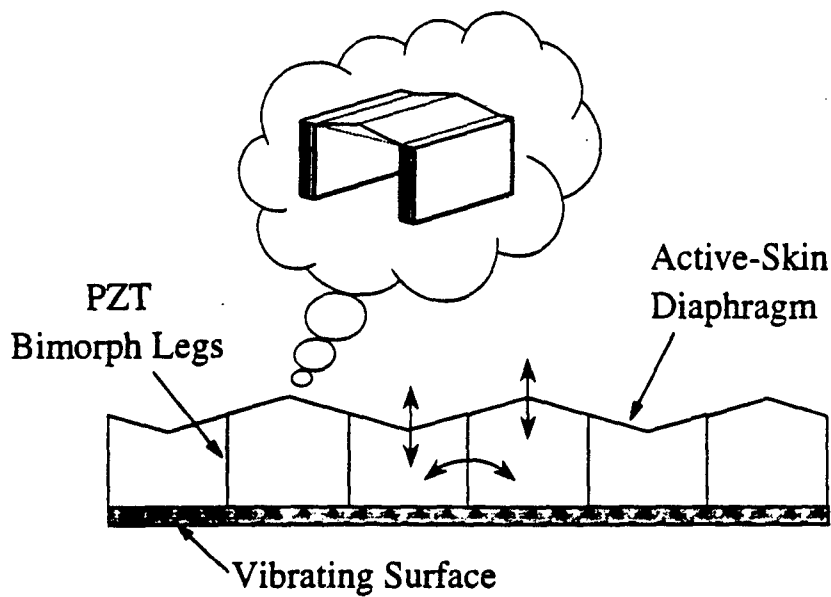


Figure 4. Double amplifier active skin [7].

In a related area, adaptive tuned vibration absorbers (ATVA's) have been used as actuators in ASAC approaches. An ATVA has the capability of adaptively tuning its resonance frequency usually by changing the stiffness factor. Electro-mechanical ATVA's have been used to control sound radiation from structures and it has been demonstrated that the best reduction in sound is when the ATVA's are globally detuned from the excitation frequency [8]. This is achieved by minimizing a radiation cost function and is thus a variant of ASAC [8].

## SENSORS

Most recent work in sensors has been directed towards developing sensors which, although integrated into the structure, give an estimate of the radiated sound pressure or power. These approaches can be generally divided into distributed, continuous, shaped sensors and arrays of discrete sensors. A number of workers have developed volume velocity distributed sensors for planar structures [9,10,11]. These sensors are usually cut from PVDF material and are based upon reformulating the sound radiation from the structure into what is known as "radiation modes" [1]. Figure 5 shows an array of volume velocity sensors used to control broadband, low frequency, radiation from a panel [12]. The characteristic quadratic sensor weighting associated with simply supported plate modes is apparent.

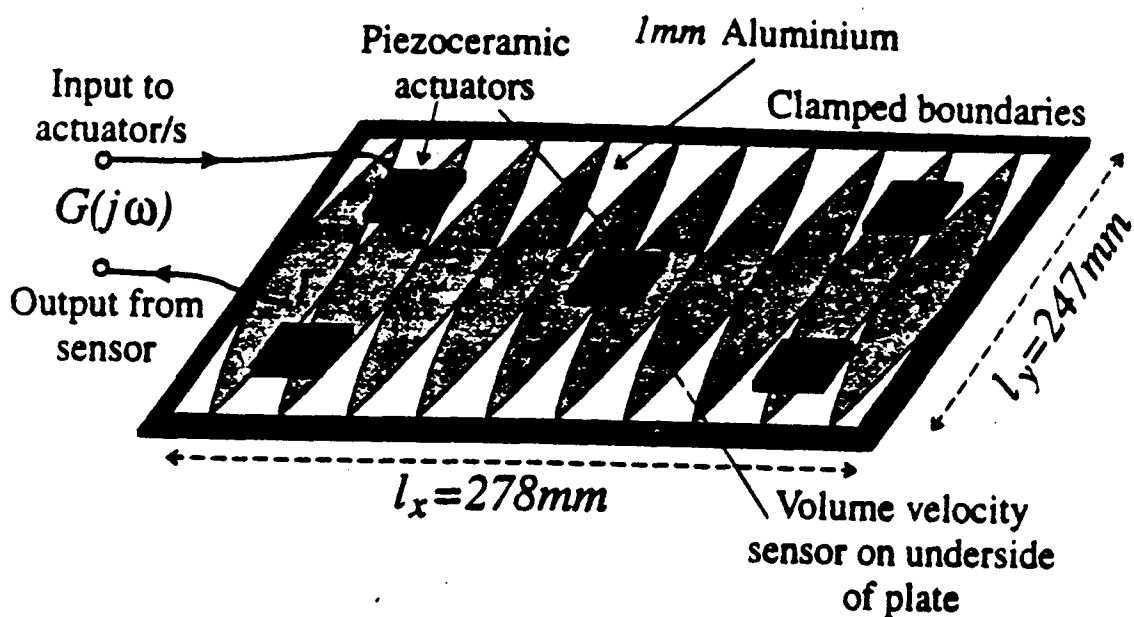


Figure 5. Volume Velocity sensors for control of low frequency broadband sound radiation from a plate [12].

In another approach, Maillard and Fuller [13] have developed a discrete structural acoustic sensing approach (DSAS) in which discrete sensors (usually accelerometers) are located on the structure in an array. The output of the accelerometers are passed through FIR filters which model the structure's radiation Green function [1] and are then summed (c.f. the Rayleigh Integral Approach) to give estimates of far-field pressure at discrete angles as shown in Figure 6. These time domain radiation estimates can then be used as error information in ASAC approaches to replace microphones in the far-field as shown in Figure 6.

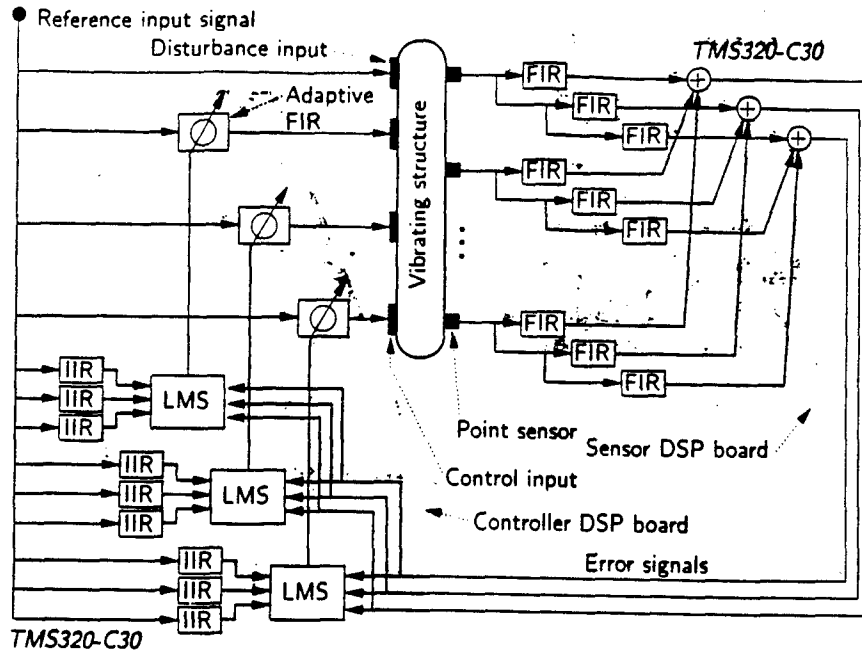


Figure 6 . Discrete structural acoustic sensing used in ASAC of cylinder radiation [13].

## CONTROL APPROACHES

Most recent work in ASAC control approaches have been directed towards applying robust, MIMO feedback control approaches to the control of structurally radiated sound. In general, these approaches extend the work of Baumann et al [14] who developed the concept of a “radiation filter” in which structural states are converted to causal, radiation states.

Vipperman and Clark [15] have combined multivariable feedback active control with the radiation filter approach of Baumann and the sensoractuator discussed above to develop a ASAC System, which provides robust control of sound radiation from plates excited by random or transient disturbances. Elliott et al have recently investigated the use of adaptive feedback control approaches based upon the “internal model” control method in which the feedback problem is turned into a feedforward problem using inverse filtering to remove the output of the plant from the feedback loop [16]. These internal model approaches have been recently applied to the control of sound transmission through panels [12].

In other work the feedforward MIMO LMS approach has been extended to well conditioned control approaches which employ a very high number of actuators and sensors. Carneal and Fuller [17] have developed a “Bio” controller in which multiple actuators are controlled in a hierarchical manner. A “master” actuator(s) is controlled by a high level, sophisticated controller (such as a LMS Filtered-x paradigm [1]), while “slave” actuators which are located nearby the master actuator are controlled by simple, local rules(such as phase inversion). The approach, although usually sub-optimal, allows the construction of an adaptive, distributed actuator and has been successfully applied to ASAC systems. Cabell and Fuller [18] have investigated the use of Singular Value Decomposition (SVD) based LMS control approaches which can be used to break the noise field into principle components and used to group individual actuators together into a single channel (i.e. construct a distributed actuator).

## SYSTEM ANALYSIS, IDENTIFICATION AND OPTIMIZATION

In general, analysis of complex, real structural acoustic systems have been based upon using commercially available FEM/BEM packages, [e.g. 19,20]. These codes provide the system frequency response function (FRF) at single frequencies. Usually these FRF's are converted to time domain information by using software [e.g. 21] to construct causally constrained FIR or IIR filters to represent the system impulse responses. The filters can then be used to model the ASAC system dynamics for time domain disturbances (such as random, broadband and transient) and then can be used to investigate the use of various actuator, sensor and control systems using the control theory analysis of Ref. 1 for example.

System identification is also being used in the design of ASAC systems. In general, these techniques concentrate on finding the (usually) small scale structural motions, which are associated with the sound radiation. These small scale motions are often embedded in motions of much larger amplitude which do not radiate effectively, thus making the use of standard identification techniques unreliable. Near field acoustic holography (NAH) is one technique currently being used to identify the structural motions associated with sound radiation [22]. In NAH arrays of pressure measurements are used in conjunction with a wavenumber FFT to predict both the global pressure field as well as the coupled structural motion. An inverse system identification approach has been developed by Paxton and Fuller [23]. In this technique, ANC is used to create the interior field of an aircraft by canceling the interior sound field due to a structural disturbance such as an engine. With the controller locked and the original disturbance removed, the ANC system is used to re-create the (inverse) sound field and drive the structure so as to reproduce only those structural motions that are well coupled to the interior sound field as shown in Figure 7. The normal

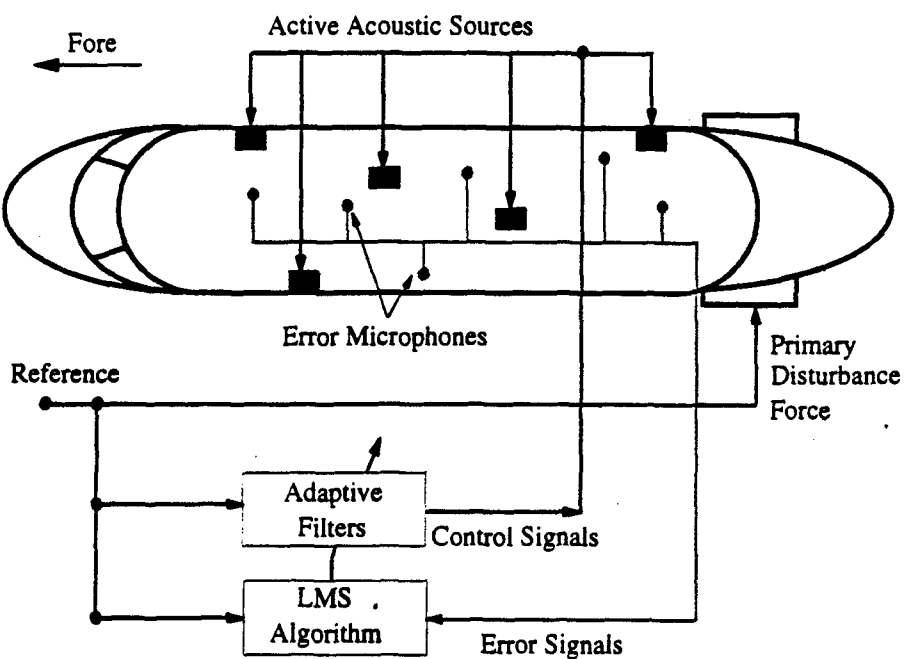


Figure 7. Active noise control system used to reproduce interior cabin field due to a structural disturbance [23].

structural displacement of the fuselage is then measured at an array of points and decomposed into singular values and associated vectors using SVD analysis and are given for an example test in Table 1 [23]. The table shows that the inverse (internal acoustic) excitation results in a lower number of significant singular values and also lower magnitude

Singular-Value	Primary Excitation	Internal Acoustic Excitation
1	3.68	1.59
2	2.81	0.69
3	1.79	0.55
4	1.32	0.41

Table 1. Singular value magnitudes for the disturbance (primary) and internal, locked ANC, acoustic excitation [23].

of singular values (and thus associated vibration). The larger singular values of the internal acoustic excitation indicate the important structural vibration patterns in terms of sound radiation. Optimal arrays of structural actuators can then be designed to excite these dominant singular vectors.

Once the system has been modeled or identified, then various approaches have been used to optimize the system configuration (generally decide the location, number, shape of the transducers). The most common approach is to measure a discrete number of transfer functions or impulse responses associated with a large number of actuators and sensors. Various discrete optimization techniques, such as genetic algorithms [24] and sub-set selection [25] are used to determine the best transducer configuration based upon a pre-determined performance criterion. Such approaches are an efficient method for determining the best control configuration before expensive, realistic testing begins.

## APPLICATIONS

There have been many recent applications of ASAC, most at the laboratory or R & D level. Here we discuss recent commercially available ASAC systems which are being marketed and some which show near term market potential.

An ASAC system has been developed by Ultra Electronics in the UK for control of interior noise in aircraft [26]. In this system inertial electromagnetic actuators are attached to the fuselage frames as shown in Figure 8 and microphones mounted in the trim are used as error sensors. In tests on such a system, applied to a DeHavilland Dash-8 aircraft(propeller driven), the ASAC system showed a significant improvement in control when compared to an ANC system particularly at the higher-harmonics as shown in Table 2 [26]. Many such

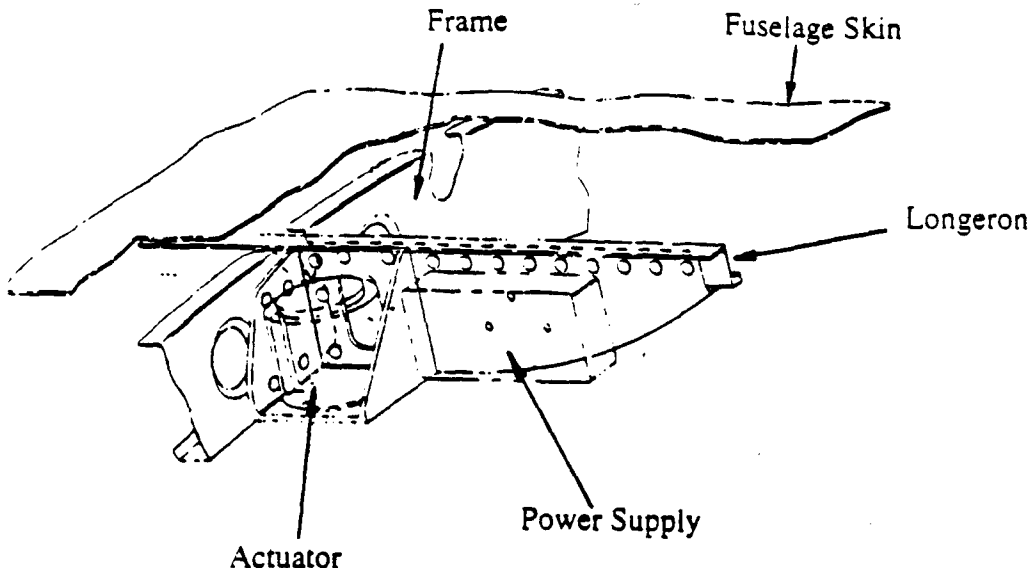


Figure 8. Inertial electromagnetic actuators used in the Dash-8 ASAC application [26].

	Noise Reduction (dB)			
	1 BF	2 BF	3 BPF	4 BPF
ASAC	10.5	7.6	4.4	3.0
ANC	8.0	6.6	3.6	0.4

Table 2. Averaged noise reductions using two active control approaches in a Dash-8 [26].

control systems are in use around the world today. A related ASAC system is being marketed by Lord Corporation in the U.S. [27]. The Lord system is similar except it has been applied as a production item to a Cessna Citation X, which is a turbo-fan engine aircraft. In this case the inertial actuators are located on the engine mounts (acting on the back) and error microphones are located in the cabin [27]. In this manner only the acoustically significant vibrations at the engine mounts are controlled which is similar to the ASAC principle. Very good global reduction of the turbo-fan N1 and N2 tones is achieved with this system. Both Refs. 26 and 27 used a feedforward LMS controller.

Quiet Power of the U.S. has successfully applied an ASAC system to reduce transformer radiated noise [28]. A diagram of the system is shown in Figure 9. The Quiet Power system consists of a combination of acoustic drivers and ceramic piezoelectric actuators bonded to the transformer casing as actuators while error microphones located in the radiated sound field are used. The acoustic drivers are used to control the 120Hz signal while the piezoelectric devices control the higher harmonics where the displacement requirements are less. The control approach is a MIMO feedforward LMS algorithm. Global reductions of the overall radiated sound field of the order of 12-15 dBA are achieved for a large power transformer. The significant frequencies are usually the fundamental (120Hz) and the first three harmonics (240, 360 and 480 Hz). The system has been applied to a number of operating transformer sites in the US and Canada.

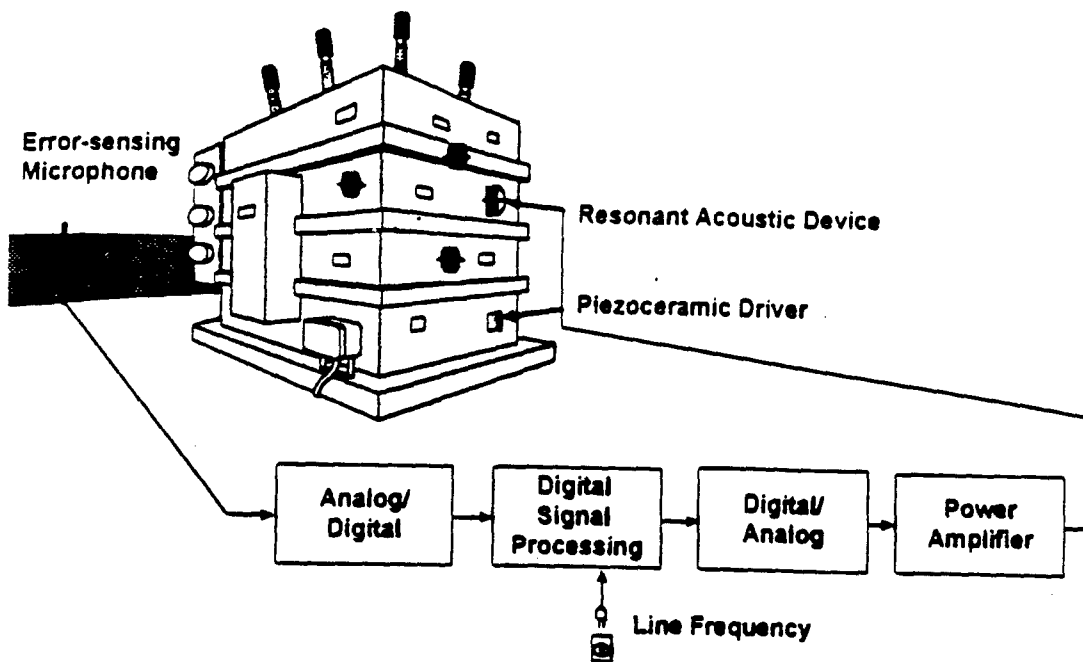


Figure 9. The Quiet Power ASAC System for reduction of power transformer noise [28].

Two areas which show much near term potential use of ASAC are in the reduction of train and automobile interior noise. Muller BBM in Germany [29] has recently demonstrated global reductions of train interior noise using electromagnetic actuators attached to the wheel bogies and error microphones in the cabin (reduction of the order of 7 dB were achieved). In related work, researchers at Catholic University Leuven in Belgium have shown that an ASAC system consisting of electromagnetic shakers attached to an automobile car chassis and used in conjunction with microphones in the car interior can provide significant global sound reduction [30]. If the cost effectiveness of these systems can be increased then it is likely they will be commercialized in the near future.

## CONCLUSIONS

It can be seen that the field of ASAC is quickly expanding and starting to gain a technical maturity. The focus of the new research appears to be on actuators and sensors which can be integrated into the structure. The use of robust feedback MIMO controllers has recently appeared as well. Commercial systems based upon the ASAC technique are now starting to appear.

## REFERENCES

1. Fuller, C.R., Elliott, S.J. and P.A. Nelson, "Active Control of Vibration," Academic Press, London, 1996.
2. Hooker, M. W., "Properties and Performance of RAINBOW piezoelectric actuators," Industrial and Commercial Applications of Smart Structures Technologies , SPIE 3044, 1997

3. Bryant, R. G., "THUNDER Actuators," Proceedings of the 5th Annual Workshop: Enabling Technologies for Smart Aircraft Systems, NASA Langley Research Center, Hampton, VA, 1996.
4. Newnham, R.E., Dogan, A., Xu, Q.C., Onitsuka, K., Tressler, J. and Yoshikawa, S., "Flexextensional "Moonie" Actuators," Proceedings of the 1993 IEEE Ultrasonics Symposium, 509-513, 1993.
5. Vipperman, J. S. and Clark, R. L., "Implementation of an Adaptive Piezoelectric Sensoriactuator," AIAA Journal, 34(10), 2102-2108, 1996.
6. Guigou, C. and Fuller, C.R., "Foam -PVDF Smart Skin for Aircraft Interior Sound Control," Proceedings of the 3rd AIAA/CEAS Aeroacoustics Conference, Atlanta, GA, 423-440, 1997 (also AIAA Paper 97-1637-CP).
7. Johnson, B. D, Fuller, C. R. and Burdisso, R. A., "The Use of a Piezoelectric Double Amplifier Active-skin in the Control of Panel Radiation," Journal of the Acoustical Society of America, 101(5), Pt.2, p. 3108, 1997.
8. Charette, F., Fuller, C. R. and Carneal, J. P., "Adaptive Vibration Absorbers for Control of Sound Radiation from Panels," Proceedings of the 3rd AIAA/CEAS Aeroacoustics Conference, 235-245, Atlanta, GA, 1997 (AIAA Paper 97-1619-CP).
9. Johnson, M.E. and Elliott, S. J. , "Volume velocity Sensors for Active Control," Proceedings of the Institute of Acoustics, 15(3), 441-420, 1993.
10. Guigou, C., Berry, A. and Charette, F., "Active Control of Plate Volume Velocity Using Shaped PVDF Sensor," Proceedings of the ASME Conference on Adaptive Structures and Composite Materials: Analysis and Application, Chicago, IN, 247-255, 1994.
11. Snyder, S.D. and Tanaka, N., "On Feedforward Active Control of Sound and Vibration Using Vibration Error Signals," Journal of the Acoustical Society of America, 94(4), 2181-2194, 1993.
12. Johnson, M. E., Sors, T. E, Elliott, S. J. and Rafaely, B. "Feedback Control of Broadband Sound Radiation Control Using a Volume Velocity Sensor," Proceedings of Active 97, Budapest, Hungary, 1007-1020, 1997.
13. Maillard, J. P. and Fuller, C. R., "Advanced Time Domain Wave-number Sensing for Structural Acoustic Systems III. Experiments on Active Broadband Radiation Control of a Simply-supported Plate," Journal of the Acoustical Society of America , 98(5), 2613-2621, 1995.
14. Baumann, W. T., Saunders, W. T. and Robershaw, H. H., "Active Suppression of Acoustic Radiation from Impulsively Excited Structures," Journal of the Acoustical Society of America, 90(6), 3202-3208, 1991.
15. Vipperman, J. S. and Clark, R. L., "Multivariable Feedback Active Structural Acoustic Control With Adaptive Piezoelectric Sensoriactuators," submitted to the Journal of the Acoustical Society of America, 1997.
16. Elliott, S. J., Sutton, T. J., Rafaely, B. and Johnson, M. "Design of Feedback Controllers Using a Feedforward Approach," Proceedings of Active 95, Newport Beach, CA, 863-874, 1995.
17. Carneal, J. P. and Fuller, C. R. , "A Biologically Inspired Controller for Sound and Vibration Applications," Proceedings of the 35th AIAA/ASME/AHS/ASC Structures, Structural Dynamics and Materials Conference, Hilton Head, SC, 1994 (also AIAA Paper 94-1785)

18. Cabell, R. H. and Fuller, C. R., "Frequency Dependence of Decoupling Filters for Multichannel Feedforward Active Noise Control," *Journal of the Acoustical Society of America*, 101(5), Pt. 2, Plc. 3109, 1997.
19. "Sysnoise Users Manual," Numerical Integration Technologies, Leuven, Belgium, 1992.
20. "Comet Acoustics User Guide," Automated Analysis Corporation, Ann Arbor, MI, 1995.
21. "Matlab-Reference Guide," The Math Works Inc., Natick, MA, 1992.
22. Williams, E. G. and Houston, B.H., "New Green Functions for Nearfield Acoustical Holography in Aircraft Fuselages," *AIAA Paper 96-1703*, 1996.
23. Paxton, S., Fuller, C. R. and Gibbs, G. P., "An Experimental Technique for the Inverse Identification of the Structural Acoustic Behaviour of Aircraft Cabins," *Proceedings of the 2nd AIAA/CEAS Aeroacoustics Conference*, State College, PA,
24. Hansen, C. H., Simpson, M. T. and Wangler, C. T., "Application of Genetic Algorithms to Active Noise and Vibration Control," *Proceedings of the 4<sup>th</sup> International Conference on Sound and Vibration*, St. Petersburg, Russia, 371-388, 1996.
25. Ruckman, C.E and Fuller, C.R, "Optimizing Actuator Locations in Active Noise Control Systems Using Subset Selection," *Journal of Sound and Vibration*, 186(3), 395-406, 1995.
26. Ross, C.F and Purver, M.R.J., "Active Cabin Noise Control," *Proceedings of Active 97*, Budapest, Hungary, XXXIX-XLVI, 1997.
27. Miller, L., "Lord Active Control Systems," Presentation at Mechanical Engineering Dept, VPI&SU, Blacksburg, VA, 1997.
28. Brungardt, K., Vierengel, J and Weissman, K., "Active Structural Acoustic Control of Noise From Power Transformers," *Proceedings of Noise-Con 97*, University Park, PA, 173-182, 1997.
29. Schirmacher, R., Holzl, G., Redmann, M. and Scheuren, J. , "Active Noise and Vibration Control for a High Speed Railcar: A Case Study," *Proceedings of Active 97*, Budapest, Hungary, pp. 557-564, 1997.
30. Sas, P. and Dehandschutter, W., "Design of Active Structural and Acoustic Control Systems for the Reduction of Road Noise in a Passenger Car," *Proceedings of the 6<sup>th</sup> International Conference on Structural Dynamics: Recent Advances*, ISVR, University of Southampton ,England, 21-43, 1997.

## **APPENDIX 36**

## ADVANCED ACTUATORS AND SENSORS FOR THE ACTIVE CONTROL OF SOUND AND VIBRATION

C. R. Fuller, Vibration and Acoustics Laboratories, Department of Mechanical Engineering,  
Virginia Polytechnic Institute and State University, Blacksburg, Virginia, USA, 24061

### ABSTRACT

This paper summarizes advanced actuators and sensors for use in the active control of sound and vibration. Emphasis is placed upon the class of distributed, strain type actuators and sensors which enable selective structural coupling and filtering through their shape. Some discussion on grouping of arrays of actuators and advanced processing of the output of arrays of sensors is included. The use of integrated actuators and sensors into the structure is shown to be directly related to the field of "intelligent" or "smart" structures.

### INTRODUCTION

An important element of any practical control system is the transducers used for the implementation of the control. Actuators are used to apply control signals to the physical system in order to change its response in a desired manner. Actuators can be generally grouped into two main types: *fully active* actuators are used to apply a secondary vibrational input to the structure and are able to supply mechanical power; *semi-active* or *adaptive* actuators behave essentially as passive elements in that they store or dissipate energy and are used to adapt the passive mechanical properties of the structure. Sensors are used to make measurements of the physical system response. This information is then used to estimate important disturbance and system variables which are employed as the basis of control signals or to monitor the performance of the control system. In general the use of sensors can be generally grouped into two main types: *arrays* of point sensors whose output is electrically processed to estimate the required variable and *distributed*, continuous sensors which filter the response information through their own shape characteristics.

This paper briefly overviews some of the more useful advanced actuator and sensor approaches used in the active control of sound and vibration. The material discussed is not intended to be completely comprehensive, rather, it is intended to give an introduction to a relatively new class of control transducer systems.

### 1) ADVANCED ACTUATORS

By far the most common advanced actuators used in applications of active sound and vibration control are induced strain actuators, such as the material systems based upon piezoelectric, electrostrictive, magnetostrictive and shape memory alloy and thus much of the discussion is focussed on these devices. However some discussion of other actuator systems such as

electroreological fluids is presented. Often the goal in developing an advanced actuator for the sound and vibration application is centered on motion amplification (especially at low frequencies) or impedance matching and some discussion of this nature is also included.

### 1.1) Piezoelectric material and definitions

The most common piezoelectric material used are polycrystalline ceramics in which the piezoelectric effect is induced by *poling* the material (Uchino, 1994). Figure 1 shows an element of piezoelectric material. Three axes are used to identify directions in the element termed the 1, 2 and 3 in respective correspondence to the x, y and z axes. The z axis is usually taken parallel to the poling direction. The constitutive equations for a linear piezoelectric material when the applied electric field is not large can be written as (Uchino, 1994),

$$\varepsilon^i = S_{ij}^E \sigma_j + d_{mi} E_m \quad (1a)$$

$$D_m = d_{mi} \sigma_i + \xi_{ik} E_k \quad (1b)$$

where the indices  $i, j = 1, 2, \dots, 6$  and  $m, k = 1, 2, 3$  refer to different directions within the material coordinate system. In equations (1a) and (1b)  $\varepsilon$ ,  $\sigma$ ,  $D$  and  $E$  are respectively the strain, stress, electrical displacement and electrical field. In addition  $S^E$ ,  $d$  and  $\xi$  are the piezoelectric strain constant and the permittivity of the material (IEEE, 1988).

The piezoelectric strain constant  $d$  is defined to be the ratio of the developed free strain to the applied electrical field. In particular the strain constants  $d_{33}$ ,  $d_{31}$  and  $d_{32}$  are important. The subscript 33 implies that the voltage is applied or charge collected (since the piezoelectric effect is reciprocal) in the 3 direction of Figure 1 for a displacement or force in the same direction. The subscript 31 implies that the voltage (or charge) is applied in the 3 direction while the displacement occurs in the x direction. The strain in the z direction can be simplified, for one-dimensional motion, in the absence of an applied load to

$$\varepsilon_{pe}^3 = d_{33} V/h_a \quad (2)$$

where  $V$  is the applied voltage and  $h_a$  is the element thickness in the z direction. For the same applied field the actuator will also deflect in the x and y directions and the resultant strains in the x and y directions are respectively,

$$\varepsilon_{pe}^1 = d_{31} V/h_s \quad (3a)$$

$$\varepsilon_{pe}^2 = d_{32} V/h_s \quad (3b)$$

By convention when a field (relatively small in magnitude to the poling field) is applied to the element in the same direction as the poling vector (see Figure 1), the element will expand in the z direction. At the same time, due to Poisson coupling, the element will shrink in the x and y directions. Thus the  $d_{33}$  constant is typically specified as a positive value while the  $d_{31}$  and  $d_{32}$  are usually negative for piezoelectric ceramics. The above relations apply for the static deflection of piezoelectric elements. However when the applied voltage is oscillating at a frequency well below the element resonance, the relations can be used to approximately give the magnitude of the oscillating strain.

### 1.2) Piezoelectric stack actuators

A common arrangement of a piezoelectric actuator is the stack configuration shown in Figure 2. The stack is usually constructed from multiple layers of piezoelectric elements and is designed to provide a large deflection in the z direction when a voltage is applied over electrodes on the top and bottom of the stack (or each component element). Two configurations of the stack actuator are shown. In Figure 2(a) the actuator is working *in parallel* against an external stiffness (representative of the structure that the actuator is working on) while in Figure 2(b) the actuator is working *in series*. The coupled deflection  $w$  of the parallel system (with  $F = 0$ ) is given by (Fuller et al., 1996).

$$w = \frac{d_{33} V}{1 + K/K_s} \quad (4)$$

where  $K$  is the external spring stiffness constant and  $K_s = E_a A_a / L_a$  is the equivalent actuator spring constant with  $E_a$ ,  $A_a$  and  $L_a$  the Young's modulus, cross sectional area and length of the actuator. Two things are apparent. Firstly the unconstrained displacement of the actuator is reduced by the external stiffness load. Secondly, as a consequence the actuator applies a force to the external stiffness proportional to the difference between the unconstrained and coupled displacement. Thus the smaller the coupled deflection of the actuator the larger the force it applies. This impedance aspect of the actuator is an important design consideration. Some applications require large deflections and low force (e.g. an active acoustic source in air) while others have the reverse requirement (a series active mount). The most common use of stack type fully active actuators has been in active vibration mounts where the active element is usually applied in series with the passive isolation system (Scribner et al., 1993).

### 1.3) Piezoelectric wafer type actuators

The other common form of piezoelectric actuator is the wafer configuration shown in two

dimensional form in Figure 3. In this arrangement two identical piezoelectric elements are bonded onto (or embedded in) each side of the structure at identical locations. The elements are connected 180° out-of-phase so that when one element expands the other shrinks. The nett result of the actuator, since each element is off the central axis, is to bend the structure. The actuator is termed a wafer, since the element is long in the axes transverse to the poling direction. Thus the largest deflections occur in the x and y directions along the surfaces bonded to the structure. By static analysis of the deflection of such a finite actuator attached to a plate, it can be shown that the actuator behaves as forcing function given by a line moment at the edges of the piezoelectric actuator (Fuller et al., 1996). The magnitude of the moment (per unit length) can be calculated from the relation (Fuller et al., 1996),

$$m_x = m_y = E_p I_p K^f \epsilon_{pe} \quad (5)$$

where the geometric factor  $K^f$  is given in Table 1 for the one dimensional and two dimensional cases. In Table 1  $E$ ,  $I$  and  $v$  are the Young's modulus, moment of inertia and Poisson's ratio respectively. The subscripts pe, b and p refer to the piezoelectric element, beam and plate. The structure is of thickness  $2h_b$  while the actuator is of thickness  $h_a$ .

**Table 1 Summary of Geometric Strain Constants**  
(after Fuller et al., 1996)

Excitation Condition	Geometric constant $K^f$
1-D Anti-symmetric wafer	$\frac{3E_{pe}[(h_b + h_a)^2 - h_b^2]}{2E_{pe}[(h_b + h_a)^3 - h_b^3] + 2E_b h_b^3}$
2-D Anti-symmetric wafer	$\frac{3E_{pe}[(h_b + h_a)^2 - h_b^2](1 - v_p)}{2E_{pe}[(h_b + h_a)^3 - h_b^3](1 - v_p) + 2E_p h_b^3(1 - v_{pe})}$

The unconstrained strain  $\epsilon_{pe}$  is given by equations (3a) or (3b). The excitation of structures by such actuators can thus be mathematically represented as a line moment source term in the structure dynamic differential equation. For example the excitation of a thin plate by a wafer actuator is given by

$$m(x, y) = E_p I_p K^f \epsilon_{pe} [\delta'(x-x_1) - \delta'(x-x_2)] [H(y-y_1) - H(y-y_2)] \\ + E_p I_p K^f \epsilon_{pe} [H(x-x_1) - H(x-x_2)] [\delta'(y-y_1) - \delta'(y-y_2)] \quad (6)$$

where  $\delta(\cdot)$  and  $H(\cdot)$  are the Dirac Delta and Heaviside functions respectively. The symbol  $(')$  implies differentiation with respect to the argument. For a finite simply supported plate the modal response of the plate to a harmonic voltage applied to the 2D wafer actuator is given by (Fuller et al., 1996)

$$W_{mn} = \frac{4E_p I_p K^f \epsilon_{pe}}{m'' S_p (\omega_{mn}^2 - \omega^2)} \left[ \frac{-(k_m^2 - k_n^2)}{k_m k_n} (\cos k_m x_1 - \cos k_m x_2) (\cos k_n y_1 - \cos k_n y_2) \right] \quad (7)$$

where  $m''$  is the mass per unit area of the plate,  $S_p$  is the plate area,  $\omega_{mn}$  are the plate natural frequencies (Fuller et al., 1996). In equation (7),  $k_m = m\pi/L_x$  and  $k_n = n\pi/L_y$  while  $(x_1, y_1)$  and  $(x_2, y_2)$ , specify the corners of the actuator. The most important observation from equation (7) is that the amplitude of the response of individual plate modes can be chosen by selecting the location and shape of the piezoelectric actuator. This is a very important and desirable attribute because often the goal in active control is to reduce selected modes without increasing others (an effect termed *control spillover*). Piezoelectric distributed wafer actuators thus show much potential to alleviate the spillover problem.

#### 1.4 Piezoelectric motion amplifiers

As discussed above piezoelectric devices, because of their high internal stiffness, tend to be high force, low deflection devices. Many applications require large deflections and lower forces (for example a loud speaker operating at low frequencies) and thus much attention has been directed towards developing configurations of piezoelectric actuators that amplify their deflection (at the cost of lowering their force). Perhaps the earliest and best known configuration designed to achieve this is the *moonie* actuator shown in diagrammatic form in Figure 4 (Newnham, et al. 1993). This actuator consists of a piezoelectric stack actuator with two half moon shaped metal caps attached to each end of the stack as shown. Thus as the stack shrinks, the metal caps are squeezed upwards and because of their curvature, the transverse deflection is greater than the stack deflection. A typical moonie provides an amplification of about 20 times the deflection of the piezoelectric stack alone. Such devices are being commercially developed in the US and will be soon readily available.

## 1.5 Piezoelectric resonance actuators

Other piezoelectric actuators are designed to provide very high actuation forces in a compact lightweight arrangement. Usually this is achieved by using a stack actuator carrying a small mass as shown in Figure 5. Since the piezoelectric stack has an appreciable stiffness the arrangement provides a SDOF mass-spring system. High output force can thus be achieved if the actuator parameters are adjusted to be on or close to resonance at the operating frequency. Figure 6 presents a typical blocked force output of a PCB piezoelectric inertial actuator with different inertial masses. A typical pk-pk input voltage maximum would be 100V thus giving an output force of approximately 40 lb-f in an actuator that weighs only slightly more than the inertial mass. Damping also plays an important role in the actuator design. Much higher output forces can be achieved by increasing the Q of the actuator. However this also leads to a very peaky output characteristic which often causes control instability problems. Usually some damping is added to the device to smooth out the response curve as shown in Figure 6. Another more recent development employs a mass-spring actuator system as in Figure 6 except that the actuator stiffness is tunable (von Flotow, et al., 1994). Thus the actuator can be adapted to track changes in the disturbance frequency and always be on-resonance. Such an actuator falls into the class of a semi-active or adaptive device.

## 1.6 Active-passive piezoelectric composite actuators

The above inertial actuator could also be considered an active-passive device, in that an active force is used to enhance the passive resonance behavior thereby resulting in high output force at low frequencies with a low control voltage. There are other active-passive actuators which take advantage of both the passive and active mechanism to provide a large bandwidth of control. Figure 7 shows a schematic of what has been termed an *active constrained layer* used for damping structural vibrations (Baz and Ro, 1995). The device consists of a passive visco-elastic layer constrained between two thin layers of piezoelectric material. The signal from the bottom piezoelectric layer (when it is stretched by the attached structure) is amplified, inverted and fed to the top piezoelectric layer. Thus if the bottom layer is stretched, the top layer shrinks, with the effect that the shear in the visco-elastic layer is significantly increased. The nett effect is that the passive damping behavior of the visco-elastic layer is significantly increased, particularly at low frequencies. Another active-passive actuator is the smart foam concept developed by Fuller et al. (1995) and shown in Figure 8. In this case the device consists of polyurethane blown foam with embedded layers of PVDF piezoelectric film. As in the case of the moonie described in Section 1.4 the PVDF is sinusoidally curved to amplify the transverse displacement (since this couples well with the normal acoustic particle velocity of the surrounding acoustic medium) as shown in Figure 9. The foam thus provides acoustic absorption at high frequencies while the active embedded layer significantly increases the low frequency absorption. Such smart foam layers have been used for wide band control of structural radiation as well as sound absorption (Fuller et al., 1995).

## 1.7 Magnetostrictive actuators

A related material system to piezoelectrics are magnetostrictive materials which elongate with the application of a magnetic field (Goodfriend and Shoop, 1991). Figure 10 shows a typical magnetostrictive actuator developed by Edge technologies using the material Terfenol-D which consists of an alloy of the metals terbium, dysprosium and iron. The Terfenol-D rod is surrounded by a magnet and an electrical coil. The rod is typically prestressed by cap which markedly increases its output strain and range of linear behavior as shown in Figure 11. Magnetostrictive actuators have the advantages of compactness, very high output force (from 220-1770N) and large bandwidth of response. On the other hand they tend to be relatively heavy, expensive and consume higher electrical power.

## 1.8 Shape memory alloy (SMA) actuators

The shape-memory effect can described very basically as follows: a material in the low temperature martensitic condition when plastically deformed and with the external load removed, will regain its original shape when heated. The material phenomenon that "memorizes" its original shape is the result of the reverse transformation of the deformed martensitic phase to the higher temperature austenite phase (Jackson, 1972). The most common SMA is the nickel-titanium alloy known as Nitinol. Nitinol is the SMA of choice for use as an actuator because of its high resistivity which allows for resistive heating through the passage of an electrical current in the material itself. Figure 12 shows plots of typical recovery stresses of Nitinol as a function of temperature and initial strain. A typical material system utilizing SMA as an actuator consists of plastically elongated SMA thin wires embedded in a composite material as shown in Figure 13. When the wires are heated, by passing an electrical current through them, the wires "try" to contract to their "memorized" length and thus generate a predictable in-plane force in the base structure. The SMA actuators can be used in two main ways. When an oscillating voltage is applied to the SMA it acts as a fully-active actuator and provides vibration control inputs. However, although the SMA can apply extremely large forces, its frequency response is very small (of the order of a few Hertz) due to thermal dissipation limitations. The SMA can also be used as a semi-active actuator by applying steady state voltages to the wires. The result is that variable in-plane forces can be applied internally to the composite system, with the effect that the dynamic passive properties of the composite system can be adapted in a controllable way. For example, Table 2 presents the change in natural frequencies calculated for a SMA composite panel when it is activated (Liang et al., 1991). Additional calculations also demonstrate a corresponding significant change in shape of the associated modal functions. Thus the advantages of the SMA systems are extremely high force and deflection while disadvantages are a low bandwidth of response, non-linear behavior, high power consumption and thermal build-up.

**Table 2 Change of the first ten plate natural frequencies**  
 (after Liang et. al., 1991)

Mode	Natural frequencies (Hz)									
	1	2	3	4	5	6	7	8	9	10
Inactive	41.3	82.8	114.8	144.4	166.9	224.0	233.7	245.5	290.7	317.9
Active	71.5	129.7	146.6	203.4	239.5	246.9	296.5	322.4	355.4	403.4

### 1.9 Electrorheological fluid actuators

Electrorheological (ER) fluids are suspensions of highly polarized fine particles dispersed in an insulating oil (Stangroom, 1983). When an electric field is applied to the ER fluid the particles form chains which lead to changes in the viscosity of the medium of several orders of magnitude, as well as an alteration of elasticity of the fluid. The ER fluid can thus be embedded in cavities in a structure, for example, and used as a semi-active actuator to tune its overall mechanical properties such as damping and stiffness (Gandhi and Thompson, 1989). A recent development in this class of actuators uses magnetic fields to activate the fluid.

### 1.10 Actuator grouping and optimization techniques

The influence of the location and number of actuators on active control system performance has been demonstrated to be of equal importance to the number of channels of control (Wang et al., 1991). Thus much work has been dedicated towards developing approaches for optimally configuring the control actuators. There are two general approaches; in the first, continuous optimization is used when the permissible actuator locations (and possibly shapes) are continuous functions in space. For instance, Wang et al. (1991) used continuous optimization to find the optimal locations of piezoelectric actuators used to control sound radiation from vibrating plates. Continuous optimization approaches generally use some sort of iterative gradient descent method which uses a finite difference approach to evaluate the gradient vector. This generally leads to continuous approaches being very computationally intensive. A second, sub-optimal approach uses a discrete form of optimization in that only certain discrete actuator locations are available. Discrete optimization techniques such as genetic algorithms (Goldberg, 1989) or subset selection (Ruckman and Fuller, 1995) are then used and have been demonstrated to provide good results with an efficient computational overhead. If the discrete actuator locations are used in conjunction with a set of permissible discrete error sensor locations then the problem can be reduced to calculating or measuring a matrix of transfer functions from the actuators to the error sensors. The problem is then one of matrix manipulation and associated techniques such as Singular Value Decomposition can be used.

As discussed above control spillover is an important problem which often limits control performance. The standard solution is to use many independent actuators (and thus channels of control) which effectively create a distributed actuator which only drives the wanted modes in

the secondary, control field. However, the high number of channels of control creates important problems amongst which collinearity is prime. Collinearity occurs, for example when the transfer functions from a single actuator to two or more error sensors are identical or very close. The result is that the normal matrix of the optimal control vector solution is singular (or very poorly conditioned) and poor control reduction results (Ruckman and Fuller, 1995). Naturally this problem is exacerbated when many actuators and error sensors are sprinkled about in order to solve the control spillover problem. In order to overcome this problem Cabell et al. (1993) have developed an actuator grouping technique which not only attempts to minimize the control error cost function but tries to group or connect actuators together, thus reducing the number of channels of control and the collinearity problem. The grouping technique is based upon constructing a cost function which is the sum of the (standard LMS) squared error signals,  $\varepsilon_i^*$ , plus an actuator penalty term,  $\eta_{lm}$ . Thus the cost function is

$$J = \sum_{i=1}^I \varepsilon_i \varepsilon_i^* + \beta \sum_{l,m=1}^M \eta_{lm} \quad (8)$$

where  $I$  is the number of error sensors,  $M$  is the number of actuators and  $\beta$  is a relative weighting factor of the error signal and actuator penalty terms. The actuator penalty term is designed to increase as the difference between the control inputs increases. The difference between two control inputs  $l$  and  $m$  is defined to be,

$$\lambda_{lm} = c_l - c_m \quad (9)$$

A typical actuator penalty function is defined to be

$$\eta_{lm} = 1 - \frac{1}{(n-1)(1 + \lambda_{lm} \lambda_{lm}^*)^{n-1}} \quad (10)$$

In equation (10) the steepness of the penalty function can be increased by increasing  $n$ . The resulting cost function is non-quadratic in the control actuator values and non-linear optimization techniques are used to find its minimum. Cabell et al. (1993) have applied the grouping technique to active reduction of interior noise in a DC-9 fuselage using multiple, fuselage mounted piezoelectric wafer actuators. The results showed that 34 independent actuators could be grouped together into 9 independent channels of control with a resultant increase in reduction of 12dB of the cost function over the full LMS approach. The actuators were grouped so that between five and two actuators were connected together and the configuration and performance was shown to be strongly dependent upon the value of  $\beta$  and the form of the function of equation (10) used (i.e. value of  $n$ ).

## 2) ADVANCED SENSORS AND SENSOR SYSTEMS

Sensors are used to monitor the control performance or estimate disturbances applied to the system. The design of sensors is thus of prime importance. A related problem to control spillover is observation spillover. In general if the sensors observe motion which is not desired to be controlled then control energy will also be injected into unwanted system response. Sensors can be generally divided into two main implementations; distributed, continuous sensors and arrays of small, individual sensors. In this section we overview some important configurations for either arrangement.

### 2.1 Piezoelectric distributed sensors

The piezoelectric sensor material of choice is the polymer polyvinlidene fluoride (PVDF). As discussed by Collins and von Flotow (1991), PVDF material makes an excellent sensor. It is lightweight and flexible and thus causes little change to the system response. It has a high piezoelectric charge constant and can be readily shaped into complicated forms either by cutting or shaping the electrodes. Changing the polarity of the sensor is achieved by simply flipping the sensor material over in the required areas so that the polarity direction is reversed relative to the system coordinate axis. Another important aspect of the implementation of piezoelectric sensors is the development of the necessary high input impedance electronics (from the sensor side) to measure the charge over the sensor without causing "leakage". Circuit arrangements to provide high input impedance amplification etc. are discussed by Collins (1990) and Clark et al. (1992). For predicting the electrical output of piezoelectric sensors it is more convenient to use the *piezoelectric stress constant*  $e_{31}$ . The stress constant is directly related to the strain constant by the Young's elastic modulus and the Poisson's ratio of the material as discussed in Auld (1990).

The charge  $q(t)$  generated by a one dimensional piezoelectric sensor attached to the surface of a beam (assuming it does not alter the beam dynamic characteristics) is (Fuller et al., 1996)

$$q(t) = \int_0^L e_{31} f(x) \frac{\partial^2 w}{\partial x^2} (h_b + h_s) dx \quad (11)$$

where  $L$  is the sensor length,  $w$  is the beam out-of-plane displacement,  $2h_b$  and  $h_s$  are the beam and sensor thickness respectively. The sensor shape function  $f(x)$  is defined for an arbitrary sensor shape as

$$f(x) = \int_{-b/2}^{+b/2} F(x,y) P(x,y) dy \quad (12)$$

where  $F(x,y)$  is the effective electrode width and  $P(x,y)$  is the polarization vector distribution of the sensor material (usually +1 or -1) while  $b$  defines the transverse limits of the sensor.

Equation (12) reveals the essential characteristic of the distributed sensor. The sensor performs by summing the charge of the piezoelectric material due to local beam strain under the location of the electrodes. If the sensor shape is changed then different spatial windows of observation are created which change the modal observability of the sensor. For example, a sensor shaped with the function

$$f(x) = B \sin(n\pi x/L) \quad (13)$$

can be demonstrated to only observe individual modes of order  $n$  of a simply supported beam. Figure 14 shows two such sensor shapes designed to observe the first and second modes of a simply supported beam. Note that the sensor width is greatest where the strain is highest and for the  $n = 2$  sensor the polarity is flipped through the mid-point of the beam where the  $n=2$  modal response changes by 180 degrees.

The two dimensional distributed sensor equation has been derived by Lee and Moon (1990) as

$$q(t) = \int_S f(x,y) \left[ e_{31} \frac{\partial^2 w}{\partial x^2} + e_{32} \frac{\partial^2 w}{\partial y^2} + 2e_{36} \frac{\partial^2 w}{\partial x \partial y} \right] (h_b + h_s) dx dy \quad (14)$$

where  $S$  is the area covered by the sensor and  $e_{36}$  is the stress constant in the shear direction. When a sensor is used with no skew angle then  $e_{36}=0$ . Implementation of a 2-D sensor is more difficult than the 1-D case where the sensor width can be used to vary its weighting. Generally the spatial variation in weighting (necessary for spatial filtering) for a 2D sensor is achieved by varying the piezoelectric thickness or material properties although some degree of modal weighting can also be achieved in 2-D by sizing and appropriately locating the sensor (as in the case of piezoelectric actuators discussed in Section 1.3) (Clark and Fuller, 1992). Further details and applications are described by Fuller et al. (1996).

## 2.2 Modal estimation with arrays of point sensors

The above section discussed distributed continuous sensors and while they have many advantages they do have some limitations. In particular their shape and thus their characteristic observer function is fixed. This may cause control problems when the system or disturbance is changing. In many situations such as these it is advantageous to use arrays of point sensors and to electronically combine their outputs in order to construct what in effect is a discrete approximation to a distributed observer. The characteristic of the observer can be then easily adapted by altering the processing electrical circuit thus making these devices suitable for systems which change in time. Of course the trade off over the continuous distributed sensor of Section 2.1 is the increased complexity due to the electrical processing.

Consider an example structure vibrating in a series of modes. The out-of-plane displacement for single frequency response can be described as

$$w(x,y,t) = \sum_{m=1}^{\infty} \sum_{n=1}^{\infty} A_{mn} \Psi_{mn} e^{j\omega t} \quad (15)$$

where  $A$  are the modal amplitudes and  $\Psi_{mn}$  are the mode shapes. If we sample the response with  $J$  sensors and assume the response is dominated by  $J$  modes, the measurements can be represented in matrix form as

$$\begin{bmatrix} w_s^1 \\ \vdots \\ w_s^J \end{bmatrix} = \begin{bmatrix} \Psi_{11} & \dots & \Psi_{M1} \\ \vdots & \ddots & \vdots \\ \Psi_{11}^J & \dots & \Psi_{MN}^J \end{bmatrix} \begin{bmatrix} A_{11} \\ \vdots \\ A_{MN} \end{bmatrix} \quad (16)$$

We can then solve the above system of equations for the modal amplitudes ( $M + N = J$ ) which are given by

$$a = \Psi^{-1} w_s \quad (17)$$

where  $a = [A_{11} \dots A_{MN}]^T$  and  $w_s = [w_s^1 \dots w_s^J]^T$ . Thus with an array of sensors we can process the total structural response to obtain the individual modal response (in the frequency domain). These individual (or combination of) modal components can then be used as error information in the control approach resulting in minimisation of selected responses (for example, efficiently radiating modes). The method depends upon knowing the mode shapes and as discussed in Fuller et al. (1996) care must be taken in ensuring enough modes have been assumed. Spatial aliasing aspects and errors due to positioning etc. have to be considered as well. The process can be made more robust by using more measurement points than wanted modal amplitudes and using a pseudo-inverse technique as outlined in Fuller et al. (1996). Arrays of sensors are also used in state feedback control of systems to estimate the states of the system. Such an estimator is usually in the form of a Kalman filter (Fuller et al., 1996).

### 2.3 Wavenumber estimation with arrays of point sensors

In many applications it is advantageous to directly sense the wavenumber components of the structural response rather than the modal contributions discussed above. For example positive wavenumber components correspond to positive travelling waves and could be used, in principle, to selectively minimise waves and thus power in selected directions. Far-field sound radiation from planar structures can be shown to be due to only supersonic structural wavenumber components. Thus, if only these components are observed and minimised by active control then,

the sound radiation should be reduced (Fuller and Burdisso, 1992). The structural wavenumber distribution can be estimated using an array of point sensors (such as accelerometers) and processing their output using a Discrete Fourier Transform (DFT). The one-dimensional spatial Fourier Transform is given by

$$W(k_x) = \int_{-\infty}^{\infty} w(x) e^{jk_x x} dx \quad (18)$$

where  $W(k_x)$  are the wavenumber amplitudes at a particular wavenumber value  $k_x$ . This transform can be approximated using a discrete set of samples as

$$\hat{W}(k_x) = \sum_{i=1}^I w(x_i) e^{jk_x x_i} \Delta x \quad (19)$$

where  $\hat{W}(k_x)$  are the wavenumber estimates and  $I$  discrete measurements are taken over equal spacings of width  $\Delta x$  (Fuller et al., 1996). It is also possible to use Fast Fourier Transform (FFT) codes to evaluate the wavenumber distribution as described by Wahl and Bolton (1992). Note that this estimation applies for each frequency of excitation and thus is a frequency domain approach. Often it is better to estimate the wavenumber distribution in the time domain. Maillard and Fuller (1995) have developed an approach which gives time domain estimates of the wavenumber components. In their approach shown systematically in Figure 15 the outputs of an array of accelerometers is passed through a bank of digital filters and then summed. The impulse responses of the filters model the appropriate exponential terms of equation (18). Different banks of filters are used to evaluate the time varying wavenumber signal at different values of  $k_x$ . A typical sensor estimate and the theoretical wavenumber distribution for broadband excitation is shown in Figure 16. A good estimate is apparent over a broad band of frequencies. As demonstrated by Maillard and Fuller (1995) this wavenumber estimate can be used to control broadband structural sound radiating towards a particular direction.

## 2.4 Wave vector filtering with arrays of sensors

A related technique to that discussed in the previous section is separating a vibrational field into its travelling wave components using a finite difference approach rather than a DFT. While this method is less flexible than the DFT approach it requires significantly less processing by assuming that some important component wave dynamics of the structure are known (e.g. axial wavenumber). Figure 17 shows an arrangement for separating positive and negative extensional waves travelling on a rod. The force in the beam can be estimated using the difference between the two sensor outputs. Knowing the wave impedance of the beam allows determination of the difference between the positive and negative wave responses in terms of the difference between the two sensor outputs  $V^-$ . The sum of the wave responses can be estimated from the average of the two sensor outputs, i.e.  $V^+/2$ . The sum and difference of the two wave fields are added thus

eliminating the negative travelling wave and allowing determination of the positive travelling wave in-plane displacement  $u^+$  using the relation (see Fuller et al., 1996 for more details)

$$u^+ = \frac{1}{G} (V^+ + \frac{2Sc_L}{j\omega \Delta x} V^-) \quad (20)$$

where  $S$  is the cross sectional area of the rod,  $c_L$  is the longitudinal phase speed,  $\Delta x$  is the sensor spacing and  $G$  is the gain of the sensors. A similar expression can be derived to obtain the negative wave amplitude. The full mathematical derivation is given in Fuller et al., (1996). Figure 17 shows an electrical circuit designed to carry out the operations of equation (20). The two wave components can be separated with a relatively simple system, however the longitudinal phase speed of the rod-material structure must be accurately known. A further complication is, if the waves are dispersive as in bending motion. In this case, to separate out broadband bending waves, the summing and differencing is carried out after the sensor signals are passed through IIR filters used to model the broadband beam flexural dynamics between the sensor locations. Gibbs et al. (1993) has used such a system in conjunction with PVDF sensors to separate out and actively control broadband flexural waves in beams terminated by finite impedances.

## 2.5 Shape memory alloy (SMA) sensors

Section 1.8 discussed the use of SMA as an actuator in active control systems. SMA can also be used a robust, distributed sensor. The SMA can be manufactured to be super-elastic and very large strains (6%) can be measured before failure of the sensor. Figure 18 shows the output of a SMA sensor embedded in a composite, cantilevered beam (Fuller et al, 1992). The Nitinol SMA sensor was used as the active leg of Wheatstone bridge. When the SMA fiber is strained its resistance increases and the bridge is no longer balanced resulting in a output voltage across the bridge as shown in Figure 18. The output is at 4 Hz and is seen to be quite repeatable as the beam oscillates at its natural frequency. This technique has been extended by Baz et al. (1993) who used arrays of different length SMA fibers embedded in a cantilevered beam in conjunction with a matrix technique very similar to that of Section 2.2, to provide estimates of the modal amplitudes of response. The main advantages of the use of SMA as a sensor are its large strains and ability to work in hostile environments.

## CONCLUSION

A number of advanced actuator and sensor systems for the active control of sound and vibration have been briefly described. Each transducer is specialized for a particular application and has advantages and disadvantages. Choice of the best actuators and sensors is based upon a careful evaluation of the physics of the system to be controlled, the required control goals, the form of controller to be used, as well as physical, cost and power requirements. It is extremely unlikely that a transducer system can happily meet all the requirements and the design is usually a trade-off study between the pros and cons.

The emphasis of the actuators and sensors discussed in this paper are on those devices which can be directly integrated into the material structural system. When such integrated transducer-structural systems are used in conjunction with an adaptive, "learning" type control approaches, the complete system can be seen to be directly related to the rapidly growing field of *smart*, *intelligent*, or *adaptive* structures (Wada et al., 1990). Smart material systems are loosely defined to be those which can sense and react to their environment in a controllable way. Developments in the field of smart structures are likely to be used in advanced applications of active noise control because of the inherent compactness, lightweight and adaptability of this class of system.

## REFERENCES

Baz, A., Poh, S. and Gilheany, J. (1993). A multi-mode distributed sensor for vibrating beams. *Journal of Sound and Vibration*, 165(3), pp. 481-495.

Baz, A. and Ro, J. (1995). Optimum design and control of active constrained layer damping. *Transactions of the ASME Special 50th Anniversary Design Issue*, 117(B), pp. 135-144.

Cabell, R. H., Lester, H. C., Mathur, G. P. and Tran, B. N. (1993). Optimization of actuator arrays for aircraft interior noise control. *AIAA Paper No. 93-4447*.

Clark, R. L. and Fuller, C. R. (1992). Optimal placement of piezoelectric actuators and polyvinylidene fluoride error sensors in active structural acoustic control approaches. *Journal of the Acoustical Society of America*, 92(3), pp. 1521-1533.

Clark, R. L., Fuller, C. R. and Burdisso, R. A. (1992). Design approaches for shaping polyvinylidene fluoride sensors in active structural acoustic control (ASAC). *Proceedings of the Conference on Recent Advances in Adaptive and Sensory Materials and Their Application*, Blacksburg, VA, pp. 702-726 (published by Technomic Press, Lancaster, PA).

Collins, S. A. (1990). Sensors for structural control applications using piezoelectric polymer film. S. M. Thesis, Massachusetts Institute of Technology, Cambridge, Massachusetts.

Collins, S. A., and von Flotow, A. H. (1991). Active vibration isolation for spacecraft. Paper No. IAF-91-289 presented at the 42nd Congress of the International Astronautical Federation, Montreal, Canada.

Fuller, C. R. and Burdisso, R. A. (1992). A wave number domain approach to the active control of structure-borne sound. *Journal of Sound and Vibration*, 148(2), pp. 355-360.

Fuller, C. R., Elliott, S. J. and Nelson, P. A. (1996). *Active Control of Vibration*, Academic Press, London.

Fuller, C. R., Gentry, C. A. and Guigou, C. (1995). Active control of sound with foam-PVDF composite skins. *Proceedings of ICCE/2, Second International Conference on Composites Engineering*, New Orleans, LA, pp. 239-240.

Fuller, C. R., Rogers, C. A. and Robertshaw, H. H. (1992). Control of sound radiation with active/adaptive structures. *Journal of Sound and Vibration*, 157(1), pp. 19-39.

Gandhi, M. V. and Thompson, B. S. (1989). Dynamically-tunable smart composites featuring electro-rheological fluids. *Proceedings of the SPIE Conference on Fiber Optic Smart Structures and Skins II*, Boston, Massachusetts, (SPIE Publication, Vol. 1170), pp. 294-304.

Gibbs, G. P., Fuller, C. R. and Silcox, R. J. (1993). Active control of flexural and extensional power flow in beams using real time wave vector sensors. *Proceedings of the 2nd Conference on Recent Advances in Active Control of Sound and Vibration*, Blacksburg, Virginia (published by Technomic Press, Lancaster, PA) pp. 909-925.

Goldberg, D. E. (1989). *Genetic Algorithmns in Search, Optimization and Machine Learning*, Addison-Wesley, New York.

Goodfriend, M. J. and Shoop, K. M. (1991). Adaptive characteristics of the magnetostrictive alloy, Terfenol-D, for active vibration control. *Proceedings of the Conference on Recent Advances in Active Control of Sound and Vibration*, Blacksburg, VA, pp. 199-209. (published by Technomic Press, Lancaster, PA)

IEEE Standard on Piezoelectricity (1988). ANSI/IEEE Std. 176-1987, *The Institute of Electrical and Electronics Engineers, Inc.*, New York.

Jackson, C. M., Wagner, H. J. and Wasilewski, R. J. (1972). 55-Nitinol-the alloy with a memory: its physical metallurgy, properties and applications. NASA-SP-5110, Washington, District of Columbia.

Lee, C. K. and Moon, F. C. (1990). Modal sensors/actuators, *American Society of Mechanical Engineers Journal of Applied Mechanics*, 57, pp. 434-441.

Liang, C., Rogers, C. A. and Fuller, C. R. (1991). Acoustic transmission and radiation analysis of adaptive shape-memory alloy reinforced laminated plates. *Journal of Sound and Vibration*, 145(1), pp. 23-41.

Maillard, J. P. and Fuller, C. R. (1995). Advanced time domain wave-number sensing for structural acoustic systems. Part III. Experiments on active radiation control of a simply supported plate. *Journal of the Acoustical Society of America* 98(5), pp. 2613-2621.

Newnham, R. E., Dogan, A., Xu, Q. C., Onitsuka, K., Tressler, J. and Yoshikawa, S., (1993). Flextensional "moonie" actuators. *Proceedings of 1993 IEEE Ultrasonics Symposium*, pp. 509-513.

Ruckman, C. A. and Fuller, C. R. (1995). Optimizing actuator locations in active noise control systems using subset selection. *Journal of Sound and Vibration*, 186(3), pp. 395-406.

Scribner, K. B., Sievers, L. A. and von Flotow, A. H. (1993). Active narrow-band vibration isolation of machinery noise from resonant substructures. *Journal of Sound and Vibration*, 167(1), pp. 17-40.

Stangroom, J. E. (1983). Electrorheological fluids. *Journal of Physics Technology*, 14, pp. 290-296.

Uchino, K. (1994). Chapter 12: Ferroelectric Ceramics in *Materials Science and Technology*, Eds. R. W. Cahn, P. A. Haasen and E. J. Kramer, VCH Publishers Inc., New York.

von Flotow, A. H., Beard, A. and Bailey, D. (1994). Adaptive tuned vibration absorbers: tuning laws, tracking agility, sizing and physical implementations. *Proceedings of Noise-Con 94*, Ft. Lauderdale, FL, pp. 437-454.

Wada, B. K., Fanson, J. L. and Crawley, E. F. (1990). Adaptive structures. *Journal of Intelligent Material Systems and Structures*, 1, pp. 157-174.

Wahl, T. J. and Bolton, J. S. (1992). The use of the discrete Fourier transform to calculate the spatial and temporal response of line-driven, layer-wise homogeneous acoustically loaded panels. *Journal of the Acoustical Society of America*, 92(3), pp. 1473-1488.

Wang, B. T., Burdisso, R. A. and Fuller, C. R. (1991). Optimal placement of piezoelectric actuators for active control of sound radiation from elastic plates. *Proceedings of Noise-Con '91*, Tarrytown, New York, pp. 267-275.

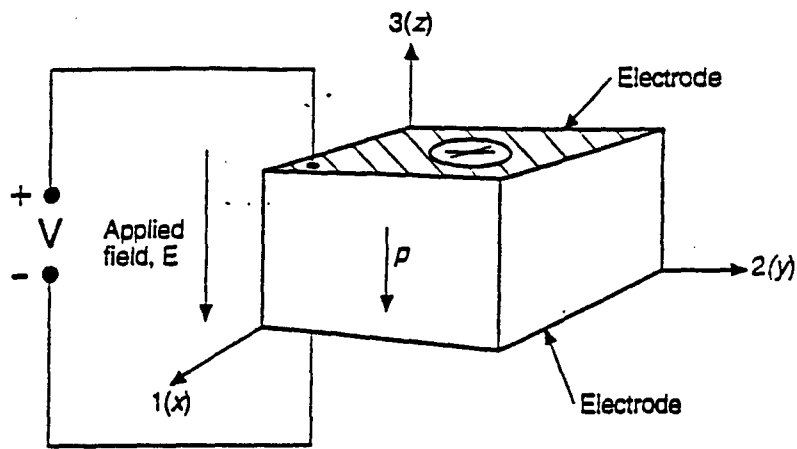


Figure 1. Piezoelectric element and notation.

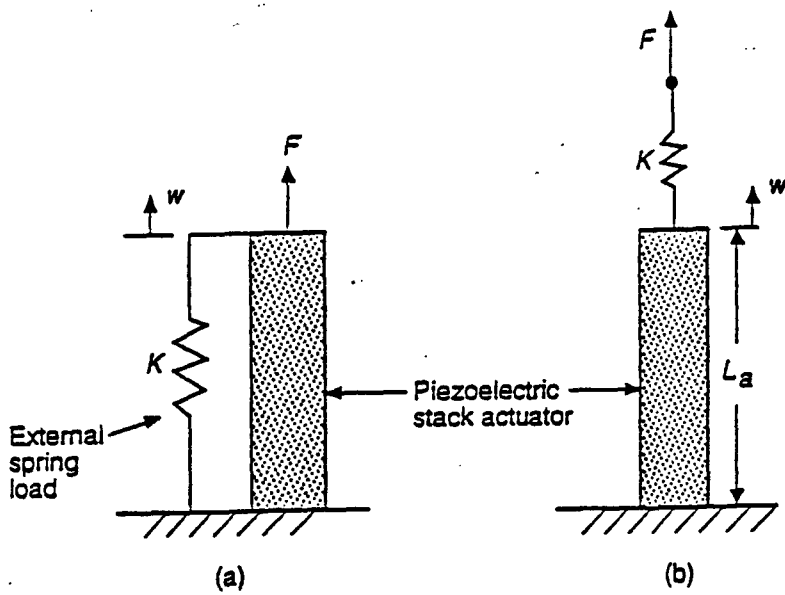


Figure 2. Piezoelectric stack actuator working against an external stiffness load in (a) parallel (b) series with the load.

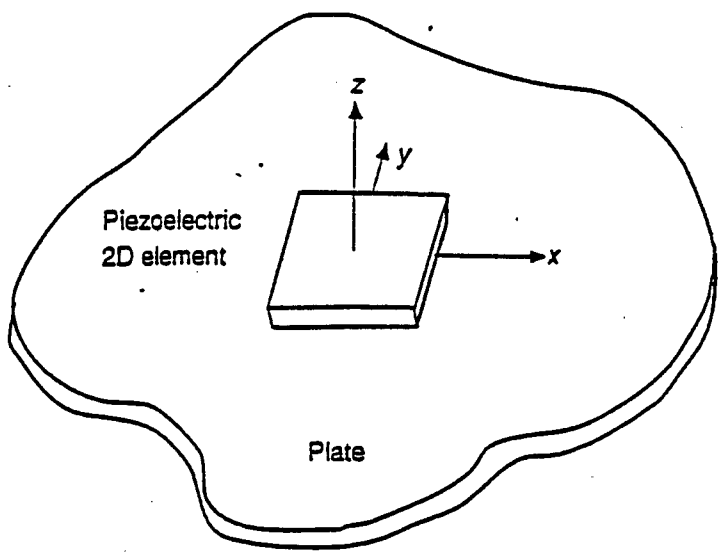


Figure 3. Two-dimensional piezoelectric wafer element and structure.

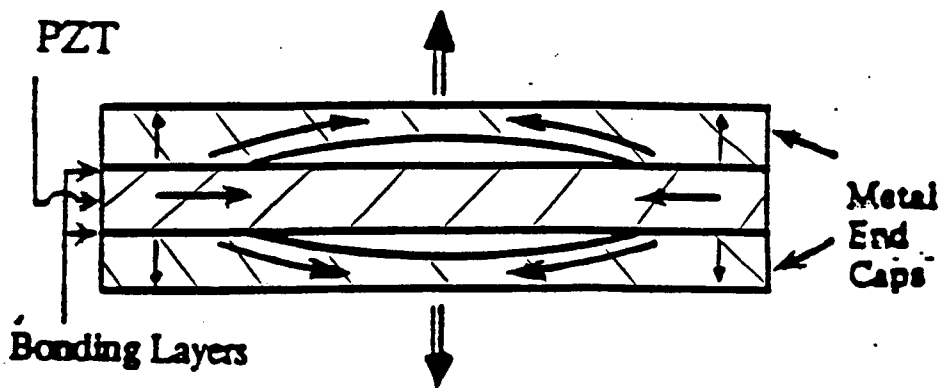


Figure 4. The geometry of the ceramic-metal composite actuator "Moonie." Arrows describe the direction of displacement.

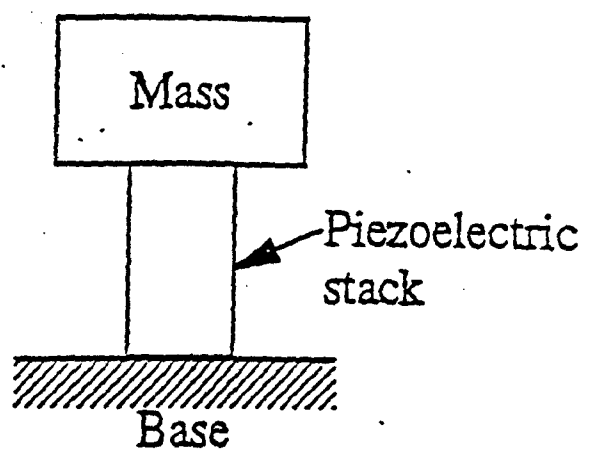


Figure 5. Piezoelectric resonance actuator.

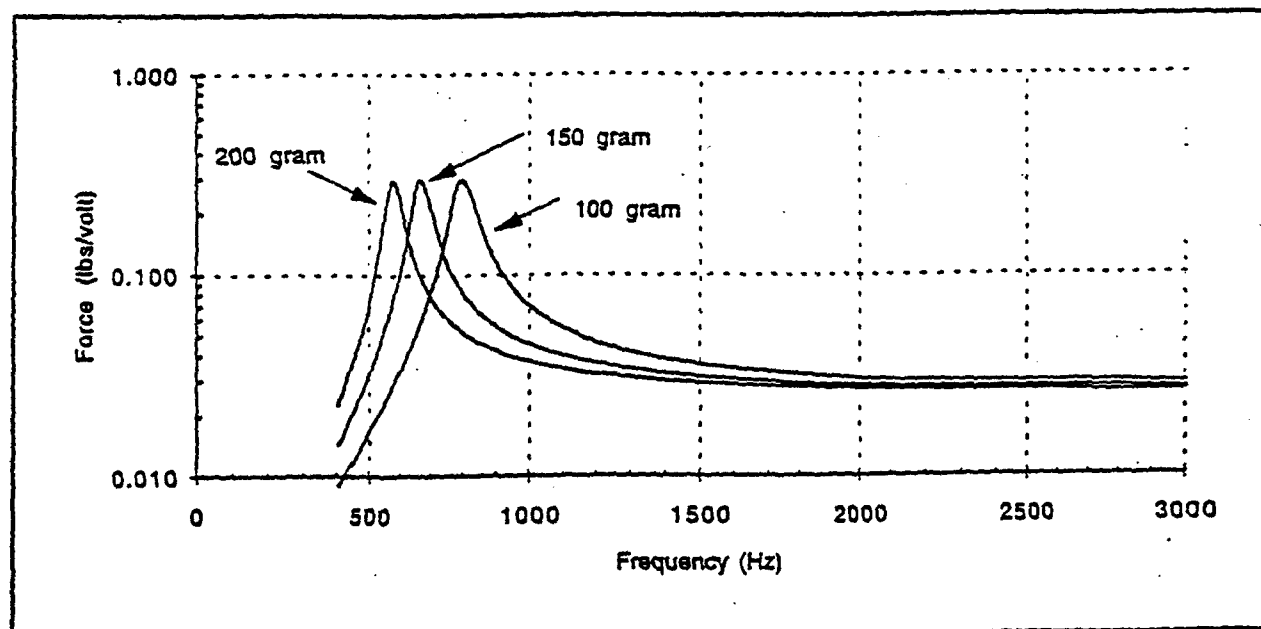


Figure 6. Typical actuator response with varying inertial mass.

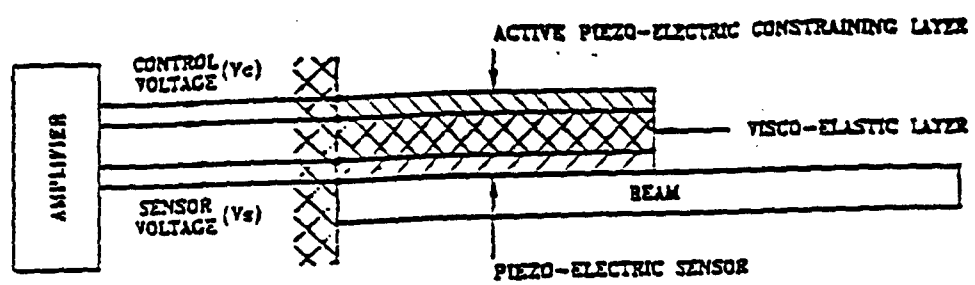


Figure 7. Schematic drawing of the active constrained layer damping.

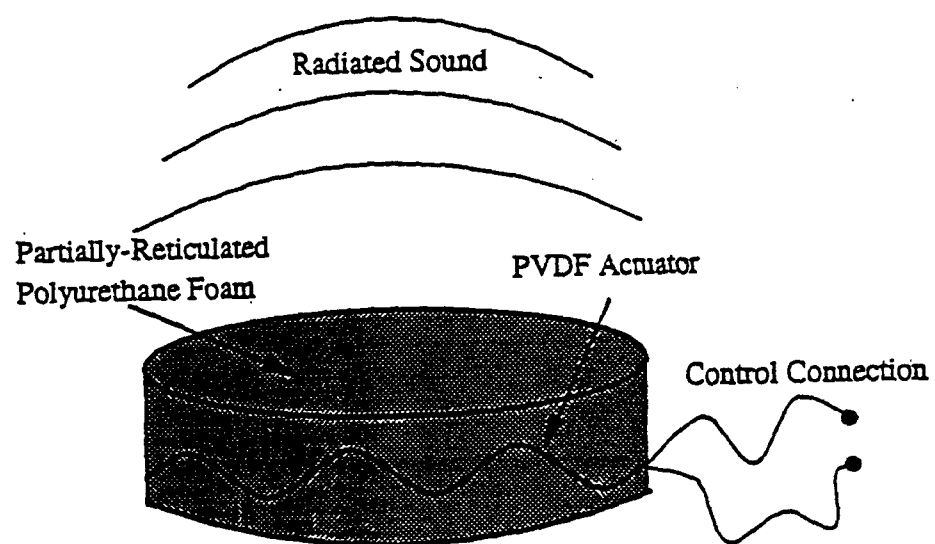


Figure 8. Smart foam.

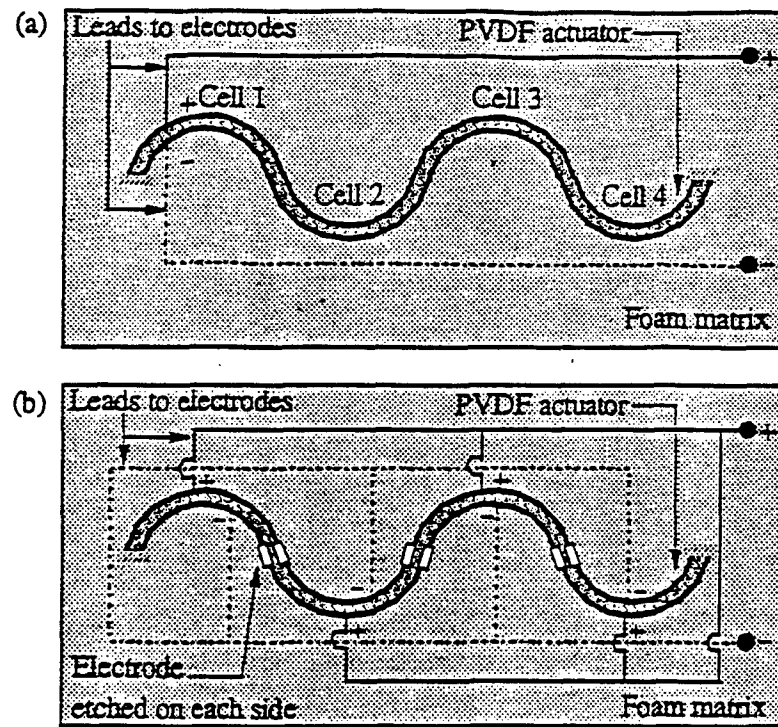


Figure 9. PVDF actuator configuration, (a) Original and (b) Parallel.

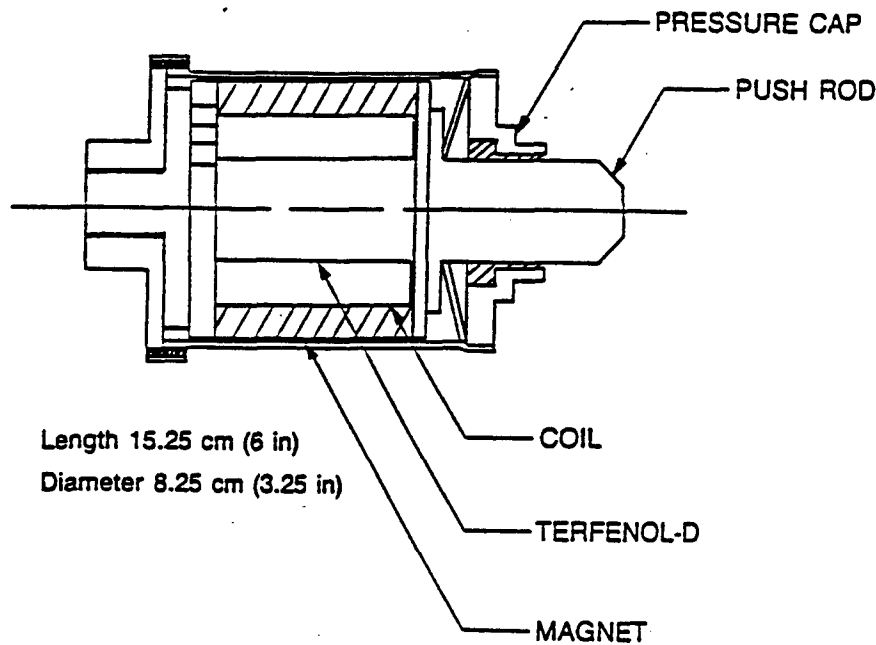


Figure 10. Arrangement of magnetostrictive actuator.

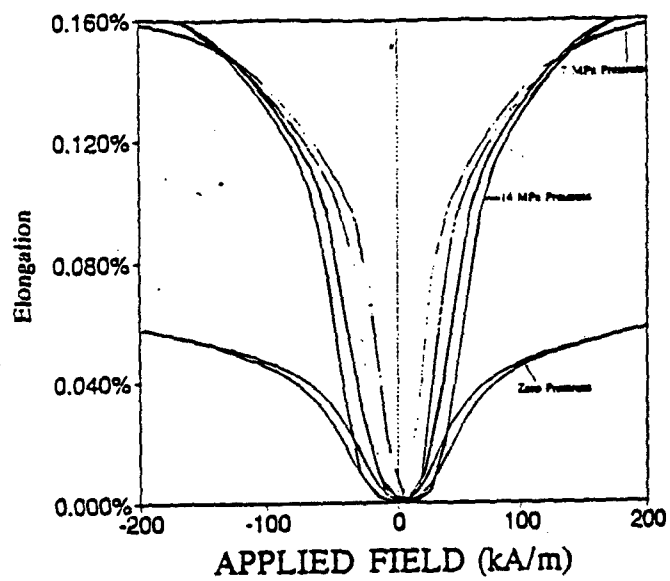


Figure 11. Typical performance of Etrema Terfenol-D.

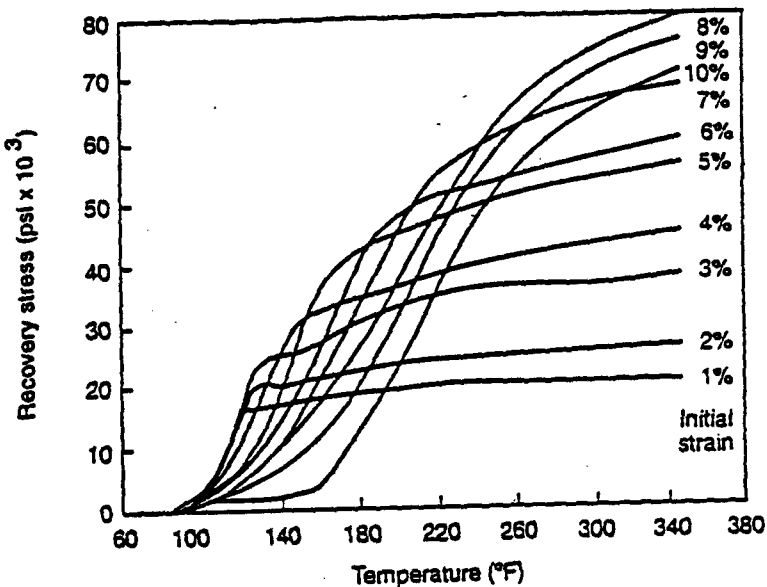


Figure 12. Recovery stress versus temperature for NiTi shape memory alloy.  
Heat rate equals 40° per minute (after Jackson, 1972).

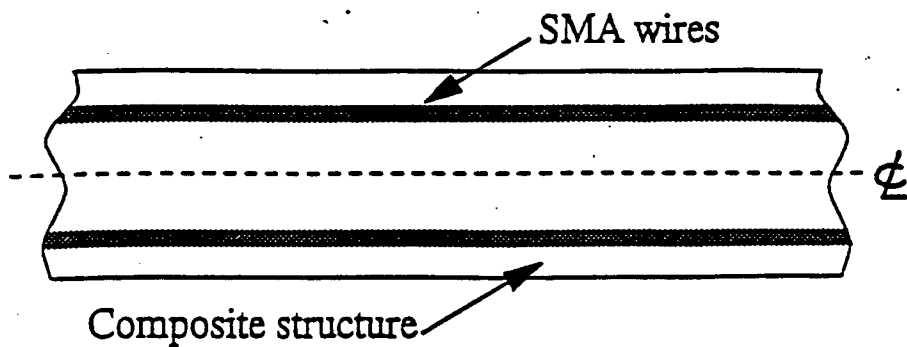
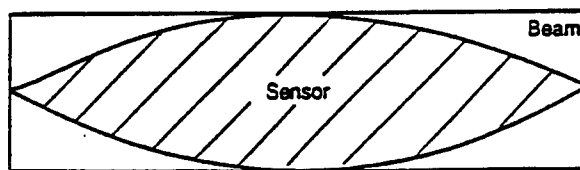
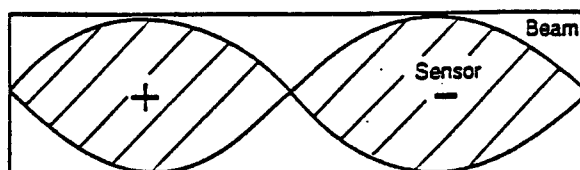


Figure 13. SMA composite material system.



(a)



(b)

Figure 14. Distributed sensor shapes for a one-dimensional simply supported beam modal observer. (a)  $n=1$  mode (b)  $n=2$  mode.

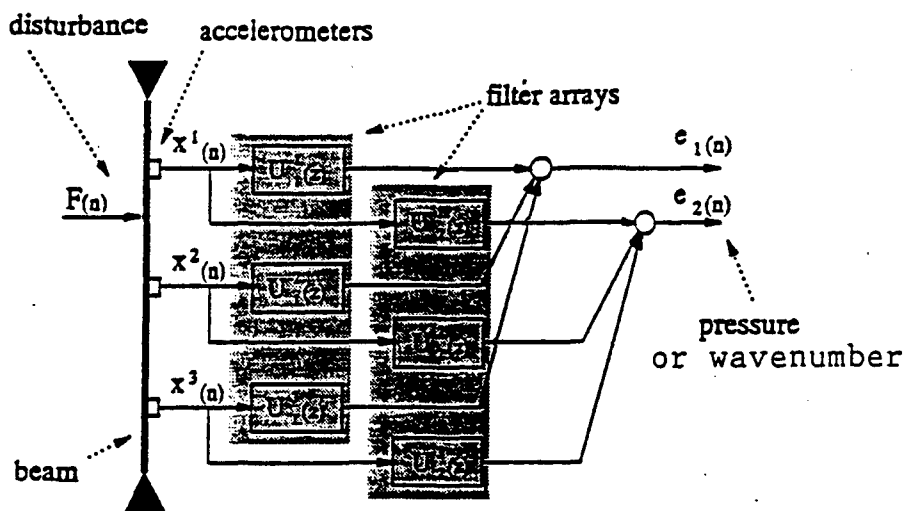


Figure 15. Wavenumber sensing configuration applied to a 1-D beam.

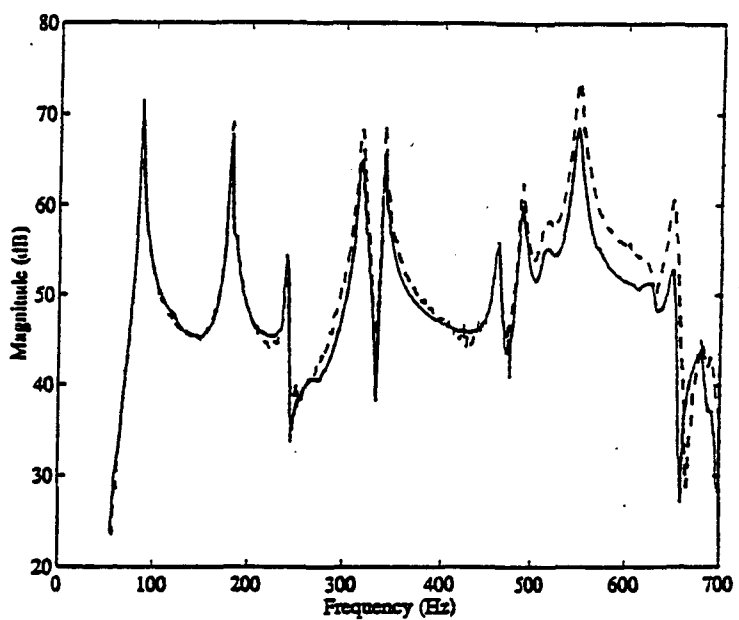


Figure 16. Actual (—) and predicted (----) wave-number component coupled to direction of sound radiation ( $\theta = 36^\circ$ ,  $\Phi = 0^\circ$ ). Note  $k_x = k_0 \sin(\theta)$ .

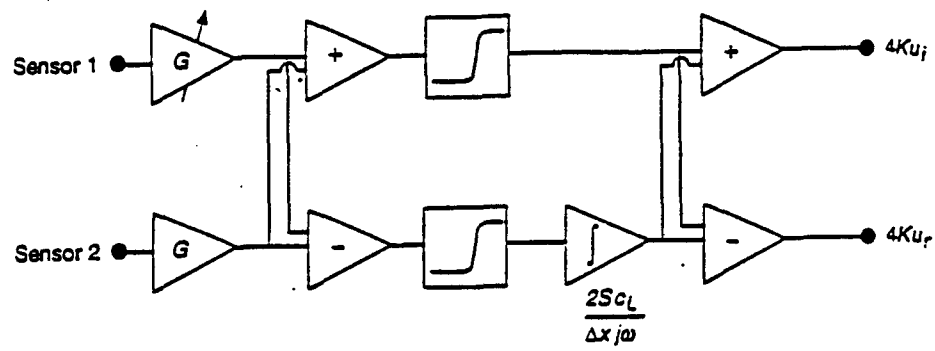


Figure 17. Circuit diagram for an analog wave vector filter in a one-dimensional, non-dispersive medium (after Elliott, 1981).

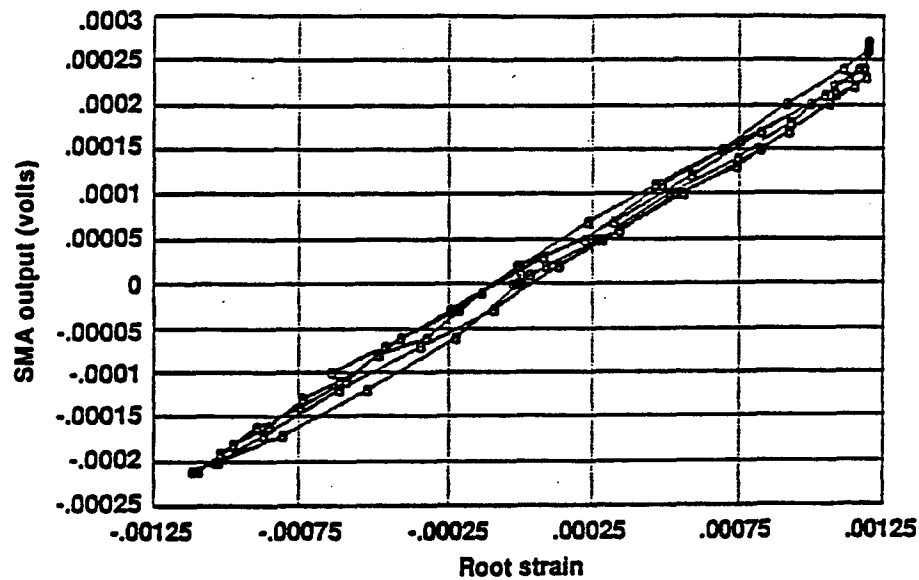


Figure 18. SMA strain sensor.

## **APPENDIX 37**

## CONTROL OF SOUND RADIATION FROM STRUCTURES USING ACTIVE SKINS

by

C.R. Fuller, C. Guigou and B.D. Johnson  
Vibration and Acoustics Laboratories  
Department of Mechanical Engineering  
Virginia Polytechnic Institute and State University  
Blacksburg, VA 24061  
USA  
*website:*<http://www.VAL.me.vt.edu/>

### ABSTRACT

The control of sound radiation from vibrating surfaces is an important problem in noise control. This paper discusses two approaches to reduce the sound radiation both based upon the use of an active skin that decouples the structural sound motion from the associated sound field. The first approach is an active-passive system that utilizes a smart foam consisting of layers of piezoelectric material embedded in areas of acoustic foam. The second system consists of a continuous layer of multiple double amplifier piezoelectric cells arranged to impart normal velocity. The physical concepts and the associated control approaches of both devices will be discussed and their use is demonstrated on control of broadband sound radiation from vibrating panels. The integration of the error sensors into the skin system is considered.

### INTRODUCTION

In the last decade there has been an increased interest in developing methods for the active control of sound radiation from vibrating structures [1]. In one promising method, termed Active Structural Acoustic Control (ASAC), actuators are attached directly to the structure and are used to modify its

structural vibration characteristics (spatial and temporal) in order to minimize the sound radiation [1]. In ASAC, the actuators tend to be compact and thus cover only a very small portion of the structure; their effect is achieved due to the distributed elastic response of the structure. This technique has worked well for a number of applications usually where the structure has a reasonable mobility and a low modal density of response. In some applications however, the structure is quite massive or stiff and it is extremely difficult to elicit the necessary control field response with practical control actuators. In this paper we discuss a variant of the ASAC approach in which the control inputs come from an *active skin* which covers all or most of the vibrating surface. The objective of the active skin is to locally change the radiation impedance (the resistive component) of the structure in order to control the total radiated power in contrast to the conventional ASAC, which alters the dynamic response of the host structure. Since it does not drive the host structure, an active skin is thus suitable for heavy or stiff structures with low mobility. The negative trade-off, however, of the active skin approach, is that since it covers the structure completely, it may require many independent sections if the structural response is complex and near or above the critical frequency. Two different skins are described; one based on ceramic piezoelectric elements and the other on a composite of acoustic foam and the piezoelectric polymer PVDF.

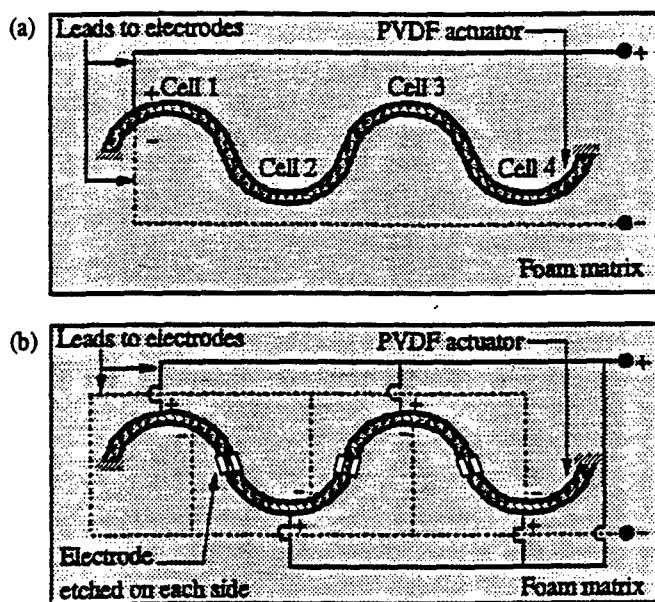


Figure 1: PVDF actuator configuration, (a) Original and (b) Parallel.

## SMART FOAM ACTIVE SKIN

Acoustic foam is commonly employed as a form of passive liner or skin in order to reduce sound radiation. For example in aircraft interiors, a layer of acoustic foam is located between the inside surface of the fuselage and the interior trim panels. Generally the foam completely covers the fuselage surface and its acoustic purpose is to reduce noise transmitting through the fuselage to the interior. However it is well known that passive treatments such as foam work well at high frequencies ( $>1000\text{Hz}$ ) and their performance is poor at low frequencies. Here we describe the use of

a smart foam active skin, which is a hybrid of the materials of passive foam and active piezoelectric elements [2]. The objective is to develop a flexible active skin that combines good high frequency passive performance with the low frequency performance of an active system. The smart skin has to be of such a form that it can be extended to cover complex distributed surfaces similar to conventional acoustic foam. A typical configuration of the smart foam is shown in diagrammatic form in Figure 1. The smart foam can be seen to consist of conventional acoustic foam with embedded layers of the flexible polymer piezoelectric material, PVDF[1]. Two aspects of the embedded PVDF are significant. Firstly the PVDF is curved in order to couple the predominantly in-plane piezoelectric effect with the required normal motion (in effect creating a motion amplifier as discussed below) and secondly, as shown in Figure 2(b), alternate half wave sections of the PVDF can be wired out-of-phase. This second aspect is designed to increase the radiation efficiency of the active element (and thus its control authority) by causing all the PVDF sections to move in the same direction when a voltage is applied across the PVDF electrodes.

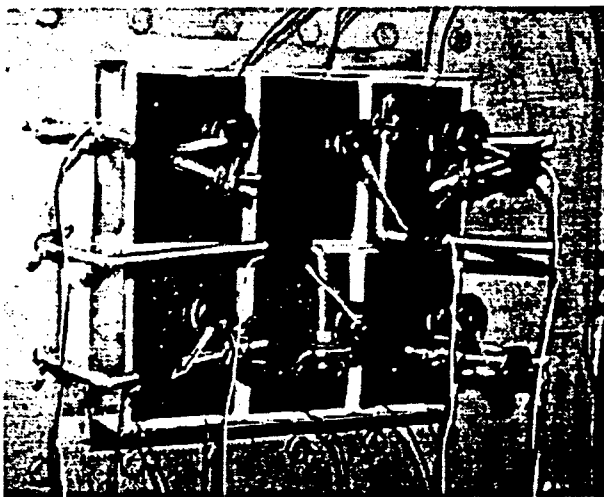
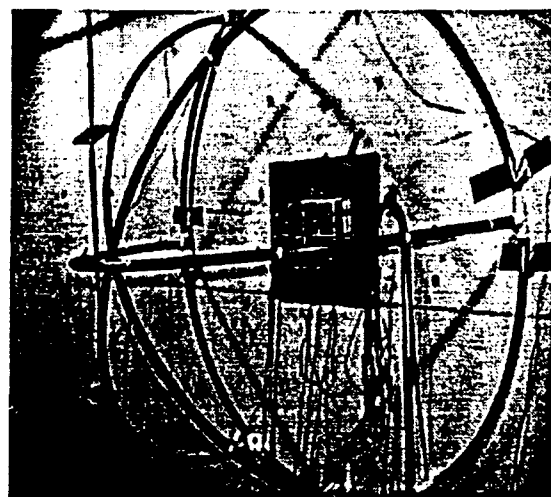


Figure 2: (a) Actuator and error sensor configuration.



(b) Spherical dome for power measurements.

Figure 2 (a) shows a picture of a smart foam active skin covering a plate of dimensions 170 x 50 x 1.5 mm. The smart foam skin can be seen to be comprised of six independently controllable skin cells constructed as described above. In addition each cell has a lightweight balsa wood wall used to increase the normal displacement by constraining the foam edge. Above each smart foam cell is a microphone located close to the foam surface and used as an error sensor in a MIMO feedforward Filtered-x LMS control approach[1] (see Figure 11 for a typical feedforward LMS arrangement). The plate and smart foam skin is located in a rigid baffle located in the VAL anechoic chamber. Figure 2(b) shows a hemispherical array of ten microphones located over the plate and in the radiated sound field. The microphones are used to estimate the total radiated sound power from the plate-smart foam system. The disturbance to the plate was provided by a piezoelectric patch actuator[1], bonded to the back. The reference signal for the LMS control approach was taken from the internal signal generator used to drive the disturbance (termed internal reference).

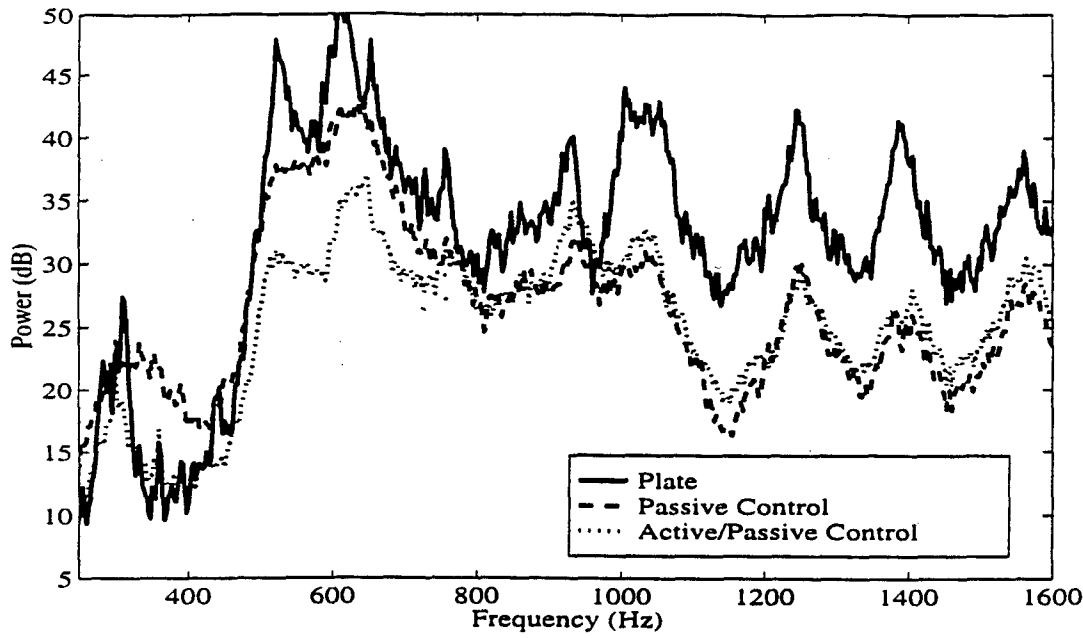


Figure 3: Radiated power for a broadband IISO case using multiple smart foam modules operating in phase.

Figure 3 presents the radiated power without control, when all the smart skin cells are wired together in phase as a single channel of control. The error signal is provided by a single microphone located close to the smart foam surface and at the plate-foam center. Also shown is the passive effect of the smart skin when it is located on the plate but not activated. It is apparent that the passive effect of the skin is good at high frequencies above 1000Hz but is limited to resonant frequencies of the base plate below this value. Turning on the active control provides reasonable attenuation at low frequencies however there are some frequency ranges where the control is negligible, for instance near 900Hz. We now extend the controller so that the six smart skin modules can be controlled independently with a six by six LMS control arrangement. Figure 4 presents these new results for the low frequency range. For the results of Figure 4 three different reference signals control configuration are also studied; one using an internal reference, one using an external reference signal taken from an accelerometer located on the plate (representing a more realistic arrangement), and an external reference signal with feed back (F. B.) from the active component of the smart skin removed[1]. It is apparent that much improved performance is achieved over the SISO case of Figure 3, particularly for the internal reference case, due to the multi-cell active skin being able to match the complex radiation impedance load near 900Hz, for example[3].

Using an external reference signal also provides reasonable attenuation; however, it is reduced from the internal case implying that the system is acausal[1]. Some of the lost performance is recovered when feedback removal is employed indicating that the smart foam vibration has some input to the plate system.

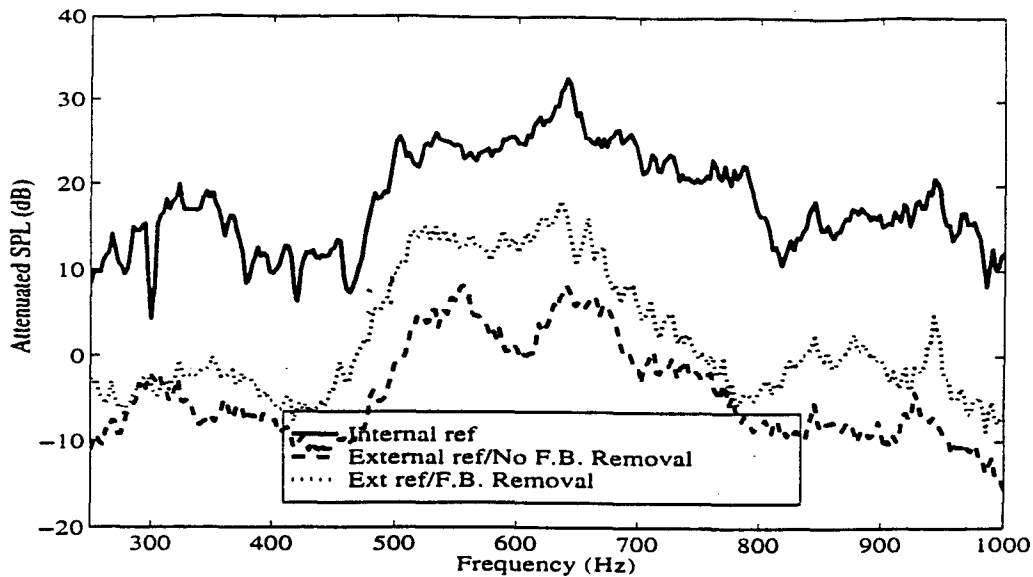


Figure 4: Attenuated SPL for broadband 6I6O case using multiple-independent smart foam modules.

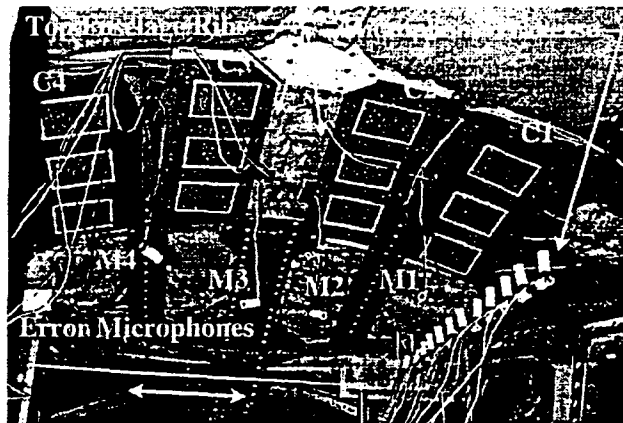


Figure 5: Cessna crown panels control arrangement.

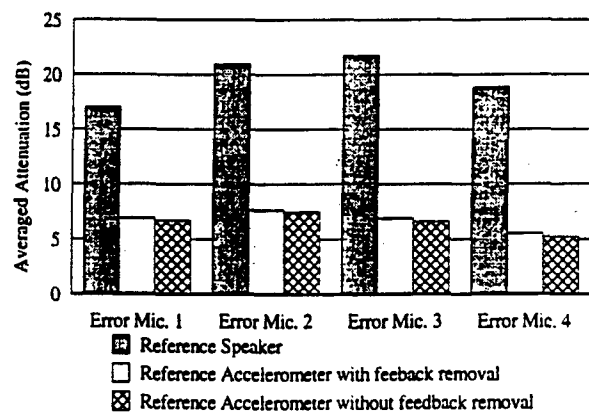


Figure 6: Averaged attenuation at error microphones for band-limited 500-900 Hz excitation.

Recently the smart foam skin has been used to demonstrate control of interior noise in aircraft[4]. Figure 5 shows a smart foam skin covering four panels in the crown section of the fuselage of a Cessna business jet. The application is focused towards reducing cockpit noise due to exterior flow separation over the crown of the aircraft. Error microphones were located as shown at the ear locations of the crew and a microphone traverse was used to measure the sound pressure levels in a plane at the crew head height. The flow noise disturbance was simulated by an exterior speaker located just over the crown of the aircraft and driven by band limited white noise. A four by four feedforward LMS control approach was implemented using a realistic reference signal taken from an

interior mounted accelerometer located on the fuselage at the aircraft crown (i.e. just under the excitation location). Figure 6 presents tabular results of the attenuation achieved at the error sensors (near the crews' ears) with an excitation band of 500 to 900Hz. Reference speaker refers to the use of a reference signal from the signal driving the disturbance. Reference accelerometer refers to the use of a fuselage mounted accelerometer as a reference sensor and in this case attenuation of the order of 2-4dB are achieved. The global attenuation measured using the microphone traverse was found to be 2.5dB with the active skin turned on. However the active skin also provides a passive attenuation of 4dB when it is installed over the bare fuselage panels and not turned on. Thus the total global attenuation of the smart foam active skin is around 6.5dB; a significant difference. It also apparent from Figure 6 that one of the main limitations on achievable attenuation is the causality of the controller when using an accelerometer as a reference signal; when the reference signal is taken from the speaker drive signal the control path delay is less and the performance increases markedly. The results do, however, demonstrate the potential of the smart foam skin in reducing structurally radiated sound in a realistic application.

### PIEZOELECTRIC DOUBLE AMPLIFIER ACTIVE SKIN

Piezoelectric transducers tend to be high force, low displacement devices[1]. In contrast, active noise control applications require high displacement actuators, particularly at very low frequencies. Thus much of the work in developing piezoelectric based actuators for active noise control applications has been in designing devices which amplify their displacement. This amplification is usually based upon a geometric lever type principle and thus results in lower output force. More explicitly the actuators are designed to have the correct source impedance relative to their load. In our application the load is air with a relatively low impedance thus the device needs to have a low source impedance for maximum power output.

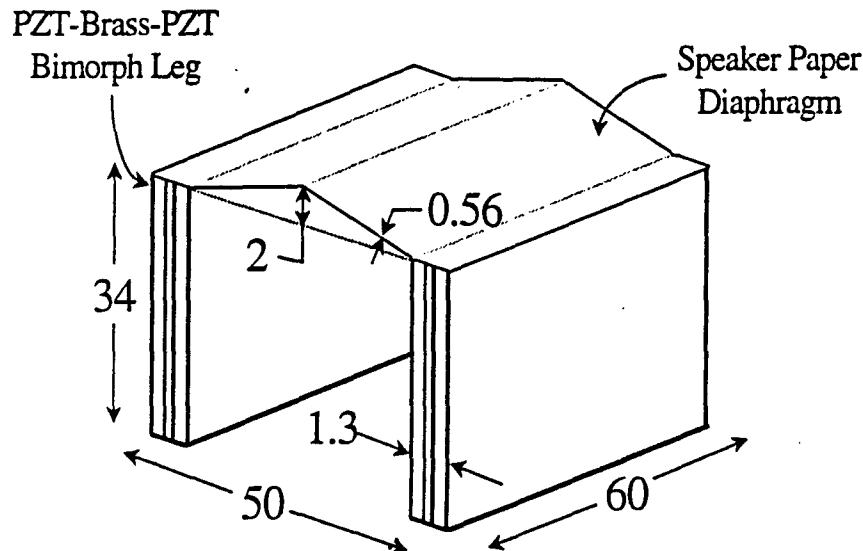


Figure 7: The Active Skin Element

Figure 7 shows a schematic diagram of a piezoelectric double amplifier actuator, which is the basis of the second active skin.[5] The legs of the element consist of piezoelectric bimorphs or unimorphs. In this case the piezoelectric transducers are manufactured from the ceramic material PZT[1]. These devices are amplifiers in that, due to their asymmetry, small in-plane motions are amplified to larger transverse tip motions at the top of the legs. The tops of the legs are connected to a triangular or curved stiff, lightweight diaphragm as shown. Thus as the legs move in, the diaphragm is squeezed upwards. Since the diaphragm axis is transverse to the tip motion, very small tip motions cause very large diaphragm motions (i.e. amplify it) in a vertical direction. Thus the complete structure comprises a double amplifier actuator and gives amplification ratios of diaphragm to piezoelectric element in-plane deflection of the order of 20:1. The whole configuration can be built in heights typically ranging from 3-6 cms, leading to a fairly compact device. In order to construct an active skin of such devices a number of them are positioned to completely cover the surface of a structure as shown in Figure 8. The devices can either be located directly on the structure as shown or positioned just above it with a small air gap. In addition the devices can be wired together as one channel of control or independently controlled depending upon the complexity of the base structural response.

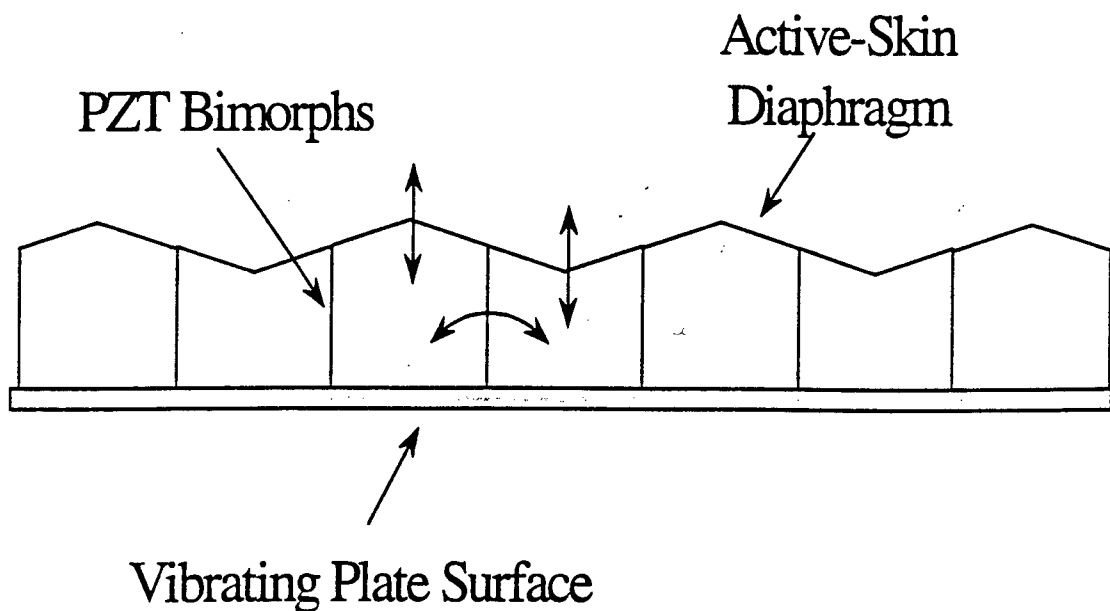


Figure 8:The Active-Skin Concept

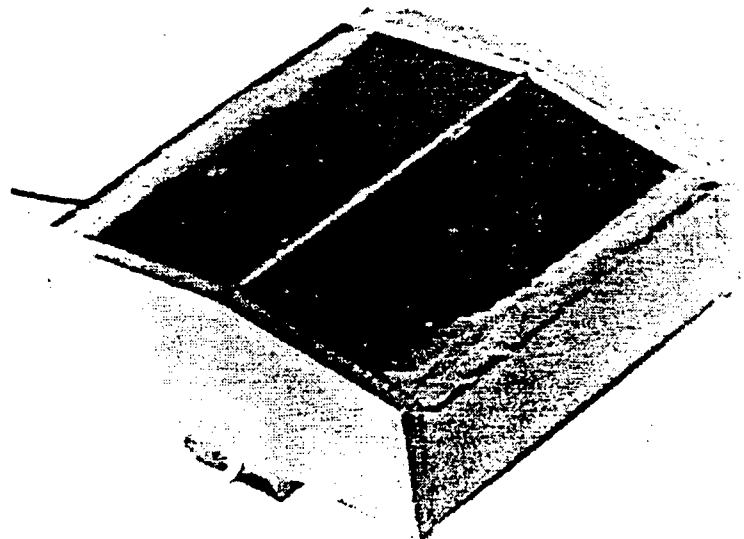


Figure 9:A Single Active-Skin Cell

Figure 9 shows an actual device designed and constructed by the Materials Research Laboratory at Penn State University. The device is 50 x 60 cms, 34 cms high and was found to have a maximum cover displacement of 300mm at 100Hz. Figure 10 shows six of the devices arranged to completely cover the surface of a 170 x 150mm aluminum plate of 1.5mm thickness. In this test arrangement the active skin cells are located on a perforated aluminum sheet which is located 5mm from the surface of the radiating plate. Thus the active skin has a small air gap between its bottom surface and the radiating surface of the structure[5]. Small accelerometers located on each active cell diaphragm are also apparent in Figure[10]. These accelerometers are used to provide time domain estimates of the radiated pressure in the far-field from the measured surface vibration data, termed Structural Acoustic Sensing (SAS) and described in detail in Reference 6.

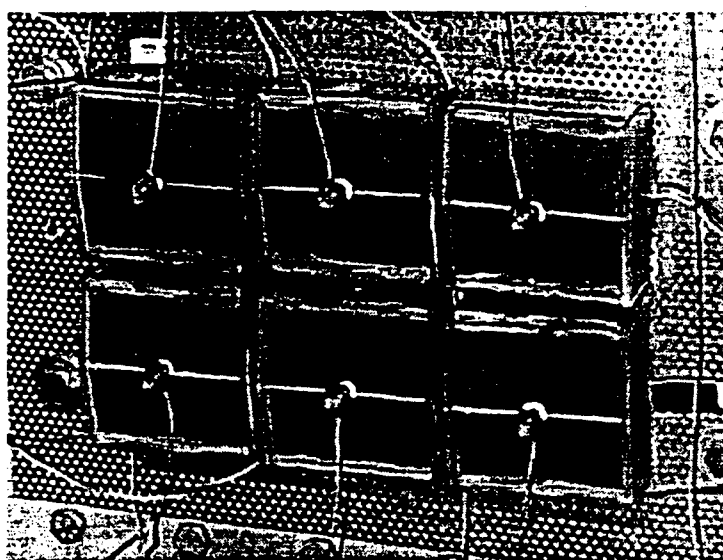


Figure 10: The Active-Skin in a top-mounted SAS configuration.

The test plate and the active cells were mounted in a rigid baffle located in the anechoic chamber at VAL. A noise disturbance to the plate was provided by a small shaker attached to the back of the plate and driven with band limited random noise. The radiated sound from the plate-skin structure was measured using an array of 16 microphones located on a hemispherical tube structure as described above and a microphone traverse which could measure the sound directivity in the horizontal mid-plane of the plate. The total radiated power from the plate could be calculated from the 16 pressure levels measured by the microphone hemispherical array[5].

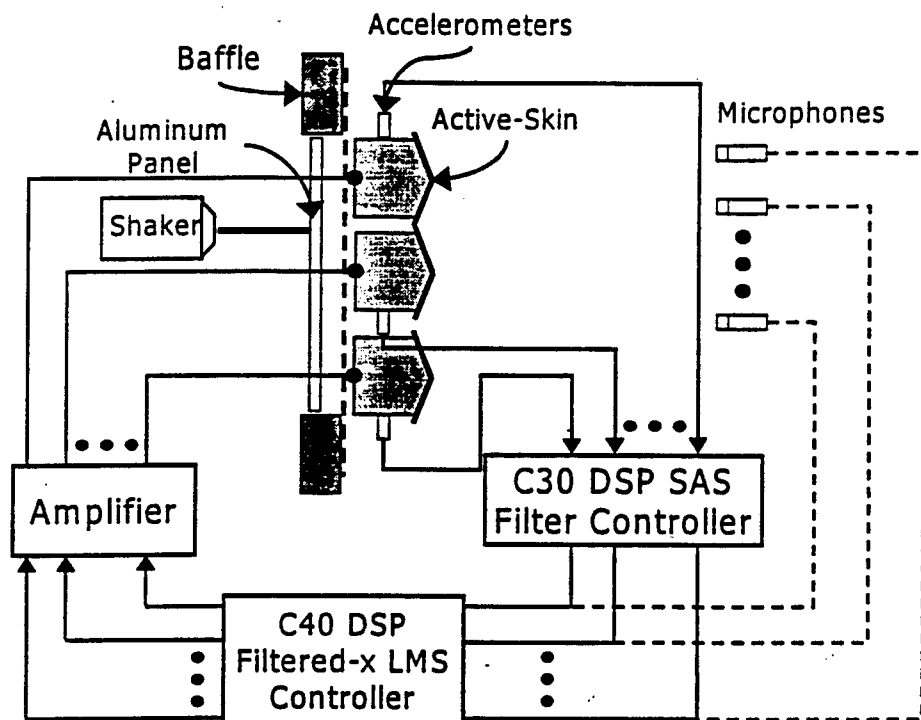


Figure 11: The Active-Skin Experimental Setup

Figure 11 depicts a schematic of the experimental rig and the control arrangement. The control approach used was the Filtered X LMS algorithm [1] implemented on a TMSC40 DSP. The shaker was driven with band limited noise of 175 to 600 Hz. The Filtered X algorithm was executed with a 2000Hz sample rate and 175 and 96 tap FIR filters were used for the control and system identification paths respectively. Since six independent cells were located on the structure to comprise the active skin, a six by six controller was implemented[5]. Two tests were performed using different error sensors. In the first test, six microphones evenly distributed over the microphone array were used as conventional pressure error sensors located in the radiated far field. In the second test the diaphragm accelerometer signals were used in the structural acoustic sensing approach described in Ref. 6 to estimate the pressures at the same locations as the previous error microphones. These estimates were then used as error signals for the LMS algorithm.

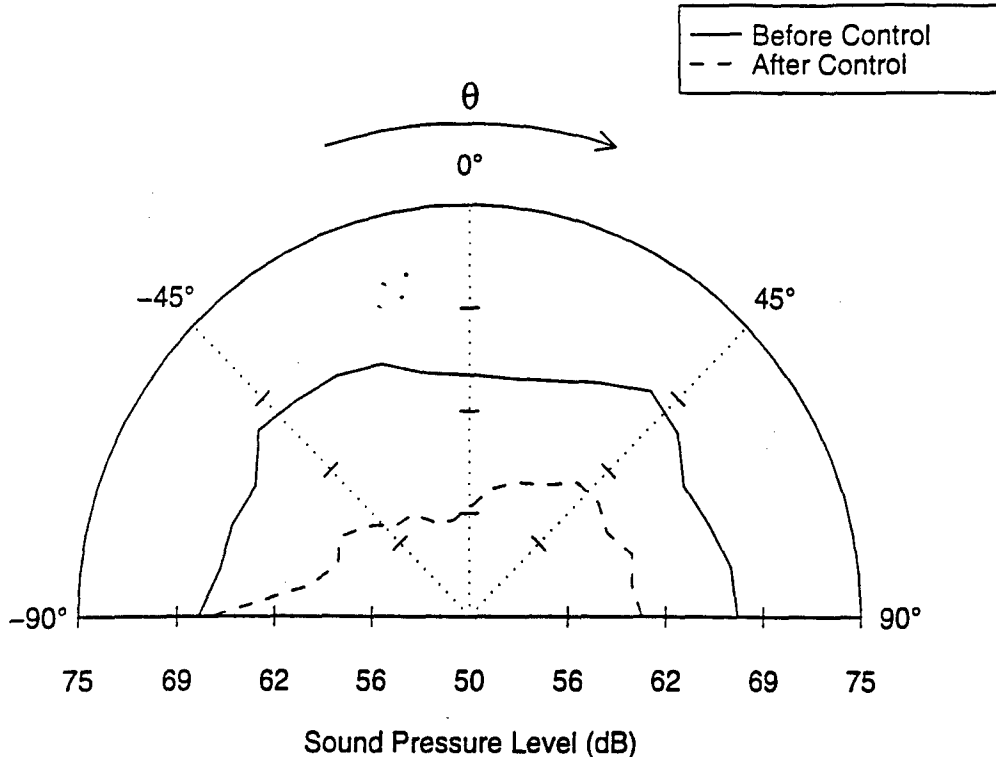


Figure 12: Total In-plane Acoustic Directivity (SPL), top mounted accelerometer configuration with microphone error sensing.

Figure 12 presents experimental results of the directivity of the total radiated sound power measured using the far-field microphone traverse before and after the control using the active skin elements. It is apparent that the active skin provides global sound pressure level attenuation of the order of 10dB which is impressive since the excitation band encompasses multiple modes of vibration of the radiating plate[5]. Figure 13 shows the corresponding radiated power versus frequency. Good control is seen over the complete bandwidth of 170 to 600 Hz except around 350 and 530Hz which are anti-resonances of the plate-active skin system. The overall sound power reduction for the results of Figure 13 is 10.9dB. Further experiments were conducted using the accelerometers in the SAS approach and the results are presented in Figure 14. Good attenuation is evident across the frequency band except near the system anti-resonance and the overall reduction is now 9.5dB, which is still impressive. Thus the results demonstrate that it is possible to utilize an active skin which can provide significant attenuation of sound radiated from a structure vibrating in complex response shapes. The successful use of the accelerometers is significant in that it shows that an active skin with completely integrated actuators and sensors can be constructed that provides very significant broad-band sound attenuation of sound radiated from structures under broadband excitation[5].

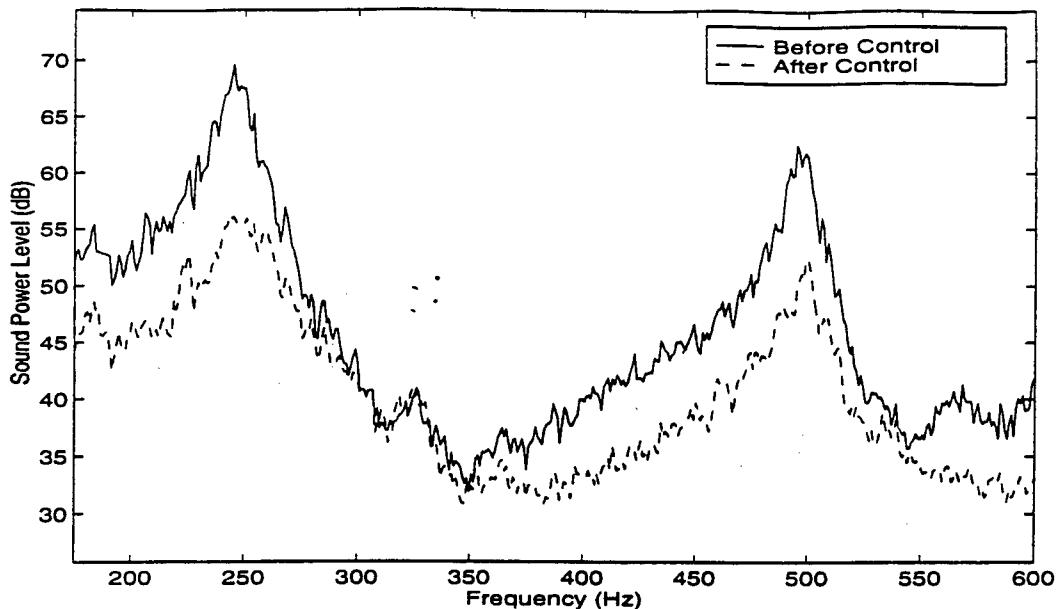


Figure 13: Radiated Sound Power Spectra, top mounted accelerometer configuration with microphone error sensing.

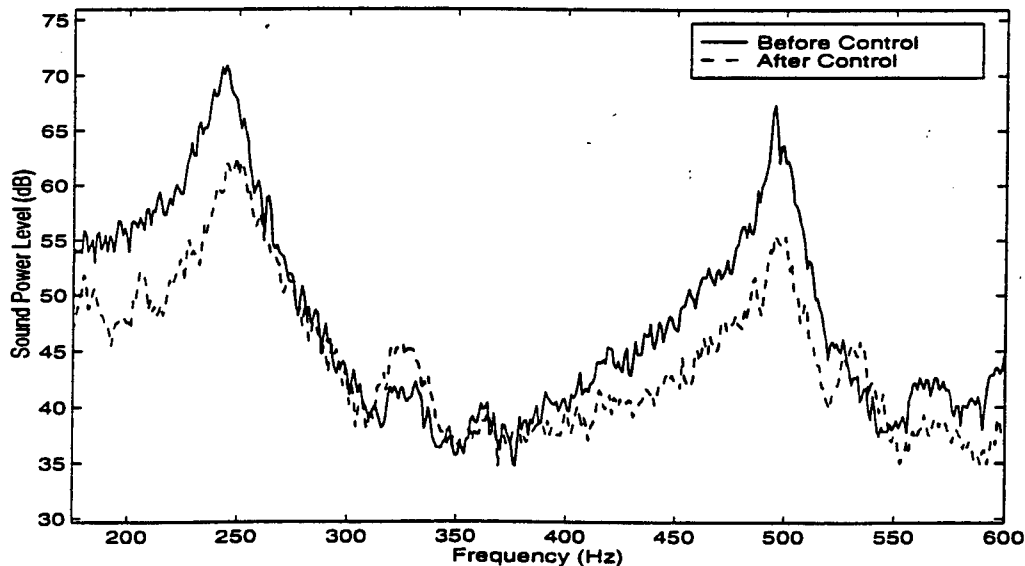


Figure 14: Radiated Sound Power Spectra, top mounted accelerometer configuration with SAS error sensing.

## CONCLUSIONS

This paper has briefly discussed the concepts, configurations and implementations of an active skin for reducing sound radiated from vibrating structures. The results presented have demonstrated the high potential for such an approach when the radiating structure is massive, stiff (i.e. low mobility) or the source vibration pattern is complex. The active skin has also demonstrated the possibility of combining active and passive control approaches in order to increase the control bandwidth and the

efficiency of the active portion. A configuration has been demonstrated, which also shows that the error sensors can be integrated directly into the skin but still result in a far-field sound reduction.

#### ACKNOWLEDGEMENTS

ONR/DARPA, ARO and NASA LaRC, whose support is gratefully acknowledged, funded most the work described in this paper.

#### REFERENCES

1. Fuller, C.R., Elliott, S.J. and Nelson, P.A., "Active Control of Vibration", Academic Press, London, 1996.
2. Gentry, C.A., Guigou, C. and Fuller, C.R., "Smart Foam for Applications in Passive-Active Noise Radiation Control", *Journal of the Acoustical Society of America*, Vol 101 (4), 1771-1778, 1997.
3. Gentry, C.A., Guigou,C. and Fuller, C.R., "Smart Foam for Active/Passive Plate Radiation Control", submitted to the *Journal of the Acoustical Society of America*, 1997.
4. Guigou, C. and Fuller, C.R., "Foam-PVDF Smart Skin for Aircraft Interior Sound Control", *Proceedings of the SPIE Smart Structures and Materials Conference*, San Diego, CA, SPIE Vol 3044, 68-78, 1997.
5. Johnson, B.D. "Control of Broadband Structural Radiation from Structures Using a Piezoelectric Double-Amplifier Active Skin", *Master of Science Thesis*, Department of Mechanical Engineering, VPI&SU, Blacksburg, VA, 1997.
6. Maillard, J.P. and Fuller, C.R. "Advanced Time Domain Wave-Number Sensing for Structural Acoustic Systems. Part III. Experiments on Active Broadband Radiation Control of a Simply Supported Plate", *Journal of the Acoustical Society of America*, Vol 98(5), 2613-2621, 1995.

## **APPENDIX 38**

## ACTIVE VIBRATION CONTROL

C. R. FULLER

### 1 INTRODUCTION

Passive control of vibrations in structures including isolation mounts have been discussed in Chapter 71 and Ref. 1. These methods work well at high frequencies or in a narrow frequency range but often have the disadvantage of added weight and poor low-frequency performance. Active vibration control has demonstrated the potential to solve many of these problems. Although the potential of active vibration control has been well known for many years, recent advances in fast digital signal processing (DSP) computer chips have made these systems realizable.

In active vibration control secondary vibration inputs are applied to the structure in order to modify its response in a desired manner. The major components of an active vibration control system are the plant, actuators, sensors, and a controller. The plant represents the physical system to be controlled. Error sensors are needed to measure the system response while control actuators provide the necessary inputs to the plant to modify its response. The controller implements the chosen control algorithm to ensure that the controlled (or closed-loop) system behaves as required. The closed-loop system consists of the open-loop (uncontrolled) system dynamics combined with the dynamics of the controller and thus behaves in a modified form. These components will be discussed separately below and then unified into a coupled system behavior by use of example applications. Basic theory for each of the components is also discussed in order to provide the framework for analyzing controlled system behavior.

The arrangement of an active control system is usually based upon the physics of the system to be controlled and thus, as illustrated below, is often application dependent. There are many texts on active control of vibration, mainly focused on the control theory. The text by Meirovitch<sup>2</sup> provides an excellent theoretical basis while the text of Fuller et al.<sup>3</sup> describes in detail both feed-forward and feedback control theory, actuators and sensors as well as many relevant applications. Chapter 84 also discusses the related area of active noise control. It should be noted that active control is not a panacea for every vibration problem, and its application should be chosen with care depending upon a number of important characteristics such as the temporal nature of the disturbance, the spatial nature of the noise field, and the dynamic characteristic of the disturbance.<sup>4</sup>

### 2 CONTROL ACTUATORS

Actuators are used to introduce control forces into the plant in order to modify its behavior, and their design/selection (in conjunction with the sensors) is often the most important step in an active noise control project. Actuators can take various forms that are dependent upon system requirements such as the required control authority (amount of control force, moment, strain, or displacement), power, frequency response, and physical constraints such as size, mounting requirements, and so on. Actuators are generally classified into two main categories: *fully active* actuators that apply a secondary vibrational response to the structure and *semiactive* actuators that are passive elements and can be used to adaptively adjust the mechanical properties of the system.

## 2.1 Electrodynamic Actuators

Electrodynamic actuators or shakers consist of a moving wire coil mounted inside a permanent magnet. As they are readily available and their behavior is relatively well understood (see Ref. 5 and Chapters 63 and 72), electrodynamic shakers are presently the most common control input as a fully active device. They are usually installed by either attaching directly to the structure by a stinger or placing in series or parallel with passive mounts, as in the case of active isolation (see Section 5.1). While electrodynamic actuators have the advantage of relatively large control displacement, they are usually bulky and require some form of support structure. However, there are many applications at low frequencies in which their use is more than adequate. Electrodynamic actuators are usually modeled in terms of control inputs as point forces and they are thus "spectrally white" in terms of the spatial wavenumber response of the excited structure.

Typical structural components encountered in practice can often be simply represented as beams or plates. The transverse response  $w$  of a simply supported thin beam to an oscillating point force  $F e^{i\omega t}$ , representative of a control shaker, can be described as<sup>6</sup>

$$w(x, t) = \frac{-2F}{M} \sum_{n=1}^{\infty} \frac{\sin(n\pi x_f/L) \sin(n\pi x/L)}{\omega^2 - \omega_n^2 + i2\zeta_n \omega_n \omega} e^{i\omega t}, \quad (1)$$

where  $x$  is the axial coordinate,  $x_f$  is the location of the force,  $L$  is the length of the beam,  $\omega$  is the frequency of excitation,  $M$  is the total mass of the beam, and  $\zeta_n$  is the modal damping ratio. In Eq. (1),  $\omega_n$  is the natural frequency of the  $n$ th mode of the beam.<sup>6</sup> The transverse vibration displacement  $w$  of a simply supported thin panel excited by a point force  $F e^{i\omega t}$  is also described by<sup>6</sup>

$$\begin{aligned} w(x, y, t) &= \frac{-4F}{M} \sum_{m=1}^{\infty} \sum_{n=1}^{\infty} \frac{\sin(m\pi x_f/L_x) \sin(n\pi y_f/L_y) \sin(m\pi x/L_x) \sin(n\pi y/L_y) e^{i\omega t}}{\omega^2 - \omega_{mn}^2 + i2\zeta_{mn} \omega_{mn} \omega}, \\ &\quad (2) \end{aligned}$$

where the force is located at  $(x_f, y_f)$ ,  $\omega_{mn}$  is the natural frequency of the  $(m, n)$ th mode, and  $M$  is the total mass of the plate. Response of other more complex systems to point forces can be found in well-known texts such as Ref. 6.

## 2.2 Piezoelectric Actuators

As discussed in Ref. 7, piezoelectric transducers consist of material that expands or contracts when an electric field is applied over it. By applying an oscillating voltage to the piezoelectric element, its strain can be made to oscillate at the same frequency as the input. Three major types of piezoelectric material are readily available: (1) a ceramic form such as PZT, which has relatively high control strain but is brittle; (2) a polyvinyl form such as PVDF, which is flexible but has less control strain for the same configuration; and (3) a piezoelectric rubber, which is useful for underwater applications. Piezoelectric material is configured in the two main forms of *stack* and *wafer*, as shown in Fig. 1. Piezoelectric stacks are configured so that when a voltage is applied across the electrodes, the stack usefully expands in its long or 3-3 axis.<sup>7</sup> Stack arrangements such as Fig. 1 are thus suitable for actuators in vibration isolation in the two configurations of parallel and series shown in Figs. 1a and 1b.

For a given applied voltage  $V$  the net static displacement  $\delta$  of the piezoelectric ceramic actuator shown in the parallel configuration of Fig. 1a can be calculated from

$$\delta = \frac{d_{33}V + F/K_a}{1 + K/K_a}, \quad (3)$$

where  $d_{33}$  is the strain constant of the piezoelectric material in the 3-3 axis,<sup>7</sup>  $K$  is the external spring stiffness,  $K_a$  is the actuator stiffness ( $K_a = E_a A_a / L_a$ , where  $L_a, A_a$ , and  $E_a$  are the actuator length, cross sectional area, and Young's modulus, respectively); and  $F$  is the external load force. Note Eq. (3) can be used as the basis of an approximate dynamic analysis, as discussed in Ref. 3. The significant advantage of the piezoelectric stack is that it can provide high force; however, its displacement is limited (relative to electrodynamic actuators), which, as discussed later, implies that its use is primarily in series active isolation implementations.

The other common form of piezoelectric actuator is the wafer arrangement shown in Fig. 1c. In this form the transducer usefully strains in its thin transverse axis (3-1 or 3-2) when a voltage is applied across the electrodes. The wafer is usually bonded or embedded directly into the structure and actuates the structure by applying surface or interior strains. Figure 1c shows piezoelectric elements arranged to create pure bending. In this configuration two colocated elements are employed and wired 180° out of phase so that as one element expands, the other contracts. As discussed in Ref. 8, the surface-mounted colocated actuator for a perfect bonding layer (which is a good approximation if the glue layer is thin) effectively applies a line moment to the structure at the boundaries of the actuator. The magnitude of this linear

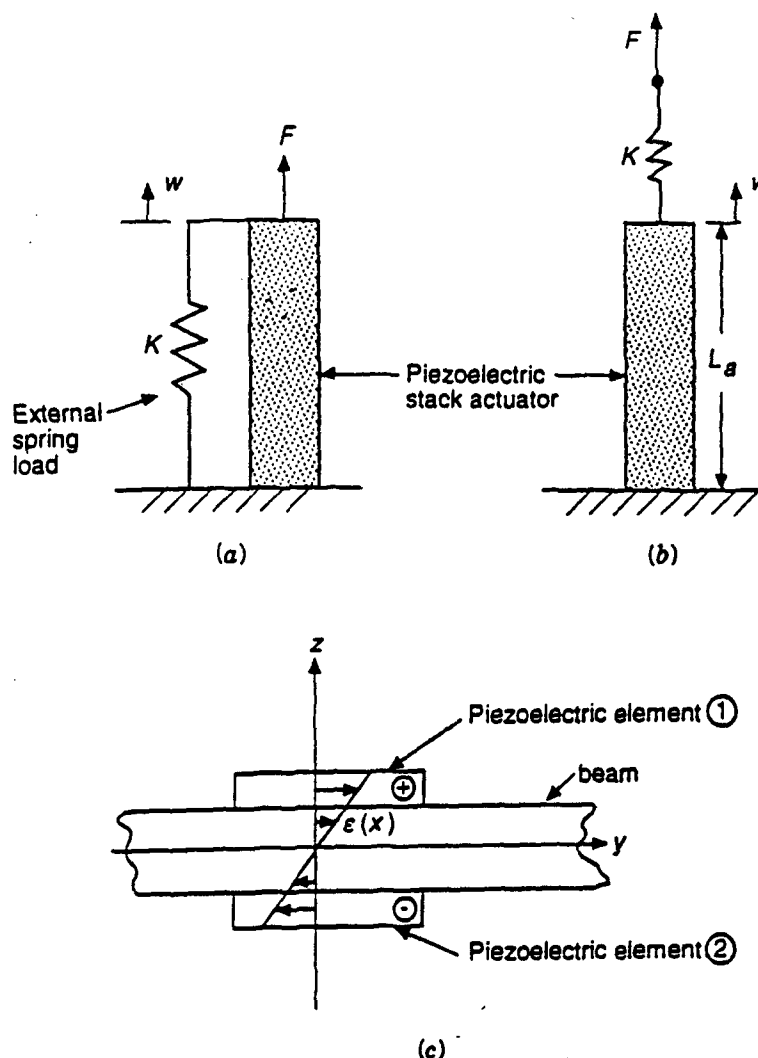


Fig. 1 Piezoelectric actuator configurations: (a) stack in parallel; (b) stack in series; (c) colocated wafer.

moment density for a one-dimensional structure such as a simply supported beam is given by<sup>9</sup>

$$m_x = \frac{-E_b 2Ph^2 \epsilon_{pe}}{3(1-P)}, \quad (4)$$

where the piezoelectric element unconstrained strain  $\epsilon_{pe} = d_{31} V/t$ . The constant  $P$  is defined as

$$P = \frac{-3th(2h+t)}{2(h^3+t^3)+3ht^2} \frac{E_{pe}}{E_b}. \quad (5)$$

In Eqs. (4) and (5)  $E_b$  and  $E_{pe}$  are the Young's elastic modulus of the beam material and piezoelectric element, respectively, while  $h$  is the half thickness of the beam,  $t$  is thickness of the piezoelectric element,  $V$  is the applied

voltage, and  $d_{31}$  is the piezoelectric transverse strain constant. For a two-dimensional patch system in spherical bending of a plate the effective moments  $m_x, m_y$  of the actuator are given by<sup>10</sup>

$$m_x = m_y = \frac{-E_p(1+\nu_{pe})}{3(1-\nu_p)} \frac{2P'h^2\epsilon_{pe}}{(1+\nu_p - (1+\nu_{pe})P')}, \quad (6)$$

where

$$P' = P \frac{1-\nu_p^2}{1-\nu_{pe}^2}. \quad (7)$$

In Eqs. (6) and (7)  $\nu_{pe}$  and  $\nu_p$  are the Poisson's ratio of the piezoelectric and the plate material, respectively. More information of piezoelectric elements and their

properties as well as definitions of important terms can be found in Ref. 7. Excitation of beam and plate structures with piezoelectric patches are discussed in Refs. 9 and 10. Piezoelectric actuators can be used either in a semiactive or a fully active form.

### 2.3 Advanced Actuators

The desire for an optimum actuator has stimulated development of new materials and configurations. The requirements, depending upon application, are typically high force and/or displacement, large bandwidth of operation, lower power consumption, and ease of use.

*Shape memory alloy* (SMA) shows much potential for high-force actuation at DC to very low frequencies. The mechanism by which SMA fibers or films exhibit their characteristic shape memory effect can be described very basically as follows: An object in the low-temperature martensitic condition, when plastically deformed and the external stresses removed, will regain its original (memory) shape when heated. The process is the result of a martensitic phase transformation taking place during heating. When SMA is heated through its transformation temperature, the elastic modulus of the material changes dramatically, and if the material is initially stretched, it will shrink back to its original size. If the SMA is constrained during this procedure, very high restoring forces are generated. More information on SMA can be found in Ref. 11.

The SMA systems are usually configured by embedding the material in a structure in a similar manner to layups of composite structures. It can be activated in a steady-state manner, applying steady-state in-plane forces that can be used to tune the resonant frequencies or change the mode shapes of the system (i.e., as semiactive actuator).<sup>12</sup> Over a very limited frequency range it can be used as an oscillating control input (i.e., a fully active actuator) by positioning the SMA off the central axis of the structure and driving with an oscillating voltage.<sup>12</sup> The advantage of the SMA is the extremely high force and deflection that it can provide at very low frequencies. Disadvantages are high power consumption, a need for heat dissipation, and a limited frequency response, which depends entirely upon the cooling rate. Use of SMA in the control of transient vibration of a cantilevered beam as well as sound radiation control is discussed in Ref. 12.

*Magnetostriuctive* materials also show much possibility as advanced fully active actuators in that they fill the performance gap between low-force, high-displacement electromagnetic actuators and high-force, low-displacement piezoelectric devices. A typical actuator using the material Terfenol-D and approximately 11 cm length and 5 cm diameter can produce forces in excess of 450 N

over a frequency range of 0–2.5 kHz.<sup>13</sup> However, the power requirements tend to be somewhat higher than electrodynamic and piezoelectric devices.

*Electrorheological* (ER) fluids are suspensions of highly polarized fine particles dispersed in an insulating oil.<sup>14</sup> The viscosity and the elasticity of the ER fluid can be changed several orders of magnitudes when an electric field is applied to the medium. The ER fluid can thus be embedded in structural systems and used as a "semiactive" actuator to tune the system's properties such as damping and stiffness by varying the voltage applied to the ER fluid.<sup>15</sup>

## 3 ERROR SENSORS

Error sensors are employed to measure the motion of the system to be controlled. This information either is used directly as the variable(s) to be minimized or is used to calculate a related state of the system to be controlled. Sensors come in three main forms: point sensors, arrays of point sensors, and distributed sensors. Choice of the particular configuration is dependent upon the system variable to be controlled, as discussed below.

### 3.1 Accelerometers, Force Transducers, and Impedance Heads

Accelerometers are commonly used as error sensors due to the ease of use and reliability of performance. Their implementation and behavior is discussed in more detail in Chapter 72. When attached to a vibrating structure, they can provide estimates of the time-varying acceleration (as well as velocity and displacement with signal processing) at the point of attachment. Due to their small size, at low frequencies accelerometers provide a point sampling of the structural motion and thus are "spectrally white" in wavenumber response. Thus an individual accelerometer will equally sense all structural wavenumber or modally weighted contributions. Use of an accelerometer output as an error signal will result in direct control of the structural motion at that point.

Force transducers can also be used as error sensors, particularly in applications such as active isolation, where they may be placed in series with passive isolation. Minimization of the force transducer output will result in zero dynamic force being applied to the receiving structure. The point input impedance of a structure such as at a disturbance location can be estimated using an impedance head that consists of a colocated accelerometer and force transducer. The output of the impedance head can then be used as a narrow-band error sensor variable in order to minimize the real part of the

structural input impedance and thus disturbance input power flow into the structure.

Choice of one of the above transducers as an error sensor is dependent upon the form of application. This will be illustrated in the later example applications.

### 3.2 Arrays of Point Sensors

Usually it is more effective to use accelerometers as error sensors in an array configuration whose output signal is processed to provide some global or distributed state associated with the system.

The *kinetic energy* of a thin vibrating system can be minimized by using a distributed array of accelerometers positioned over the required controlled domain. An estimate proportional to out-of-plane kinetic energy of the structure is given by

$$E = \sum_{i=1}^N |\dot{w}_i|^2, \quad (8)$$

where  $N$  is the total number of accelerometers and  $\dot{w}$  is the out-of-plane velocity obtained by integrating the acceleration signal. The variable  $E$  can be minimized, or if an  $N$ -channel controller is available, each accelerometer can be used as an individual control channel. The required number and spacing of accelerometers are determined by the Nyquist sampling criterion applied in the spatial domain: two accelerometers must be spaced within at least a half-wavelength of the highest mode required to be observed and controlled. Alternatively, the accelerometers can be appropriately distributed throughout the surface whose global motion is to be controlled. Use of a lower number of accelerometers (relative to the number of actuators) often leads to large minimization at their locations but increased levels of vibration at other locations. This effect is termed control spillover. In general, to ensure controllability, a system state or mode has to be individually observed.

*Wavenumber* components of structural motion can be obtained using arrays of equispaced accelerometers arranged along a coordinate axis. The spatial one-dimensional Fourier transform can be approximated using a discrete Fourier transform such as<sup>3</sup>

$$\hat{W}(k) = \sum_{n=1}^K w_m(x_n) e^{ikx_n \Delta x}, \quad (9)$$

where  $w_m(x_n)$  is the measured out-of-plane complex displacement at position  $x_n$ . In Eq. (9) there are  $N$  measurement points equally spaced at a distance  $\Delta x$ . Note Eq. (9)

can also be expanded into a time-space transform if necessary. The output of Eq. (9) can be used to provide an error signal. Minimization of spectral components  $W(k)$  then will provide control of selected wavenumber values. For example, in a finite structure vibrating at a single frequency, the wavenumber components will be discrete and associated with particular modes or waves traveling in the positive or negative directions. In many situations it is appropriate to control these components directly.

*Modal decomposition* of the structural motion is also a useful processing technique. To achieve this, an array of accelerometers is used to measure out-of-plane motion at a number of points. Thus, knowing the structural mode shapes and using a pseudoinverse technique, the modal amplitudes can be estimated from<sup>16</sup>

$$[A] = ([L]^T [L]^{-1}) [L]^T [w_{me}], \quad (10)$$

where  $[A]$  is a vector of  $m$  unknown modal amplitudes and  $[w_{me}]$  is a vector of  $n$  measured displacements at  $(x_n, y_n)$ . In Eq. (10)  $[L]$  is an  $n \times m$  matrix associated with the mode shapes  $\Psi$  of the system, defined as

$$[L] = \begin{bmatrix} \Psi_1(x_1, y_1) & \Psi_2(x_1, y_1) & \cdots & \Psi_m(x_1, y_1) \\ \vdots & \ddots & & \\ \Psi_1(x_n, y_n) & & & \end{bmatrix}. \quad (11)$$

Equation (10) can also be readily modified to decompose narrow-band traveling-wave fields into individual wave components and can be implemented for broadband random disturbances, as outlined in the work of Gibbs et al.<sup>17</sup> Equation (10) can thus provide indirect error information of a global nature associated with each mode. Minimization of a modal estimate will ensure that a particular mode is globally controlled in a vibrating structure. This is of use when particular modes are more important than others in a control strategy.

*Kalman filtering* techniques are used extensively in linear quadratic (LQ) control problems,<sup>3</sup> where all the internal state variables of the system to be controlled must be known. When all the states are not measurable, they have to be estimated using a mathematical model of the dynamic system and measurements of the output variables. For Gaussian disturbances, the Kalman filter is the optimal estimator that minimizes the variance of the estimation error.<sup>18</sup>

*Power flow* can be estimated from an array of accelerometers mounted on the structure. For the simplest case of traveling waves on a thin beam the net narrow-band bending power flow can be calculated by

using two measurement points and finite-difference theory, as described in Chapter 74 and Ref. 19:

$$P(\omega) = \frac{2EIk_f^2}{\Delta x \omega^3} \operatorname{Im}(S_{21}). \quad (12)$$

In Eq. (12)  $k_f$  is the flexural wavenumber at frequency  $\omega$ ,<sup>6</sup>  $\Delta x$  is the spacing of the two acceleration measurement points, and  $S_{21}$  is the cross spectrum between the output of the two accelerometers. Use of Eq. (12) as an error signal will thus result in minimization of net power flow in the structure. Extension of Eq. (12) to include near fields is also discussed in Ref. 19 (see also Chapter 74). As discussed above, it is also possible to decompose the motion of the structure into wave component amplitudes using a pseudoinverse technique. The power flow associated with each direction of propagation or wave type can be then estimated and used as an error signal. Using approaches such as these, it is possible to actively control termination impedances of beams.<sup>20</sup>

### 3.3 Distributed Piezoelectric Sensors

Piezoelectric material, when strained from its free state, also creates a charge.<sup>7</sup> Thus, when configured properly, piezoelectric material with attached electrodes to collect the charge can be used as an error sensor. The most common arrangement is to bond the piezoelectric material to one side of the surface of the structure whose motion is to be sensed. If the piezoelectric material is very thin, then it can be assumed that its presence has no effect on the motion of the structure. For a two-dimensional structure covered with a finite layer of piezoelectric material the charge output  $q(t)$  of the sensor (in rectangular coordinates) can be calculated from<sup>21</sup>

$$q(t) = (h_p + h_s) \iint_S \Gamma(x, y) \left[ \epsilon_{31} \frac{\partial^2 w}{\partial x^2} + \epsilon_{32} \frac{\partial^2 w}{\partial y^2} + 2\epsilon_{36} \frac{\partial^2 w}{\partial x \partial y} \right] dx dy, \quad (13)$$

where  $w(x, y)$  is the plate out-of-plane response,  $\Gamma(x, y)$  is the sensor shape function,  $h_p$  and  $h_s$  are the thickness of the plate and sensor, and  $\epsilon_{31}$ ,  $\epsilon_{32}$ , and  $\epsilon_{36}$  are the piezoelectric stress-charge coefficients where the superscripts 1, 2, 3, refer to the  $z$ ,  $x$ , and  $y$  directions of a three-dimensional coordinate system.<sup>7</sup> In effect, the piezoelectric material integrates the surface strain of the structure

over its area  $S$  (i.e., in the 1–2 plane) and thus provides continuous distributed sensing. The actual voltage output of the piezoelectric material is dependent upon the electrical circuitry used to measure the piezoelectric output. Shaped piezoelectric sensors are surface-mounted sensors that are of specified finite size and shape. Particular motions or modal components of the vibrating structure can be observed by cutting the piezoelectric material into a specialized shape. The charge output of an example rectangular piezoelectric strip mounted on a simply supported plate so that it extends completely over the plate in the  $x$ -direction but is narrow in the  $y$ -direction is given by<sup>22</sup>

$$q(t) = K \sum_{m=1}^{\infty} \sum_{n=1}^{\infty} \frac{L_x L_y}{nm\pi^2} [\cos(m\pi) - 1] \cdot \left[ \cos\left(\frac{n\pi d}{L_y}\right) - \cos\left(\frac{n\pi c}{L_y}\right) \right], \quad (14)$$

where  $L_x, L_y$  is the dimension of the plate in the  $x, y$  directions,  $K$  is a constant that modifies the charge output due to the external electrical load impedance,  $m$  and  $n$  are modal orders, and  $d$  and  $c$  are the vertical locations of the sensor boundaries in the  $y$ -direction. Note Eq. (14) shows that for all even modes in the  $x$ -direction ( $m = 2, 4, 6, \dots$ ) the sensor output is zero. Thus the sensor acts as a spatial wavenumber or modal filter only observing odd modes in the  $x$ -direction. Positioning and sizing of the piezoelectric strip can be adjusted to observe required modal or wavenumber components.

In order to observe individual particular modes of motion, the piezoelectric strip can be cut into a shape corresponding to a system characteristic function. The output of a shaped sensor positioned on a finite simply supported beam is given by

$$q(t) = K \sum_{m=1}^{\infty} \int_0^L \Gamma(x) \Psi_m dx, \quad (15)$$

where the mode shape is  $\Psi_m = \sin(m\pi x/L)$ . If the shape function  $\Gamma(x)$  is chosen equal to a mode shape  $\Psi_m(x)$ , then, by orthogonality, Eq. (15) predicts that the sensor will only observe that mode. Figure 2 presents an example of a sensor shaped to only observe the  $m = 2$  mode of the simply supported beam. Note that the sensor width is largest where the surface strain of the beam is highest. Thus, shaped sensors can provide a time-domain estimate of modal amplitudes of structural response, with minimal signal processing, in contrast to the previous method using arrays of accelerometers. However, once the sensor is shaped, its estimate is fixed, whereas the

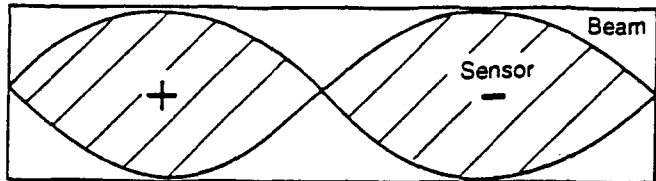


Fig. 2 Shaped distributed piezoelectric strain sensor on a simply supported beam.

output of the accelerometer array can be manipulated by signal processing to observe various modes or waves.

The most commonly used piezoelectric sensing material is PVDF. It can easily be cut or etched into particular shapes. It is readily attached to the surface with double-sided tape or other means. Care must be taken to attach leads to the bottom of the element, and when the shaped sensor has phase changes throughout its segment (as in Fig. 2), each segment output should be wired together with the correct relative polarity in order to give the required sensor output.

## 4 CONTROL APPROACHES

The function of the controller is to process the error information received from the error sensors in order to calculate control signals so as to cause the controlled or closed-loop system to behave in a required manner. Control approaches can be divided into two main categories: *feedforward* and *feedback* approaches, as discussed by Fuller et al.<sup>3</sup>

In general, feedforward control has found application when the designer has direct access to information about the disturbance signal to the system. On the other hand, feedback control has primarily been applied when the disturbance cannot be directly observed. In this case the control signals are obtained from the sensor(s) whose output is affected by both disturbance source and the control actuator(s). Chapter 84 also has relevant material on the active control paradigms discussed here.

### 4.1 Feedforward Control

Figure 3 presents a simple, illustrative arrangement of single-channel feedforward control; in this particular case the object is to minimize the vibration of a mechanical system at the error sensor,  $e$ . The most common form of electrical feedforward controller  $H$  is an adaptive finite impulse response (FIR) filter whose coefficients are updated by a control algorithm in order to drive the error signal to a minimum. A critically important aspect of the feedforward approach is obtaining a reference or training signal that provides a coherent estimate of the dis-

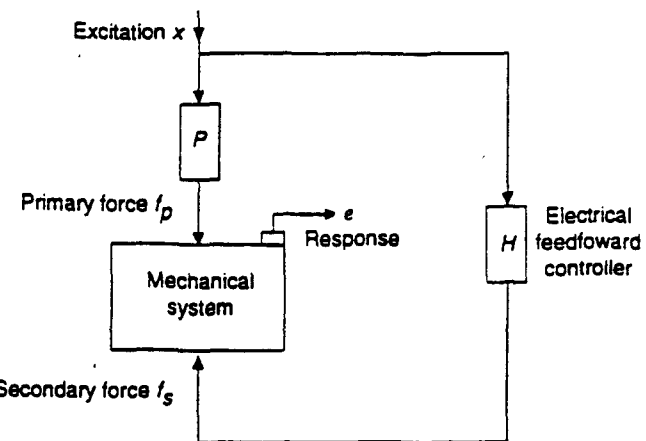


Fig. 3 Simple feedforward control arrangement.

turbance signal and is "fed forward" through the adaptive filter to provide the control signal. The most commonly used update equation for dynamic systems is the time-domain Filtered X version of the Widrow-Hoff least mean squared (LMS) algorithm written in single-channel form as<sup>23</sup>

$$w^i(n+1) = w^i(n) - 2\mu e(n)f(n), \quad (16)$$

where  $w^i(n)$  is the  $i$ th coefficient of the adaptive filter at time  $n$ ,  $\mu$  is a convergence parameter, and  $e(n)$  is the error signal at time  $n$ . The filtered reference signal  $f(n)$  is given by

$$f(n) = \sum_{j=1}^P c^j x(n-j), \quad (17)$$

where  $c^j, i = 1, 2, \dots, P$ , are the weights of a fixed FIR digital filter that models the plant dynamics from the actuator signal to the error signal and  $x(n)$  is the reference signal taken directly from the disturbance. Equation (17) essentially accounts for the delay between the control system input and the error sensor output. The adaption equation (16) also assumes no feedback of control signal to the reference signal. The fixed FIR filter is usually constructed before switching on the controller or with a low-level probe signal, as described in Refs. 3 and 4. In essence the Filtered X LMS algorithm is a gradient-descent technique that finds the minimum of a quadratic cost function defined as the squared modulus of the error signal.

The choice of the filter format is dependent upon the noise disturbance. For a narrow-band signal it is necessary to use only two filter coefficients. Control of broadband signals requires a larger filter in terms of coef-

ficients, and causality aspects associated with relative delay through the control path become more important.<sup>3</sup> The Filtered X algorithm can be readily extended to a multichannel configuration, as discussed in more detail in Ref. 24.

Note that the use of a reference signal estimate from the disturbance implies that the system will respond only to information coherent with the reference signal. The system will thus appear open loop to all other disturbances uncorrelated with the error signal. The maximum achievable attenuation of the power of the error signal for a single-input, single-output feedforward control arrangement can be calculated from<sup>3,4</sup>

$$\Delta dB = -10 \log(1 - \gamma_{de}^2), \quad (18)$$

where  $\gamma_{de}^2$  is the coherence between the disturbance and the error signals.

Similar to feedback control, it can be demonstrated that closed loop systems under feedforward control have new eigenvalues and eigenfunctions<sup>25</sup> and that, for narrow-band disturbances, feedforward and feedback approaches are essentially equivalent.<sup>3</sup> Due to convergence time requirements (the adaptive filter has to search for the minimum of the error surface), the feedforward algorithm does not presently work well with transients applied to nonmodelled systems but is suitable for pure tones or steady-state broadband signals. As the control filter is adaptive and "learns" the system by minimizing a cost function, it is not necessary to have an accurate model of the open-loop system behavior from the control actuator to the error sensor. For a single-channel time-domain controller applied at a single frequency, it is only required to estimate the fixed transfer function between the control input and error sensor within an accuracy of  $\pm 90^\circ$  to ensure controller convergence.

The behavior of feedforward controlled systems can also be analyzed using linear quadratic optimal control theory. For the system of Fig. 3 a quadratic cost function is constructed by squaring the modulus of the error signal (or summing the squared modulus of the error signals). The optimal control input is found by setting the gradient of the cost function to zero (i.e., at the minimum).

For a system with  $L$  error sensors the quadratic cost function is formed by summing the squared modulus of the error signals,

$$J = \sum_{l=1}^L |e_l|^2. \quad (19)$$

The optimal control inputs to minimize the cost function are found by setting the gradient of the cost func-

tion to zero, as described by Nelson and Elliott.<sup>26</sup> For a multiple-input, multiple-output arrangement the optimal vector  $q_{s0}$  of control inputs to minimize the cost function is specified by

$$q_{s0} = A^{-1} Z^H w_p, \quad (20)$$

where  $Z$  is a matrix of complex transfer impedances relating the control force inputs to the response at the error sensors, the matrix  $A = Z^H Z$  and  $w_p$  is the noise or primary complex field at the error sensors. More details on how to use Eq. (20) as well as calculating the minimum of the cost function can be found in Ref. 26. The above analysis is for a single-frequency, steady-state excitation and represents the maximum achievable performance. For random signals, the actual control performance will depend upon whether the control filters are physically realizable and other related issues, as described in Ref. 4.

## 4.2 Feedback Control

Figure 4 presents a typical arrangement of single-channel feedback control of motion of a general mechanical system. In this arrangement the control signal is derived from a sensor on the structure and is then "fed back" through a controller (or compensator) to provide a control input. The optimal controller is derived in order to perform a specified control task. Hence, generally speaking, for feedback control the system changes its dynamic characteristics for *all* disturbances applied to it, in contrast to the feedforward approach discussed previously.

The open-loop equation of motion of a single-degree-of-freedom system excited by a disturbance force  $f_p(t)$  can be written in the form<sup>3</sup>

$$m\ddot{w}(t) + c\dot{w}(t) + kw(t) = f_p(t), \quad (21)$$

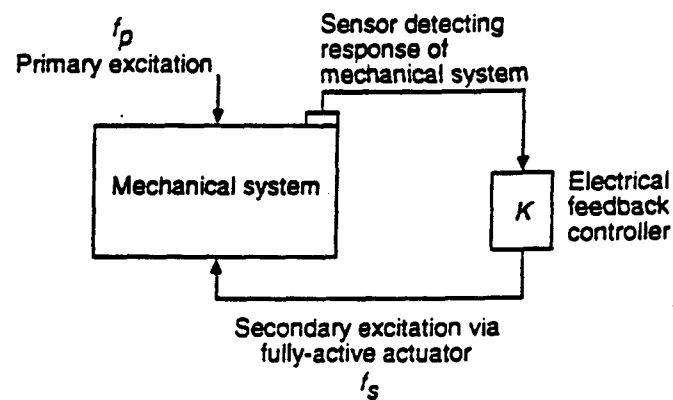


Fig. 4 Simple feedback control arrangement.

where  $m$ ,  $c$ , and  $k$  are the system mass, damping, and stiffness, respectively. For the mechanical system in Fig. 4 this may correspond to the response of one mode. Extensions to distributed systems are described in Refs. 2 and 3. The open-loop transfer function (i.e., the ratio of the response to the disturbance) of this system can be evaluated using the Laplace transform<sup>3</sup> and is given by

$$G(s) = \frac{W(s)}{F_p(s)} = \frac{1}{ms^2 + cs + k}. \quad (22)$$

We now apply a secondary control force to the structure by feeding back a signal taken from the response of the system through a compensator with a transfer function  $K$  to drive the control force  $f_s(t)$ . The closed-loop transfer function of the system with stiffness control (for example) is now given by

$$\frac{W(s)}{F_p(s)} = \frac{G(s)}{1 + G(s)K(s)} = \frac{1}{ms^2 + cs + (K + k)s}, \quad (23)$$

where  $s$  is the Laplace variable and  $K$  is the compensator gain or transfer function. Note that the closed-loop system effectively has a new effective stiffness  $(K + k)$  and thus new poles.

For transient control the objective is often to increase the damping of the system. In this case the closed-loop poles are moved further into the left  $s$ -plane by varying the compensator gain  $K$ . However, an important aspect of feedback control is stability, which can be determined by inspection of the position of the closed-loop poles as described in Ref. 27. Too much compensator gain  $K$ , for example, can lead to an unstable control system. Often, in practice, the stability is assessed from input-output measurements made on the system before control. The Nyquist stability criterion is then applied to check if the system is stable, as described in Ref. 26. The outcome is that the closed-loop system is stable only if the polar plot of the open-loop frequency response function does not enclose the point  $(-1, 0)$  in the complex Laplace plane  $s$ . Different forms of the compensator  $K$  to the simple example discussed above can be chosen, depending upon the required control performance, and these are discussed in Ref. 3.

If it is possible to achieve a stable feedback system, then the error signal power is approximately reduced by an amount proportional to the loop gain,<sup>4</sup> and the attenuation is given by

$$\Delta dB = -10 \log \left| \frac{1}{1 + GK} \right|^2. \quad (24)$$

In Eq. (24),  $G(s)$  is the transfer function through the plant and  $K(s)$  is the transfer function through the compensator.

In general, in order to calculate the optimal controller  $K$ , it is required to have an accurate model of the system to be controlled. This can be done through calculations such as finite-element methods or more usually through estimates using system identification approaches as described in Ref. 3. Although multi-input, multi-output feedback control can have a larger implementation requirement than feedforward control, it ensures that the system is controllable for all forms of linear noise disturbances if a realizable controller can be defined.

Extension of feedback control to multi-input, multi-output arrangements can be achieved using state space methods as outlined in Refs. 27 and 3. Other important factors affecting the performance and stability of feedback controllers are reviewed in Ref. 4.

## 5 EXAMPLE APPLICATIONS OF ACTIVE VIBRATION CONTROL

The following examples illustrate some of the wide diversity of present applications of active vibration control. Other implementations of active vibration control are discussed in Ref. 3.

### 5.1 Active Isolation of Vibration

A classic approach to reducing unwanted machinery noise and vibration is to control these disturbances at transmission bottle necks (e.g., the machinery mount). Active vibration isolation has been studied by a number of authors, as summarized in Ref. 3, and a few representative examples will be presented here.

There are four possible configurations for active isolation: The two most common are *series*, in which the actuator opposes the load path, and *parallel*, where the active force is applied in parallel with the load path. As discussed by Scribner et al.,<sup>28</sup> if the actuator is placed in parallel, it must overcome the stiffness of the passive mount and the actuator deflection requirements are relatively larger. If the actuator is in series, then while the deflection requirements are lower than the parallel implementation, the actuator must carry the load and, as will be seen later, the force requirements at resonance are higher. Two other, less common implementations are when the active force is directly applied to the exciting system and when the active or secondary force is applied directly to the receiving structure at the mount location. This latter implementation is termed *opposed*. Both implementations have the disadvantage of requiring

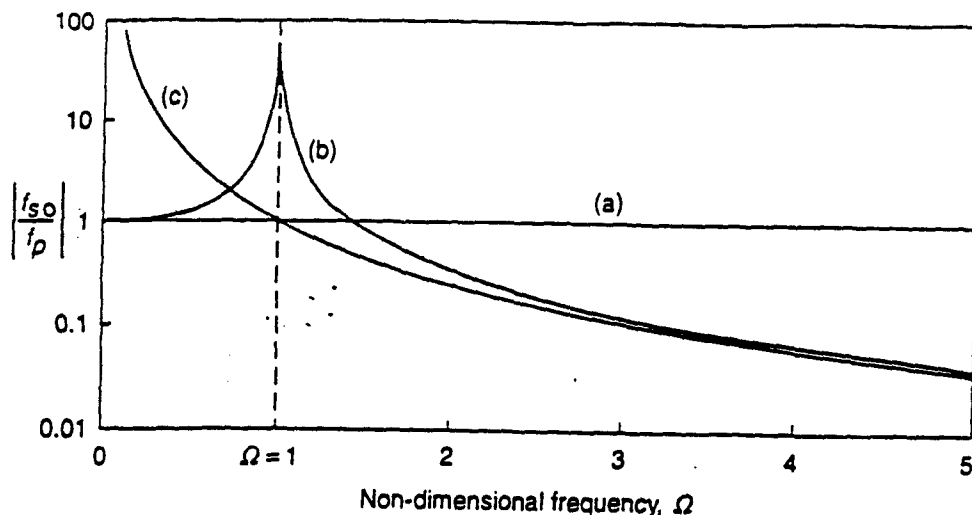


Fig. 5 Control force required for (a) direct, (b) opposed, and (c) parallel active vibration isolation systems.<sup>29</sup>

ing some form of inertial exciter (e.g., an electrodynamic shaker that is provided with a mass against which it can react).

Figure 5 presents the magnitude of the ratio of the secondary control force  $f_{s0}$  to the primary disturbance force  $f_p$  required for a "parallel" and "opposed" implementation calculated by Nelson et al.<sup>29</sup> for a lumped-parameter single-degree-of-freedom mass-spring system. The nondimensional frequency  $\Omega = \omega/\omega_n$ , where  $\omega_n$  is the natural frequency of the mass-spring system on a rigid base. Also shown is the relatively trivial case of when the control force is directly applied to the exciting mass and thus exactly equals the disturbance magnitude in order to drive the motion to zero. The results of the opposed case are similar in trend to the series implementation, which is discussed in much more detail in Ref. 30. The results show that at resonance the force requirements of the opposed system are much larger while below resonance the converse is true. Well above resonance the force requirements of both arrangements are similar. For control systems designed to operate near the plant resonance the above characteristics usually imply that electrodynamic actuators (i.e., relatively large deflection, lower force) are used for the parallel implementation while piezoelectric ceramic actuators (i.e., relatively larger force, low deflection) are used for the series arrangement.

Scribner et al. has theoretically and experimentally studied the use of piezoelectric ceramic actuators in a "series" implementation of active isolation using a classical feedback approach<sup>28</sup> focused upon sinusoidal disturbances. Figure 6 presents typical values of open-loop and closed-loop behavior of the ratio of transmitted to applied force versus frequency. In this example the com-

pensator natural frequency was set to 877 Hz and a large enhancement in transmitted force is observed near this design frequency. However, in the frequency range of  $825 \leq f \leq 850$  Hz, high attenuation in the transmitted force is achieved. Scribner et al.<sup>28</sup> also demonstrated how the controller could be implemented in a self-tuning implementation so as to track a disturbance frequency, even through structural resonance.

Nelson et al.<sup>3,29</sup> have also analytically and experimentally investigated narrow-band isolation of the vibration of a rigid raft from a flexible receiving structure using multiple active isolators configured in the parallel arrangement. In this case the active inputs were provided by four electromagnetic coil actuators used in conjunction with a multichannel adaptive LMS feedforward control approach. The error signals were taken from either four accelerometers located adjacent to the mount points or eight accelerometers distributed over the surface of the receiving structure. The results demonstrate that the use of eight accelerometers was more effective than four in attenuating the total energy of the receiving structure over much of the frequency range. This behavior illustrates the advantage in feedforward control of using more sensors than actuators; a "square" feedforward control system with equal number of actuators and sensors will always drive the response to zero at the error sensors. However, it is often more beneficial to use more error sensors than actuators when global reduction is required. The results presented in Ref. 3 also show that the passive isolation (i.e., no active control) produced an increase in the receiving structure vibration at some of its resonance frequencies. This characteristic illustrates the importance of the receiving structure dynamics on the isolation performance.

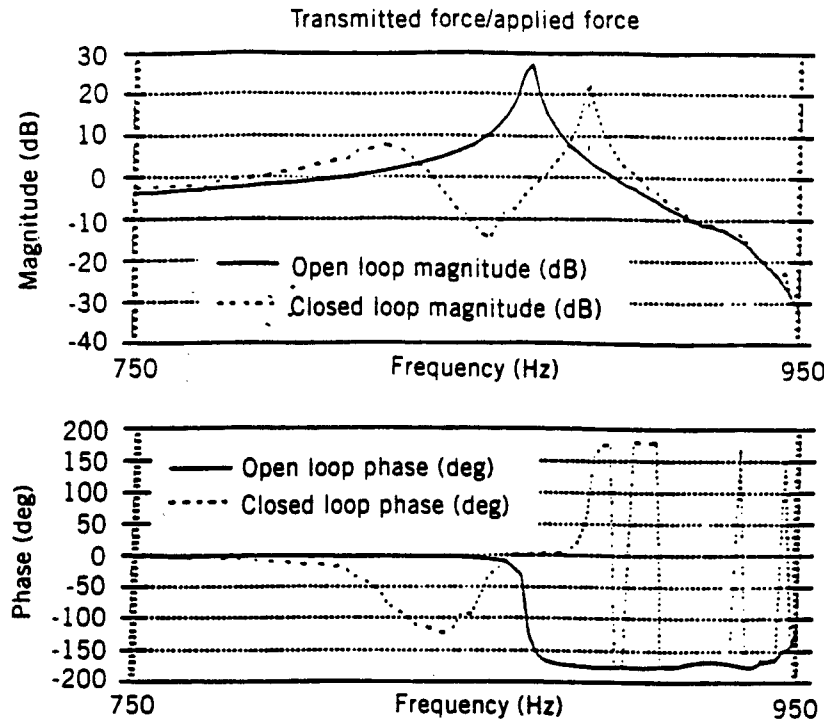


Fig. 6 Performance of a series active vibration isolation system.<sup>28</sup>

## 5.2 Active Control of Power Flow in Beams

Many structures are composed of basic elements that can be usefully approximated as beams and can transmit unwanted vibrations. The vibrational energy eventually spreads out through the ever increasing complexity of the structure making it more difficult to control. Thus direct reduction of vibrational power flow in the support beams is an area of great interest. In effect this problem is a subset of the active isolation problem discussed above.

Figure 7 shows an experimental arrangement where a semi-infinite beam is driven by a shaker at a single frequency positioned at one end (the disturbance). Piezoelectric ceramic actuators and sensors are positioned on the beam as shown and are wired so as to produce and sense pure bending, as discussed in Section 2.2. The out-of-plane velocity is measured with a laser vibrometer. The control objective is to minimize the power flow transmitted in the beam. Also shown in Fig. 7 is a schematic of a single-channel feedforward control implementation designed to minimize the square of the output of the piezoceramic error sensor which, for a semi-infinite thin beam system, is proportional to total power flow.<sup>31</sup>

The control algorithm used in the arrangement of Fig. 7 was the single-channel Filtered X paradigm of Eq. (16). The controller, indicated by the dashed boundary, was

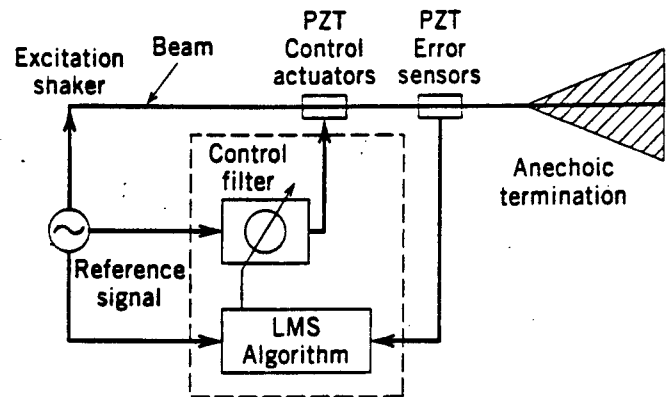


Fig. 7 Experimental arrangement and control block diagram for feedforward active reduction of narrow-band power flow in a beam with piezoelectric actuators and sensors.<sup>31</sup>

implemented on a TMS320C25 digital signal processing chip with a reference signal taken directly from the disturbance oscillator. Net power flow in the beam was also calculated using the finite-difference equation (12) with the laser vibrometer data. Figure 8 presents a typical result for the measured power flow before and after control is implemented.<sup>31</sup>

Figure 8 shows that when control is applied, the power flow is attenuated by approximately 35 dB at the error sensor. The results of Fig. 8 are net power flow and thus

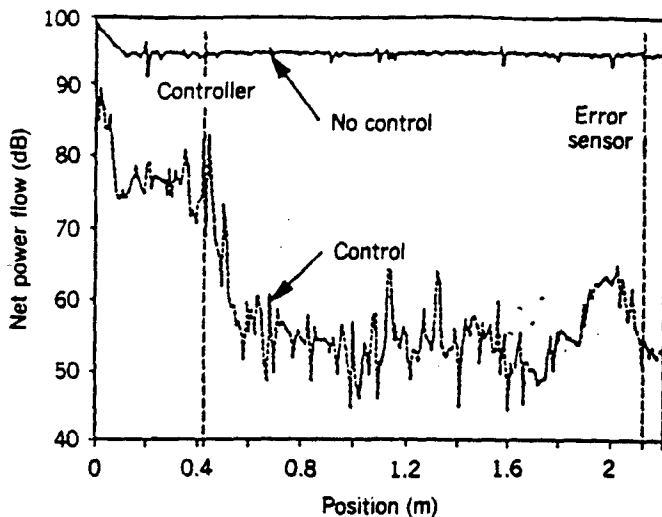


Fig. 8 Power flow distribution with and without control for the system of Fig. 7;  $f = 302 \text{ Hz}^{31}$

imply that power flow is highly attenuated at all points downstream of the error sensor. Two other observations of interest are found in the figure. First, the input power at the drive point is attenuated by around 20 db. Thus the control is achieved mainly by the control actuator creating a reactive discontinuity at its location, reflecting waves back to the drive point and lowering its resistive input impedance. Second, the net power falls past the distributed piezoelectric control actuator, and this implies that the control actuator has also *absorbed* some vibrational power. Extension of the above approach to control of power flow in finite beams, simultaneous control of flexural and extensional waves in beams, and broadband disturbances are discussed in Refs. 31, 32, and 33, respectively. The method has also been successfully applied to attenuation of power flow in struts used to

mount the engine and gearbox of a helicopter to the fuselage structure.<sup>34</sup>

### 5.3 Distributed Active Vibration Control of Plates

The control of vibration of distributed structural elements such as plates is also an important problem. Figure 9 is an experimental arrangement used by Rubenstein et al.<sup>35</sup> to implement linear quadratic Gaussian state space feedback control<sup>3</sup> of the vibration of a simply supported plate. The response of the system is sensed using an array of 12 accelerometers of the plate. The output of the accelerometers is passed through modal filters to obtain modal amplitudes and then through a Kalman filter to obtain the states of the system. The optimal controller  $K(\hat{Q})$  can then be obtained using a Riccati equation solution of the state space feedback control arrangement.<sup>3</sup> In this experiment the steel panel was  $0.6 \times 0.5 \text{ m}$  and 3 mm thick. The disturbance and control were implemented by electrodynamic shakers. Figure 10a shows a typical closed-loop response for mode 1 when the disturbance is narrowband, continuous excitation, while Fig. 10b gives closed-loop response to a transient disturbance applied at near  $t = 0.65 \text{ s}$ . In both cases high modal attenuation of the disturbance is achieved. Thus state space feedback methods show much potential for distributed active vibration control of a wide range of input disturbances. Note that state space feedback control implies complete control of specified states of the system as opposed to feedforward control, which usually controls a direct output of the plant at the error sensors (displacement, velocity, etc.). As discussed previously, the state space approach also guarantees control of the system to a wide range of disturbances without requiring access to a reference signal.

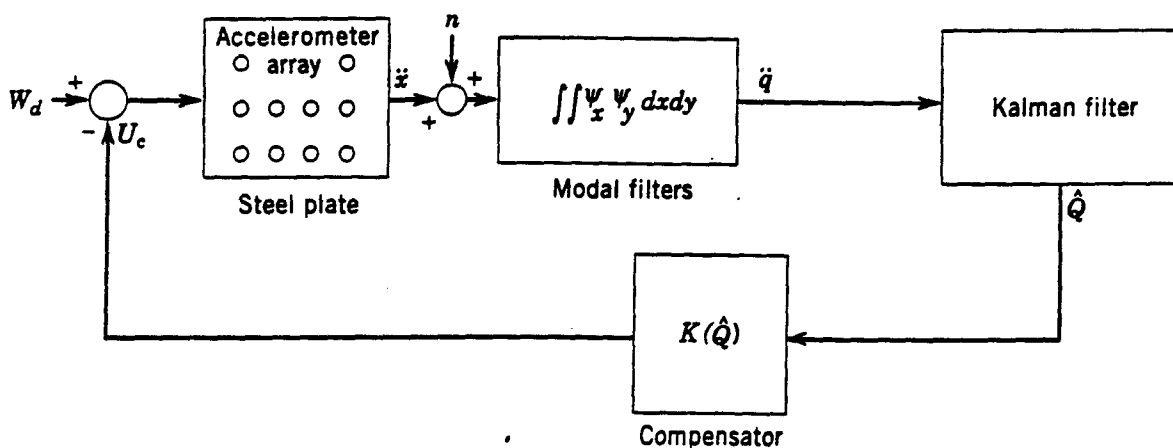


Fig. 9 Linear Quadratic Gaussian (LQG) feedback control system for active reduction of plate vibrations.<sup>35</sup>

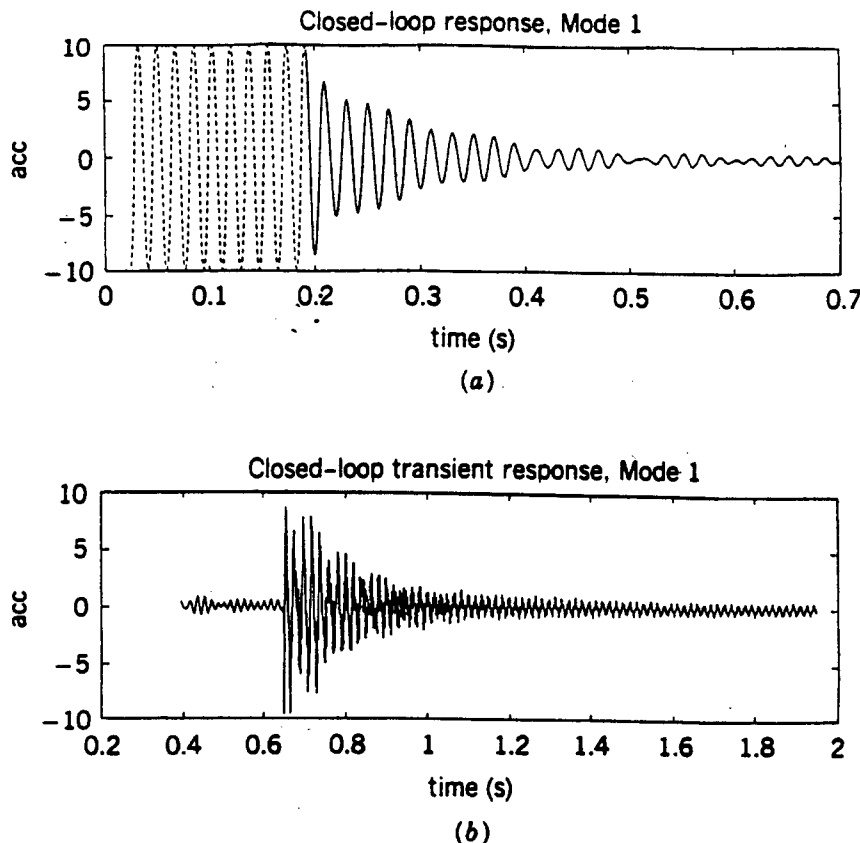


Fig. 10 Closed-loop response of the system of Fig. 10 for mode 1 with (a) narrow-band steady disturbance and (b) transient disturbance at  $t = 0.65$  s.<sup>35</sup>

#### 5.4 Active Structural Acoustic Control

Vibrating structures often radiate or transmit unwanted sound. An effective technique to control the structural sound radiation is to apply control inputs directly to the structure while minimizing the radiated sound or components of structural motion associated with the sound radiation.<sup>3,36</sup> The technique called active structural acoustic control (ASAC) thus falls in the class of general active vibration control techniques. Figure 11 shows an experimental arrangement in which the sound radiation from a simply supported plate is to be minimized.<sup>22</sup> The noise disturbance is provided by a point force shaker attached to the plate and driven by a pure tone. The control inputs are multiple colocated piezoelectric ceramic actuators bonded to the plate surface and wired to produce pure bending. The error sensors are either microphones in the radiated far field or shaped PVDF sensors attached to one side of the plate. The shaped PVDF sensors are rectangular strips positioned on the plate, as discussed in Section 3.3, so as to observe only the odd-odd modes (the efficient modal radiators at low frequencies). The control arrangement is the multichannel feedforward implementation of the Filtered X algorithm discussed

previously. The reference signal is taken from the noise input signal generator and is filtered as outlined in Eq. (17) before it is used in the LMS update equation, as described in Section 4.1.

Figure 12 presents results at 349 Hz, which is near the (3, 1) resonant frequency of the plate. The dotted line is for a case where three piezoelectric ceramic actuators are used in conjunction with three error microphones in the radiated far field, and it is apparent that global attenuations of approximately 25 dB are achieved. The dashed line is a similar case except that now two piezoceramic actuators are used in conjunction with two PVDF strips arranged in the  $x$ - and  $y$ -direction on the plate, as outlined in Section 3.3. The results again demonstrate good global control of approximately 20 dB in the radiated sound levels. These results and others discussed in Ref. 3 demonstrate the potential of using ASAC to reduce radiated sound. For the ASAC technique there are two main mechanisms of control.<sup>16</sup> *Modal suppression* corresponds to a direct reduction of the dominantly radiating modes or a fall in the plate wavenumber spectrum. *Modal restructuring* corresponds to the residual plate response having a lower overall radiation efficiency while its total magnitude of response is reduced

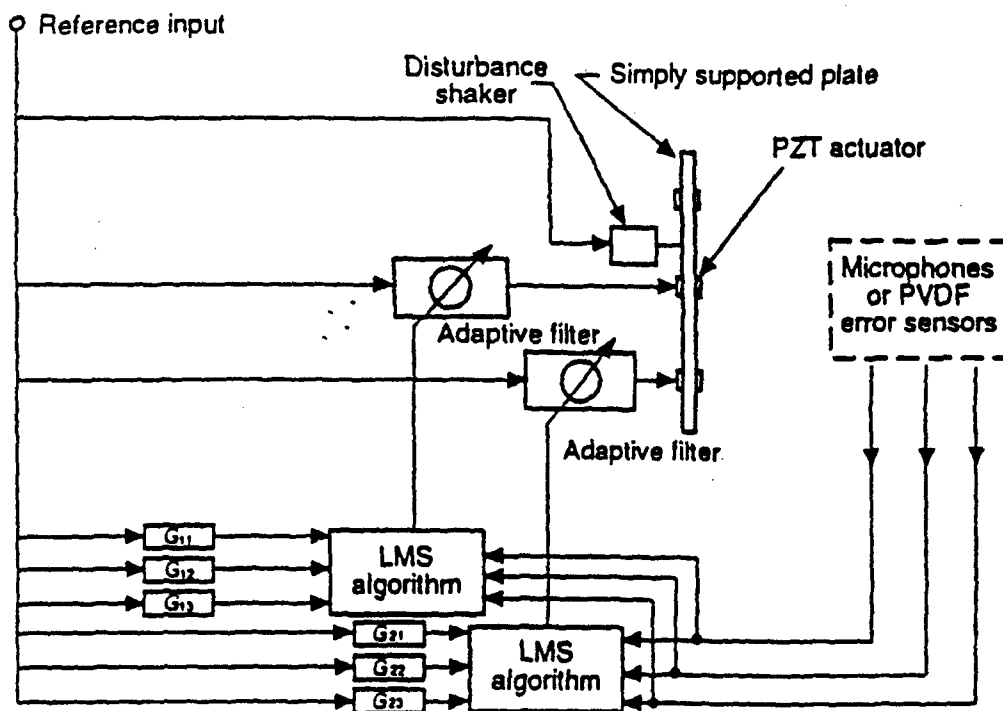


Fig. 11 Experimental arrangement and control block diagram for active reduction of sound radiation from a plate (ASAC).<sup>22</sup>

only slightly or may even increase. This second case corresponds to attenuation of only supersonic components of the plate wavenumber spectrum while subsonic, nonradiating components are left unaffected. Thus the ASAC technique takes maximum advantage of the natural structural-acoustic coupling behavior to reduce the dimensionality of the controller. The technique has been successfully applied to the control of interior noise in air-

craft and the reduction of transformer radiated noise, as discussed in Refs. 3 and 4.

From a system point of view, when multiple integrated actuators and sensors such as piezoelectric devices are used in conjunction with a non-model-based, adaptive controller, the application (such as ASAC discussed above) can be seen to be closely related to the field of *smart, adaptive, or intelligent structures* (see Ref. 37 for a review of this field). Developments in the field of smart structures are likely to be used in advanced active vibration control and ASAC because of the inherent compactness, light weight, and adaptability of this class of systems.

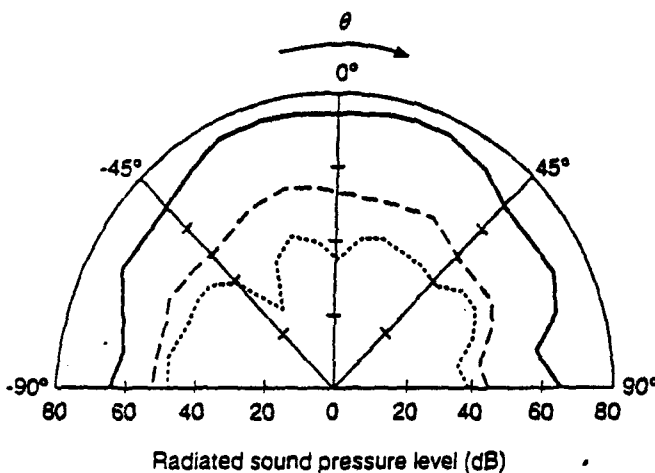


Fig. 12 Active structural acoustic control performance for the system of Fig. 11: (—) uncontrolled (----) controlled with PVDF structural error sensors; (.....) controlled with far-field error microphones;  $f = 349$  Hz.<sup>22</sup>

## REFERENCES

1. L. L. Beranek, *Noise and Vibration Control*, INCE, Washington, DC, 1988.
2. L. Meirovitch, *Dynamics and Control of Structures*, Wiley, New York, 1990.
3. C. R. Fuller, S. J. Elliott, and P. A. Nelson, *Active Control of Vibration*, Academic, London, 1996.
4. C. R. Fuller and A. H. Von Flotow, "Active Control of Sound and Vibration," *IEEE Control Systems Mag.*, December, 1995, pp. 9-19.
5. Ling Dynamic Systems, *User Manual*, Ling Dynamic Systems, Herts, England, 1973.

6. L. Cremer, M. Heckl, and E. E. Ungar, *Structural-Borne Sound*, Springer-Verlag, Berlin, 1988.
7. A. J. Moulson and J. M. Herbert, *Electroceramics: Materials, Properties, Applications*, Chapman and Hall, London, 1990.
8. E. F. Crawley and J. de Luis, "Use of Piezoelectric Actuators as Elements of Intelligent Structures," *AIAA J.*, Vol. 25, No. 10, 1989, pp. 1373-1385.
9. R. L. Clark, C. R. Fuller, and A. L. Wicks, "Characterization of Multiple Piezoceramic Actuators for Structural Excitation," *J. Acoust. Soc. Am.*, Vol. 90, No. 1, 1991, pp. 346-357.
10. E. K. Dimitriadis, C. R. Fuller, and C. A. Rogers, "Piezoelectric Actuators for Distributed Vibration Excitation of Thin Plates," *J. Vib. Acoust.*, Vol. 113, 1991, pp. 100-107.
11. C. M. Jackson, H. J. Wagner, and R. J. Wasilewski, "55-Nitinol-The Alloy with a Memory: Its Physical Metallurgy, Properties and Applications," NASA-SP-5110, Washington, DC, 1972.
12. C. A. Rogers, "Active Vibration and Structural Acoustic Control of Shape Memory Alloy Hybrid Composites: Experimental Results," *Proceedings of International Congress on Recent Developments in Air-And Structure-Borne Sound and Vibration*, Auburn University, AL, 1990, pp. 695-707.
13. C. G. Miller, "High Force, High Strain, Wide Bandwidth Linear Actuators Using the Magnetostrictive Material Terfenol-D," in C. A. Rogers and C. R. Fuller (Eds.), *Proceedings of Recent Advances in Active Control of Sound and Vibration*, (supplement) Technomic, Lancaster, PA, 1991.
14. J. E. Stangroom, "Electrorheological Fluids," *J. Phys. Tech.*, Vol. 14, 1983, pp. 290-296.
15. M. V. Gandhi and B. S. Thompson, "Dynamically-Tunable Smart Composite Featuring Electro-rheological Fluids," *Proceedings of the SPIE Conference on Fiber Optic Smart Structures and Skins II*, Boston, MA, 1989, pp. 294-304.
16. C. R. Fuller, C. H. Hansen, and S. D. Snyder, "Active Control of Sound Radiation from a Vibrating Rectangular Panel by Sound Sources and Vibration Inputs: An Experimental Comparison," *J. Sound Vib.*, Vol. 145, No. 2, 1991, pp. 195-215.
17. G. P. Gibbs, C. R. Fuller, and R. J. Silcox, "Active Control of Flexural and Extensional Power Flow in Beams using Real Time Wave Vector Sensors," *Proceedings of the 2nd Conference on Recent Advances in Active Control of Sound and Vibration*, Technomic, Lancaster, PA, 1993, pp. 909-925.
18. K. J. Astrom and B. Wittenmark, *Computer Controlled Systems*, Prentice-Hall, Englewood Cliffs, NJ, 1984.
19. J. M. Downing and K. P. Shepherd, "Power Flow in Beams Using a 5-Accelerometer Probe," *Proceedings of Noise-Con 88*, Purdue University, IN, 1988, pp. 335-340.
20. J. Scheuren, "Active Control of Bending Waves in Beams," *Proceedings of Inter-Noise 85*, Munich, 1985, pp. 591-595.
21. C. K. Lee, W. W. Chiang, and T. C. O'Sullivan, "Piezoelectric Modal Sensors and Actuators Achieving Critical Damping on a Cantilever Plate," *AIAA Paper*, No. 89-1390, 1989.
22. R. L. Clark and C. R. Fuller, "Modal Sensing of Efficient Radiators with PVDF Distributed Sensors in Active Structural Acoustic Approaches," *J. Acoust. Soc. Am.*, Vol. 91, No. 6, 1992, pp. 3321-3329.
23. B. Widrow and S. D. Stearns, *Adaptive Signal Processing*, Prentice-Hall, Englewood Cliffs, NJ, 1985.
24. S. J. Elliott, I. M. Stothers, and P. A. Nelson, "A Multiple Error LMS Algorithm and Its Application to the Active Control of Sound and Vibration," *IEEE Trans. Acoust., Speech and Signal Process.*, ASSP-35, 1987, pp. 1423-1434.
25. R. A. Burdisso and C. R. Fuller, "Theory of Feedforward Controlled Systems Eigenproperties," *J. Sound Vib.*, Vol. 153, No. 3, 1992, pp. 437-451.
26. P. A. Nelson and S. J. Elliott, *Active Control of Sound*, Academic, London, 1992.
27. W. L. Brogan, *Modern Control Theory*, Prentice-Hall, Englewood Cliffs, NJ, 1982.
28. K. B. Scribner, L. A. Sievers, and A. H. von Flotow, "Active Narrow Band Vibration Isolation of Machinery Noise From Resonant Substructures," *J. Sound Vib.*, Vol. 167, No. 1, 1993, pp. 17-40.
29. P. A. Nelson, M. D. Jenkins, and S. J. Elliott, "Active Isolation of Periodic Vibrations," *Proceedings of Noise-Con 87*, Penn State University, State College, PA, 1987, pp. 425-430.
30. A. H. von Flotow, "An Expository Overview of Active Control of Machinery Mounts," *Proceedings of the 27th Conference on Decision and Control*, Austin, TX, 1988.
31. G. P. Gibbs and C. R. Fuller, "Experiments on Active Control of Vibrational Power Flow Using Piezoceramic Actuators and Sensors," *AIAA J.*, Vol. 30, No. 2, 1992, pp. 457-463.
32. C. R. Fuller, G. P. Gibbs, and R. J. Silcox, "Simultaneous Active Control of Flexural and Extensional Waves in Beams," *J. Intell. Mat. Systems Struct.*, Vol. 1, No. 2, 1990, pp. 235-247.
33. S. J. Elliott and L. Billet, "Adaptive Control of Flexural Waves Propagating in a Beam," *J. Sound Vib.*, Vol. 163, 1993, pp. 295-310.
34. S. J. Elliott, T. J. Sutton, M. J. Brennan, and R. J. Pinnington, "Vibration Reduction by Active Wave Control in a Strut," *Proceedings of the IUTAM Symposium on the Active Control of Vibration*, Bath, England, 1994, pp. 1-8.
35. S. Rubenstein, W. R. Saunders, G. K. Ellis, H. H. Robertshaw, and W. T. Baumann, "Demonstration of a LQG Vibration Controller for a Simply Supported Plate," in C. A. Rogers and C. R. Fuller (Eds.), *Proceedings of Recent Advances in Active Control of Sound and Vibration*, Technomic, Lancaster, PA, 1991, pp. 618-630.
36. C. R. Fuller, "Analysis of Active Control of Sound Radiation from Elastic Plates by Force Inputs," *Proceedings of Inter-Noise 88*, Avignon, France, 1988, pp. 1061-1064.
37. B. K. Wada, J. L. Fanson, and E. F. Crawley, "Adaptive Structures," *Mech. Eng.*, November, 1990, pp. 41-46.